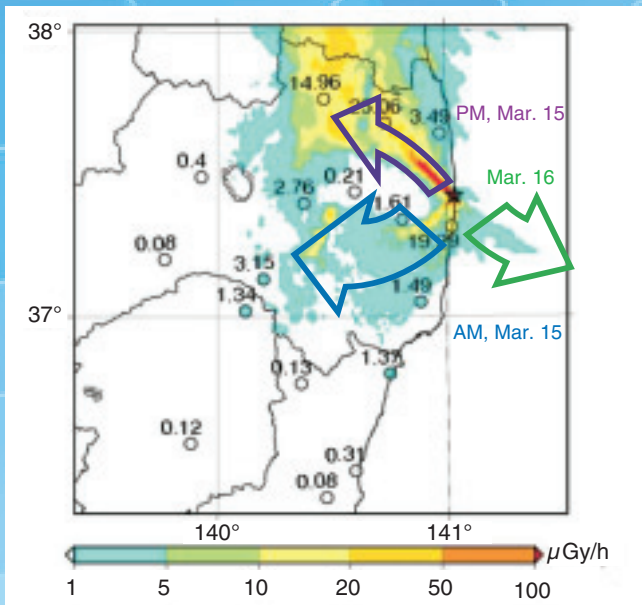
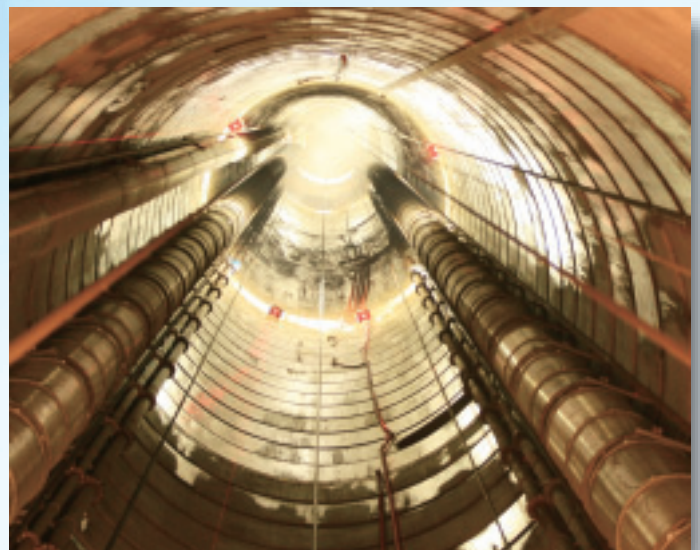


2011

JAEA R&D Review



Analytical results of air dose rate due to the 11 March, 2011 nuclear accident obtained by using WSPEEDI



Portion of the Main Shaft above GL -400 m when viewed from GL -400 m at Mizunami

Message from the President

鈴木 篤之

President Atsuyuki Suzuki



Japan Atomic Energy Agency (JAEA) implements a wide range of research and development, from our main expertise in nuclear energy and its uses to the more foundational development and creation of scientific and industrial technologies, in its role as the sole comprehensive R&D institute for nuclear energy in Japan. As we mark the 7th year of our establishment, we also approach the halfway point of the second mid-term plan.

On March 11th of this year, an unprecedented nuclear crisis occurred at the Tokyo Electric Power Company, Incorporated Fukushima Daiichi Nuclear Power Station. Immediately after the accident, the JAEA began working on various fronts together with Government and related local authorities to grasp the reality of the situation and help bring it under control.

This included dispatching specialists to the Nuclear Safety Commission of Japan, among others, to provide technical advice and scientific expertise as well as to conduct environmental radiation monitoring and analysis under the instruction of Japan's Ministry of Education, Culture, Sports, Science, and Technology (MEXT). Furthermore, in order to enhance processes such as on-the-spot environmental monitoring and decontamination technology verification and to strengthen cooperation with the appropriate prefectural authorities, a framework was constructed with the president of the JAEA serving as chief of headquarters for a base of operations established inside of Fukushima Prefecture. In the future, in addition to participating in undertakings such as decontamination, which are directed at swiftly restoring environmental conditions, we would like to proactively aid in the development of the infrastructure and technologies necessary to bring crises to a close, including the safe management of hazardous fuel and contaminated matter.

Such is the case with one of our four core operations, the "MONJU" fast breeder reactor. In addition to reevaluating the effects of external power supply loss caused by the tsunami during the accident at Fukushima, we are reassessing our safety measures while steadily proceeding with regularly scheduled work, including restoring relay equipment in the reactor core and repairing the reactor ducts. Also, although quite a few our important facilities were damaged, albeit nothing to do with nuclear safety, by the March 11th earthquake, we are working diligently to complete plans for our other three core operations. These include the R&D of quantum beam applied technologies, using the Japan Proton Accelerator Research Complex (J-PARC), for instance, the R&D of fusion energy technologies based on the International Thermonuclear Experimental Reactor (ITER) and the Broader Approach (BA) activities, and technological development regarding the geological repository of high-level radioactive wastes. Despite tight budget constraints, we are also steadily going forward with the

decommissioning of our own nuclear facilities and with the planning and implementation of underground disposal programs for radioactive waste arising from Japanese research facilities.

We believe it is important to proactively share and utilize the achievements of this organization's R&D.

This publication constitutes a review of our achievements in the fiscal year 2010. It provides you with a look at some of the work that has been carried out, and also invites you to check the references listed and contact the researchers if there are any topics that you wish to learn more about. I would be most gratified if I could hear from you with any comments on this publication.

I hope that you enjoy this publication. Thank you for your interest.

About This Publication and the Outline of Organization of JAEA	8
--	---

1 *Research and Development of Advanced Nuclear System*

Toward Commercialization of Fast Breeder Reactor Cycle	10
---	-----------

1. Japan's Initiative for International Harmonizing of Safety Standards – Establishment of Safety Design Criteria for Sodium-Cooled Fast Reactors –	11
2. Safety Evaluation of Core Disruptive Accidents – Development of Level-2 PSA Methodology for FBRs –	12
3. Residual Heat Removal Using Buoyancy Force – Evaluation Method for Core Hot Spot under Natural Circulation –	13
4. Reliability of Recovery Operation for Reactor Trip Failure – Evaluation of “MONJU” Accident Management by Employing Probabilistic Safety Assessment Technique –	14
5. Toward Extending the Service Life of Fast Breeder Reactor Plants – Evaluation of Aged and Repaired Welded Joints –	15
6. Enhancement of Safety and Economic Competitiveness of Fast Breeder Reactor Plant – Steel Plate Reinforced Concrete Containment Vessel –	16
7. Validation of JENDL-4.0 with “MONJU” Reactor Physics Data – ²⁴¹ Am Data Testing by Cross-Section Adjustment Technique –	17
8. Manufacturing MOX Raw Powder Uniformly and Effectively by Controlling Electromagnetic Waves – Study on Highly Effective Microwave Heating –	18
9. Research on Mechanical Properties of Fuel Claddings for High Burnup in Fast Breeder Reactors – Effects of Neutron Irradiation on Mechanical Properties of ODS Steel Claddings –	19
10. Technology for Removal of Excess Oxygen from MOX Fuels during Irradiation – Research and Development for MOX Fuel by Using Oxygen Getter –	20
11. For Effective Fuel Dissolution in Reprocessing – Development of Simulation Code for FBR Spent Fuel Dissolution –	21
12. Selective Electrochemical Dissolution of Spent Fuel – Behavior of Anodic Dissolution of U-Pu-Zr Alloy during Pyrochemical Reprocessing –	22
13. A New Extraction Process for Future Reprocessing – Development of Uranium and Plutonium Co-Recovery Process (Co-Processing Process) –	23

2 *Research and Development on Geological Disposal of High-Level Radioactive Waste*

R&D for Improving the Technology and Reliability of Geological Disposal in Japan	24
---	-----------

1. Transfer of Knowledge of Geoscience Technology – Information Synthesis and Interpretation System (ISIS) –	25
2. Evaluation of Uplift/Erosion Scenarios in the Far Future – Analysis Reflecting a Feature of Geomorphic Change in Japan –	26
3. First Release of Overpack Database – Information on Overpack Designing and Manufacturing and Experimental Data are Provided Intelligibly –	27
4. Revealing the Pore Structure and Diffusion Mechanism in Rock – Analysis of Pore Structure of Siliceous Mudstone Using Nano X-ray Computed Tomography –	28
5. Predicting the Future from Ancient Tectonism – History of Fault Development in Fractured Rocks –	29
6. Challenges in Collecting Nanoscale Particles from Groundwater – Development of New Ultrafiltration Techniques Maintaining In situ Pressure and Anaerobic Conditions –	30
7. Understanding Regional Stress in a Rock Mass – Estimation of Regional Stress Using Measured Stress –	31
8. Rock Mass Response to Shaft Excavation – Fault System Controlling Rock Mass Behavior in Soft Sedimentary Rocks –	32

- | | | |
|-----|---|----|
| 9. | Improvement in Reliability of Geological Disposal Technology
– Use of Low-Alkaline Cement in the Construction of a Gallery – | 33 |
| 10. | Investigation of Shallow Groundwater Migration at Snowy Cold Region
– Research of Shallow Groundwater Flow Based on Groundwater Level and Geological Structures in the Horonobe Area – | 34 |

3 Nuclear Fusion Research and Development

Toward the Practical Use of Fusion Energy 35

- | | | |
|-----|---|----|
| 1. | Significant Progress in ITER Coil Procurement
– Mock-Up Trials for ITER Toroidal Field Coils – | 36 |
| 2. | H ⁺ Beam Acceleration Close to ITER Requirement
– Development of 1 MeV Accelerator for ITER Neutral Beam Injector – | 37 |
| 3. | Fulfillment of ITER Criteria for RF Energy Transmission Efficiency
– Development of Electron Cyclotron Heating and Current Drive for ITER – | 38 |
| 4. | Innovative In-Vessel Mirror for Current Profile Measurement in ITER
– Development of Retroreflector for ITER Poloidal Polarimeter – | 39 |
| 5. | Progress in Satellite Tokamak Programme Project as part of Broader Approach Activities
– Construction Activities of JT-60SA Tokamak Right on Track – | 40 |
| 6. | Observation of Multistage Transition in Radial Electric Field
– A New Discovery Unexpected in the Case of the Standard Model – | 41 |
| 7. | Planning and Executing Joint Experiments, Leading International Team
– Toward Validation of Neutral Beam Current Drive Theory for ITER – | 42 |
| 8. | Exploring the Possibility of Inducing Plasma Rotation by Fusion Reactions
– Intrinsic Torque Generation by α -Particles – | 43 |
| 9. | Early Realization of Fusion Reactor
– International Fusion Energy Research Centre Project in the Broader Approach Activity – | 44 |
| 10. | Study on Formation of Temperature Profile of Plasma Core
– First-Principles Simulation of Plasma Transport – | 45 |
| 11. | Manufacture of Small Tritium Target for Use in Generating Neutrons in Fusion Reactor at JAEA
– Stable Procurement of Small Tritium Targets – | 46 |
| 12. | Validation of Fusion Reactor Materials
– Design and Construction of IFMIF/EVEDA Li Test Loop – | 47 |

4 Quantum Beam Science Research

Development of Quantum Beam Technology 48

- | | | |
|----|---|----|
| 1. | Toward the Realization of the Strongest and Brightest Electron Source in the World
– Development of a 500-kV Photocathode DC Electron Gun for Realizing Next-Generation Light Source – | 49 |
| 2. | Improvement of the Reflectivity of Relativistic Flying Mirrors
– Demonstration of Efficient Reflection of Laser Light from Plasma Waves – | 50 |
| 3. | Evaluation of Polarization of Soft X-rays
– Soft X-ray Optics and Polarization Analysis – | 51 |
| 4. | Development of Spin Contrast Variation Technique
– Verification Study with a Simplified Model System – | 52 |
| 5. | Clarification of Hidden Electronic Character Using Synchrotron Radiation X-ray
– Orbital State of Excited Electron Identified by Polarization-Analyzed Resonant Inelastic X-ray Scattering – | 53 |
| 6. | Toward Domain Observation Using Coherent X-rays
– Multiple-Length-Scale Approach Revealing the Nature of High-Functional Solids – | 54 |
| 7. | Mechanism of Performance Improvement of Hydrogen Storage Materials
– Structural Determination of Additives by X-ray Absorption Spectroscopy – | 55 |

8.	Development of Novel Rare-Earth-Recognition Compound – For Efficient Separation and Purification of Rare-Earth Elements –	56
9.	How to Produce Rare-Earth Metals by Ourselves? – Recovery of Rare-Earth Metals from Hot Springs –	57
10.	Purification of Factory Waste Gases Using By-Products Ozone – Electron Beam/Catalyst System for Purification of Waste Gases under Practical Gas-Flow Conditions –	58
11.	Low-Barrier Hydrogen Bond in Protein – Neutron Protein Crystallography Casts Light on a New Factor Important of Drug Design –	59
12.	Role of Electric Fields Produced by Heavy-Ion Irradiation in DNA Damage – Is Occurrence of Clustered DNA Damage Promoted by the Electric Fields? –	60
13.	Persistent Chromosomal Aberration Caused by Ionizing Radiation – Appearance of Micronuclei in Descendants of γ -ray-Irradiated Plant Cells –	61

5 Nuclear Safety Research

To Clarify Phenomena Threatening Nuclear Safety 62

1.	Origin of Hydrogen Embrittlement of Fuel Claddings – Calculation of Hydrogen Effect on Resistance to Crack Propagation –	63
2.	Evaluating Safety Performance of Oxidized Fuel Cladding – Investigation of Test Methods for Evaluating Fuel Integrity in Loss-of-Coolant Events –	64
3.	For Reliable Evaluation of Corrosive Conditions in Reactor Core – Enhancement of Technology for Water-Chemistry Evaluation –	65
4.	Research on Corrosion Resistance of Reactor Pressure Vessel – Evaluation of Degradation of Thermally Affected Stainless Steels by Microstructural Analysis –	66
5.	Development of Evaluation Method for Crack Growth Associated with Large Earthquakes – Accurate Prediction of the Crack Growth Rate of Piping Materials –	67
6.	Core Power Stability under Strong Earthquake – Neutron-Coupled Thermal Hydraulic Calculation under Seismic Acceleration –	68
7.	How to Evaluate the Radioactivity in a Nuclear Reactor under Operation? – System Development for Evaluating the Radioactivity in the Reactor –	69
8.	Estimation of Gaseous Iodine Revolatilization under Severe Accident Conditions – Application of Iodine Chemistry Reactions to Plant Evaluation –	70
9.	What Accelerates Dissolution of High-Level Waste Glass? – Effects of Magnesium Ions in Solution –	71
10.	Toward Safe Decommissioning of Nuclear Facilities – Development of Safety Assessment Code for Decommissioning Activities –	72

6 Advanced Science Research

For Evolution of Nuclear Science 73

1.	Magnetic Flow Turns Electronics into Spintronics – Discovery of New Principles for Generating Spin Currents –	74
2.	Detection of Electron Spins in Ferromagnets Using Spin-Polarized Positron – Development of Highly Spin-Polarized Positron Beam –	75
3.	Discovery of New Type of Fission – The Fission of ^{180}Hg is not Influenced by the Shells of Fragments –	76
4.	Unconventional Superconductivity in Uranium Compounds – Correlation between the Anomalous Electron Scattering and Superconductivity in URu_2Si_2 –	77
5.	Biological Nanoparticle Production Factory – Recovery of Heavy Elements by Using Microorganisms –	78

7 Nuclear Science and Engineering Research

Establishment of Basis for Nuclear Energy R&D, and Development of Innovative Technology	79
1. Nuclear Polarization Controlled by a Laser Beam	80
– Dynamic Nuclear Self-Polarization Induced by Circularly Polarized Light –	
2. Simulated Melting and Solidification of Metal	81
– Extension of Mechanistic Liquid-Gas Two-Phase Flow Analysis Method –	
3. Approach for Realization of Transmutation Technology	82
– Issues Pertaining to Reactor Design for Accelerator-Driven System –	
4. Change in Fuel Microstructure Induced by Helium Accumulation and Release	83
– Expansion and Annealing Correlation for Lattice and Bulk –	
5. Great Challenge of Separation of Minor Actinides by Solvent Extraction	84
– Trial Use of Hydrophilic and Lipophilic Diamides –	
6. How Hydrophilic are Actinide Ions?	85
– Determination of Standard Gibbs Energy of Transfer at Aqueous/Organic Interface –	
7. Prediction of Irradiation-Assisted Stress Corrosion Cracking of Structural Materials in Nuclear Reactors	86
– Study on Material Degradation Diagnosis Method Using Magnetic Sensor –	
8. Analysis of Isotopic Composition without Touching the Sample	87
– Isotope Analysis of Nuclear Fuel Using Resonance Absorption Spectrometry –	
9. Towards Prediction of Dispersion of Hazardous Materials in Urban Area	88
– Development of Local-Scale High-Resolution Atmospheric Dispersion Model –	
10. Production of Medical RIs Using Accelerator Neutrons	89
– Development of an Innovative RI Production Method –	

8 Nuclear Hydrogen and Heat Application Research

Research on HTGR and Nuclear Heat Applications to Establish a Low-Carbon Society	90
1. Toward a Reactor with Highest Safety Standards	91
– Development of HTGR Based on Inherent Safety Features –	
2. Development of High-Pressure Ceramic Components for Hydrogen Production	92
– Strength Estimation Method for Component Design –	

9 Development of Decommissioning and Radwaste Treatment Technology

Executing Decontamination & Dismantling and Radwaste Treatment & Disposal	93
1. Rational Decommissioning Planning	94
– Development of Project Management Data Evaluation System –	
2. Development of Decontamination Technique for Radioactive Wastes Using Supercritical Fluid	95
– Reverse Micelle Formation in Supercritical Carbon Dioxide –	
3. Toward Analysis of Radionuclides in Solidified Products	96
– Preparation of Reference Materials Containing Volatile Nuclides –	

10 Computational Science and E-Systems Research

Advanced Computing and Simulation Technology to Support Atomic Energy Research and Development	97
1. Determination of Properties of Nuclear Fuels through Numerical Simulation	98
– First-Principles Calculations of Electronic States of Plutonium Dioxide –	

- 2. Solving the Mystery of Hydrogen-Induced Strength Degradation 99
 - Development of Atomic-Scale Model of Hydrogen and Iron Atoms –
- 3. Finding Important Information in Experimental or Simulation Results 100
 - Proposal of Visualization Technique for Capturing Temporal and Spatial Fluctuations –
- 4. Understanding Fluid Motion in a Spent Fuel Pool 101
 - Proposal of Fluid Analysis Model including Turbulent Effect near Surfaces and Walls of Pool –

11 *Scientific & Technical Development for Nuclear Nonproliferation*

Development of Nuclear Nonproliferation Technology to Support Peaceful Use of Nuclear Energy 102

- 1. Evaluation of Japan's Nuclear Non-proliferation Efforts in Terms of Providing Guidance to Other States 103
 - Key Elements to Win the Confidence in the Peaceful Nature of the Nuclear Energy Use and Recommendations for the Future –

12 *Development of Experimental Techniques / Facilities at JAEA R&D Centers*

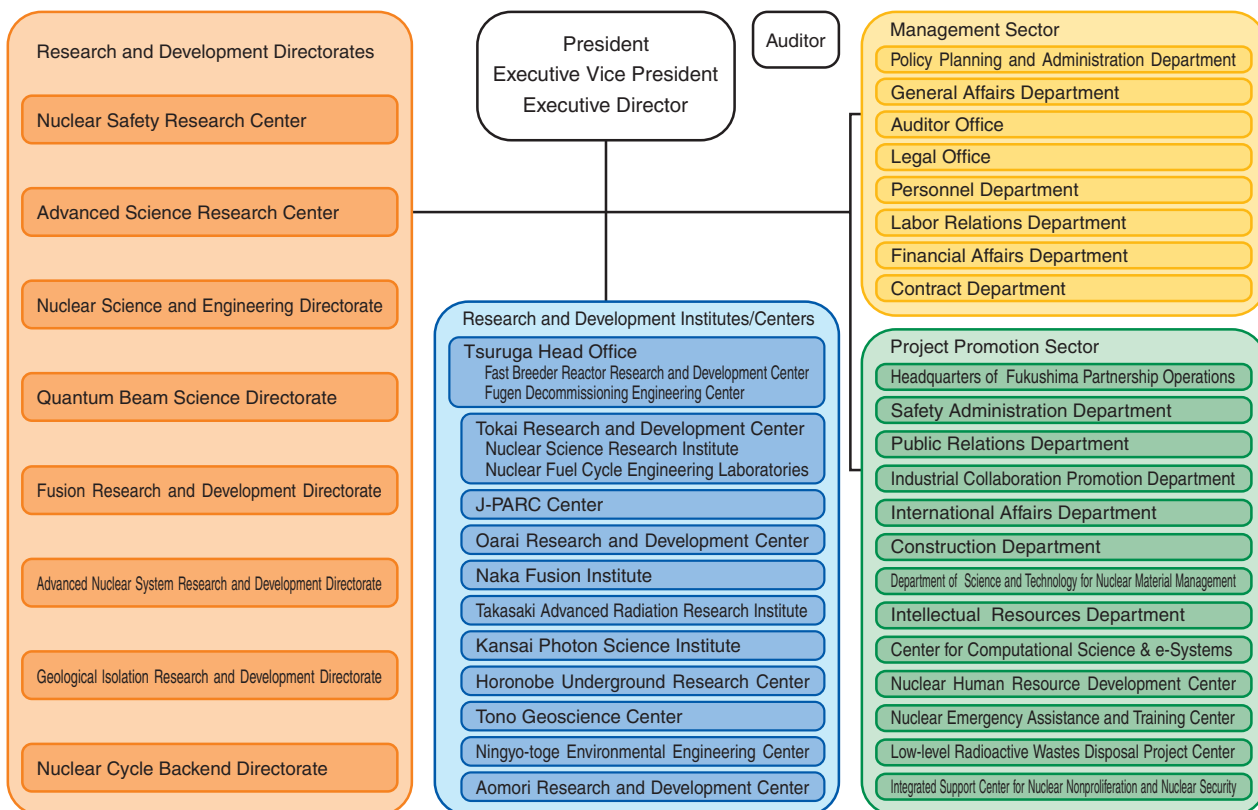
- 1. What Was Acquired from Restarted “MONJU” Operation 108
 - Results of the “MONJU” Core Confirmation Test –
- 2. Low-Cost and Labor-Saving Method for Replacement of Acrylic Panels of a Large Glove Box 109
 - Innovative Panel Replacement Technique Using Bag-In/Bag-Out Method –
- 3. Removal of Liquid Impurities in Crystal by Sweating 110
 - Purification of Uranyl Nitrate Hexahydrate Crystal by Isothermal Sweating Effect –
- 4. Effective Preparation of MOX Pellets 111
 - Development of a New Method for Fabricating MOX Pellets Having Low Oxygen-to-Metal Ratio Using Residual Carbon –
- 5. Precise Control of High-Intensity Proton Beams 112
 - Beam Handling by the Digital Low-Level RF Control System –
- 6. Polarizing the Spins of Pulsed Neutron Beams 113
 - Development of Neutron Polarizing Devices for J-PARC –
- 7. Improving the Safety of Liquid-Metal Facilities 114
 - Countermeasures for Lithium Leak in the IFMIF/EVEDA Lithium Test Loop –
- 8. Viewing the Behavior of Fuel Pellets 115
 - Irradiation Behavior Investigation of FBR Fuel by High-Resolution X-ray CT –
- 9. Challenges to Domestic Production of ⁹⁹Mo Using JMTR 116
 - Development of a New Mo Adsorbent for ⁹⁹Mo-^{99m}Tc Generator –
- 10. Expansion of Measurable Dose Range 117
 - Development of Dosimetry for Quality Assurance in Radiation Processing –
- 11. Excavation of Research Tunnels Deep Underground 118
 - Excavation and Construction of Shafts and Tunnels at the Mizunami Underground Research Laboratory –
- 12. A Trial for Uranium Wastes Assay Used Neutrons!! 119
 - Developments of NDA Tools of Uranium Wastes Drums: NWAS –

About This Publication and the Outline of Organization of JAEA

This publication aims to introduce the latest our R&D results in each field, divided into their respective chapters. The R&D results presented in each chapter, correspond to the activities of the relevant R&D Directorates. As shown in the Organization Chart, the various R&D Directorates carry out their activities through R&D Centers or Institutes. Some of these consist of only one site, while others are located two or more locations, depending on the components of their R&D activities. The R&D Centers and Institutes are located all over Japan, as shown in the map below. The following brief introductions give an outline of research undertaken by each R&D Directorate through the various R&D Centers/Institutes.

1. The **Advanced Nuclear System Research and Development Directorate** is carrying out R&D aimed at commercializing the fast breeder reactor (FBR) and its nuclear fuel cycle. The R&D of plant technology using the prototype fast breeder reactor “MONJU” is undertaken at the Tsuruga Head Office (Fast Breeder Reactor Research and Development Center), the R&D of innovative FBR technology is conducted at the Oarai Research and Development Center, and the R&D on manufacturing plutonium fuel and reprocessing spent FBR fuel, among others is conducted at the Tokai Research and Development Center (Nuclear Fuel Cycle Engineering Laboratories).
2. The **Geological Isolation Research and Development Directorate** is carrying out multidisciplinary R&D aimed at improvement in reliability of geological isolation of high-level radioactive waste in Japan. A particular focus involves establishing techniques for investigating the deep geological environment through researches both at the Tono Geoscience Center in crystalline rocks and at the Horonobe Underground Research Center in sedimentary rocks. At the Tokai Research and Development Center, the focus is on improving technologies for designing disposal facilities and safety assessment. In addition, work has been on going to develop a next generation knowledge management system based on the above R&D activities.
3. The **Fusion Research and Development Directorate** is executing research and development activities as a domestic agency of the International Thermonuclear Experimental Reactor (ITER) project and an implementing agency of the Broader Approach (BA) activities. The procurement activity of the ITER project, the upgrade of JT-60 to superconducting machine as the BA activity, fusion plasma research and the R&D on various element technologies are carrying out in Naka Fusion Institute. Moreover, the International Fusion Energy Research Center project and the Engineering Validation and Engineering Design Activities of the International Fusion Material Irradiation Facility are executed mainly in the Aomori Research and Development Center.
4. The **Quantum Beam Science Directorate** is engaged in research using neutron in the Tokai Research and Development Center (Nuclear Science Research Institute) and J-PARC Center, research using electron beam, gamma ray, and ion beam in the Takasaki Advanced Radiation Research Institute, and research using lasers and synchrotron radiation at the Kansai Photon Science Institute.

Japan Atomic Energy Agency -Outline of Organization-



as of December, 2011

5. The **Nuclear Safety Research Center** is in charge of researching for national safety regulations on nuclear power plants, nuclear fuel cycle facilities and radioactive waste disposal facilities, among others, based in the Tokai Research and Development Center and the Tsuruga Head Office.
6. The **Advanced Science Research Center** conducts pioneering research in basic fields of nuclear power science, mainly through the Tokai Research and Development Center (Nuclear Science Research Institute) and Takasaki Advanced Radiation Research Institute.
7. The **Nuclear Science and Engineering Directorate** is engaged in key and basic research on various element technologies that support the use of nuclear power. These efforts are carried out in the Tokai Research and Development Center (Nuclear Science Research Institute) and the Oarai Research and Development Center.
8. The **Nuclear Hydrogen and Heat Application Research Center** conducts R&D on technology for the use of high-temperature heat supplied from high-temperature gas-cooled reactors and technology for hydrogen production using this heat in the Oarai Research and Development Center.
9. The **Nuclear Cycle Backend Directorate** develops technology for safe and rational decommissioning of nuclear power facilities as well as measures for processing and disposal of radioactive waste, in the Tokai Research and Development Center.
10. The **Center for Computational Science & e-Systems** develops pioneering simulation technology and basic technology in computational science, as well as operating and maintaining computer equipment, mainly in the Tokai Research and Development Center (Nuclear Science Research Institute).
11. The **Department of Science and Technology for Nuclear Material Management** and Integrated Support Center for Nuclear Nonproliferation and Nuclear Security develops technology for nuclear nonproliferation and safeguards to ensure the peaceful use of nuclear energy, in the Tokai Research and Development Center (Nuclear Science Research Institute) and Techno Community Square Ricotti.
12. The **R&D Centers and Institutes** located at 11 sites in Japan, manage and improve the performance of the facilities and equipments to support the above-mentioned R&D Directorates in the safe and efficient R&D activities.

R&D Centers of JAEA



Toward Commercialization of Fast Breeder Reactor Cycle

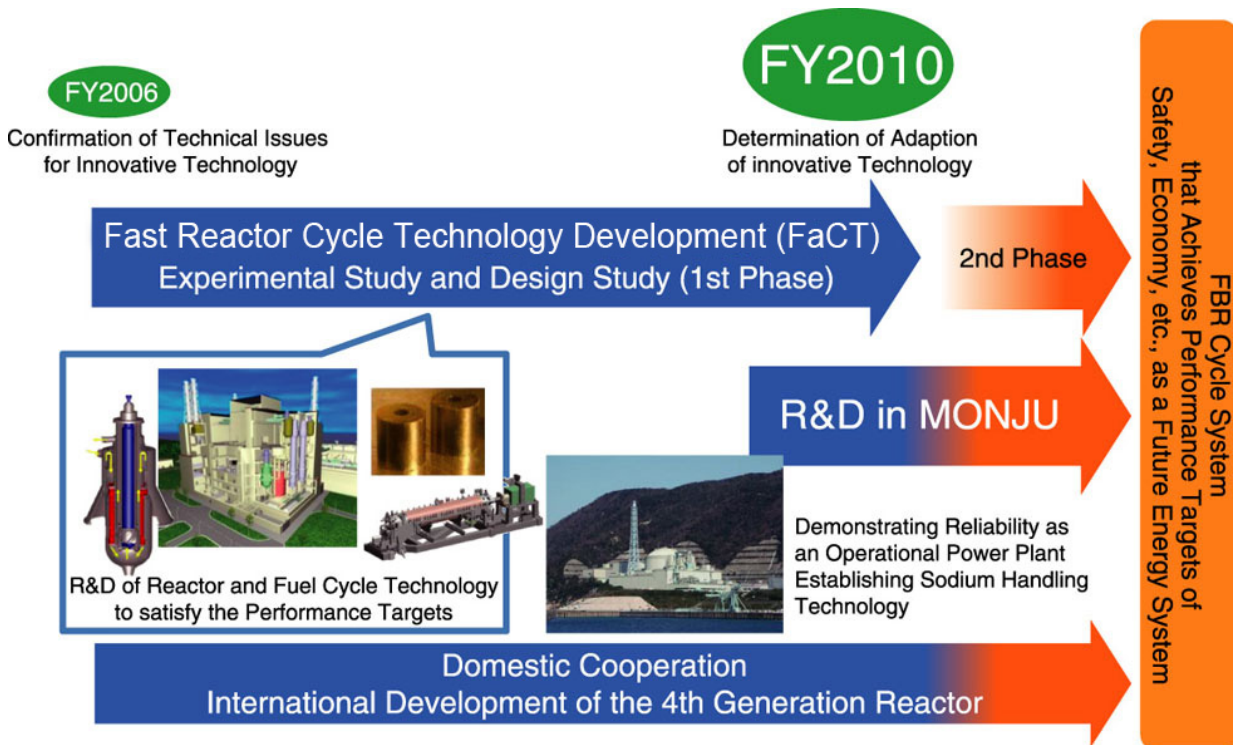


Fig.1-1 Overview of research and development aiming to commercialize FBR cycle

With the aim of future commercialization of the FBR cycle that has superior performance than other energy-supply systems in terms of safety, economy, environmental preservation, effective resource use, and nuclear-proliferation resistance, we are conducting an experiment and a design study on innovative technology to satisfy the performance target.

We are promoting the research and development (R&D) of “Fast Reactor Cycle Technology Development” named “FaCT project” and R&D in “MONJU” in order to commercialize the fast breeder reactor (FBR) and the related fuel cycle (Fig.1-1).

We set the performance target of the FaCT project such that the power supply needs of the future will be satisfied. Further, we have been conducting an experiment and a design study of innovative technology based main concept, which is a combination of the concepts of a sodium-cooled fast reactor using an oxide fuel, advanced reprocessing, and a simplified pelletizing fuel fabrication. In the end of FY2010, we had determined the innovative technologies to be adapted to realize a commercial system and completed the first phase. The system start-up test of the “MONJU” was resumed and the core confirmation test was completed in FY2010. The summary of the topics that will be discussed in the following pages is as follows.

In order to establish a safety design criteria as an international standard for the next-generation (4th-generation) reactor, we developed a safety design concept for FBR, with multilateral cooperation (Topic 1-1). In addition, we developed an evaluation method to quantify the frequency and impact of a hypothetical core-disruption accident (Topic 1-2) and a method for evaluating the performance of a core-cooling system by natural convection at the loss of

pump power supply (Topic 1-3). We also demonstrated the feasibility of accident management (AM) at “MONJU” (Topic 1-4). In this study, by performing tests on actual materials, we identified the parameters for evaluating material integrity (Topic 1-5). We predicted the feasibility of a steel-plate-reinforced concrete containment vessel that satisfied both safety and economic requirements (Topic 1-6). Using the results of “MONJU” core confirmation test, we showed that the nuclear data was highly reliable (Topic 1-7).

For the fuel fabrication, we showed that microwave heating is suitable to make the raw fuel powder appropriate for the mass production system (Topic 1-8). To develop the long lived fuel, we confirmed the integrity of the irradiated cladding material of the next-generation fuel (Topic 1-9), and we showed the feasibility of using an extra oxygen absorber to prevent corrosion on the inner surface of the cladding (Topic 1-10). On the basis of the hot experiment using spent fuel for the preliminary study on process operation for increasing efficiency, we developed a dissolution simulation code for the reprocessing technology (Topic 1-11). In relation to the pyroprocessing for the metallic fuel, we showed the issues to enhance the dissolution efficiency (Topic 1-12). In addition, we are also conducting an experimental study to establish a new process for the installation stage of the FBR cycle (Topic 1-13).

1-1 Japan's Initiative for International Harmonizing of Safety Standards — Establishment of Safety Design Criteria for Sodium-Cooled Fast Reactors —

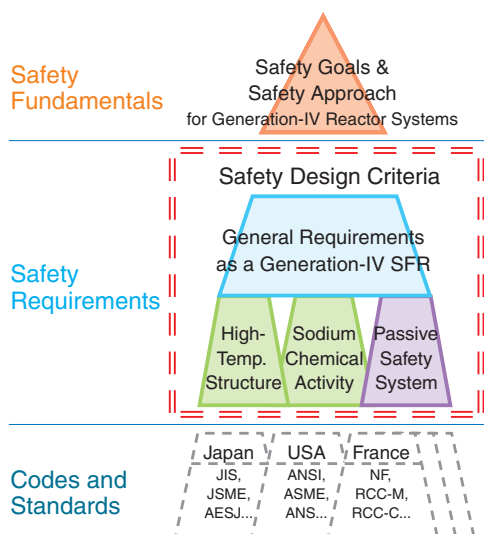


Fig.1-2 SDC in the hierarchy of safety standards
SDC systematically specify design concepts of various systems and equipment in compliance with safety fundamentals. No international standards have been established so far for Generation-IV reactors including SFR.

Generation-IV (Gen-IV) International Forum (GIF) has mainly promoted the research & development (R&D) of reactor systems and equipment, and recently, cooperation to establish safety design criteria (SDC) has started.

Fig.1-2 shows the hierarchy of safety standards. The SDC rank between the upper fundamental standards, and the lower codes and standards. Systems and equipment are manufactured by following the codes and standards, and the SDC systematically specify their design concepts that satisfy fundamental safety principles. No international standards for Gen-IV reactors, including sodium-cooled fast-breeder reactor (SFR), have been established so far, and this will be the first attempt to address this issue.

There are three points to be remembered while formulating the SDC. The first is that the safety standards for the Gen-IV reactor should be stringent, the second is that specific technical features of SFR should be taken into account, and the third is that the R&D results for innovative technologies and the lessons learned from the accident at the Tokyo Electric Power Company, Incorporated Fukushima Daiichi Nuclear Power Station, should be considered.

Fig.1-3 shows their relationship and the process for establishing SDC. “Very low likelihood and degree of reactor core damage” is one of the safety objectives at GIF, and we need to accomplish this objective by following the safety approach of considering unexpected conditions that are

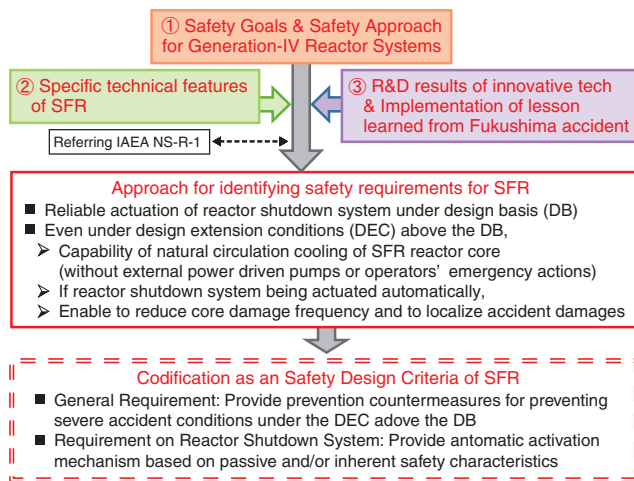


Fig.1-3 Process for establishing new SDC
To clarify the high level of safety required for Generation-IV reactor systems, the SDC have been established by taking into account the technical features of SFR, research and development results of innovative technologies, and lessons learned from the accident at Fukushima Daiichi NPS.

severer than the design conditions. SFR has features that could induce the reactivity to increase when core becomes disrupted, and even in an emergency, the overall decay heat can be removed by natural circulation. Then, a reactor can be cooled naturally even in an emergency if recriticality is prevented by controlling reactivity. It is highly expected that Self-Actuated Shutdown System (SASS), a new technology that has been successfully tested in an in-reactor experiment, will have practical application in the case of the SFR.

Thus, the SFR safety goals established at GIF will be achieved when automatic activation of a reactor shutdown system is realized even when unexpected accidents occur, whereas the existing requirements to ensure the activation of the reactor shutdown system should be satisfied without the failure of the design conditions. We can include this in the SDC (1) to adopt measures to prevent core damage in the case of conditions that are severer than the ones specified as the design conditions and (2) to provide an automatic activation system for facilitating the activation of the reactor shutdown system by using natural forces. We also tried to establish SDC for cooling systems and containment systems by following the same process.

We will try to propose this SDC at GIF as a concept that will enable the achievement of a higher level of safety, and subsequently, we will aim to realize international standardization.

Reference

Okano, Y. et al., Safety Principles and Safety Approaches for Next Generation Sodium-Cooled Fast Reactor, Proceedings of 2011 International Congress on Advances in Nuclear Power Plants (ICAPP' 11), Nice, France, 2011, paper 11037, p.719-727, in CD-ROM.

1-2 Safety Evaluation of Core Disruptive Accidents – Development of Level-2 PSA Methodology for FBRs –

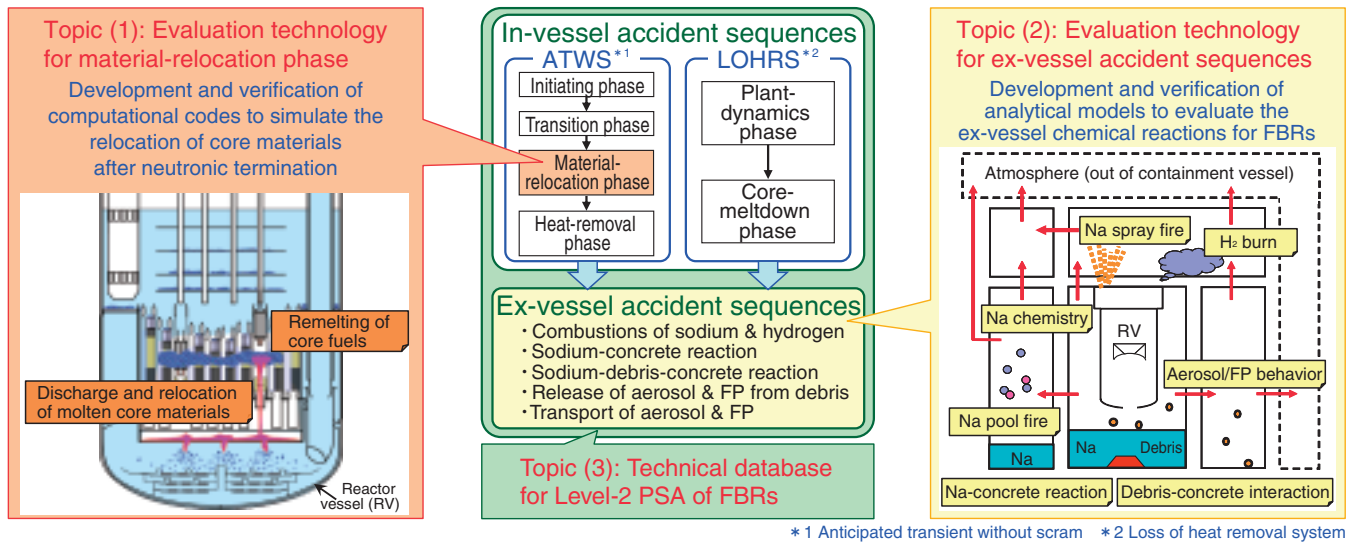


Fig.1-4 Development of Level-2 PSA Methodology for FBRs

Lacking technologies were newly developed, and the evaluation methodology for Level-2 PSA of FBRs was consolidated.

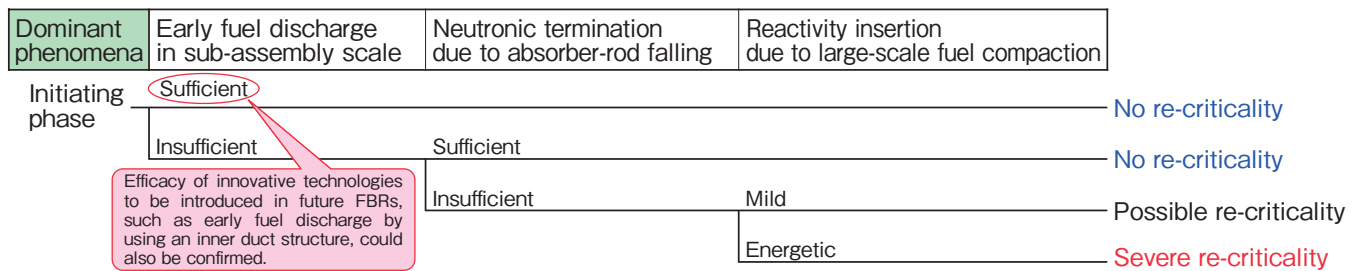


Fig.1-5 Construction of event tree in Level-2 PSA for FBRs (transition phase in ATWS)

Dominant phenomena were identified by sensitivity analyses, and factors of grave results such as re-criticality were clarified.

In the safety assessment of FBRs, it is necessary to evaluate whether appropriate measures have been taken against phenomena that have negligible probabilities but would lead to grave consequences if they occurred, and whether the risks (probability × consequence) are within acceptable bounds. Probabilistic safety assessment (Level-2 PSA) is an effective approach for the study of these issues, because it can deal with the uncertainties of event progressions from the core disruptive accident (CDA) to the release of radioactive material. In the Level-2 PSA for FBRs, it is important to develop evaluation technologies that take the FBR features into account.

In the present study, the methodology for the Level-2 PSA of FBRs was consolidated by developing new technologies that were lacking in previous studies: (1) an evaluation technology for the material-relocation phase; (2) an evaluation technology for ex-vessel accident sequences; and (3) a technical database for Level-2 PSA of FBRs (Fig.1-4).

In (1), the computational codes MUTRAN and SIMMER-LT were developed and verified for the simulation of material relocations after neutronic termination in CDAs. In (2), the analytical models CORCON and VANESA were developed and verified on the basis of new experiments for the evaluation of chemical reactions particular to FBRs. In (3), the dominant phenomena were identified by sensitivity analyses, and were used to construct event trees, in which the factors leading to grave consequences such as re-criticality were clarified (Fig.1-5). In addition, related experimental/analytical results were compiled into a technical database to quantify the branch probabilities in the event trees. These developments enabled us to execute the Level-2 PSA for FBRs.

The present study was sponsored by the Ministry of Education, Culture, Sports, Science and Technology of Japan (MEXT).

Reference

Nakai, R., Suzuki, T. et al., Development of Level 2 PSA Methodology for Sodium-Cooled Fast Reactors (1) Overview of Evaluation Technology Development, Proceedings of 8th International Topical Meeting on Nuclear Thermal-Hydraulics, Operation and Safety (NUTHOS-8), Shanghai, China, 2010, N8P0095, 12p., in CD-ROM.

1-3 Residual Heat Removal Using Buoyancy Force

– Evaluation Method for Core Hot Spot under Natural Circulation –

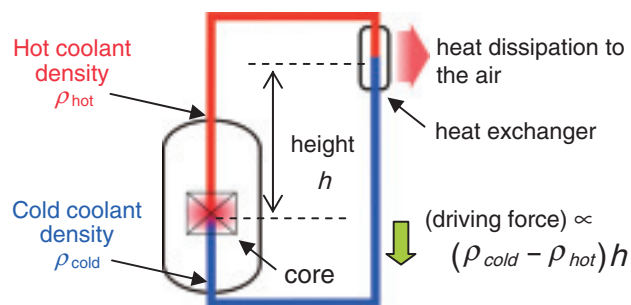


Fig.1-6 Natural circulation in the heat transport systems
Coolant flow is driven by buoyancy force without pumps.

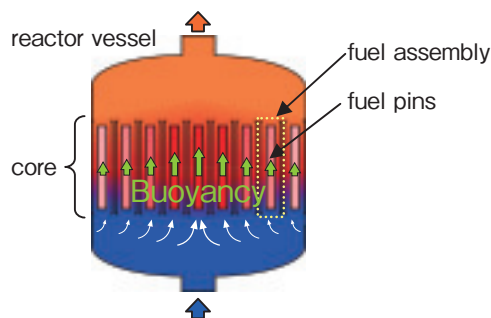


Fig.1-8 Flow redistribution in a core
Since a higher temperature induces a larger flow rate because of buoyancy, the coolant temperature distribution in a core becomes flatter than that under forced convection.

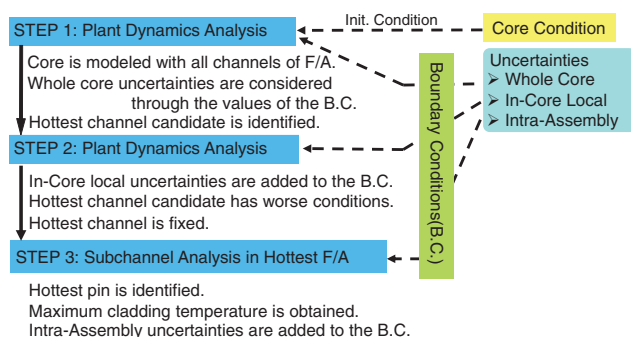


Fig.1-7 Evaluation method for core hot spot under NC
Three-step thermal hydraulics analysis is carried out to identify the hottest fuel assembly (F/A) and the hottest fuel pin under natural circulation conditions. Uncertainties are considered through their boundary conditions.

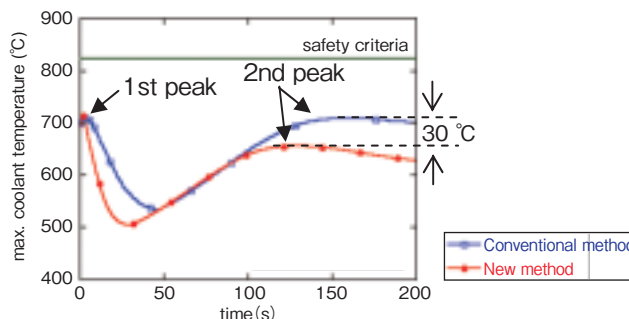


Fig.1-9 Evaluated hottest coolant temperatures (loss-of-external-power event)
The new method can evaluate a core hot spot reasonably with eliminating too much conservativeness.

Although the residual heat after reactor scram ($\approx 5\%$ of rated operation) decreases with time, for reactor safety, it is important to maintain the circulation of coolant through the core and to remove the decay heat.

In sodium-cooled fast reactors, natural circulation (NC) occurs because of buoyancy, which is proportional to the large temperature difference between the heat source (core) and heat sink (heat exchanger) and its height difference, as shown in Fig.1-6. The “JOYO” and “MONJU” reactors in Japan are designed to remove the residual heat in the core by NC of the coolant, even if the electric pumps should not be able to operate. The advanced fast reactor (JSFR) has a fully NC decay heat removal system.

A safety criterion for the core structural integrity under decay heat removal operations is the hottest coolant temperature, which is evaluated by conservative consideration of various uncertainties. Under NC, however, the coolant flow rate and temperature distributions in the core

change dynamically, and the uncertainty does not always affect in the same way, so it should be treated differently from the situation when under forced convection. We developed a new evaluation method (Fig.1-7) that can consider the characteristic phenomena particular to NC and their flattening effects on the coolant temperature distribution in the core (Fig.1-8). The hottest coolant temperature evaluated at the secondary peak can be reduced by approximately $30\text{ }^{\circ}\text{C}$ compared to that in the conventional method (Fig.1-9). The results of this study are applied to the development of reactors that make use of natural circulation.

The present study was performed under a contract with Mitsubishi Fast Breeder Reactor (MFBR) Systems, Inc., as part of the study “Development of evaluation methods for decay heat removal by natural circulation under transient conditions”, which was entrusted to MFBR Systems, Inc., by the Ministry of Education, Culture, Sports, Science and Technology of Japan (MEXT).

Reference

Doda, N. et al, Development of Core Hot Spot Evaluation Method for Natural Circulation Decay Heat Removal in Sodium Cooled Fast Reactor, Proceedings of the 14th International Topical Meeting on Nuclear Reactor Thermalhydraulics (NURETH-14), Toronto, Canada, 2011, NURETH14-170, 13p., in CD-ROM.

1-4 Reliability of Recovery Operation for Reactor Trip Failure

— Evaluation of “MONJU” Accident Management by Employing Probabilistic Safety Assessment Technique —

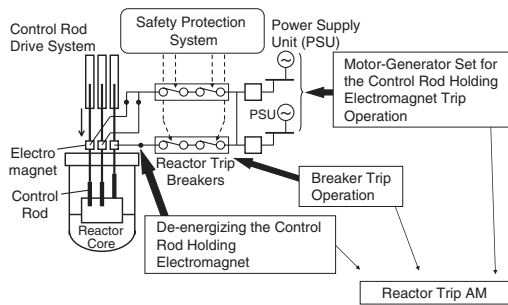


Fig.1-10 Schematic diagram of reactor trip AM

Operators can safely trip a reactor by following the AM procedures shown in this figure.

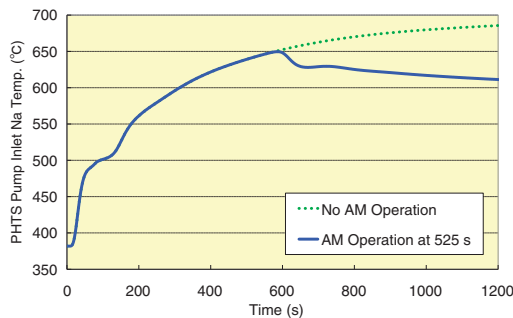


Fig.1-11 Inlet sodium temperature PHTS pump in the case of ULOHS

Operators get about 8 min to perform de-energizing of the control rod electromagnet in ULOHS.

This section describes a method and an application of quantitative evaluation of accident management (AM) reliability for the “MONJU” fast breeder reactor in the event of a reactor trip failure, as shown in Fig.1-10; this evaluation is based on the probabilistic safety assessment (PSA) technique. There are two types of event sequence categories of Anticipated Transient Without Scram (ATWS): failure of reactor trip breakers’ opening function and control-rod-insertion function. Therefore, Primary Heat Transport System (PHTS) pump operation is maintained, and reactor-trip AM reliability can be expected to be high in the former case because this case has longer allowable time than other cases.

Using the present method, the allowable time can be estimated on the basis of plant-transient-response analysis using the Super-COPD code that was developed for use in obtaining the best estimates of the plant dynamics of “MONJU”. In this allowable-time estimation, the temperature is considered to be 650 °C, which is the potential sodium temperature corresponding to PHTS pump failure. The assumed AM operating condition in the analysis condition only involves de-energizing of the control rod holding electromagnet because this procedure can be

Table 1-1 Simulator training results

*Blind test results were adjusted using the differences of the average informed test results.

Operation Completion Time (s)	Adjusted Time (s)
36	125
51	127
52	129
66	137
82	140
108	141
127*	155
129*	171
137*	197
190	216
196	279
216*	285
326*	326

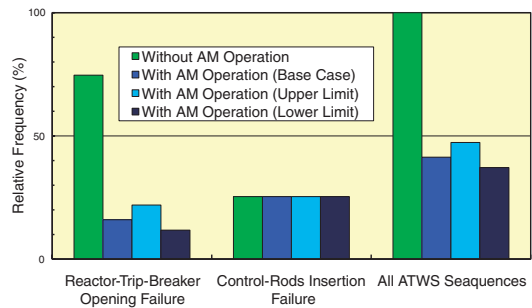


Fig.1-12 ATWS frequency reduction owing to reactor trip AM operation

This AM is ineffective in control-rod-insertion failure because as a result of its short allowed time, all ATWS frequency decreased by 50%.

performed in the main control room. The probability of failure of an operator involved in AM, within the allowable time was estimated on the basis of the time records obtained from simulator trainings, as shown in Table 1-1.

Application of this method in “MONJU” resulted in the estimation that the allowable time for an Unprotected Loss-Of-Heat Sink (ULOHS) event that is a representative ATWS event sequence would be about 8 min as shown in Fig.1-11, and this estimated allowable time was more than the longest observed allowable time of 5 min even after considering the uncertainty of the analysis conditions.

The operation failure probability would be less than 0.1 even after taking the uncertainty into consideration. The reliability of the de-energizing operation in an ULOHS event that is initiated by the failure of a reactor trip breaker to open can be evaluated quantitatively from these estimation results.

Using the abovementioned information, it is shown that in the case of a level-1 PSA, the total frequency of ATWS that is core damage accompanying a reactor trip failure at “MONJU” could be decreased by at least 50% by reactor trip AM even after considering the uncertainty, as shown in Fig.1-12. Thus, the reactor trip AM reliability is verified.

Reference

Sotsu, M. et al., Assessment of FBR MONJU Accident Management Reliability in Causing Reactor Trips, Journal of Nuclear Science and Technology, vol.47, no.10, 2010, p.867-883.

1-5 Toward Extending the Service Life of Fast Breeder Reactor Plants — Evaluation of Aged and Repaired Welded Joints —

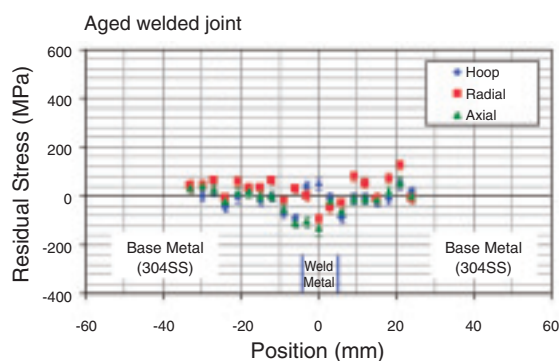


Fig.1-13 Residual stress distributions at the welded joint used in Phenix

The residual stress of the aged welded joint is low, which shows that the residual stress decreases while the FBR plant is in operation.

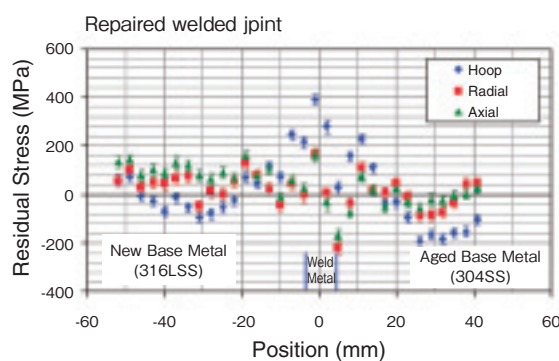


Fig.1-14 Residual stress distributions at the repaired welded joint

This joint was not used after repairing. Repair welding increased residual stress, but the residual stress will decrease while the FBR plant is in operation, as shown in Fig.1-13.

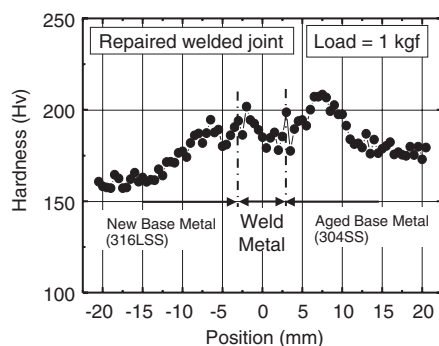


Fig.1-15 Hardness test results of the repaired welded joint

This joint was not used after repairing. The hardness of the aged base metal increased due to the repair welding, but it is low in the immediate vicinity of the weld metal; thus, a difference in hardness exists.

To extend the service life of fast breeder reactor (FBR) plants, the effect of aging (use for a long time in FBR plants) on the mechanical properties of the structural materials needs to be evaluated. The evaluation of welded joints is considered particularly important. However, very few evaluations have been performed on the aging of welded joints in use for a long time in FBR plants; thus, acquisition and evaluation of data on aging is desired. In this study, the focus is on welded joints' residual stress and hardness that are the properties corresponding to the strength of the material. The evaluations were performed on a welded joint of austenitic stainless steel that had been in use for a long time (approximately 88000 h at 526~545 °C) in the secondary cooling pipe of the fast breeder reactor Phenix in France.

Measurement of the residual stress of the welded joint was carried out using a neutron ray, and the results are shown in Fig.1-13. The residual stress is observed to be low for the aged welded joint (AWJ), and it decreases (relaxes) while the plant is in operation. The hardness distribution in the AWJ is almost uniform, but this is not shown in the figures. There are no areas where degradation in mechanical properties is observed.

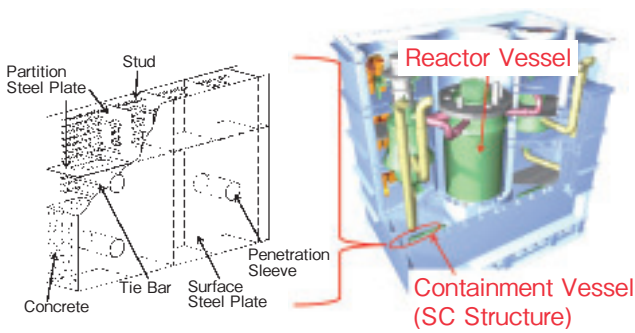
An actual plant is likely to have repaired welded joints

(RWJs) in which an unaged material (new material) might be welded onto a material that has been used for a long time (aged material). In such welded joints, the mechanical properties are anticipated to be inferior to those of a welded joint in which both materials are new, because one part of the welded joint is composed of the aged material. Therefore, to extend the plant service life, it is also important to evaluate the effects of such RWJ. Fig.1-14 shows the measured residual stress of an RWJ in which a new material was welded onto an aged material that had been in use at Phenix. Repair welding causes residual stress; however, as shown in Fig.1-13, the residual stress will reduce while the plant is in operation. Therefore, in an operating FBR plant, the influence of residual stress on mechanical properties is assumed to decrease. Fig.1-15 shows the hardness test results of the RWJ. It is observed that hardness varies near the aged base metal part of the welded joint. A pronounced change in hardness can cause stress concentration, which might degrade the mechanical properties of the welded joint. Although further investigation of the mechanical properties of the RWJ is needed, the results of this study suggest that the change in hardness is an important index in the evaluation of mechanical properties of RWJ.

Reference

Obara, S., Takaya, S. et al., Influence of FBR Plant Service and Repair Welding on Microstructure and Residual Stress of Austenitic Stainless Steel Weld Joint, Hozengaku, vol.9, no.1, 2010, p.32-38 (in Japanese).

1-6 Enhancement of Safety and Economic Competitiveness of Fast Breeder Reactor Plant — Steel Plate Reinforced Concrete Containment Vessel —



- Stud: components to combine steel plate with concrete
- Partitioning plate and tie bar: components for reinforcement

Fig.1-16 SC structure and SCCV

The SC structure that consists of two facing steel plates with concrete filled in between jointed by headed studs, and tie bars and/or partitioning plates used for reinforcement, is used as containment vessel.

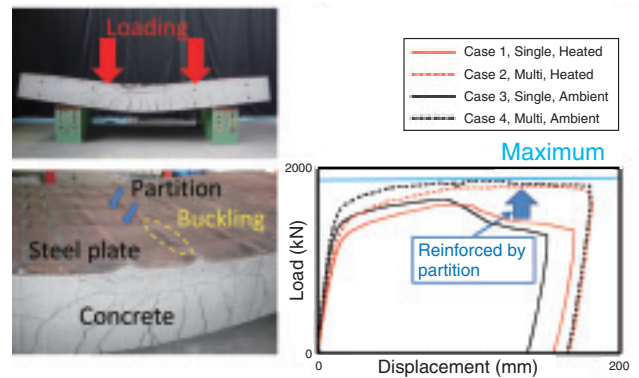


Fig.1-17 Results of out-of-plane bending test

Comparison between case 1 and case 2 shows the significant role of the concrete confined between the partition plates in increasing the bearing strength.

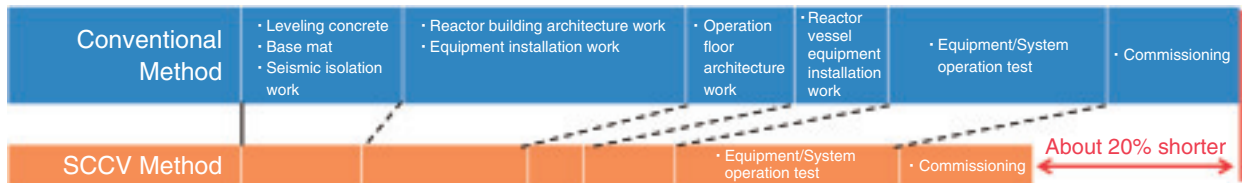


Fig.1-18 Shortening of construction period when SCCV is used

SCCV construction method could shorten the construction period by 20% compared to the conventional method.

The Japan Sodium Cooled Fast Reactor employs a steel plate reinforced concrete containment vessel (SCCV) (Fig.1-16). The steel plate reinforced concrete (SC) structure consists of concrete and steel plates with headed studs and is reinforced by tie bars and/or partitioning plates.

In the case of hypothetical sodium combustion, the inner plates would be exposed at high temperatures. Even under such severe conditions, the SCCV must be capable of withstanding high temperatures and high pressure and preventing leakage of radioactive nuclides. A series of tests were carried out at temperatures up to 700 °C to determine the potential characteristics of the SCCV. For example, out-of-plane bending tests were carried out to verify the influence of heat and the influence of the concrete confined between the partition steel plates on the bearing strength. Specimens were loaded to break to determine their maximum strength. Tests were carried out with a single partition specimen and a multipartition specimen with five partition plates. Fig.1-17 shows the failure mode of the multipartition specimen. Although the compression plate that acts as the boundary of the SCCV yielded and buckled, no surface crack was observed. The figure also shows the bending load-displacement relationships at a high temperature and ambient

temperature. In order to directly compare the relationships for the single partition and multipartition specimens, the loads in the case of the single partition specimen were increased by a factor of five. In this figure, the concrete confined between the partition plates is observed to increase the bearing strength. The decrease in the bearing strength at high temperatures was not apparent, thanks to the concrete confinement.

From a design study point of view, the SC structure is considered to be effective in shortening the SCCV construction period when modular construction is adopted. The reactor building is divided into several modular units. The parts of a module that are made of steel are firstly assembled in a factory. The assembled steel modules are transported by a barge from the factory to the dock near the reactor building site and installed on the base mat. Therefore, the modular construction could reduce the construction period by 20% owing to the elimination of reinforcing bar installation work, which is needed for a conventional reinforced concrete (RC) structure (Fig.1-18).

Additional tests are planned for commercializing and standardizing the SCCV.

Reference

Kato, A. et al., Experimental and Feasibility Study on Steel-Plate-Reinforced-Concrete Containment Vessel for Japan Sodium-Cooled Fast Reactor, Transactions of 21st International Conference on Structural Mechanics in Reactor Technology (SMiRT 21), New Delhi, India, 2011, paper ID# 819, 8p., in CD-ROM.

1-7 Validation of JENDL-4.0 with “MONJU” Reactor Physics Data

— ²⁴¹Am Data Testing by Cross-Section Adjustment Technique —

Table 1-2 Calculation accuracy before and after cross-section adjustment

Calculation accuracy of criticality data at 200 °C is compared between before and after the adjustment for two cores and two nuclear data files. In the case of JENDL-3.3, the accuracy shows strong core dependence before the adjustment.

Core	Nuclear data			
	JENDL-3.3		JENDL-4.0	
	Before*	After*	Before	After
(a) Core (1994)	-0.08	0.01	0.20	0.00
(b) Core (2010)	-0.26	-0.04	0.15	-0.01
Accuracy difference (b) - (a)	-0.18	-0.05	-0.05	-0.01

* Before (or After) cross-section adjustment (Unit: % Δ k/k)

Fast reactors have the potential to reduce high-level radioactive waste by recycling minor actinides (MAs) and Pu. Mixing MAs with the fuel would deteriorate the prediction accuracy of core parameters because nuclear data of MAs are less reliable than those of major nuclides owing to limited validation data. Core parameter data under the presence of a significant amount of MA do not exist for ²⁴¹Am, a major target MA to be recycled.

“MONJU” restarted its system start-up test in 2010, and the ²⁴¹Am content in the fuel was three times larger than that in the previous test carried out in 1994. Comparison of the calculation accuracy of core parameters between the cores may help in validating ²⁴¹Am nuclear data.

The main difference between the cores lies in their fuel composition, but the difference is also seen for nuclides other than ²⁴¹Am. In this study, we try to extract an influence of the ²⁴¹Am composition change on the calculation accuracy by employing the cross-section adjustment technique. The technique adjusts cross sections (or nuclear data) within their uncertainties so that calculated values of core parameters are close to experimental values. We can infer the reliability of the nuclear data from the extent of the adjustment.

Uncertainties related to experiments and calculations

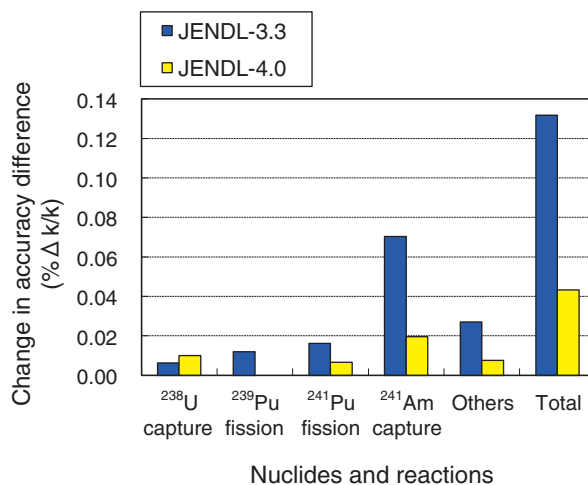


Fig.1-19 Effect of cross-section adjustment on accuracy difference

Change in the accuracy difference (as defined in Table 1-2) due to the cross-section adjustment is analyzed for major nuclides and reactions. ²⁴¹Am capture is the dominant contributor in the case of JENDL-3.3.

should be evaluated carefully for the correct adjustment of the nuclear data. Too small or too large uncertainties result in too large or too small adjustments. We have devoted considerable effort to minimizing the uncertainties and avoiding an unexpected bias.

Table 1-2 compares the calculation accuracy before and after the adjustment for JENDL-4.0 (published in 2010) and JENDL-3.3 (2002). In the case of JENDL-3.3, a difference of -0.2% Δ k/k is observed between the cores before the adjustment. The difference is reduced to one-fourth by the adjustment. For JENDL-4.0, a difference is as small as that achieved after the adjustment in the case of JENDL-3.3.

Fig.1-19 presents the change for major nuclides and reactions. The adjustment of the ²⁴¹Am capture cross section is the dominant reason for the reduction of the core dependence observed in the case of JENDL-3.3. This implies that there is room for improving the accuracy of ²⁴¹Am data of the original JENDL-3.3. In contrast, the change in the case of JENDL-4.0 is small, indicating the high reliability of the original.

The above results show that the “MONJU” reactor physics data are valuable for the validation of ²⁴¹Am nuclear data and that updating JENDL-3.3 to JENDL-4.0 is reasonable.

Reference

Hazama, T. et al., Adjustment of ²⁴¹Am Cross Section with Monju Reactor Physics Data, Proceedings of 2011 International Congress on Advances in Nuclear Power Plants (ICAPP'11), Nice, France, 2011, paper 11206, p.1527-1535, in CD-ROM.

1-8 Manufacturing MOX Raw Powder Uniformly and Effectively by Controlling Electromagnetic Waves

— Study on Highly Effective Microwave Heating —

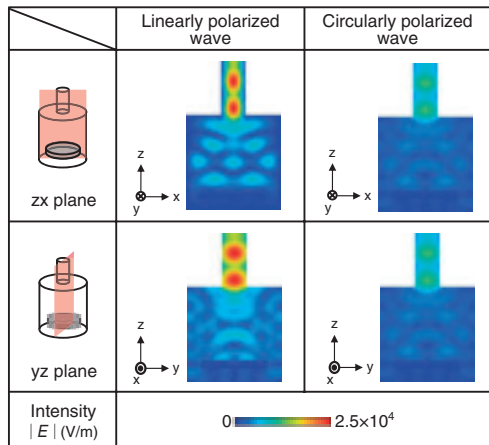


Fig.1-20 Electric field distribution in cylindrical oven
Electric field distribution in the cylindrical oven was maintained to be uniform by employing a circularly polarized wave, and it was compared to that obtained with a linearly polarized wave.

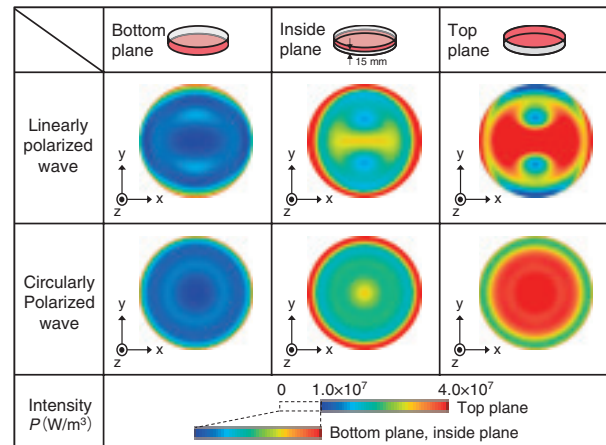


Fig.1-21 Absorbed power distribution of Pu-U mixed nitrate model in horizontal plane

More uniform absorbed power distributions of the solid-state Pu-U mixed nitrate model were realized on the all planes for the circularly polarized wave.

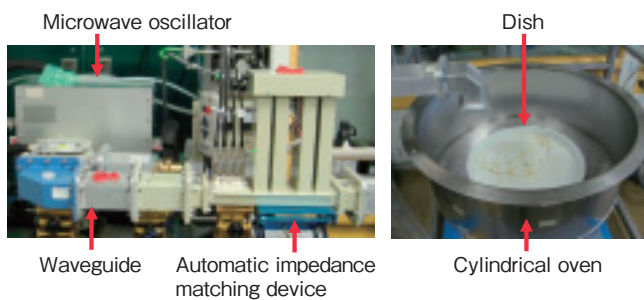


Fig.1-22 Microwave heating equipment for mass production

Microwaves generated from a microwave oscillator (magnetron) with a 3 kW output are fed to the cylindrical oven through a waveguide to heat a solution. The heating efficiency is improved by using an automatic impedance matching device.

In the mixed oxide (MOX) fuel fabrication process for a fast breeder reactor, Pu-U mixed nitrate solution, which is recovered through a reprocessing process, is heated in a microwave oven to produce a denitrate cake of MOX powder.

A turntable is used to obtain a uniform MOX raw cake, but it degrades the microwave heating efficiency by transferring heat to the outside of the oven. In order to reduce the heat loss, a method to rotate the electric field distribution, instead of the physical rotation of the cake, is investigated. To realize a rotational electric field, it is necessary to control the polarization of the microwaves.

The circularly polarized wave is a synthetic wave obtained by superimposing two linearly polarized waves that are mutually orthogonal and out of phase by 90° . It exhibits an excellent ability to uniform the electric field distribution.

In order to evaluate the behavior of the circularly polarized wave and the heating characteristics of the microwave heating equipment, electromagnetic analysis is performed by simulating the cylindrical oven with a circular waveguide. The Finite Difference Time Domain (FDTD) method is used

with a frequency of 2.45 GHz and a power of 1 kW to evaluate the electric field distribution and absorbed power distribution of a target object.

The electric field distributions of linearly polarized and circularly polarized waves in the cylindrical oven are shown in Fig.1-20. The electric field distributions for the circularly polarized wave were more uniform compared to those for the linearly polarized wave.

The absorbed power distributions of the solid-state Pu-U mixed nitrate model in the horizontal plane are shown in Fig.1-21. In the case of the circularly polarized wave realized more symmetric and uniformity at the all planes than the linearly polarized wave.

From the results of the simulations, it is expected that the heating uniformity and efficiency can be improved by controlling the polarization of the microwaves.

In the near future, the developmental state of the circularly polarized wave will be determined using the equipment shown in Fig.1-22. Experiments to confirm the heating uniformity of a solution will be carried out in the next stage.

Reference

Imai, S., Segawa, T. et al., Microwave Heating of Solid Pu/U Mixed Nitrate Medium in Cylindrical Cavity for Nuclear Fuel Cycle, Proceedings of ISAP2011, Jeju, Korea, 2011, 4p., in USB flash drive.

1-9 Research on Mechanical Properties of Fuel Claddings for High Burnup in Fast Breeder Reactors

— Effects of Neutron Irradiation on Mechanical Properties of ODS Steel Claddings —

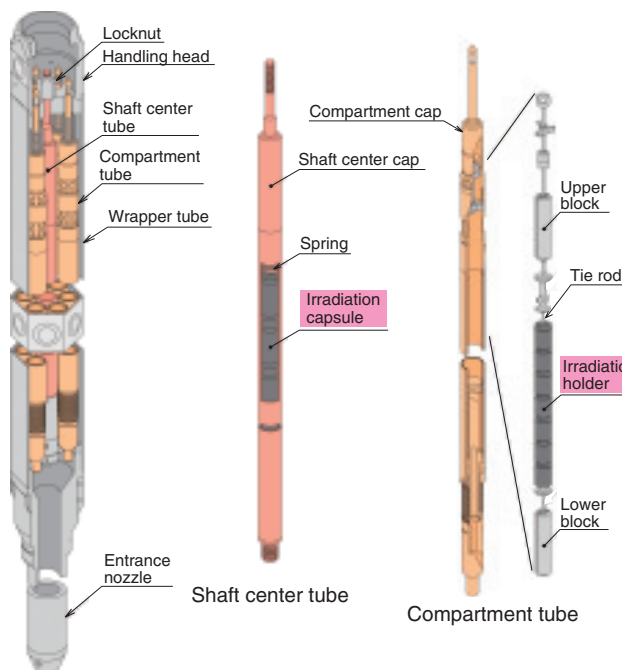


Fig.1-23 Bird's-eye view of CMIR in "JOYO"
ODS steel claddings were irradiated in "JOYO" using the CMIR.

Fast Breeder reactor (FBR) cycle systems as a major energy supply for the future have been studied for their economic competitiveness relative to light water reactor cycle systems and other electric power supplies. It is very important to achieve high-burnup high-temperature operation in order to improve the thermal efficiency of these systems. Oxide dispersion strengthened (ODS) steels are expected to be good candidate cladding material for FBRs to achieve these objectives because their high-temperature strengths are superior to those of conventional ferritic/martensitic (F/M) steel. To carry out a technological assessment of ODS steel claddings, it is necessary to acquire the mechanical properties for claddings irradiated at different conditions which are reflected in the design criteria.

ODS steel claddings were irradiated in the experimental fast reactor "JOYO" using the core material irradiation rig (CMIR), as shown in Fig.1-23, at temperatures between 683 and 1108 K with fast neutron fluences ranging from 3.0 to 6.6×10^{26} n/m² ($E > 0.1$ MeV). Post irradiation examinations were then carried out.

Changes in irradiation hardening or softening are shown by the ultimate tensile strength (UTS) ratio (irradiated UTS /

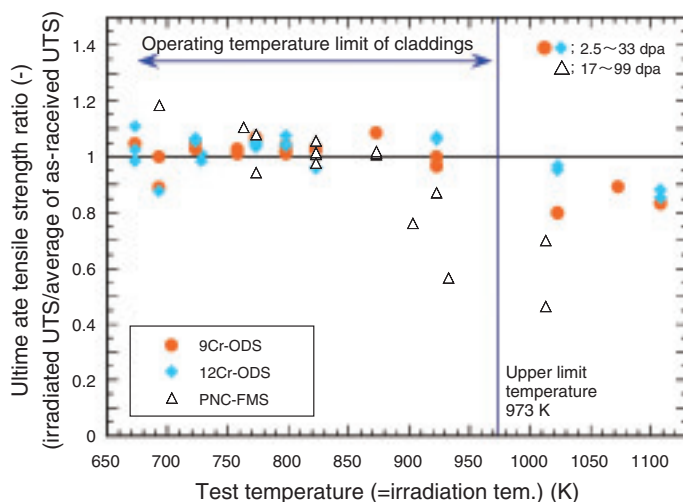


Fig.1-24 Relationship between ultimate tensile strength ratio and irradiation temperature for ODS steel claddings

Ring tensile tests were conducted before and after irradiation to investigate the effects of the irradiation on the tensile properties in the hoop direction of the claddings. A decrease in the tensile strength was indicated by an UTS ratio below 1, while the absence of significant degradation was inferred when the UTS ratio was nearly equal to 1.

average value of as-received UTS) in Fig.1-24; the present results for these ODS steel claddings, and previous results for the ODS steel and 11Cr-F/M steel (PNC-FMS) cladding irradiated in "JOYO" are also shown. In this irradiation examination, the high temperature data in about 1103 K which greatly exceeds the operating temperature limit of claddings in FBR was acquired for the first time in the world. It was indicated that the tensile strength of PNC-FMS decreased because of the recovery of martensitic structures and recrystallization at high temperatures. On the other hand, there was no remarkable decrease in the tensile strength of the ODS steel claddings, even though temperatures exceeded the operating temperature limit of 973 K consistently. It is suggested that the oxide particles, which are mainly responsible factor for the high-temperature strength of ODS steels, were stable during irradiation.

In the near future, we will be developing ODS steel claddings by using fundamental technology for the advanced FBRs. It is also important to make preparations for irradiation tests and post-irradiation examinations that would have to be carried out after "JOYO" is restarted.

Reference

Yano, Y. et al., Effects of Neutron Irradiation on Tensile Properties of Oxide Dispersion Strengthened (ODS) Steel Claddings, Journal of Nuclear Materials, vol.419, issues 1-3, 2011, p.305-309.

1-10 Technology for Removal of Excess Oxygen from MOX Fuels during Irradiation

— Research and Development for MOX Fuel by Using Oxygen Getter —

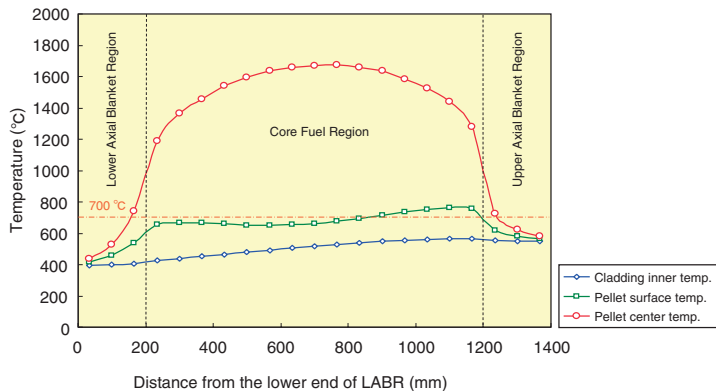


Fig.1-25 Analyzed fuel-temperature distribution

From the temperature that is less than 570 °C at the pellet-cladding gap, the temperature at the bottom end of the upper axial blanket region is expected to be 728 °C.

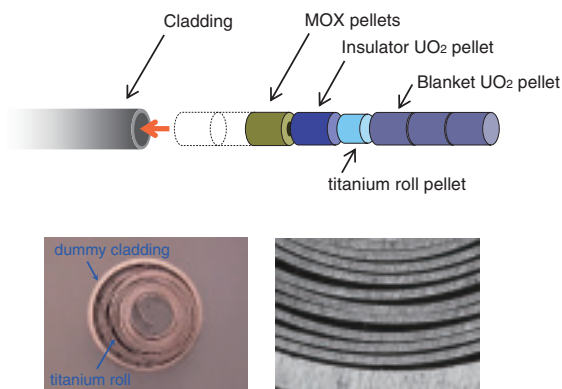


Fig.1-27 Method for preparing titanium roll pellet and cross sections of a produced roll pellet

Gaps between titanium layers and a gap between roll and cladding can be observed.

Increasing the burnup is essential for attaining economical competitiveness of fast reactor systems. Because excess oxygen accumulates in the fuel and accelerates cladding corrosion in proportion to the burnup, it should be removed. The use of an oxygen getter is one of the solutions for removing excess oxygen, but almost no papers have reported the application of the option in removing excess oxygen from pellet-type mixed oxide (MOX) fuels. Therefore, a feasibility study on the oxygen getter option for pellet-type MOX fuels is in progress.

First, a survey of oxygen getter materials was carried out and titanium was selected after considering factors such as the oxygen potential, melting point and neutron absorption. Second, the configuration of the getter material and the loading position were investigated. Contact of the getter material with the end surfaces of MOX pellets is not allowable because of the problem of compatibility. Therefore, there is practically no choice with respect to the loading position except the pellet-cladding gap or upper axial blanket region. A computational-analysis result showed that the

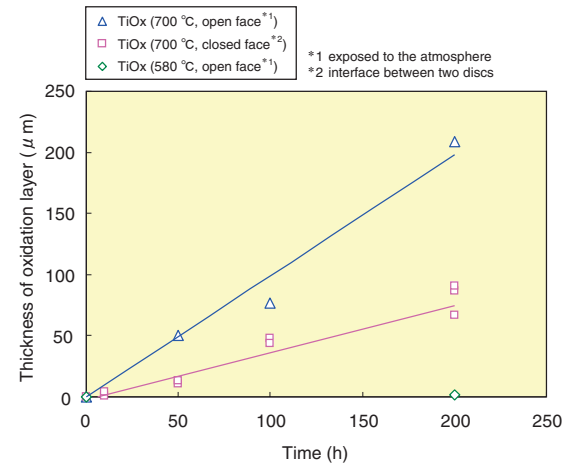


Fig.1-26 Dependence of titanium-oxidation-layer growth on heating time

Quick oxidation was confirmed at 700 °C, but oxidation was very slow at 580 °C.

temperature of the oxygen getter material at those locations was 396~728 °C (Fig.1-25). Experimental results showed fast oxidation of titanium at 700 °C but quite slow oxidation at 580 °C (Fig.1-26). This suggests that absorption of the excess oxygen by titanium is expected only when it is located at the lower end of the upper axial blanket region where the temperature reaches 728 °C. The volume of titanium increases during oxidation to TiO_2 . To avoid mechanical interaction with the cladding, the getter titanium must be installed with low smear density that is less than 50%. Although some options like metallic particle packing or porous pellet installment were also discussed, installment of titanium pellets rolled up in titanium foils with a thickness of less than 100 μm was the most recommended option. The results of a test production confirmed that a titanium pellet roll with a controlled pellet diameter and with adequate gaps between foils could be produced without welding (Fig.1-27). These results show the feasibility of using titanium pellet rolls.

Reference

Morihiro, M., Feasibility Study of Oxygen Getter materials for FBR MOX Fuel (2)-Investigation of Loading Options, Evaluation of Oxidation Behavior and Compatibilities of the Candidate Materials-, JAEA-Research 2011-018, 2011, 32p. (in Japanese).

1-11 For Effective Fuel Dissolution in Reprocessing

— Development of Simulation Code for FBR Spent Fuel Dissolution —

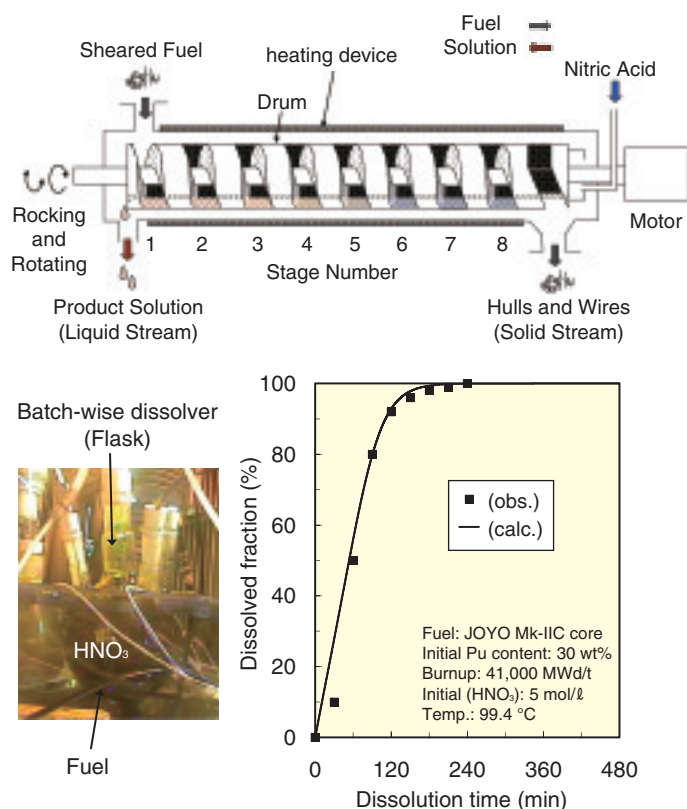


Fig.1-29 Dissolution behavior of FBR spent fuel in a batch-wise dissolver

The simulation result was in good agreement with the experimental one, and the simulation code is useful for estimating the dissolution behavior in a batch-wise dissolver.

As a part of the advance aqueous reprocessing technology for FBR fuel cycle, we have been developing rotary drum type continuous dissolver for FBR spent fuel dissolution (Fig.1-28). Some features of this dissolver make it preferable to the traditional batch-wise ones; these features include higher dissolution capacity with smaller apparatus size and the geometric advantage of a cylindrical drum with B,C installment at the drum center for criticality safety in the case of any concentration of fissile materials. In the rotary drum type continuous dissolver, effective fuel dissolution can be achieved by rocking the drum to achieve agitation and by counter flow of fuel and nitric acid. For estimating the fuel dissolution behavior under several operational conditions in this dissolver, we have been developing the simulation code for rotary drum type continuous dissolver.

This simulation code mainly consists of three modules: the first module is for evaluating chemical reaction, which considers the dissolution of UO₂ fuel and FBR spent fuel (MOX fuel) with high Pu content; the second module is for

Fig.1-28 Schematic diagram of rotary drum type continuous dissolver

Sheared fuel pins are fed intermittently to the first stage of the drum that is divided into eight stages by a helical auger and heated by a surrounded heating device, while nitric acid is supplied into the 8th stage and emerges as the dissolver solution from the 1st stage continuously. The sheared fuel pins are transferred from one stage to the next stage by rotating the drum periodically, and the solid contents such as hulls and wires are finally discharged from the 8th stage to an outer canister.

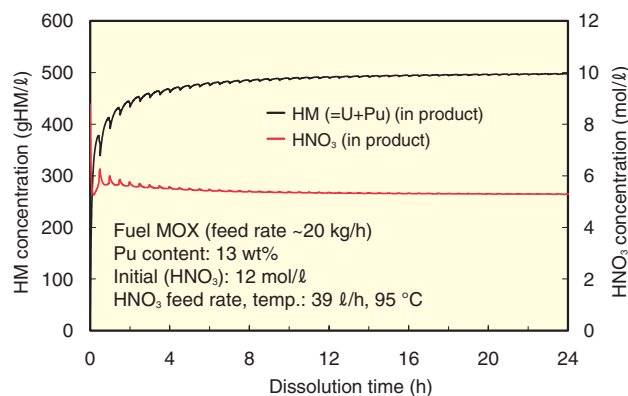


Fig.1-30 Calculation result for mixed oxide (MOX) fuel dissolution by rotary drum type continuous dissolver

The calculation result indicates the dissolver solution with the required heavy metal (HM = U + Pu) concentration can be obtained under the appropriate dissolution conditions.

calculating the mass balance, which also estimates the transfer of powdered fuel between stages by nitric acid flow and drum rocking; and the third module is for calculating the thermal balance in the dissolver surrounded by a heating device. This code can also simulate the fuel dissolution behavior in a batch-wise dissolver by regarding it as a single stage dissolver (Fig.1-29).

For the UO₂ dissolution conditions in a rotary drum type continuous dissolver, the fuel dissolution behavior simulated by this code was in good agreement with the experimental one. The condition for obtaining the required dissolver solution was also analyzed using this code and appropriate operational conditions of the rotary drum type continuous dissolver, including appropriate feed rate, and concentration and temperature of nitric acid, could be clarified (Fig.1-30). We will continue to improve the simulation code for higher reliability and try to optimize the dissolution conditions by using the code.

Reference

Sano, Y. et al., Development of Simulation Code for FBR Spent Fuel Dissolution with Rotary Drum Type Continuous Dissolver, Proceedings of 19th International Conference on Nuclear Engineering (ICONE 19), Chiba, Japan, 2011, ICONE19-43317, 6p., in CD-ROM.

1-12 Selective Electrochemical Dissolution of Spent Fuel

— Behavior of Anodic Dissolution of U-Pu-Zr Alloy during Pyrochemical Reprocessing —

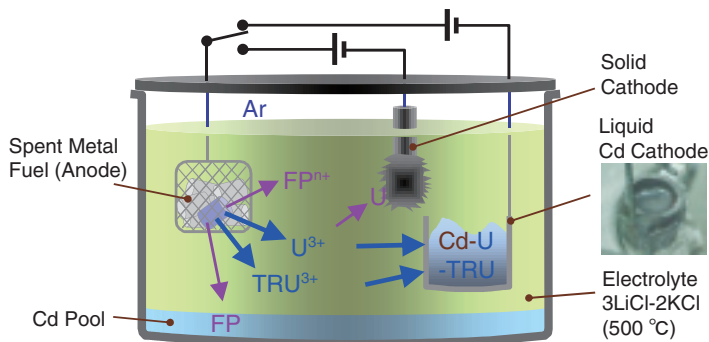


Fig.1-31 Concept underlying the electrorefining process

U and TRUs dissolved in the electrolyte could be separated from FP elements and recovered from the electrolyte on the cathode by electrolysis. Uranium metal could be deposited on a solid cathode, and uranium and TRUs could be recovered simultaneously in a LCC by controlling each cathode potential.

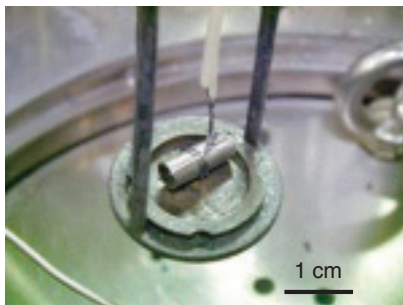


Fig.1-32 Appearance of U-Pu-Zr alloy before electrolysis
U-Pu-Zr alloy is formed as a rod of 6 mm diameter. A Ta wire is wound around the alloy.

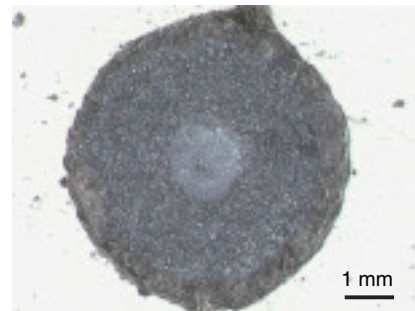


Fig.1-33 Cross section of anode after electrolysis

The remaining Zr metal forms a sponge-like residue. The white part indicates the part of the anode where the electrolyte has penetrated.

Metal fuel fast breeder reactor (FBR) technology is one of the future candidate technologies for the nuclear fuel cycle. For reprocessing the spent metallic fuel, pyrochemical reprocessing has been developed.

In pyrochemical reprocessing, transuranic elements (TRUs) such as uranium (U) and plutonium (Pu) are recovered by electrolysis. Fig.1-31 shows the concept underlying electrolysis for the separation of U, Pu, and fission product (FP) elements. Molten lithium chloride-potassium chloride (LiCl-KCl) at 500 °C is used as the electrolyte. The spent metallic fuel is loaded into a basket for use as an anode and placed in the electrolyte. Two kinds of cathodes are used: a solid cathode made of iron is used for recovering the uranium and a liquid cadmium cathode (LCC) is used for recovering TRUs. TRUs and some kinds of FP elements are anodically dissolved in the electrolyte, and U is selectively recovered from electrolyte on the solid cathode by controlling the cathode potential. U and TRUs are simultaneously recovered in the LCC, since their deposition potentials are close to each other. The metal fuel is prepared by adding zirconium (Zr) metal to U-Pu alloy. Addition of Zr to U-Pu alloy increases the melting point and strength of the

fuel rod. The co-dissolution of Zr during the electrolysis may cause some problems. Therefore, it is important that the controlling the dissolution of Zr with keeping high dissolution yield of U and Pu.

The Japan Atomic Energy Agency (JAEA) and the Central Research Institute of Electric Power Industry have installed an Ar atmosphere glove box at the Chemical Processing Facility and they have continued a collaborative study on pyrochemical reprocessing using U-Pu-Zr alloy. Fig.1-32 shows the appearance of the U-Pu-Zr alloy used for the anode. Since the dissolution potential of Zr is different from that of U, the anode potential was controlled during electrolysis. Fig.1-33 shows a cross section of the anode residue after electrolysis. U and Pu in the outer part were dissolved selectively, leading to the formation of the sponge-like Zr metal as the residue. There was no change in the outer diameter of the anode because the electrolyte had penetrated the space created by the dissolution of U and Pu. ICP-AES analysis of the anode residue showed a high dissolution yield for the TRUs (U: >99.6%; Pu: 99.9%). We are planning to obtain further experimental data on the separation of the TRUs and FP elements to improve the electrolysis technique.

Reference

Murakami, T., Kitawaki, S. et al., Anodic Behavior of a Metallic U-Pu-Zr Alloy during Electrorefining Process, Journal of Nuclear Materials, vol.414, issue 2, 2011, p.194-199.

1-13 A New Extraction Process for Future Reprocessing

— Development of Uranium and Plutonium Co-Recovery Process (Co-Processing Process) —

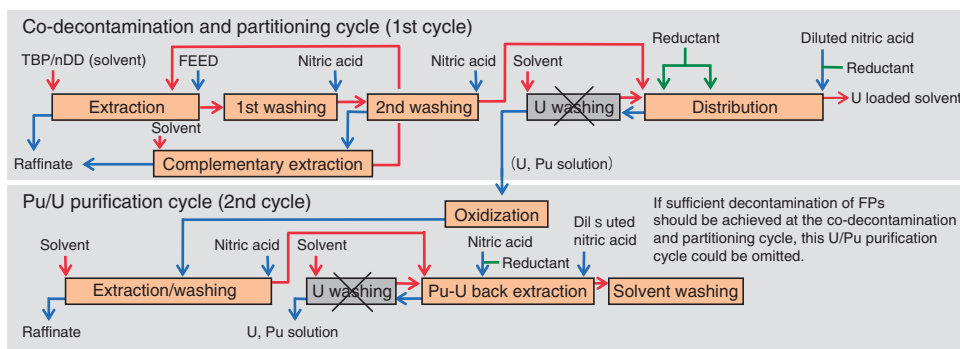


Fig.1-34 Schematic image of co-processing process

The elimination of the U washing stage (crossed-out part of Fig.1-34), which is used in the conventional PUREX process, is one of the characteristics of the co-processing process. It prevents Pu isolation in the process and improves proliferation resistance.



Fig.1-35 The situation of Pu stripping in the partitioning unit

An investigation of the smooth transition from the current light-water-reactor (LWR) cycle to the fast-breeder-reactor (FBR) cycle was carried out in association with government ministries, electric utilities, plant vendors, and the Japan Atomic Energy Agency (JAEA). One of the important items of the investigation was the appraisal of several reprocessing processes that will be applied after the end of the lifetime of the Rokkasho Reprocessing Plant. As a result, the co-processing process, which is a modification of the PUREX process for non-isolation of Pu, was selected as the most promising process^[1].

The co-processing process was developed through a flowsheet study on process calculation and its verification by miniature mixer-settler tests. In order to secure the internationally acceptable proliferation resistance, the flowsheet of the process was set up to prevent the isolation of Pu, even with changes in operational conditions such as reagents and flow rates. Furthermore, if the performance indices (such as decontamination factors (DF) of fission products (FPs)) of the co-decontamination and partitioning

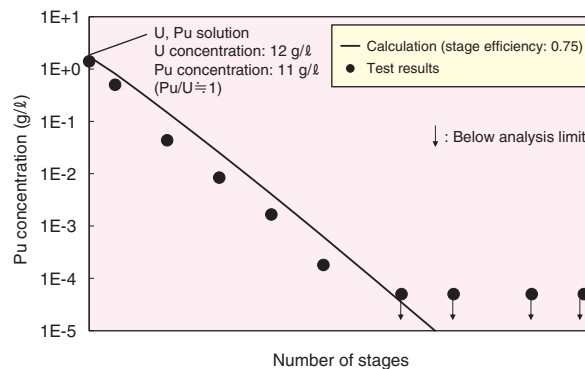


Fig.1-36 Pu concentration profile in the partitioning unit (organic phase, Pu/U = 3%)

The Pu stripping performance was good and the U/Pu ratio in the product solution was about 1.

cycle were good enough, then the omission of the subsequent Pu/U purification cycle could be viable (Fig.1-34).

The mixer-settler tests focusing on the partitioning unit were carried out using U/Pu nitric solution at the Operation Testing Laboratory (OTL) of the Tokai Reprocessing Plant. The Pu/U ratios of the feed solutions were prepared as 1%, 3%, and 20%; these compositions were adopted considering the composition of future spent fuels from LWR, LWR-MOX, and FBR systems and their mixing treatments. The stripping performance of Pu accompanied by U was good in the cases of Pu/U ratios of 3% and 20% (Fig.1-35 and Fig.1-36). The U/Pu ratios of the product solutions were suitable for the fabrication of FBR-MOX fuel ($0.5 < U/Pu < 2.0$)^[2]. Further experiments should be conducted under the condition of a Pu/U feeding ratio of 1% to ensure the applicability of the co-processing process for all future types of fuels.

This work is the result of a study entrusted to the JAEA by the Ministry of Economy, Trade and Industry (METI).

References

- [1] Investigation Council for FBR Cycle Demonstration Process, Future Exploitation of Nuclear Fuel Cycle-Appraisal of Technical Issues-, 28th Regular Meeting of Atomic Energy Commission, no.11, 2009, 52p. (in Japanese).
- [2] Japan Atomic Energy Agency, Result Report of 2010-Development of Decontamination Technology for Recovered Uranium from FBR Fuel-, 2011, (in Japanese), in CD-ROM, Available at JAEA Library.

R&D for Improving the Technology and Reliability of Geological Disposal in Japan

In essence, geological disposal is aimed at isolating high-level radioactive waste (HLW), which is produced during nuclear power generation, from human environments over a long period of time. This is a critical issue that the present generation must take responsibility for dealing with and that remains crucial irrespective of the revision of the national nuclear energy policy in response to the accident at the Tokyo Electric Power Company, Incorporated, Fukushima Daiichi Nuclear Power Station. In Japan, spent fuel from power reactors is reprocessed to extract reusable uranium and plutonium for power generation purposes. The liquids separated from the spent fuel during chemical reprocessing are solidified into a stable glass form. In the Japanese concept, vitrified wastes are encapsulated in a thick steel overpack, which is surrounded by highly compacted bentonite and then placed in a stable geological environment below 300 m (Fig.2-1).

Geological disposal of HLW will be a long-term project lasting over 100 years. The project begins from site selection and continues to repository construction and operation, which will be followed by post-closure monitoring. It is thus of great importance to proceed with the project efficiently, as a national responsibility, by continuously reinforcing the technical base and, more importantly, enhancing public confidence. To this end, we have made, and will continue to make, steady progress in research and development (R&D) in various fields, such as geoscientific research, engineering technology and safety assessment, to improve the technology and reliability of geological disposal in Japan. Our efforts are also focussed on promoting public understanding through disseminating relevant information and opening our R&D facilities to the public.

A particular focus of our R&D at present is on projects at two underground research laboratories (URLs) – one at Mizunami for research on crystalline rocks and the other at Horonobe for research on sedimentary formations (Fig.2-2) – with the main aim of developing a sound technical basis for the implementation of the disposal project and the formulation of safety regulations. In March 2011, shaft excavation reached a depth of 497 m at Mizunami and 250 m at Horonobe and some research galleries were made available for use. Multidisciplinary investigations are ongoing as the reliability of a variety of investigation techniques should be

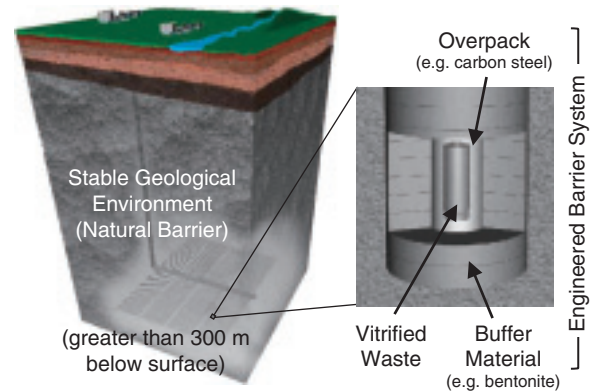


Fig.2-1 Basic concept of geological disposal of high-level radioactive waste (HLW) in Japan

tested and confirmed before site characterisation begins in earnest. Underground tunnels serve as a place for the public to experience deep geological environments first-hand and appreciate our R&D activities. In addition, studies on tectonics, volcanic and faulting activities and so on have been in progress in order to evaluate the long-term stability of geological environments in Japan.

In parallel with such geoscientific research, we are conducting an extensive laboratory programme at Tokai to improve geological disposal technology. Studies have been carried out over wide range of topics, such as performance assessment of multi-barrier systems and experiments on engineered barrier systems and on the long-term chemical and migration behaviour of radionuclides under actual geological conditions. These studies involve the use of geological environment data obtained at both URLs. In 2010, databases for glass dissolution and for overpack corrosion were developed by compiling and reviewing all available experimental data.

On the basis of such R&D activities, we have been working on improving a prototype knowledge management system that was developed in 2009, in order to systematically provide multiple lines of evidence and R&D results in the form of a knowledge base.

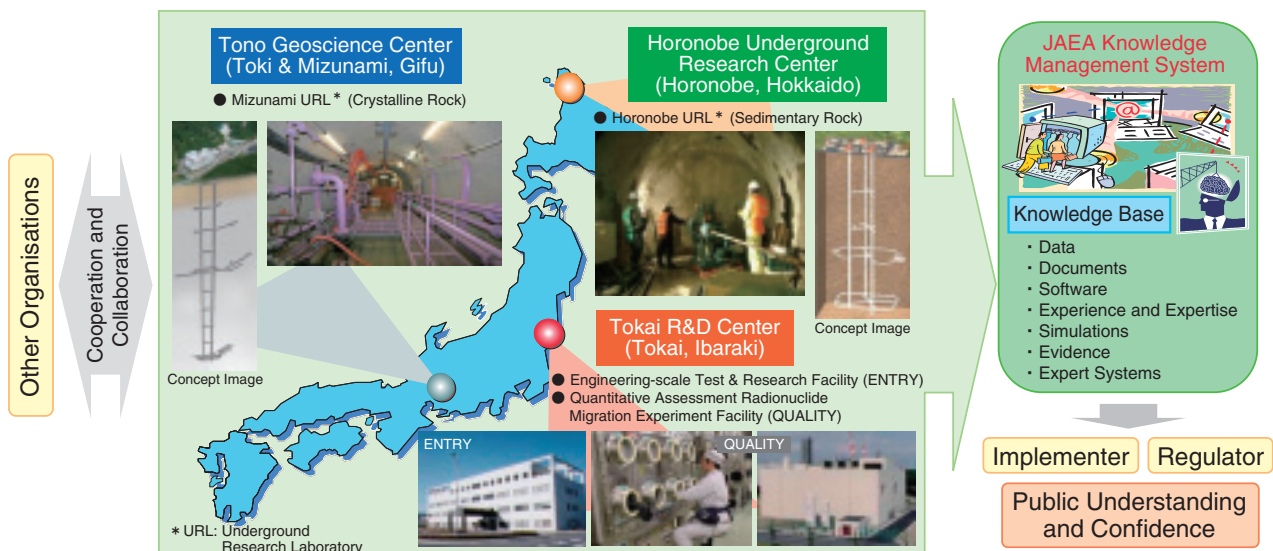


Fig.2-2 JAEA's R&D activities

2-1 Transfer of Knowledge of Geoscience Technology – Information Synthesis and Interpretation System (ISIS) –

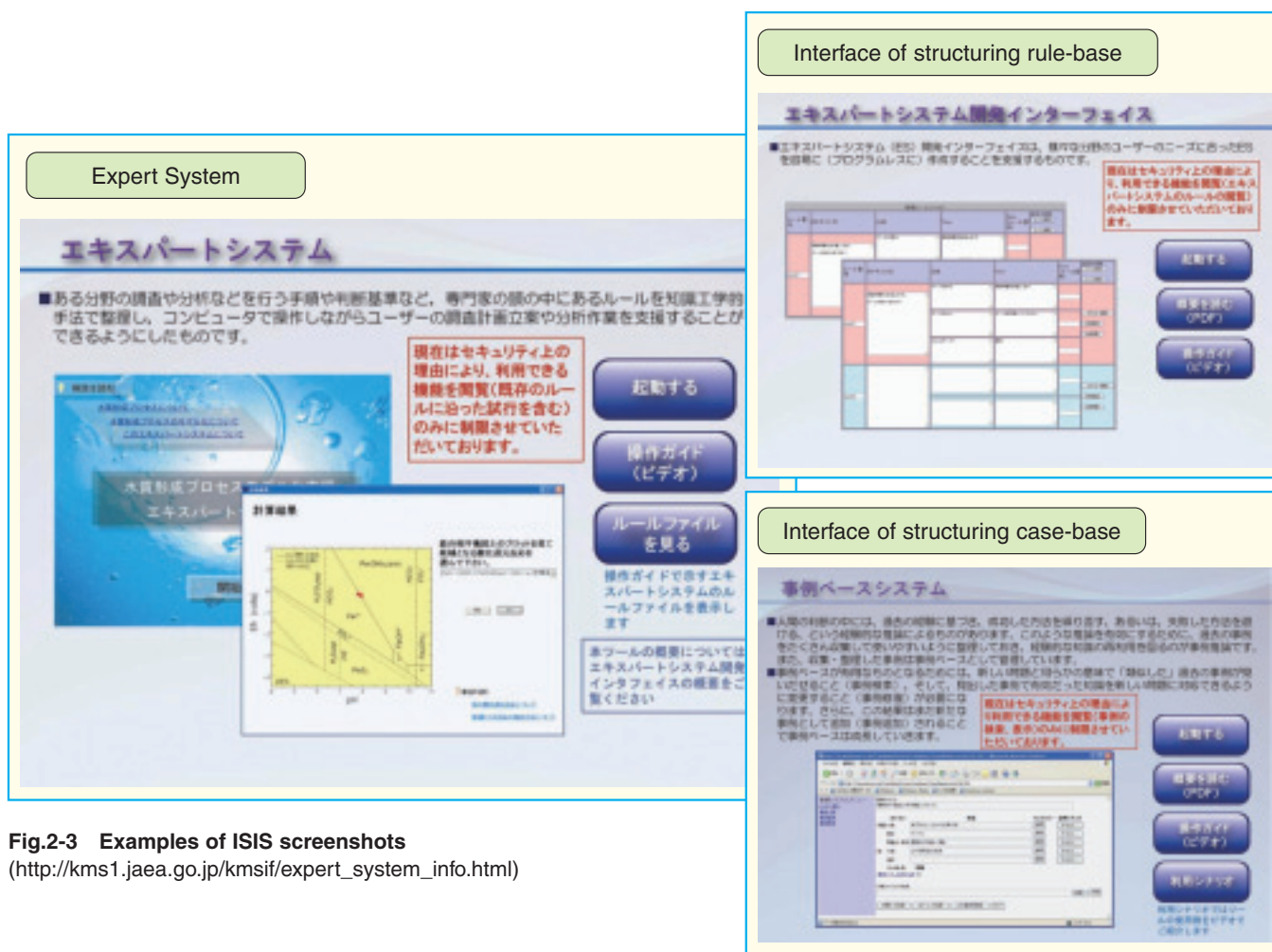


Fig.2-3 Examples of ISIS screenshots
(http://kms1.jaea.go.jp/kmsif/expert_system_info.html)

When site characterization is performed in a stepwise manner, i.e., a literature survey followed by preliminary and detailed investigations, it is necessary to make full use of all the available knowledge accumulated through experience at underground laboratories. This knowledge consists of both explicit and implicit knowledge. Explicit knowledge includes databases, literature, and software, whereas implicit knowledge includes the experience and know-how of experts, which is called tacit knowledge. Traditionally, tacit knowledge was transferred from master to disciple or from father to son on the field site, in a limited manner. In order to transfer knowledge to many young engineers and future generations, it is necessary to externalize this implicit knowledge (such as decision-making rules and failure cases) as much as possible, and to update the externalized implicit knowledge continuously.

To this end, a method has been developed to externalize the knowledge of experts. Decision-making rules in the procedures of planning, investigation, and evaluation for site

characterization are expressed as rules, i.e., in IF ... THEN format. Another methodology, consisting of compiling a database of failure cases that are difficult to represent with rules, has also been developed using case-based reasoning technology. Geoscience experts who do not have expertise in information technology can input and revise the rules and cases using a user-friendly interface.

The expert system, which supports staff in the construction of geochemical models and so on, is to be developed with this methodology using rule-based and case-based reasoning (Fig.2-3). The Information Synthesis and Interpretation System (ISIS), which supports the implementer in planning, performing, and evaluating the preliminary investigation, will be developed through integration of each expert system.

This work was carried out under a contract with the Agency for Natural Resources and Energy, Ministry of Economy, Trade and Industry, in the fiscal years 2008 and 2009.

Reference

Semba, T., Osawa, H. et al., Practical Application of the KMS: 2) Site Characterisation, Proceedings of 12th International Conference on Environmental Remediation and Radioactive Waste Management (ICEM2009), Liverpool, UK, 2009, ICEM2009-16355, 8p., in CD-ROM.

2-2 Evaluation of Uplift/Erosion Scenarios in the Far Future — Analysis Reflecting a Feature of the Geomorphic Change in Japan —



©Neimo-swimmer 1000

Fig.2-4 Typical topography in the middle-reach of a river

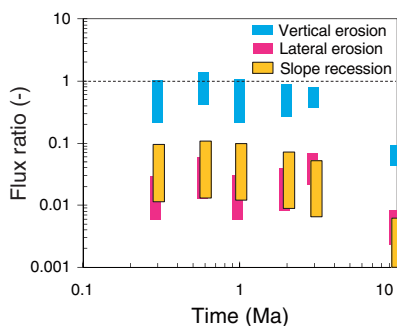


Fig.2-6 Illustration of the calculated impact of repository exposure
All the radionuclides are assumed to remain in the vicinity of the repository. The radiological toxicity of the nuclides is converted to that of ^{238}U .

In Japan, areas where rapid uplift has been recorded in the past 100 thousand years are disqualified as potential sites for geological disposal of nuclear waste. However, analyses of uplift/erosion scenarios are essential to ensure the robustness of a deep HLW repository system, considering that uplift/erosion would take more than 100 thousand years to expose a repository.

In a previous study, a simple but conservative conceptual model was adopted, in which an entire repository was exposed at once and was eroded uniformly, although Japan has an undulating topography, mainly because of fluvial erosion.

In this study, the topographical changes caused by fluvial erosion were examined and the following were identified: (1) erosion/sedimentation on riverbeds, (2) lateral erosion to form terraces, and (3) recession of the valley-side slope (Fig.2-4).

Besides, it is evident that riverbed deepening depends on glacial cycles. In the middle reach of rivers, there is increased production of detritus during a glacial epoch, which lasts for 80 ka. Sedimentation progresses as the detritus accumulates

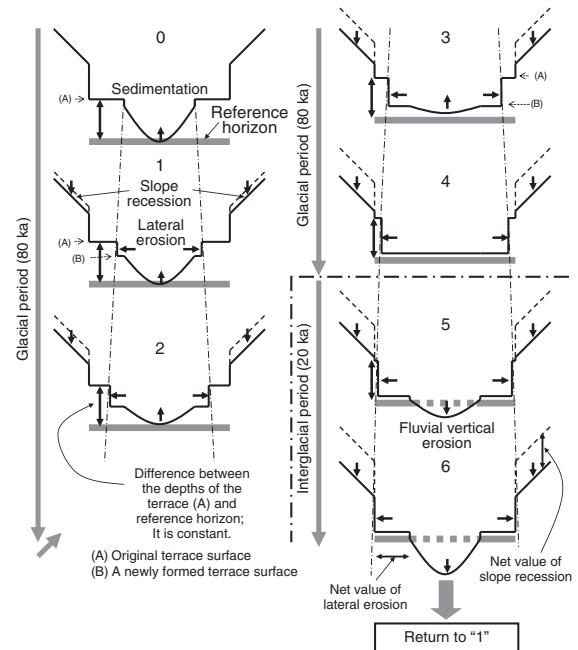


Fig.2-5 Conceptual model of fluvial erosion (one glacial cycle)

Sedimentation (in the glacial period) and erosion (in the interglacial period) progress on riverbed. Lateral erosion and slope recession continue. A new terrace is formed in one cycle. If this cycle continues, the reference horizon will be denuded gradually by vertical erosion, lateral erosion, and/or slope recession.

on the riverbed because of the decrease in the intensity and frequency of floods. As a result, fill-top terraces are formed. In contrast, the production of the detritus decreases and the intensity and frequency of floods increase during the interglacial period, which lasts for 20 ka resulting in riverbed deepening.

On the basis of this phenomenological understanding, a conceptual model of fluvial erosion was created (Fig.2-5).

The mechanism of topographical change is expected to remain the same in the far future, when the repository will be exposed. Consequently, the bedrock surrounding the repository will be denuded gradually, over a period of more than tens of thousands of years.

The radiological impact of the exposed repository was compared with the natural radiological toxicity (Fig.2-6). The results showed that depending on various conditions, such as repository depth, uplift rate, and topography (ridge-to-ridge distance, terrace height, etc.), the average toxicity of the detritus formed during repository denudation would be lower than or almost equal to that of the uranium deposit in Japan (0.05 wt% U_3O_8).

Reference

Miyahara, K. et al., Consequence Analysis of Fluvial Erosion Scenarios for an HLW Repository, Journal of Nuclear Science and Technology, vol.48, no.7, 2011, p.1069-1076.

2-3 First Release of Overpack Database

— Information on Overpack Designing and Manufacturing and Experimental Data are Provided Intelligibly —

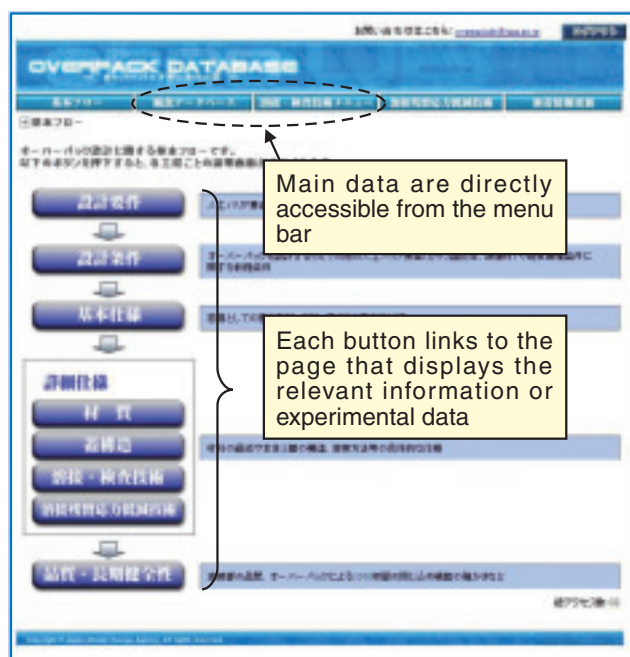


Fig.2-7 First page displayed after logging in to the database

Objects required for overpack designing are listed as buttons in the flow diagram. Each button links to the relevant page, which displays the desired information or experimental data. Users can directly access the main data, i.e., the corrosion data and welding/inspection test data, from the menu bar, without having to go through the flow diagram.

(<http://www.jaea.go.jp/O4/tisou/toppage/top.html>)

An overpack is one of the components of an engineered barrier system for the geological disposal of high-level radioactive waste. The overpack is required to prevent groundwater from coming in contact with vitrified waste until the short-lived radionuclides decay (the time required for the decay is assumed to be 1000 years in the current concept). The required lifetime of overpack is far longer than those of ordinary industrial structures made of metallic materials. Hence, overpacks need to be specially designed, manufactured, and assessed for long-term integrity. Research and development of welding/inspection techniques for sealing the body and lid joint of the overpack and assessment of its corrosion resistance against groundwater are in progress at several institutes, and the results have been summarized as reports or research papers. These results should be used for overpack designing and establishing safety regulations that are suitable for the actual repository site conditions (groundwater chemistry, pressure, temperature, etc.). However, considerable effort and time are required to find the necessary information or data from the literature. In order to make practical use of the research results, we decided to

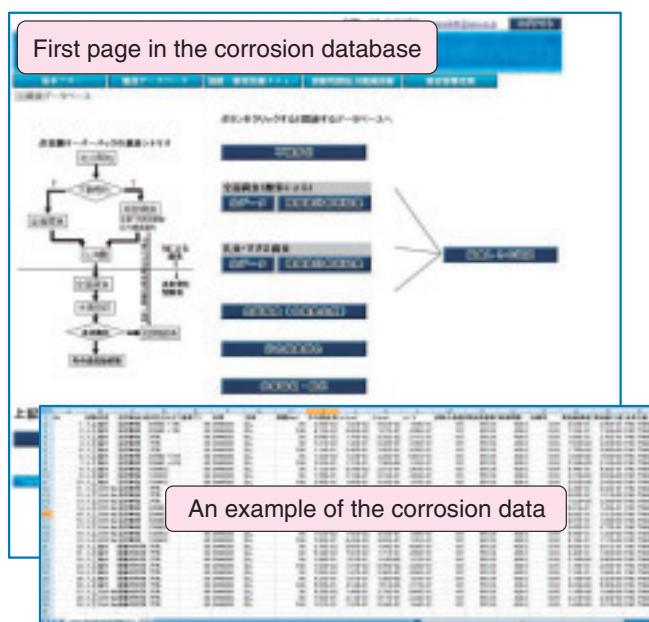


Fig.2-8 An example of the corrosion database pages

The corrosion modes to be considered in a repository environment are arranged in a time-series diagram, and the button for each corrosion mode links to the page providing the relevant experimental data in a tabular format.

construct a database system that enables users to efficiently find the information and experimental data. We have developed a database that integrates the data pertaining to the welding/inspection techniques and corrosion resistance and implemented it on the JAEA web site.

The database was developed in cooperation with the Radioactive Waste Management Funding and Research Center, where research and development of the welding/inspection technique was carried out.

In this database, a flow diagram of the overpack designing is shown on the main page (Fig.2-7). When a user clicks on the button for the diagram, examples of previous investigations or experimental data (Fig.2-8) are displayed. The user can search for and refer to a variety of information about the overpack. The main test data, i.e., corrosion data and welding/inspection test data can be accessed directly from the menu bar without using the flow diagram. This database is publicly accessible. We are planning to expand and revise the database by incorporating the latest research results and technical information.

Reference

Taniguchi, N. et al., Development of Overpack Database, JAEA-Data/Code 2009-022, 2009, 56p. (in Japanese).

2-4 Revealing the Pore Structure and Diffusion Mechanism in Rock

— Analysis of Pore Structure of Siliceous Mudstone Using Nano X-ray Computed Tomography —

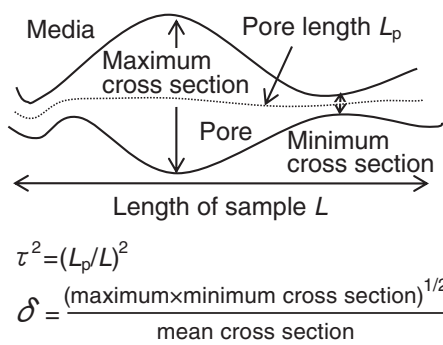


Fig.2-9 Definitions of tortuosity (τ^2) and constrictivity (δ)

The image obtained is analyzed on the basis of the definitions.

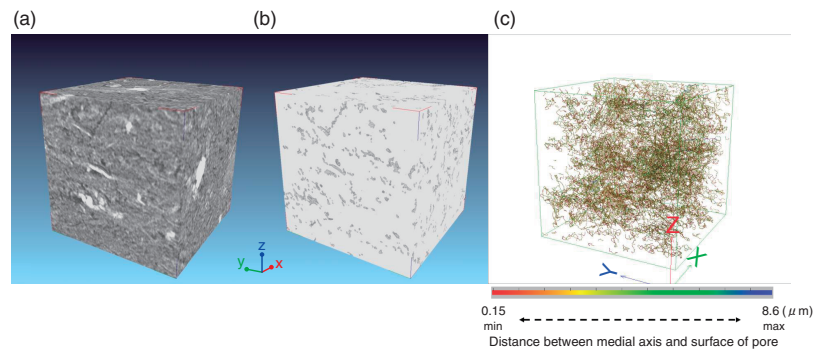


Fig.2-10 The porous network of the rock matrix with sub-micron-sized features is imaged and analyzed

(a) Three-dimensional image (512^3 with a voxel size of 270 nm) of siliceous mudstone of the Wakkanai formation, (b) after segmentation (dark gray areas denote pore spaces), and (c) medial axes with color indicating the distance between each axis and the pore surface.

Table 2-1 Results of image analyses and tritiated water (HTO) diffusion tests

A comparison of the pore structure and diffusion tests suggests that the pore connectivity collates with the diffusion-accessible porosity, and that the dominant parameters in an HTO diffusion system are the tortuosity and diffusion-accessible porosity.

Image analysis						Diffusion experiments		
Direction to the ground	Direction	Starting face voxels connected to end face	Average of tortuosity	1/tortuosity	Average of constrictivity	Accessible porosity	Effective diffusion coefficient/ m^2s^{-1}	Geometry factor
Vertical	Z	20	6.97	0.14	0.47	0.19	8.80×10^{-11}	0.19
Horizontal	Y	152	4.75	0.21		0.22	1.02×10^{-10}	0.19
Horizontal	X	55	8.64	0.11				

Diffusion in a rock matrix is one of the key processes for the migration of radionuclides from high-level radioactive waste. The diffusion coefficient is an important factor in the safety assessment for deep geological disposal of high-level radioactive waste. Diffusion in a rock matrix is affected by the rock porosity and pore geometry. A typical diffusion model represents the geometry factor as follows: effective diffusion coefficient/(accessible porosity \times diffusion coefficient in bulk water) = constrictivity/tortuosity (Fig.2-9). Empirically, the geometry factor is equal to 1/tortuosity in the case when the pore diameter is much larger than the solute diameter; however, there is no verification of the pore geometry by direct measurement. In this study, these measurements were performed by using nano X-ray computed tomography (CT) to identify the actual tortuosity and constrictivity values of siliceous mudstone samples of the Wakkanai formation at a depth of 500 m in a borehole of the Horonobe underground research center. In addition, a comparison of the results with the pore-space properties obtained from a set of tritiated water (HTO) through-diffusion tests was performed on the rock samples.

The pore structure of the rock was revealed as shown in Fig.2-10. Table 2-1 shows the results of the image analyses and HTO diffusion tests. The value of 1/tortuosity is close to the geometry factor obtained from the diffusion test. These

results support the empirical law in the case when the pore diameter is much larger than the solute diameter.

The values of the effective diffusion coefficient and accessible porosity obtained from HTO diffusion tests in the vertical direction are lower than those obtained in the horizontal direction. What is the origin of this result? The tortuosities obtained by image analyses are similar in both directions. This corresponds with the fact that the geometry factors evaluated from the HTO diffusion tests are similar in both directions. On the other hand, the number of start-face voxels connected to the end face in the Z-direction is lower than in other directions. This result is consistent with the results from the HTO diffusion tests, which show that the accessible porosity in the vertical direction is smaller than in the horizontal direction. This indicates that the number of connective pores and the diffusion-accessible porosity are the origins of the diffusion anisotropy. Thus, we performed a quantitative evaluation of the pore structure of the rock matrix. This method is a useful tool for the clarification of diffusion mechanisms.

The present study was the “Project for Assessment Methodology Development of Chemical Effects on Geological Disposal System”, which was entrusted to us by the Ministry of Economy, Trade and Industry (METI).

Reference

Takahashi, H. et al., 3D X-ray CT and Diffusion Measurements to Assess Tortuosity and Constrictivity in a Sedimentary Rock, *diffusion-fundamentals.org*, vol.11, issue 89, 2009, p.1-11.

2-5 Predicting the Future from Ancient Tectonism — History of Fault Development in Fractured Rocks —

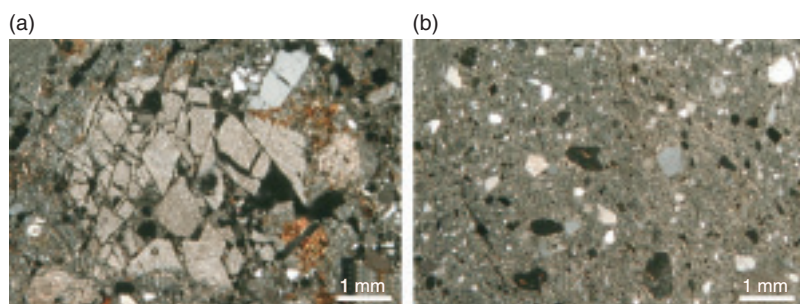


Fig.2-11 Photomicrographs of fractured rocks in a fault zone

(a) Numerous cracks develop in rock fragments and minerals. (b) Rock fragments and minerals are comminuted, and fine clay minerals fill the gaps as a result of further fracturing and alteration.

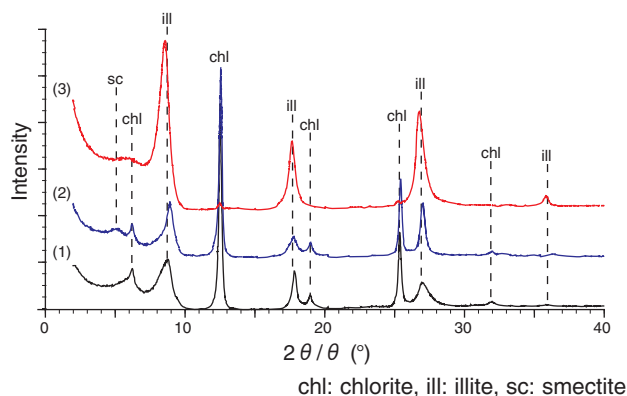


Fig.2-12 X-ray diffraction (XRD) pattern for fault gouge

Clay mineral components detected by XRD analysis: (1) No treatment, (2) ethylene glycol treatment (detection of smectite), and (3) hydrochloric acid treatment (detection of chlorite).

Rock fracturing, which is caused by fault displacement, leads to the formation of “fault zones” characterized by the aggregations of rock fragments and development of numerous cracks. The depth of the fault zone formation and the direction of fault displacement can be reconstructed on the basis of the deformation features of the rocks and minerals in a fault zone.

There are many faults in the Japanese Islands located on the boundary of the continental and oceanic plates. Prediction of future fault activities is significant for not only earthquake disaster prevention but also safety management of the geological disposal of high-level radioactive waste.

We have reconstructed the history of fault development on the basis of the spatial distribution and characteristics of the fault zones. In our study, we have revealed the spatial distribution of the fault zones through detailed field mapping and described the characteristics of fault zones through field sketches of fault outcrops and observations of fractured rocks and minerals by optical and electronic microscopes (Fig.2-11). Such a reconstructed history can be an important rationale for predicting future fault activities.

Water-rock interaction and subsequent formation of alteration minerals are observed in fault zones because the cracks in fractured rocks often become dominant

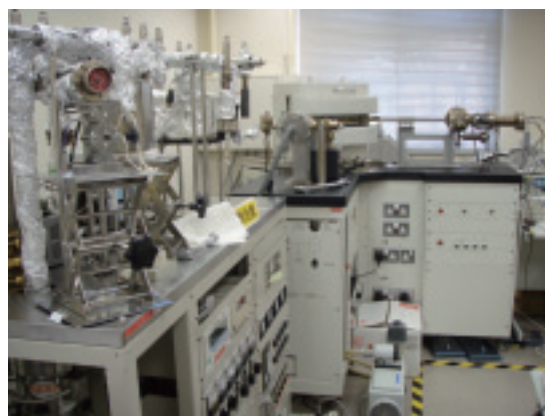


Fig.2-13 Noble-gas mass spectrometer for K-Ar dating

The isotopic ratio of argon is measured, and the absolute age of illite is calculated.

groundwater paths. The type and distribution of the alteration minerals reflect the underground environment (water quality, temperature, etc.) where fault zones are situated when the water-rock interaction occurs. Thus, the study of alteration minerals is important for understanding the change in the underground environment, which is associated with fault zone development.

Clay minerals are typical alteration minerals formed in a fault zone. Fault gouge, which is an unconsolidated thin layer in a fault zone and composed of very fine minerals and rock fragments, is formed by intense, repetitive fault activities associated with rock fragmentation and water-rock interaction. Clay minerals such as illite, smectite, chlorite, and kaolinite are often present in a fault gouge (Fig.2-12). Illite is used in radiometric dating based on the measurement of the product of the radioactive decay of an isotope of potassium into argon (K-Ar dating; Fig.2-13). Thus, K-Ar dating of illite can be useful for determining the absolute age of fault development from the reconstructed history. However, it is technically difficult to distinguish authigenic, very fine illite, in a fault gouge, from other potassium-bearing minerals in and around a fault zone. We have also challenged the development of such a difficult radiometric age dating method.

Reference

Niwa, M. et al., Spatial Distribution and Characteristics of Fracture Zones Near a Long-Lived Active Fault: A Field-Based Study for Understanding Changes in Underground Environment Caused by Long-Term Fault Activities, *Engineering Geology*, vol.119, 2011, p.31-50.

2-6 Challenges in Collecting Nanoscale Particles from Groundwater

— Development of New Ultrafiltration Techniques Maintaining In situ Pressure and Anaerobic Conditions —

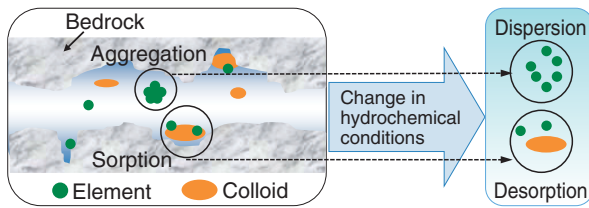


Fig.2-14 Change in colloids with the change in the hydrochemical conditions of groundwater

Physicochemical properties of colloids can be changed with the hydrochemical conditions of groundwater, such as pH, Eh, change by pressure release, and exposure to the atmosphere during sampling.

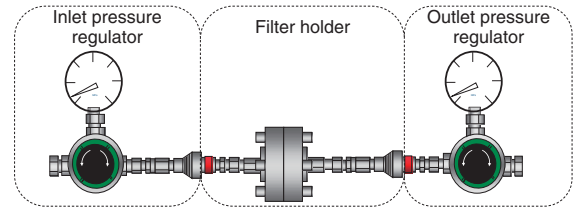
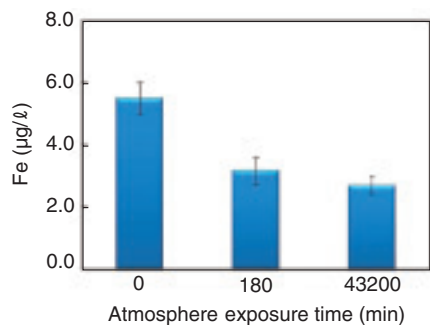
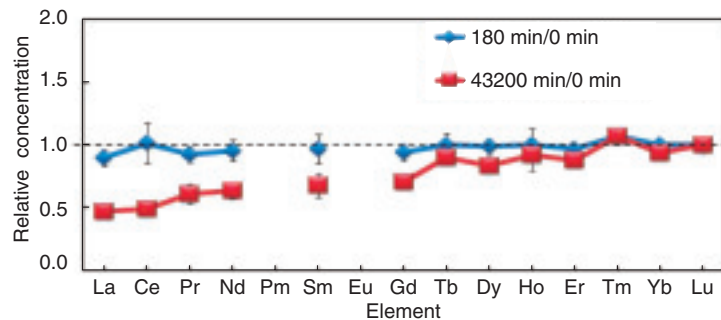


Fig.2-15 Schematic of the ultrafiltration instrument that maintains pressurized/anaerobic conditions

The instrument, made of Stainless Used Steel (SUS) materials, was designed to maintain anaerobic conditions at a high hydraulic pressure (10 MPa). The inlet and outlet pressure regulators can be used to adjust the differential pressure and thus prevent excess resistance pressure of the membrane filter (around 0.35 MPa).



* Error bars indicate the standard deviations of triplicate ICP-MS measures.



* Error bars indicate the standard deviations of triplicate ICP-MS measures.
* Concentration of Eu was lower than detection limit of ICP-MS (<0.1 ng/l), Pm does not exist in nature.

Fig.2-16 Concentration of Fe (left) and relative concentration of rare earth elements (right) in filtered groundwater at different atmosphere exposure times

The concentration of Fe decreased with the exposure time, suggesting that Fe in the groundwater aggregated on the filter by oxidation (left). The blue markers denote the data at 180 min normalized by the data at 0 min; red markers denote the data at 43200 min normalized by the data at 0 min. The concentration of the rare earth elements decreased with the exposure time, suggesting that the rare earth elements in the groundwater adsorbed onto the Fe colloids aggregated on the filter by oxidation (right).

Understanding the behavior of elements in an underground environment is important for safety assessment of the geological disposal of high-level radioactive waste. The behavior of elements in an underground environment is mainly controlled by groundwater flow and its interaction with rocks (e.g., adsorption). Additionally, the migration velocity of the elements is accelerated or delayed by colloids (particles in the size range 1 to 1000 nm). However, physicochemical properties of colloids can be changed when the hydrochemical conditions of groundwater change by pressure release and exposure to the atmosphere during sampling (Fig.2-14). This can pose problems when studying the colloids in groundwater. In this study, in order to solve the problem, an ultrafiltration instrument that maintains the in-situ pressure and anaerobic conditions was developed (Fig.2-15).

Ultrafiltration of groundwater at a depth of 200 m was conducted. Chemical analyses of the groundwater were also

conducted on samples filtered under atmospheric conditions (exposure time: 180 and 43200 min) and pressurized/anaerobic conditions (exposure time: 0 min), i.e., by using the ultrafiltration instrument (Fig.2-16). The result of the analysis under atmospheric conditions indicates that Fe in the groundwater aggregated and formed colloids by oxidation. Moreover, it was expected that rare earth elements had been adsorbed onto the Fe colloids. Therefore, it was clear that the problem of the colloids changing could be solved by using the ultrafiltration instrument.

The filter in the filter holder can be set aside and transported while maintaining the pressurized/anaerobic conditions. Thus, the colloids adsorbed on the filter can be used for various analyses. In the future, we aim to elucidate the effect of the colloids on the behavior of the elements in groundwater by evaluating the physicochemical properties of the colloids collected by the ultrafiltration instrument.

Reference

Aosai, D. et al., Development of New Ultrafiltration Techniques Maintaining In-Situ Hydrochemical Conditions for Colloidal Study, Proceedings of the ASME 13th International Conference on Environmental Remediation and Radioactive Waste Management (ICEM2010), Tsukuba, Japan, 2010, ICEM2010-40074, 8p., in CD-ROM.

2-7 Understanding Regional Stress in a Rock Mass

— Estimation of Regional Stress Using Measured Stress —

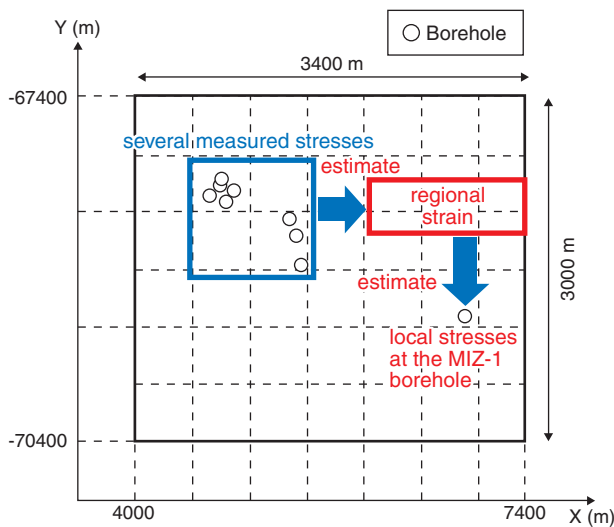


Fig.2-17 Analysis area and stress measurement points

The regional strain was estimated by using several measured local stresses in the area within the blue square. The local stresses at the MIZ-1 borehole were estimated by providing a displacement equivalent to the estimated regional strain around the area boundary.

For the geological disposal of high-level radioactive waste, many deep underground facilities are likely to be constructed within an area of a few square kilometers. Evaluation of the rock stress field is necessary to ensure the safe operation of the facilities and to minimize the area of the rock mass affected by excavations as well as damage to the rock mass. An understanding of the local stress is important for the evaluation of the safety of the region near the facilities. An understanding of the regional stress field is necessary to evaluate the safety in the area around the facilities. While numerous local stress measurements are needed to understand regional stress, it is difficult to obtain a large number of measurements because of cost and time constraints and labor requirements. The local stress can be obtained by using the hydraulic fracturing stress measurement technique and performing laboratory studies on drill core samples.

In this study, we propose a method for the estimation of regional stress from a limited number of local stress measurements, based on the following assumptions:

- The regional stress estimate depends on the boundary conditions used.
- The local stresses are the sum of the overburden pressure

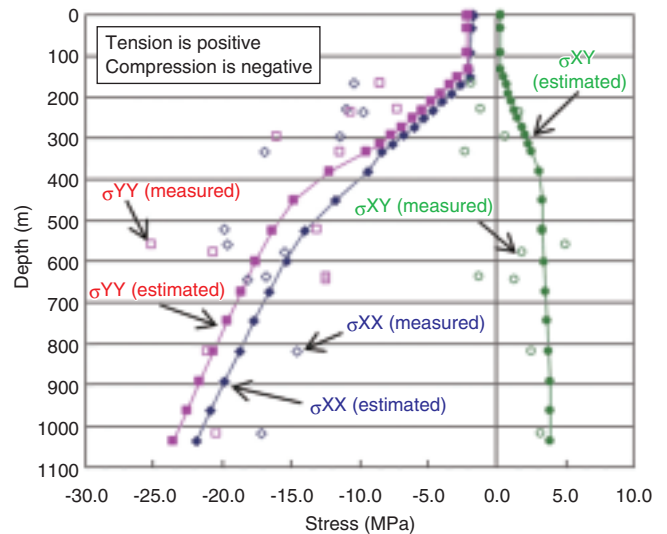


Fig.2-18 Analysis area and stress measurement points

The magnitudes of the measured and calculated stresses differ slightly, but the change with depth is quite similar. In particular, the change in the slope of the curves at 600 m is evident.

and the horizontal stress associated with plate tectonic forces.

In this study, the regional strain was used as a substitute for the regional stress because the strain is proportional to the stress in elastic analysis. The process for estimating the regional strain is described below:

- Model a target area on the basis of surface-based investigations and define each element on the basis of actual rock properties.
- Identify the reference strain and apply a displacement equivalent to it to the model boundary. Calculate the stresses corresponding to the applied displacements for the target area.
- Calculate the ratio of the measured stresses to the stresses calculated in (2) above by the least squares method. Estimate the regional strain by multiplying the reference strain with the ratio (Fig.2-17).

The estimated regional stress was compared with the measured stresses in the MIZ-1 borehole to evaluate the validity of the estimated regional strain. The magnitudes of the measured and calculated stresses differed slightly, but the change with depth was quite similar. In particular, the change in the slope of the curves at 600 m was evident (Fig.2-18).

Reference

Tanno, T. et al., Development of Method for Evaluation of Three Dimensional Distribution of in situ Stress State and Preliminary Estimation of Applicability, Rock Stress and Earthquakes: Proceedings of 5th International Symposium on In-Situ Rock Stress (ISRS-5), Beijing, China, 2010, p.521-526.

2-8 Rock Mass Response to Shaft Excavation

— Fault System Controlling Rock Mass Behavior in Soft Sedimentary Rocks —

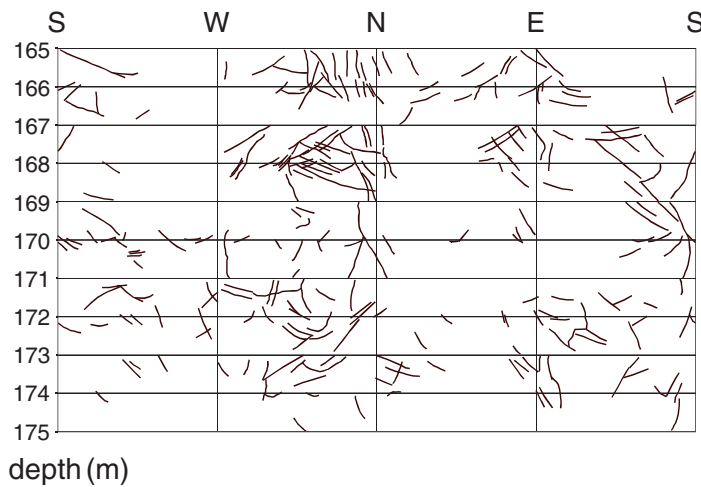


Fig.2-19 Development view acquired through fault observation in the shaft

Fault data were obtained from the wall of the Ventilation Shaft at the Horonobe Underground Research Laboratory. Many faults, with a typical length of about 1 m, can be recognized on the shaft wall.

An understanding of rock mass behavior during shaft excavation is important for the development and improvement of technology and engineering techniques related to the construction of deep underground facilities such as those for radioactive waste disposal.

This paper focuses on the stress field that produced a fault system in the Horonobe area of Japan, considering the relationship between the fault system and the rock mass response to shaft excavation in soft sedimentary rocks. A general consensus on underground excavation through soft rocks is that the role of discontinuities such as faults is far less important than that of the present rock stress. However, hydraulic-fracturing-based investigations in boreholes and studies of tectonic plate movements in the Horonobe area indicate that the influence of the fault system on the rock mass response to shaft excavation is not negligible; the reason for the influence is that the greatest convergence in the

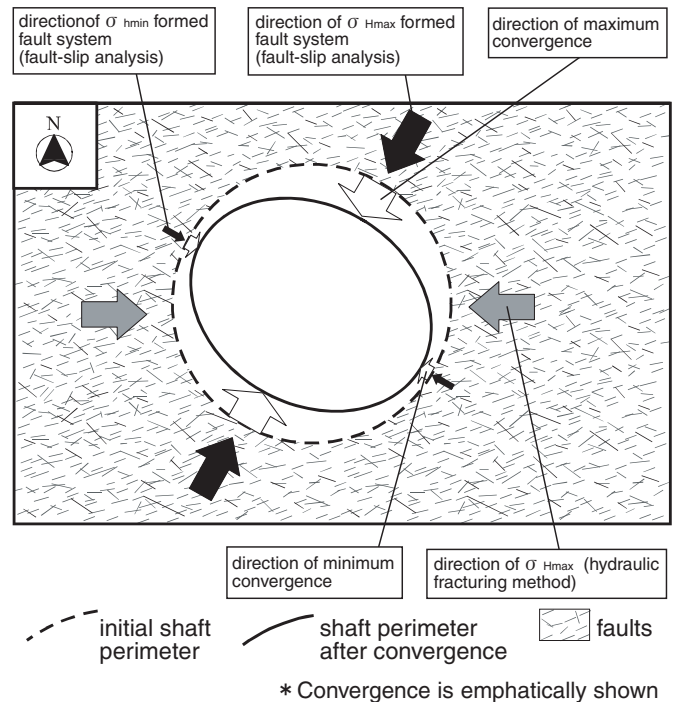


Fig.2-20 Conceptual diagram showing shaft convergence and stress

The diagram shows the relationships among the estimated direction of the major horizontal principal paleostress that produced the fault system, the direction of predominant convergence, and the direction of the present major horizontal principal stress.

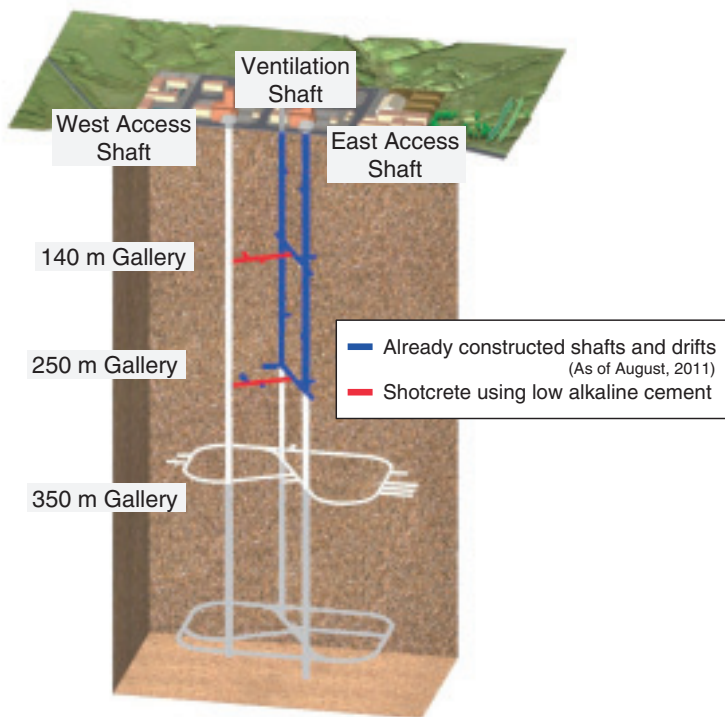
shaft during excavation was found to be oriented NNE-SSW, while the present major horizontal principal stress is oriented E-W (Fig.2-19).

We performed a fault-slip analysis of faults observed on the shaft wall and reconstructed the paleostress field that produced the fault system. When the faults were produced, the maximum horizontal principal stress was oriented mainly NNE-SSW and the minimum horizontal principal stress was oriented mainly WNW-ESE. These directions were close to the directions of the maximum and minimum convergences in the shaft, respectively (Fig.2-20). The result of this study shows that the rock mass deformation resulting from underground excavation is probably controlled by the fault system in the target area. It also suggests that the assessment and prediction of rock mass behavior on the basis of paleostress fields responsible for fault systems are possible.

Reference

Tokiwa, T. et al., Influence of a Fault System on Rock Mass Response to Shaft Excavation in Soft Sedimentary Rock, Horonobe Area, Northern Japan, International Journal of Rock Mechanics & Mining Sciences, vol.48, issue 5, 2011, p.773-781.

2-9 Improvement in Reliability of Geological Disposal Technology – Use of Low-Alkaline Cement in the Construction of a Gallery –



* This layout may be changed depending on the results of future investigations

Fig.2-21 Layout of the Horonobe URL

Red line: Construction using low alkaline cement (HFSC).

In Japan, high-level radioactive waste repositories are to be constructed at a depth of more than 300 m below the surface. Shotcrete and lining will be used in the construction to ensure safety during the construction and operational periods. Concrete, a composite alkaline material, is composed of aggregate, cement, and additives. Low-alkaline cement has been developed for achieving long-term stability of the barrier systems that may be adversely affected by the alkaline arising from high-alkaline cement material. JAEA has developed a type of low-alkaline cement named HFSC (highly fly-ash contained silica-fume cement). HFSC contains silica-fume and coal ash (about 60% in weight).

JAEA is now constructing an underground research laboratory (URL) at Horonobe for the purpose of research on deep geological science and repository engineering technology (Fig.2-21). As an in situ experiment, HFSC was used as shotcrete in the construction of 140 m and 250 m galleries in the URL (Fig.2-22 and Fig.2-23). The aim of this in situ experiment was to assess the performance of HFSC shotcrete in terms of mechanics, workability, durability, and so on. The workability of HFSC was evaluated by comparing it with the workability of ordinary Portland cement (OPC). The experiment results confirmed that the strength of HFSC

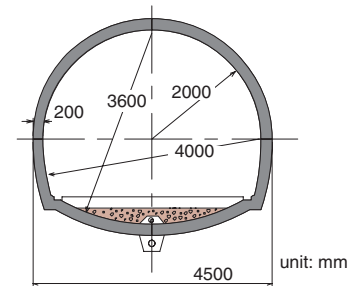


Fig.2-22 Typical cross section of the galleries



Fig.2-23 Spraying HFSC shotcrete in the drift

The concrete manufactured on the ground is carried in from the east access shaft to the depth concerned, and it sprays to the wall from the spray nozzle attached to the arm of a small backhoe.

shotcrete with local aggregates was greater than the design strength and that the workability of HFSC shotcrete was equivalent to that of OPC shotcrete. Further, it was shown that HFSC shotcrete could be used to construct a drift in the underground facility. There are some types of low-alkaline cement, and these have been used in a few small-scale field experiments. However, HFSC is the only low-alkaline cement that has been used in a full-scale field experiment in the world.

Next, the influence of HFSC and OPC on groundwater and rock will be evaluated by sampling water and core from the drift wall. HFSC shotcrete would be used in the construction of a gallery constructed at a depth of than 250 m, and the effect of the HFSC on the change in geological features such as the increase of initial rock stress and salinity of groundwater according to the depth would be investigated. HFSC will be used in construction not only as shotcrete but also as the concrete for constructing the segmental liner concrete in shafts. The effectiveness of using HFSC concrete in deep underground construction and the effect of HFSC shotcrete and/or lining on geological features will be evaluated.

Reference

Nakayama, M. et. al., Low Alkaline Cement Used in the Construction of a Gallery in the Horonobe Underground Research Laboratory, Proceedings of the ASME 13th International Conference on Environmental Remediation and Radioactive Waste Management (ICEM2010), Tsukuba, Japan, 2010, ICEM2010-40038, 6p., in CD-ROM.

2-10 Investigation of Shallow Groundwater Migration at Snowy Cold Region — Research on Shallow Groundwater Flow Based on Groundwater Level and Geological Structures in the Horonobe Area —



Fig.2-24 Implementation of the surface hydrological survey

The upper panel shows a photograph taken during the snow season. A snow tractor is utilized in our survey. The lower panel shows a photograph taken during the snow-free season. We put on two layers of a long-sleeved jacket, mosquito net masks, and leather gloves, and we also used mosquito, horsefly and hornet repellent.

To assess the safety of geological disposal of high-level radioactive waste, it is important to understand groundwater flow as a driving force of mass transport. To estimate groundwater flow by performing a numerical simulation, the upper hydraulic boundary condition of an aquifer must be appropriately evaluated and configured on the basis of the water supply. Therefore, shallow groundwater flow system, including water infiltration from the surface to shallow underground, subsurface runoff, and deep groundwater recharge, should be considered on the basis of hydrological information.

We have been carrying out the following surface hydrological observations in Horonobe, Hokkaido: meteorological observation, observation of river flux, observation of shallow groundwater level, and snowfall observation (Fig.2-24). In this study, to elucidate the mechanism of the water supply from the surface to the shallow underground region during cold snowy conditions, we estimated and analyzed the results of meteorological and long-term groundwater-level observations by using

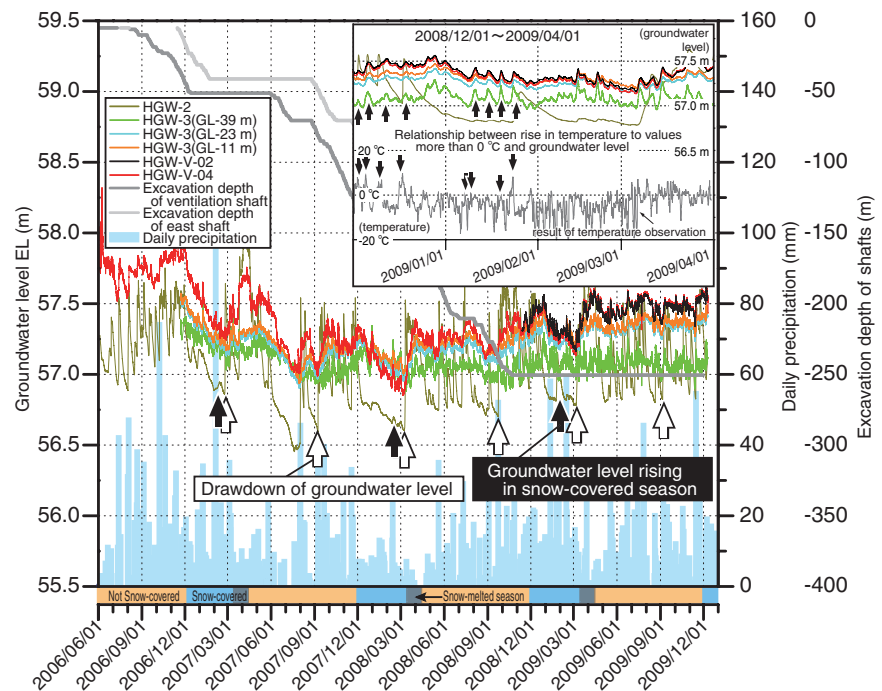


Fig.2-25 Results of groundwater-level observation around the Horonobe URL
Results of the groundwater-level observation, the daily precipitation, and the depth of shaft excavation from June 2006 to December 2009. The data are for several shallow boreholes near the Horonobe URL. It is considered that the groundwater level rose as the temperature increased to more than 0 °C in the snow season.

approximately 3~50 m deep boreholes, by considering the geological structures in the surrounding area. The results indicate that during snow season, the snow melting from the bottom of a snow cover supplies the shallow underground region with water and that the groundwater level rises due to the melting of the snow on the surface as the temperature rises above 0 °C (Fig.2-25). In addition, from the results of long-term observations, it has been clarified that the shaft excavation for the construction of the Horonobe underground research laboratory (URL) does not cause a drop in the shallow groundwater level.

Previously, it was very difficult to estimate accurately the water balance throughout the year for snowy cold regions, because obtaining hydrological and meteorological data and carrying out geological survey in snow season is difficult. This study supplies qualitative information about water infiltration from the surface to underground region in cold snowy areas and implements the evaluation of the hydrogeological environment throughout the year.

Reference

Yokota, H. et al., A Study of Shallow Groundwater Flow Based on Groundwater Level and Geological Structures in the Horonobe Area, Hokkaido, Chikassui gakkai-shi (Journal of groundwater hydrology), vol.53, no.2, 2011, p.193-206 (in Japanese).

Toward the Practical Use of Fusion Energy

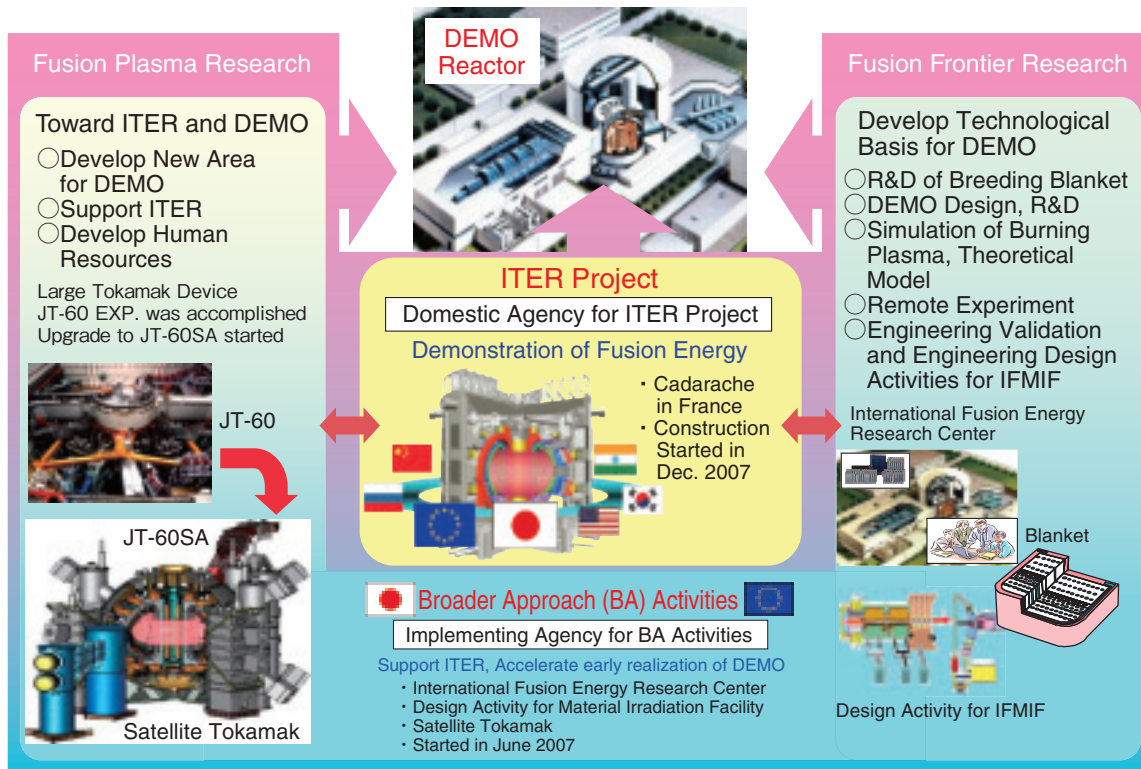


Fig.3-1 Steps involved in the development of fusion DEMO reactor

Fusion plasma and fusion frontier research is being pursued to develop a DEMO reactor, aiming for the early realization of fusion energy.

Crucial research and development on fusion plasma and fusion frontier is being pursued through intensive international cooperation, i.e., through the International Thermonuclear Experimental Reactor (ITER) project, Broader Approach (BA) activities, and other collaborations (Fig.3-1), aiming at the practical use of fusion energy.

ITER project

The ITER project is an international cooperative project that aims at demonstrating the scientific and technological feasibility of fusion energy through the construction and operation of an experimental reactor. The ITER agreement came into force in October 2007, and JAEA was designated as the domestic agency for the ITER project in Japan. JAEA has proceeded with preparing the equipment that Japan was allotted to provide, has been successful in terms of technological development (Topics 3-2, 3-3, and 3-4), and has started the mass production of a superconducting coil conductor (Topics 3-1) ahead of any other country participating in the ITER project.

BA activities

BA activities is a joint project by Japan and EU that aims at executing support research for the ITER and pursuing research and development activities for the development of a DEMO reactor, which is the next step of ITER, with the goal of early realization of fusion energy. The BA agreement came into force in June 2007, and JAEA was designated as the

implementing agency for BA activities in Japan.

BA activities includes three projects: projects at the International Fusion Energy Research Center (IFERC), Engineering Validation and Engineering Design Activities for the International Fusion Material Irradiation Facility (IFMIF/EVEDA), and the Satellite Tokamak Program (STP). Topic 3-9 shows an outline of the IFERC project and the related schedule. Topic 3-12 describes the results of the research related to IFMIF/EVEDA. In STP, the construction activities of JT-60SA progressed well, including the design and manufacture of the components (Topic 3-5).

Fusion plasma research

The critical requirement for development of the future fusion reactor is achieving high economical efficiency, namely, sustaining high fusion power in a compact reactor core. It is necessary to improve the plasma pressure, for example, to accomplish this. Topics 3-6, 3-7 and 3-8 are the results that can contribute to achieve high plasma pressure.

Fusion frontier research

In the fusion reactor, it is necessary to utilize the neutrons from the fusion reaction effectively for fuel production. Topic 3-11 includes the results that can contribute to the efficient conduction of experiments in this regard. Moreover, Topic 3-10 discusses the result that can form the basis for the control of the DEMO reactor.

3-1 Significant Progress in ITER Coil Procurement — Mock-Up Trials for ITER Toroidal Field Coils —

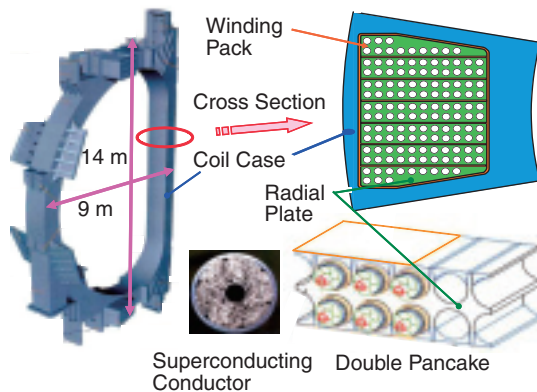


Fig.3-2 Configuration of TF coil

A DP is composed of a RP and a conductor, which is inserted in the grooves of the RP. The winding is composed of seven DPs and is inserted in a coil case, and together, the winding and the case comprise the TF coil.



Fig.3-3 Insulated one-third-scale double pancake (5.1 m × 3.8 m)

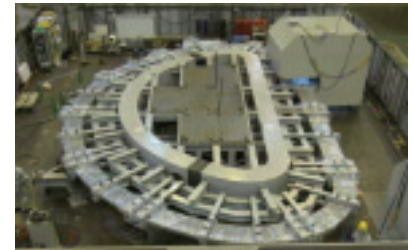


Fig.3-4 Full-scale radial plate (13 m × 8 m)
The mock-up is composed of ten segments, which are welded by the machine.



Fig.3-5 Full-scale segments of coil case

Mock-ups of two segments (A1 and B3) were fabricated to validate the welding technology and evaluate welding distortion.

The superconducting (SC) coil system in the International Thermonuclear Experimental Reactor (ITER) confines the plasma and controls the plasma shape by generating high magnetic fields of more than 10 T. A toroidal field (TF) coil, which is one of the important components in the ITER project and the biggest SC coil in the world, is 14 m high, 9 m wide, and weighs 300 tons; it consists of a winding pack and a coil case (Fig.3-2). The winding pack is composed of seven double pancakes (DPs). In a DP, an SC conductor is inserted in the grooves of a D-shaped radial plate (RP). Nineteen TF coils, including one spare, will be fabricated in the project. We will procure nine coils and ten additional coil cases. We started mock-up trials for the TF coil in June 2010.

When winding the conductor, the dimensional accuracy of the winding is required to insert the wound conductor into the grooves of the RP. By trial fabrication of one-third-scale DP mock-ups, we could confirm that the developed automatic winding machine can efficiently control the accuracy (<0.006%) of windings of a dummy conductor and a SC

conductor. One DP using an SC conductor was heat-treated to measure the deformation during heat treatment, and the data obtained were considered for the actual fabrication. The other DP using a dummy conductor was inserted into the RP, resin-impregnated (Fig.3-3), and cut for inspection. The effectiveness of the insulation technology was verified by the mock-up trial. A full-scale RP mock-up was fabricated (Fig.3-4) to evaluate the welding distortion.

Mock-ups of segments A1 and B3 of a coil case were fabricated to establish the fabrication technology (Fig.3-5). The main challenge in the fabrication of the coil case was to form a 260 mm deep weld on one side of the case. This problem was overcome by using narrow-gap automatic tungsten inert gas (TIG) welding. Welding distortion in the mock-ups was investigated to establish the weld procedure.

In the near future, we plan to fabricate a full-scale DP by using the fabricated full-scale RP and thus verify the effectiveness of the DP fabrication technology.

Reference

Matsui, K. et al., Progress of Mock-Up Trials for ITER TF Coil Procurement in Japan, Fusion Engineering and Design, vol.86, issues 6-8, 2011, p.1531-1536.

3-2 H⁻ Beam Acceleration Close to ITER Requirement — Development of 1 MeV Accelerator for ITER Neutral Beam Injector —

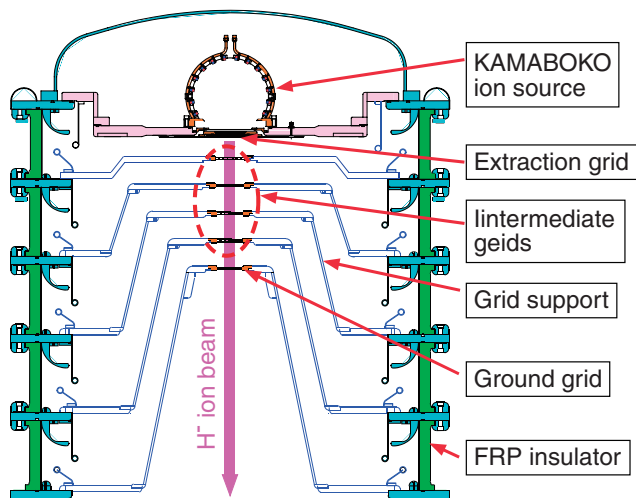


Fig.3-6 Cross-section of MeV accelerator for the development of ITER neutral beam injector (NBI)

Negative hydrogen ions (H⁻) produced in the ion source are accelerated electrostatically up to 1 MeV. With respect to the current required for the accelerator of the ITER NBI (40 A), MeV accelerator aims to demonstrate 0.5 A beam acceleration at the same current density (200 A/m²).

In the ITER project, two sets of neutral beam injectors (NBI) are installed for plasma heating and for plasma current drive, and each set can deliver an injection power of 16.5 MW for 1 h. In the NBI, a D⁰ beam is injected into the fusion plasma after neutralizing high energy D⁻ ion beam generated by the accelerator. By considering the geometrical losses and neutralization efficiency in the NBI system, the required beam current and beam energy are 40 A (200 A/m²) and 1 MeV respectively. To fulfill these requirements, we have developed the “MeV accelerator” (Fig.3-6) as a proof-of-principle accelerator for the ITER NBI at the MeV test facility in JAEA.

The MeV accelerator is a five stage electrostatic accelerator. The H⁻ ions produced in a KAMABOKO ion source are extracted through the many apertures of the extraction grids. The extracted H⁻ ions are then accelerated up to 1 MeV by applying a potential difference of 0.2 MV between the acceleration grids (overall 1 MV across the five stages).

Fig.3-7 shows the improvement in the performance of the MeV accelerator and also includes recently obtained data. In the previous accelerator till 2007, the energy and current density were limited to 0.8 MeV, and 140 A/m², respectively,

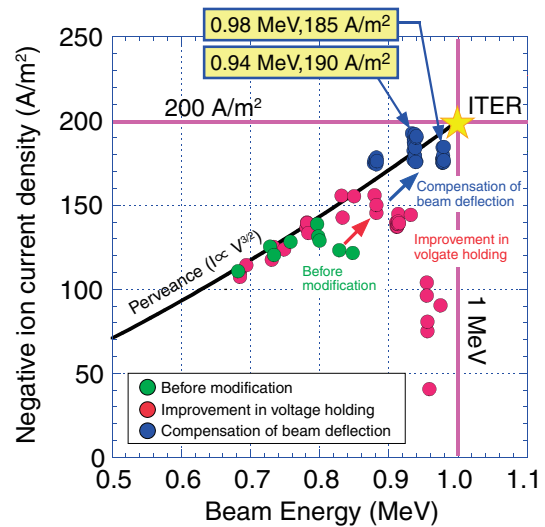


Fig.3-7 Progress of MeV accelerator performance

Improvement in the capability for voltage holding and compensation of beamlet deflection enabled stable H⁻ beam acceleration. The performance of the MeV accelerator was improved, and the energy and current density of 0.98 MeV, and 185 A/m², respectively, were obtained.

because of the insufficient capability for voltage holding. Many discharge marks were found in the interior of the accelerator after the high voltage test. It was found that these discharges start from the point where the local electric field strength is high, e.g., at a step and a corner in the grid support. To lower the electric field strength at these points, the MeV accelerator was modified by expanding the gaps among the grids. After these modifications, the capability for voltage holding improved, and the energy and current density increased to 0.86 MeV, and 160 A/m², respectively. Furthermore, it was found that the H⁻ ion beam is intercepted by the apertures in the grids, and this cause not only a decrease in the beam current but also discharges between the grids during high-energy beam acceleration. This interception of the H⁻ ion beam is due to the beam deflection caused by the magnetic field and the space charge repulsion between adjacent beamlets. To compensate the beam deflection, a new grid system was designed based on a 3D beam trajectory analysis. Thus, the MeV accelerator achieved 980 keV, 185 A/m², which are close to the required values for the ITER. We continue to further develop the NBI system to stably inject high power beams the plasma.

Reference

Taniguchi, M. et al., Long Pulse H⁻ Ion Beam Acceleration in MeV Accelerator, Review of Scientific Instruments, vol.81, issue 2, 2010, p.02B101-1-02B101-3.

3-3 Fulfillment of ITER Criteria for RF Energy Transmission Efficiency

— Development of Electron Cyclotron Heating and Current Drive for ITER —

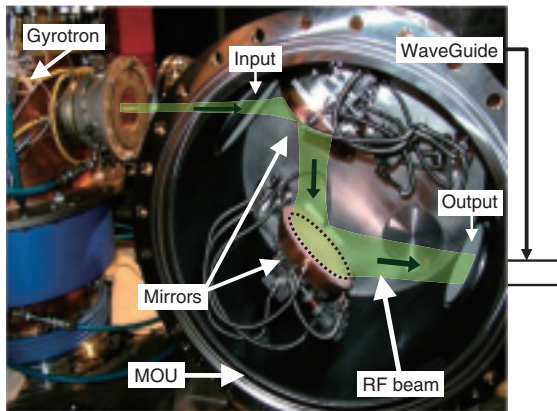


Fig.3-8 Modified MOU

The RF beam delivered from the gyrotron was injected to the corrugated waveguide through a couple of mirrors in the MOU. High purity of the HE_{11} mode was achieved by precise mirror adjustment.

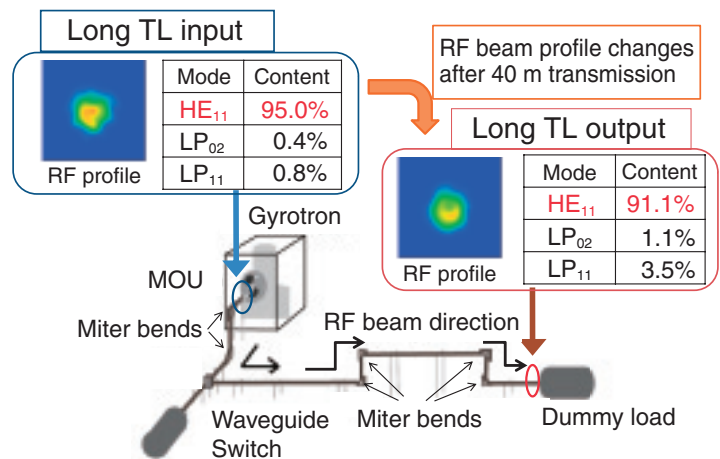


Fig.3-9 Configuration of high-power TL and RF beam profile and mode content at the TL input and output

The TL includes four miter bends, a couple of polarizers, and a waveguide switch. After transmission over 40 m of the TL, the RF field profile had a single peak and high HE_{11} mode purity was maintained.

The electron cyclotron heating and current drive (ECH & CD), which is a tool for heating and sustaining the plasma by a high-power millimeter wave, is a major heating system in the ITER. In the ITER, 1 MW/170 GHz RF power generated by the gyrotron is transmitted to the fusion plasma by a transmission line (TL) that is more than 100 m long. To achieve high transmission efficiency in the long-distance TL that includes a corrugated waveguide system (diameter: 63.5 mm), high purity of the fundamental transmission mode (HE_{11} mode) should be realized so that transmission loss is minimized.

For this purpose, we fabricated an ITER-relevant high-power, long-distance TL test system, performed an experiment for improving the HE_{11} mode purity, and demonstrated high-efficiency high-power RF transmission. First, we modified the matching optics unit (MOU) to improve the HE_{11} mode purity. The MOU includes two mirrors that transfer the RF power from the gyrotron to the

corrugated waveguide, as shown in Fig.3-8. Using the modified mirror adjustment mechanism, we optimized the mirror angles and achieved an HE_{11} mode purity of 95%. Next, we estimated the influence of long-distance power transmission on the mode purity by using the transmission system shown in Fig.3-9. A high HE_{11} mode content of 91% was maintained at the end of the 40 m long TL when the mode purity was 95%. The total power in the unwanted higher-order modes (LP_{02} , LP_{11}) that were generated was 4%, which was acceptable for the ITER.

Finally, the transmission efficiency was measured. The transmitted power was measured by the dummy load installed at the end of the TL. The transmission loss was also identified by measuring the heat deposition in the intermediate components. From the results, the transmission efficiency was confirmed to be 96%, which well exceeded the ITER requirement.

Reference

Takahashi, K., Oda, Y. et al., High Power Millimeter Wave Experiment of ITER Relevant Electron Cyclotron Heating and Current Drive System, Review of Scientific Instruments, vol.82, issue 6, 2011, p.063506-1-063506-7.

3-4 Innovative In-Vessel Mirror for Current Profile Measurement in ITER – Development of Retroreflector for ITER Poloidal Polarimeter –

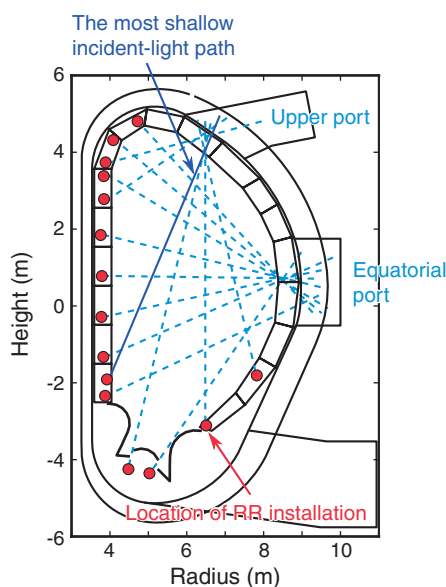


Fig.3-10 Cross section of ITER vacuum vessel and incident-light paths in ITER poloidal polarimeter

The dotted lines denote the incident light paths, and the red circles indicate the location of RR installation.

It is well known that information about the magnetic field structure in the plasma (or equivalently, the plasma current profile) is essential for steady-state and high-performance operation of Tokamak devices. In order to measure the magnetic field in the plasma, poloidal polarimeters have been installed in several devices. Such polarimeters will be installed in the ITER as well (Japan is in charge of the development of an ITER poloidal polarimeter). Far-infrared laser light injected in the plasma is reflected by a corner-cube retroreflector (RR) and returns to a diagnostic room. The angle of rotation of the polarization plane of the laser light provides information about the magnetic field (and electron density) in the plasma. RRs will be installed in dedicated holes at the center of the first wall panels of blanket modules. However, it seems difficult to implement inclined holes at the optimum locations owing to interference from the intricate system of cooling water pipes inside the first wall panels (Fig.3-11(a)). In particular, the RR for the viewing chord, which is shown by the blue solid line in Fig.3-10, occupies a large space. In order to install RRs at the optimum locations, we developed a terrace retroreflector array (TERRA) which

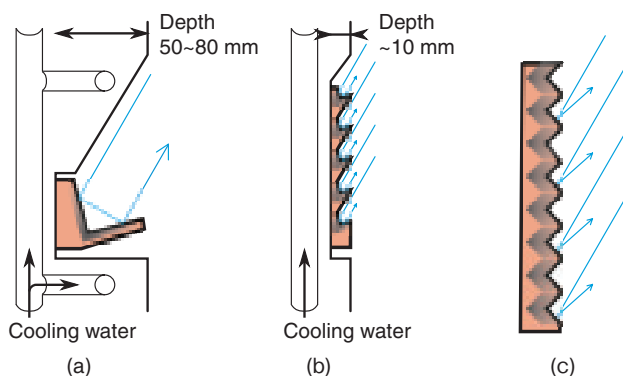


Fig.3-11 (a) Installation of RR (b) Installation of TERRA (c) Conventional RR array

The installation space for RR is larger than that for TERRA. A conventional RR array is thin but cannot return light parallel to the shallow incident-light path.

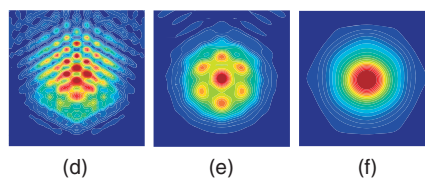


Fig.3-12 Intensity distribution of light reflected by TERRA

(d), (e), and (f) show the intensity distribution after 1, 2, and 10 m propagation. The intensity is high in the red area.

is an array of small, inclined RRs. When the angle of incident light is small a conventional RR array cannot return light parallel to the incident-light path (Fig.3-11(c)). However, TERRA can return light parallel to the incident-light path because the small RRs constituting this array are inclined. Owing to the thin structure of TERRA, the installation space is reduced (Fig.3-11(b)), and thus, high cooling capability is achieved.

The light beams reflected by the small RRs interfere with each other and propagate in a particular direction. Fig.3-12 shows the intensity of the reflected light. The intensity distribution is very complicated just after the reflection (Fig.3-12(d) and (e)). When TERRA is deformed by thermal stress, the propagation direction and intensity distribution vary. We evaluated the deformation of TERRA in the ITER and found that light power returning to the diagnostic room was about 50% of the incident light power and that the polarization state was nearly unchanged.

Accordingly, we successfully developed an innovative in-vessel mirror and provided a crucial basis for the design of the ITER poloidal polarimeter.

Reference

Imazawa, R. et al., Terrace Retro-Reflector Array for Poloidal Polarimeter on ITER, Review of Scientific Instruments, vol.82, issue 2, 2011, p.023116-1-023116-5.

3-5 Progress in Satellite Tokamak Programme Project as part of Broader Approach Activities – Construction Activities of JT-60SA Tokamak Right on Track –

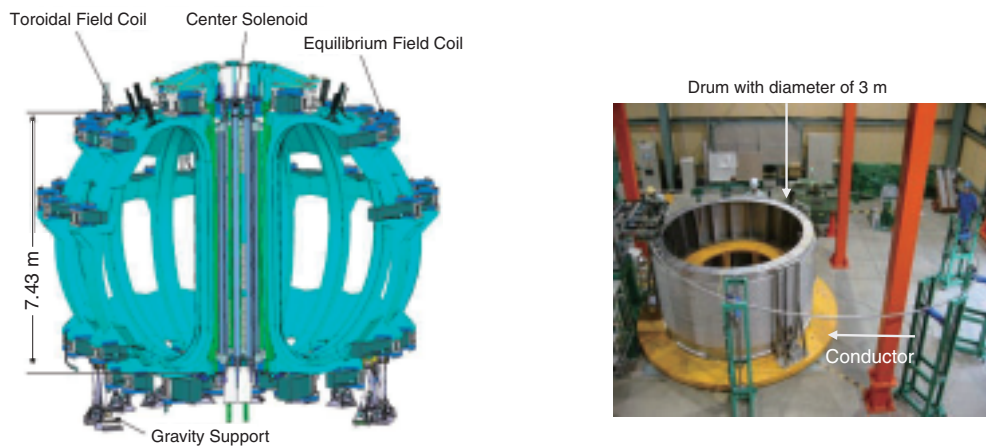


Fig.3-13 Bird's eye view of arrangement of superconducting coils and manufacturing of equilibrium field coil

The image on the left shows the assembly of the 18 TF coils, 6 EF coils, and 4 modules of CS, and the photograph on the right shows a scene of manufacturing of the superconductor for the EF coil in the conductor jacketing building at the JAEA Naka site.

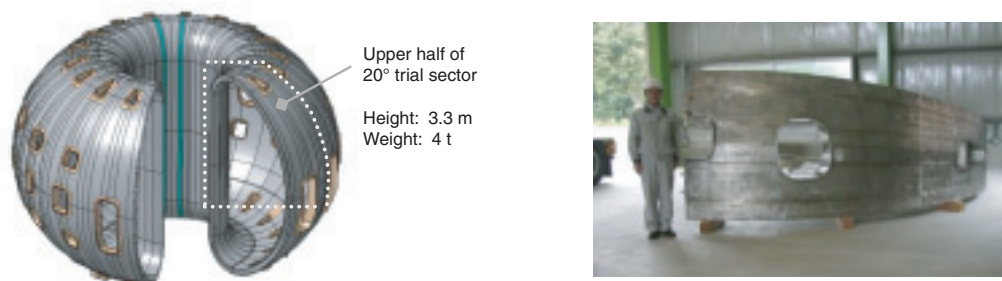


Fig.3-14 Bird's eye view of arrangement of vacuum vessel body and upper half of 20° trial sector of vacuum vessel

Series production of the VV was launched following the completion of the construction of the upper half of its 20° trial sector, and the trial sector was delivered and stored at the VV sector assembly building at the JAEA Naka site.

As part of the Satellite Tokamak Programme jointly implemented by Europe and Japan, the construction activities of JT-60SA, including the following activities, have been progressing well: design and manufacturing of the components, the preparation for the tokamak assembly that is to be started in 2012, and site preparation for generating the first plasma in 2016. The procurement arrangements (PAs) for the superconducting poloidal field (PF) magnet, vacuum vessel (VV), divertor, first-wall materials to be made by Japan, and other PAs for the magnet power supply, cryostat, high-temperature superconductor current leads, superconducting toroidal field (TF) magnet to be made by Europe were completed so far by two implementing agencies (IAs): the Japan Atomic Energy Agency (JAEA, Japan) and Fusion for Energy (Europe). The contracts were awarded between the IAs and industry, and the activities for the procurement of components were carried out according to the PAs.

The PA for the TF magnet was concluded in 2010, and the contract for manufacturing the conductor was launched. For the PF magnet, which consists of the equilibrium field (EF) coils and the central solenoid (CS), the buildings for the conductor jacketing and 80 m long coil winding were

completed at the JAEA Naka site in 2009, and manufacturing of the conductor for the EF coil was started in 2010 with the 630 m long jacketing line (Fig.3-13).

The VV trial sector was completed at the company's factory in 2010, and series production was started (Fig.3-14). The VV sector assembly building was constructed at the Naka site, and it was ready for carrying out the welding of 40° inboard and outboard VV sectors (the height of the donut-shaped vessel: 6.6 m) to be delivered from the company to the Naka site. The procurement of the first-wall materials (carbon fiber composite materials) to be used in the VV is also progressing steadily.

Along with the construction activities, disassembly of the JT-60 facility, including the removal of some parts of the heating system, the wall for the neutron shielding, and the diagnostic stage in the JT-60 experimental building, is progressing as scheduled. For the future experimental operation, the version 2.1 of the JT-60SA Research Plan was initially completed in February 2011 by Japanese scientists, 70 scientists from JAEA and 66 from universities and 13 institutes. The Research Plan will be jointly updated in December 2011 by the over 200 scientists that included 70 European scientists from 18 institutes of 9 countries.

Reference

Ishida, S. et al., Overview of the JT-60SA Project, Nuclear Fusion, vol.51, no.9, 2011, p.094018-1-094018-12.

3-6 Observation of Multistage Transition in Radial Electric Field — A New Discovery Unexpected in the Case of the Standard Model —

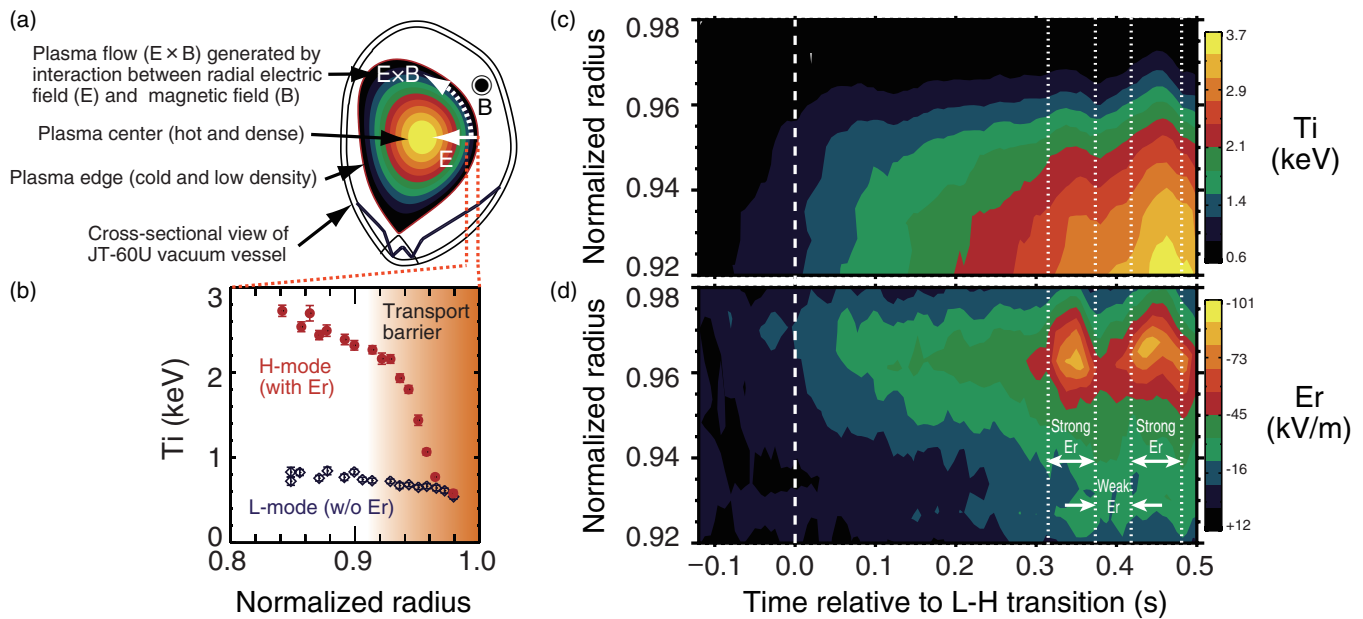


Fig.3-15 Cross-sectional view of plasma (a), an ion temperature profile (b), a contour plot of spatiotemporal structures of ion temperature T_i (c), and radial electric field E_r (d)

In an improved confinement mode (H-mode), a transport barrier is formed. As expected from the theory, the E_r profile (right bottom) is found to develop at and after the transition to the H-mode, indicating the formation of an edge “well” structure, and the steepening of the T_i profile is accelerated. During the formation of the pedestal, a spontaneously generated multistage E_r transition is observed with essentially the same confinement properties, transiently. It is noted that normalized radii with values of zero and unity are defined by the plasma center and edge, respectively.

With an economically attractive fusion reactor, a high fusion output should be achieved. Since the fusion output is proportional to the square of the plasma pressure (= temperature \times density), various operational regimes with the plasma pressure as high as possible have been developed. The high-confinement-mode (H-mode) operation involving the edge pedestal structure (thermal barrier) is nominated as a standard operational scenario for the International Thermonuclear Experimental Reactor (ITER), as shown in Fig.3-15 (left bottom). In the H-mode, the plasma pressure increases by a factor of two (it is to be noted that the fusion output increases by a factor of four) relative to the plasma pressure in the case of plasma confinement without any pedestal (L-mode). At the transition from the L-mode to the H-mode (L-H transition), it is believed that a spontaneously generated radial electric field (E_r) in the localized region just inside the plasma boundary strongly influences the essential condition for improved confinement to exist. The theory suggests that the $E \times B$ shear flow suppresses edge turbulence and that the suppression in turn inhibits transport, thus enabling pedestal formation, although the edge evolution in E_r and its connection to H-mode confinement are not well understood.

In the JT-60U tokamak, we performed an improved confinement experiment in the presence of a strong magnetic field that was similar to the magnetic field in the ITER, and we determined the spatiotemporal structures of the radial electric field by means of spectroscopy with high spatial and temporal resolution. As shown in Fig.3-15, the E_r profile (right bottom) was found to develop at and after the transition to the H-mode, indicating the formation of an edge “well” structure, and the steepening of the T_i profile (right top) was accelerated as expected in the case of the standard model. The most obvious concomitant feature was a rapid drop in the edge E_r value at the instant when the time relative to the L-H transition was ~ 0.315 s, particularly at a normalized radius of ~ 0.96 , indicating a strong deepening (approximately by a factor of two) of the E_r well structure. A clear bifurcation of the edge E_r trend into weakly negative and strongly negative trends was observed in the later H-mode phase. Both trends showed essentially the same confinement properties despite corresponding to two very different E_r structures. The results indicate that energy confinement improvement may not necessarily be connected to the $E \times B$ shear flow suppression of turbulence. These results are unexpected in the case of the standard theory, and are world leading results.

Reference

Kamiya, K. et al., Observation of a Complex Multistage Transition in the JT-60U H-mode Edge, *Physical Review Letters*, vol.105, issue 4, 2010, p.045004-1-045004-4.

3-7 Planning and Executing Joint Experiments, Leading International Team – Toward Validation of Neutral Beam Current Drive Theory for ITER –

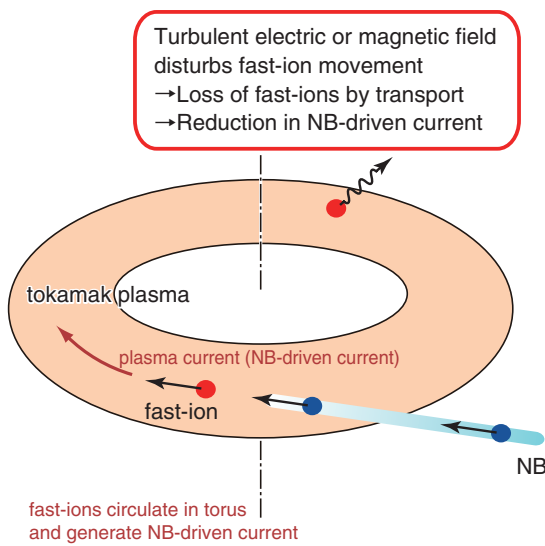


Fig.3-16 Principle of NB current drive and transport of fast-ions by turbulence in tokamak device

Fast-ions produced by ionization of the injected NB circulate in the torus plasma and generate NB-driven current. A turbulent electric or magnetic field disturbs the movement of the fast-ions, and hence, they are lost. As a consequence, the NB-driven current decreases.

In a tokamak device, the high-temperature plasma required for nuclear fusion reactions is confined by the magnetic field produced by the current in the plasma (plasma current). It is known that the plasma performance depends on the spatial profile of the plasma current. As shown in Fig.3-16, the neutral beam (NB) injected into the plasma is ionized and converted into fast-ions by collision with the plasma. The fast-ions circulate in the torus plasma and generate current, which is known as NB-driven current. The NB-driven current plays an essential role in optimizing and sustaining the plasma current profile suitable for confining high-performance plasma.

Checking the accuracy of the theoretically predicted NB-driven current is an urgent issue that must be addressed so that steady-state operation can be realized in the ITER. In order to validate the NB current drive theory, the experimentally measured NB-driven current must be compared with the theoretical current for a wide range of parameters by making full use of multiple tokamak devices with largely different NB parameters (e.g., NB energy, E_b) and plasma parameters. Hence, we planned and executed joint experiments among world-leading tokamaks, ASDEX-Upgrade (AUG, Germany), DIII-D (the United States), JT-60U (Japan), and MAST (the United Kingdom), leading the International Tokamak Physics Activity.

The measured NB-driven current mostly agreed with the

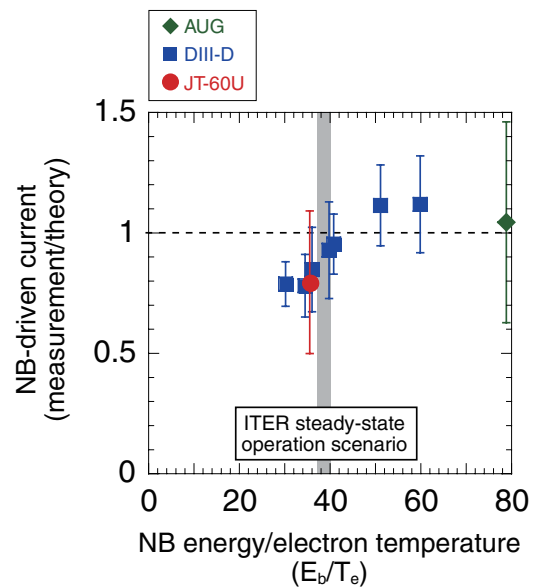


Fig.3-17 Dependence of ratio of experimental and theoretical NB-driven currents on NB-energy-to-electron-temperature ratio (E_b/T_e)

Transport of fast-ions carrying NB-driven current by turbulent electric field increases for a smaller E_b/T_e value.

theoretical value; however, at high electron temperature (T_e) or plasma pressure discharges under strong-heating or strong-current-drive conditions, the measured value was slightly smaller than the theoretical value. Since this difference could be attributed to the plasma turbulence affecting the fast-ions, we investigated the decrease in the measured current with respect to the theoretical value as a function of the effect of electrostatic turbulence on fast-ions (E_b/T_e). The results obtained for three tokamak devices (AUG, DIII-D, and JT-60U) showed the same trend (Fig.3-17). The measured current agreed with the theoretical value within the measurement error at the E_b/T_e value expected for the ITER steady-state operation scenario (shown in gray in the figure). However, the measured current became smaller than the theoretical current with a further decrease in E_b/T_e . In this regime, the effect of another type of turbulence, the electromagnetic turbulence, on the fast-ions was also pronounced, where the effect is measured in terms of the beta value characterizing the plasma pressure. Hence, we could not identify which turbulence, electrostatic or electromagnetic, was dominant in the experiments. We are currently examining the possibility of performing experiments in which the effects of E_b/T_e and the beta value can be well distinguished with direct measurement of the turbulence intensity; in addition, we need to develop a method to evaluate the effect of turbulence on fast-ions.

Reference

Suzuki, T. et al., Experimental Investigation and Validation of Neutral Beam Current Drive for ITER through ITPA Joint Experiments, Nuclear Fusion, vol.51, no.8, 2011, p.083020-1-083020-8.

3-8 Exploring the Possibility of Inducing Plasma Rotation by Fusion Reactions — Intrinsic Torque Generation by α -Particles —

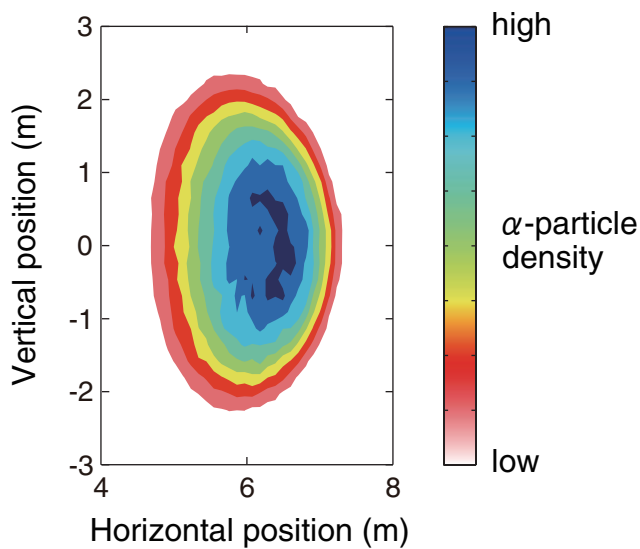


Fig.3-18 Density distribution of isotropically born α -particles
The plasma has an elliptical cross section. Concentric contours of the same color indicate the isotropic production of α -particles. A large number of α -particles are born at the plasma center, where the plasma pressure is high.

In order to sustain high-pressure fusion plasma, various instabilities inherent to the plasma must be suppressed. One of the potential methods for suppressing such instabilities involves rotating the plasma in the toroidal direction. In current tokamak experiments, neutral beam injection (NBI) can be used for efficiently applying a torque to the plasma via the formation of fast particles, thus enabling rotation control. However, in future fusion reactors, the effective torque generated by NBI may not be very large; hence, much attention has been paid to the possibility of intrinsic torque generation by fusion-born α -particles.

The torque produced by fast particles is the sum of the collisional torque generated by collisions between fast thermal particles and the radial current torque resulting from the motion of fast particles in a magnetic field. Unlike directional fast particles formed by NBI, α -particles are born isotropically (Fig.3-18), and hence, they are never believed to produce any kind of torque. The orbit-following Monte Carlo code (OFMC) for fast particles has been recently updated to incorporate a mechanism for accurately estimating the radial current torque, and the updated OFMC has been used to analyze the behavior of α -particles in a DEMO-relevant plasma. Here, DEMO (DEMONstration power plant) denotes a prototype fusion reactor. The analysis reveals that the

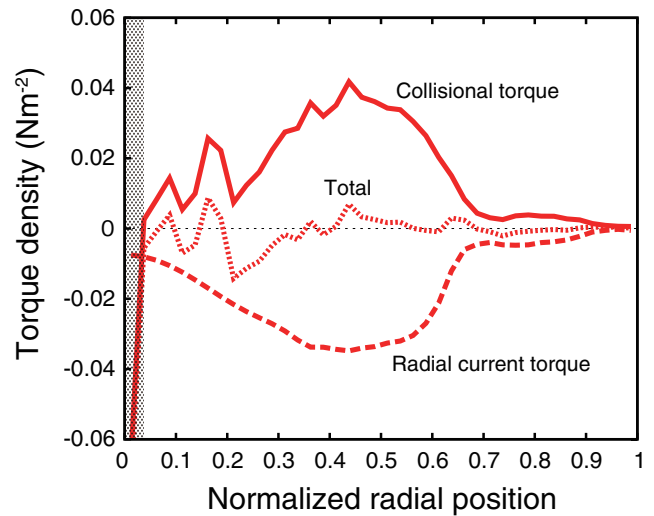


Fig.3-19 Radial profile of torque density induced by α -particles
In the region of high α -particle density, a positive (co-current) collisional torque and a negative (counter-current) radial current torque arise, but they are balanced out within the numerical error.

centrally peaked birth profile of the α -particles shows both finite collisional and radial current torques. The magnitude of these torques seems to be comparable to that of the torque due to NBI, but the collisional torque acts in the direction parallel to the plasma current, whereas the radial current torque acts in the opposite direction. Because of this mirror symmetric characteristic of the profiles, the two torques cancel out each other, and the net torque is zero (Fig.3-19). This finding implies that in a perfectly axisymmetric tokamak, the α -particles cannot produce the intrinsic torque by themselves, consistent with the law of conservation of canonical angular momentum.

However, this fact also indicates that a net torque must arise in an actual, slightly asymmetric tokamak reactor with finite toroidal-field coils that create a toroidal magnetic field ripple (bumpiness). The ripple tends to accelerate the radial transport of fast particles, leading to an increase in the radial current torque. Thus, the balance in the torque in an ideal axisymmetric system will be violated in an actual system, and a net counter torque will be generated. Accurately calculating this torque is indispensable for estimating the additional torque required for inducing toroidal rotation that helps in suppressing plasma instabilities.

Reference

Honda, M. et al., Alpha Particle-Driven Toroidal Rotation in Burning Plasmas, Nuclear Fusion, vol.51, no.7, 2011, p.073018-1-073018-9.

3-9 Early Realization of Fusion Reactor

— International Fusion Energy Research Centre Project in the Broader Approach Activity —

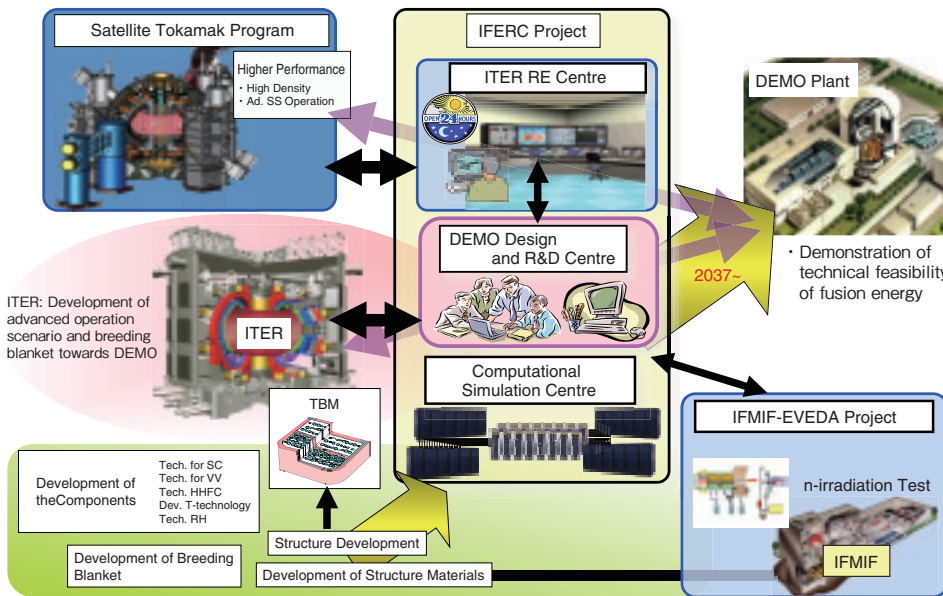


Fig.3-20 Outline of the IFERC project

The IFERC project shall perform activities on (1) DEMO Design and R&D Coordination Centre, (2) Computational Simulation Centre, and (3) ITER Remote Experimentation Centre in cooperation with the other BA projects in order to contribute to the ITER project and promote the early realization of the fusion reactor.

	2007	2008	2009	2010	2011	2012	2013	2014	2015	2016	2017
DEMO Design and R&D	Workshops/Meetings				Joint Work Phase						
CSC	Preparation/Procurement					Operation of CSC					Dismantling
REC							Preparation-1	Prep-2	Operation		
Buildings	Design	Construction	Adaptation		Maintenance						

For contributing to the International Thermonuclear Experimental Reactor (ITER) project and facilitating the early realization of DEMO, the International Fusion Energy Research Centre (IFERC) shall perform activities on (1) DEMO Design and R&D Coordination, (2) Computational Simulation Centre, and (3) ITER Remote Experimentation Centre (Fig.3-20). Activity (3) will be performed later since ITER is under construction.

The DEMO design activity is aimed at establishing a common basis for DEMO design, including the design features of DEMO and a possible common concept of DEMO to EU and Japan. Taking into account the present divergence in the DEMO concepts, the activity will be implemented on the basis of the appropriate phases. In the initial phase, the activity is carried out by holding workshops and/or meetings where “common elements” of the DEMO design are discussed for facilitating “joint work” in Phase Two. Recent design activities in Phase One have focused on discussions on the role of DEMO, design driver and constraints for the DEMO design, roadmap to DEMO, and DEMO design concepts.

On the basis of the common interests of the EU and Japan,

the DEMO R&D activities have been planned and carried out in the following five areas that are relevant to the blanket development: (1) SiC/SiC composites, (2) tritium technology, (3) materials engineering for the DEMO blanket, (4) advanced neutron multiplier for the DEMO blanket, and (5) advanced tritium breeders for the DEMO blanket. Considerable efforts have been focused on the design of experimental facilities and equipment to be developed/installed in the DEMO R&D Building at the Rokkasho Broader Approach (BA) site.

The objective of the activity relating to the Computational Simulation Centre is to provide and exploit a supercomputer for large-scale simulations to analyze experimental data on fusion plasmas, predict the performance of ITER, and contribute to the DEMO design. In the initial phase, high-level benchmark codes have been selected by a special working group and the procurement arrangement of the supercomputer has been concluded.

It is hoped that fruitful results toward the early realization of the fusion reactor will be obtained through the steady progress of the IFERC project.

Reference

Araki, M. et al., Progress of IFERC Project in the Broader Approach Activities, Fusion Engineering and Design, vol.85, issues 10-12, 2010, p.2196-2202.

3-10 Study on Formation of Temperature Profile of Plasma Core — First-Principles Simulation of Plasma Transport —

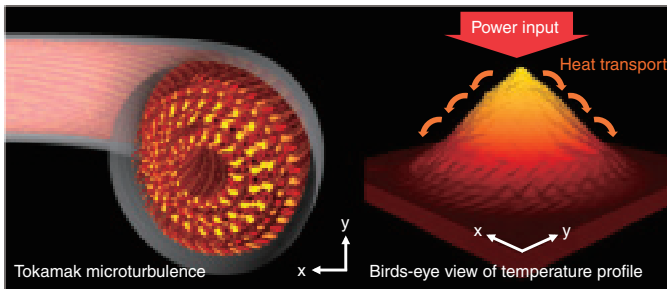


Fig.3-21 Fluctuating electrostatic potential (left) and three dimensional view of temperature profile (right)

The temperature of the plasma core is determined on the basis of the balance between the power input to the plasma core and turbulent transport that transfers the energy toward the plasma edge.

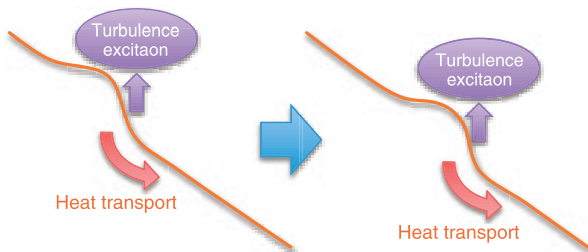


Fig.3-22 Avalanche-like heat transport

Avalanche-like propagation of temperature fluctuations is produced by a domino effect, where local steepening of the temperature gradient because of turbulent transport induces other turbulent fluctuations in the neighboring region.

The production of high-temperature plasma core is important since the core temperature affects the performance of fusion reactor. However, experimental results often have so-called stiff temperature profiles in which the temperature gradient remains below a threshold value, and as a result, the increase in the core temperature is limited. Such profiles are produced under a power balance condition between the power input to plasma core and the turbulent transport induced by fluctuations. Therefore, it was difficult to understand stiff temperature profiles or the mechanism of dynamic heat transport, which varies such that the temperature gradient remains almost constant, by performing conventional numerical experiments for evaluating turbulent transport by assuming a prescribed or fixed temperature gradient.

In this work, we developed a new numerical experiment (Fig.3-21), where both turbulent transport and self-consistent profile formations are computed based on first principle under a fixed power input as in the experiment. The temperature profiles observed in the simulation show the

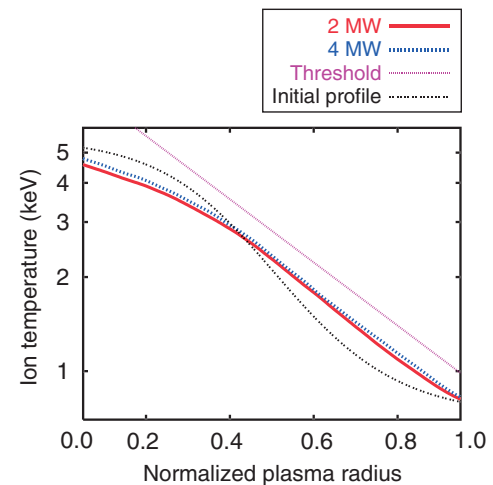


Fig.3-23 Temperature profiles (log scale) observed in numerical experiments with different power inputs

Two numerical experiments show stiff temperature profiles that are independent of the initial condition, and the temperature gradient is limited to a threshold value. Even with doubled power input, the temperature gradient is limited to the threshold value by increasing the avalanche-like heat transport, which is almost proportional to power input.

existence of a balanced state in which an increase in the input power results in an increase in the heat transport with small changes in profiles. Further, the results also show that the transport phenomena are similar to the transport phenomenon in a sand pile where dynamic transport of sand keeps a constant pile height (Fig.3-23). This transport phenomenon is induced by nonlocal avalanche-like heat transport produced by the interaction between the temperature fluctuations and turbulent transport (Fig.3-22). It is also found that in plasmas, avalanches of holes or clumps with certain temperature gradient become dominant depending on the radial electric field shear, and therefore, unidirectional propagation occurs, while in sand piles, holes and clumps coexist and propagate in opposite directions. This indicates a possibility of controlling avalanche-like heat transport by changing the structure of the radial electric field.

In this work, we first clarified the stiffness of temperature profiles on the basis of first-principles calculations, and we offered the physics basis for estimating and predicting the plasma transport properties in ITER and DEMO reactors.

Reference

Idomura, Y. et al., Study of Ion Turbulent Transport and Profile Formations using Global Gyrokinetic Full- f Vlasov Simulation, Nuclear Fusion, vol.49, no.6, 2009, p.065029-1-065029-14.

3-11 Manufacture of Small Tritium Target for Use in Generating Neutrons in Fusion Reactor at JAEA

— Stable Procurement of Small Tritium Targets —

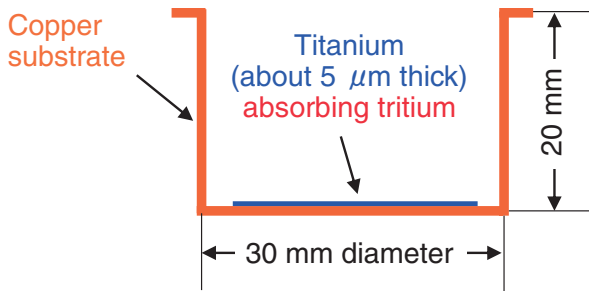


Fig.3-24 Cross section of a small tritium target
The thin titanium layer absorbs tritium of about 400 GBq.

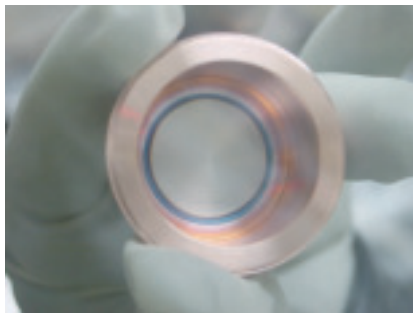


Fig.3-25 Tritium target manufactured in this study
The silver-gray part at the center is a titanium layer that absorbs tritium.

In fusion power plants, electricity is produced thermally (nuclear heating) by generating intense neutrons through nuclear fusion reactions involving deuterium-tritium (DT) plasmas. The plants also produce the fusion reactor fuel tritium through reaction between neutrons and lithium (tritium production). For safety reasons, neutrons have to be shielded so that they do not leak outside the fusion power plants (shielding). Exposure of workers to radiation from radioactive materials (activation) in equipment resulting from neutron irradiation should be reduced to the minimum possible level. One of the most important issues in fusion plant development is to demonstrate how accurately we can predict nuclear heating, tritium production, shielding, and activation for a specific design.

We produce 14 MeV neutrons by accelerating deuterium up to 350 keV with an electrostatic field and then focusing the accelerated deuterium onto a tritium target at the Fusion Neutronics Source (FNS) facility of the JAEA. We use the neutrons to carry out a study for the above issues. At a tritium target with a diameter of 30 mm (Fig.3-24), tritium is absorbed by the titanium layer evaporated on a copper

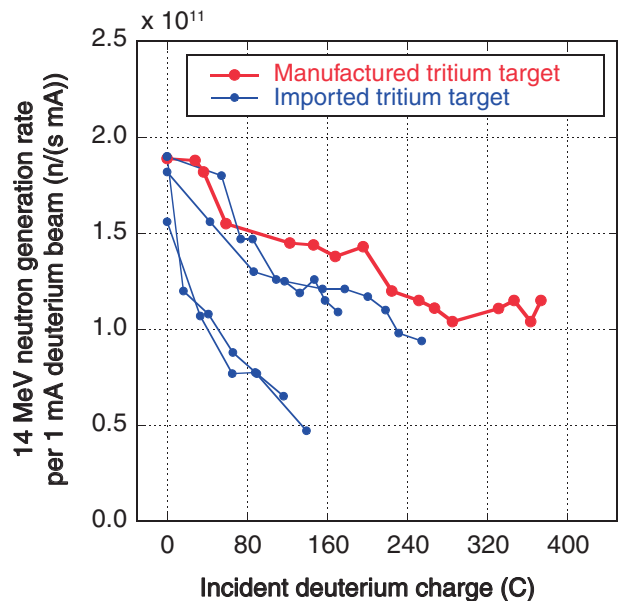


Fig.3-26 Change in neutron generation rate with incident deuterium charge

The rate of generation of 14 MeV neutrons decreases with an increase in the deuterium charge incident on the tritium target. In the case of the tritium targets manufactured in this study, however, the decrease in the neutron generation rate is smaller than the decrease for imported targets, demonstrating the high quality of the manufactured target.

substrate. A French company currently dominates the tritium target market because a mass-tritium handling facility and tritium absorption techniques are required to manufacture tritium targets. A stable and timely supply of tritium targets to the FNS is required.

In a preliminary evaluation, it was found that a titanium layer covered with impurities does not absorb tritium. In the manufacture of tritium targets, the removal of impurities from the titanium layer is important. By repeatedly conducting cold tests with deuterium, we found that the main impurity was water. We therefore developed a vacuum chamber equipped with a heater for tritium absorption. We succeeded in manufacturing eight small tritium targets with tritium amounts (about 400 GBq, 1 mg) similar to those in imported ones (Fig.3-25). At the FNS, the decrease in the generation rate of 14 MeV neutrons with an increase in the deuterium charge incident on a tritium target was examined. It was observed that the decrease in the case of the tritium targets manufactured in this study was smaller than those in the case of the imported targets (Fig.3-26).

Reference

Tanaka, S. et al., Prototype Manufacturing of Small Tritium Target inside JAEA, Journal of Plasma and Fusion Research SERIES, vol.9, 2010, p.338-341.

3-12 Validation of Fusion Reactor Materials

— Design and Construction of IFMIF/EVEDA Li Test Loop —



Fig.3-27 IFMIF/EVEDA Li Test Loop (ELTL) after completion of construction
The ELTL, which holds 2.5 ton Li, comprises three floors whose width and depth are 15 m each. The total height of the ELTL is 20 m, and a test section called TA is installed at the top of the confinement vessel.

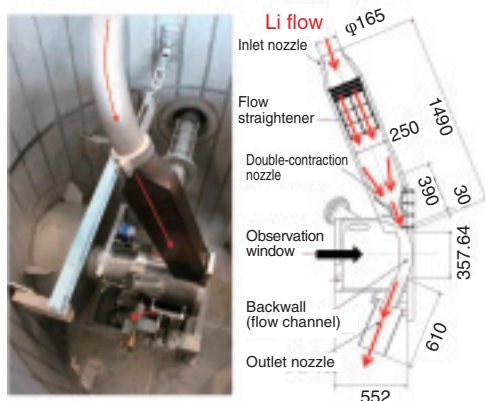


Fig.3-28 Configuration of TA (unit: mm)
Li entering the TA from the inlet nozzle flows through the flow straightener and double-contraction nozzle. The Li target formed by the nozzle flows along the concave BW.



Fig.3-29 Flow appearance of Li target
The Li target was formed in the target assembly and flowed stably in the final phase of the performance tests. (The Li target was observed through the observation windows shown in Fig. 3-28).

For developing materials to be used in the fusion DEMO reactor, it is necessary to evaluate how irradiation damage by the neutrons generated in the fusion reaction affects the candidate materials. For this purpose, the Engineering Validation and Engineering Design Activities (EVEDA) for Fusion Materials Irradiation Facility (IFMIF) project, hereafter referred to as IFMIF/EVEDA, has been launched under the Broader Approach Activities in the bilateral framework between The European Atomic Energy Community (EURATOM) and the Government of Japan. The IFMIF is an accelerator-based (D^+ -Li) source in which neutrons are generated by injecting two deuteron beams into a liquid Li stream (Li target). The major R&D activity on the Li target facility in EVEDA was centered on the construction of the IFMIF/EVEDA Li test loop (ELTL), which was used to simulate the actual IFMIF Li target. The ELTL was set in operation for two years for the purpose of collecting indispensable data that could be used to construct the IFMIF Li target and complete the IFMIF engineering design.

Construction of the ELTL was commenced in 2009 and completed within two years. Performance tests were carried out on March 10, 2011 at the O-arai Research and Development Center in cooperation with Advanced Liquid Metal Technology Experiment Section, JAEA (Fig.3-27). In the ELTL, heated (250 to 350 °C) liquid Li can be circulated,

and an obi-shaped Li target whose velocity, thickness, and width are 15 m/s, 25 mm, and 100 mm, respectively, can be formed in the target assembly (TA). The specification with regard to the velocity and the thickness at the target region are the same as that envisaged in the IFMIF, while the width is 1/3. In the TA at the top of the platform, an appropriately shaped (curved) Li target is formed by the double-contraction nozzle along the concave backwall (BW), as shown in Fig.3-28. The nozzle is designed on the basis of Shima's nozzle such that it yields a stable jet with a velocity as high as 20 m/s. The static pressure inside the Li target is enhanced by the centrifugal force generated by the flow along the BW. Consequently, boiling by the D^+ beam heat is prevented.

The performance tests conducted after the construction of the ELTL included the following: 1) Li ingot installation in the ELTL, 2) Li charging and draining, and 3) Li circulation tests. In the third set of tests, the performance of each component comprising the ELTL was confirmed to meet the predefined specifications. In the final phase of the circulation test, stable Li flow at a velocity of 5 m/s was successfully achieved in the target assembly, at an Ar gas pressure of 0.12 MPa (Fig.3-29). In the EVEDA stage, the stability of the Li target and Li purification technologies are scheduled to be validated for the engineering design of the IFMIF.

Reference

Kondo, H. et al., Design and Construction of IFMIF/EVEDA Lithium Test Loop, Journal of Engineering for Gas Turbines and Power, vol.133, issue 5, 2011, p.052910-1-052910-6.

Development of Quantum Beam Technology

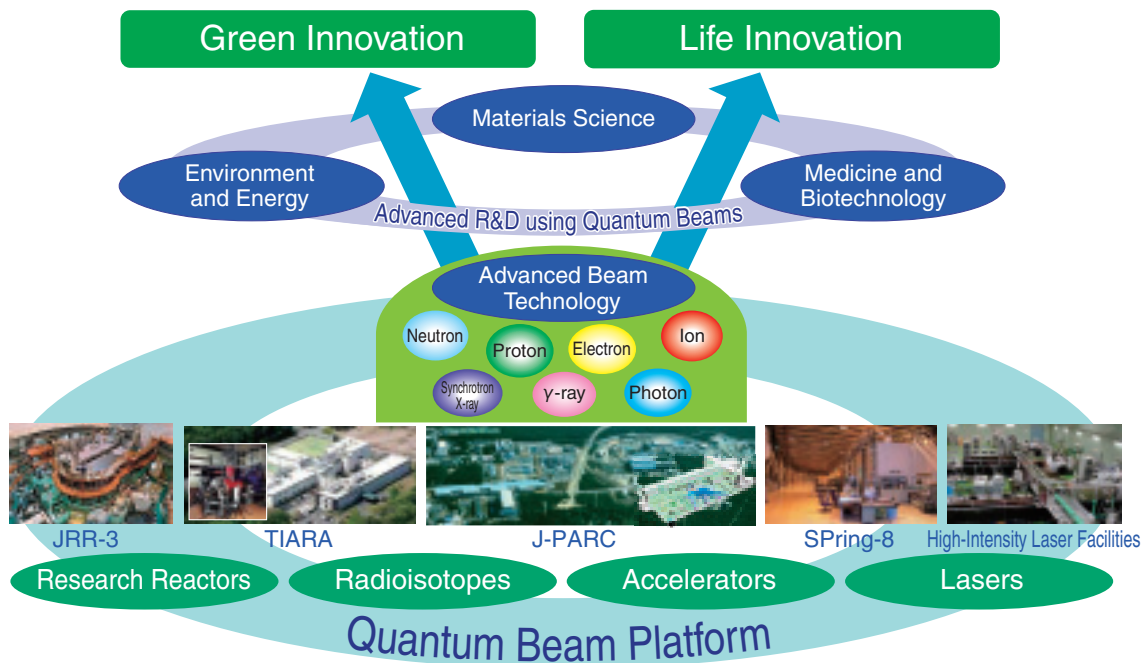


Fig.4-1 JAEA quantum beam facilities and the R&D done there

Characteristics of quantum beams

Quantum beams such as neutron beams, ion beams, electron beams, high-intensity lasers, and synchrotron X-rays have a create function, that is, they allow us to process materials on a nanometer level (atomic or molecular level) by interacting with the constituent atoms of a material to change their configuration, composition, and electronic state. Such quantum-beam interactions cause changes in the beams too, such as those in the beam direction and energy, and sometimes generate different types of quantum beams. Thus, quantum beams have a probe function as well, whereby we can obtain atomic- or molecular-level information by observing the alterations in the beam parameters.

Application of quantum beams

At JAEA, we are carrying out R&D on advanced beam technology at our beam facility complex, which includes research reactors, accelerators, and so on (Quantum Beam Platform), as shown in Fig.4-1. By utilizing the create and probe functions of quantum beams, we are promoting fundamental and applied research in a wide range of fields, such as (1) materials science, (2) environment and energy, and (3) medicine and biotechnology. We are intensively performing these R&D activities to obtain results that would lead to green innovation and life innovation, and to contribute to the progress of science and technology as well as the promotion of industry.

Recent achievements

In the field of advanced beam technology, we developed a 500-kV photocathode DC electron gun for realizing a next-generation light source, improved the reflectivity of relativistic flying mirrors for use in a high-brightness X-ray source, and developed a technology for analyzing the polarization of soft X-rays (Topics 4-1 to 4-3).

In the materials science field, we developed a new spin contrast variation technique for small angle neutron scattering, a polarization-analyzed resonant inelastic X-ray scattering method, and a multiple-length-scale observation apparatus using coherent X-rays, and used them for investigating advanced functional materials (Topics 4-4 to 4-6).

In the field of environment and energy, we succeeded in elucidating hydrogen storage mechanisms by using X-ray absorption spectroscopy, developed a novel compound efficiently separating lanthanides, and fabricated polymer adsorbents extracting rare-earth metals. Moreover, we developed a practical system to purify waste gases by using electron beams and catalysts. These results are presented in Topics 4-7 to 4-10.

In the field of medicine and biotechnology, we clarified the existence of low-barrier hydrogen bonds in photoactive yellow protein on the basis of neutron crystallography. We found that the electric field produced by heavy ions influences the generation of clustered DNA damage, and that the genetic information in plants is altered late as well as immediately after γ -ray irradiation. These findings are described in Topics 4-11 to 4-13.

4-1 Toward the Realization of the Strongest and Brightest Electron Source in the World

— Development of a 500-kV Photocathode DC Electron Gun for Realizing a Next-Generation Light Source —

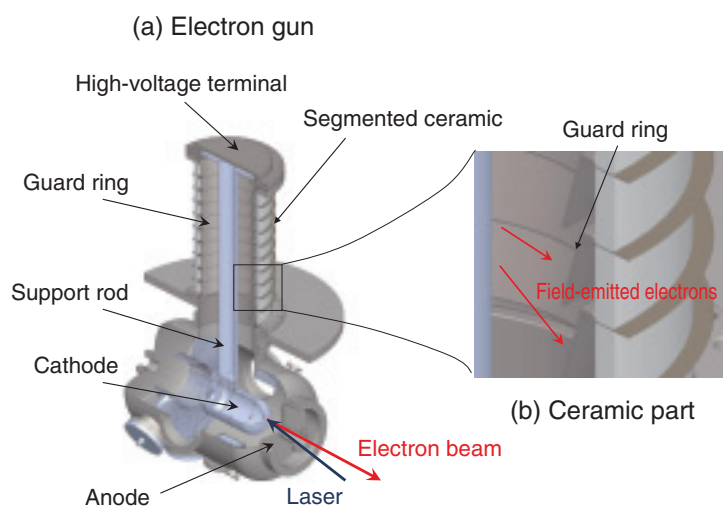


Fig.4-2 Segmented ceramic and guard ring

(a) the support rod is placed at the center of the ceramic tube.
 (b) the guard rings are installed in the segmented ceramic and prevent any damage to the ceramic by field-emitted electrons from the support rod

The realization of a light source that is 10^3 or more times as strong as the current source (next-generation light source) will make possible the nondestructive analysis of radioactive isotopes, real-time observation of chemical reactions, and high-resolution imaging of living cells. This next-generation light source is based on an electron-beam acceleration technique. Institutions around the world have been actively promoting research and development for this source.

The most important technology for realizing such a light source is beam generation by an electron gun utilizing a photocathode. In order to obtain a strong and bright electron beam, a photocathode and DC high-voltage acceleration techniques are employed in the electron gun. Light from a laser excites the electrons in the photocathode, and it emits the electrons to generate an electron beam. The electron beam is defocused because of the repulsive force of the electrons. A voltage of 500 kV or higher is required to sufficiently reduce this repulsive force. It is not easy to achieve an accelerating voltage of 500 kV with this type of electron gun. Although various developments have been made since 2002, the highest

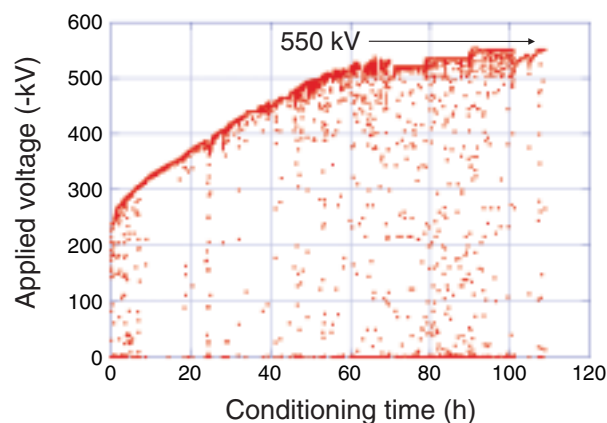


Fig.4-3 High-voltage conditioning

High-voltage conditioning is the process of removing the cause of electric discharge by using a small electric discharge.

accelerating voltage achieved was 350 kV (Jefferson Lab, USA, in 2005).

In order to obtain a strong and bright electron beam by using a photocathode electron gun, it is necessary to shorten the distance between the cathode and the anode. Therefore, a support rod has to be placed at the center of the ceramic tube (Fig.4-2 (a)). However, when the accelerating voltage was 500 kV or higher, this structure resulted in the ceramic tube getting damaged by electric discharge from the support rod. We employed a segmented ceramic structure and a guard ring (Fig.4-2 (b)) to prevent any damage to the insulator from electrons emitted by the support rod and optimized the shapes of this structure.

We carried out a high-voltage testing of the 500-kV DC photocathode electron gun developed for next-generation light sources. The electron gun was successfully conditioned up to a voltage of 550 kV (Fig.4-3) and a long-time holding test for 8 h was demonstrated at an acceleration voltage of 500 kV.

Reference

Nagai, R. et al., High-Voltage Testing of a 500-kV DC Photocathode Electron Gun, Review of Scientific Instruments, vol.81, issue 3, 2010, p.033304-1-033304-5.

4-2 Improvement of Reflectivity of Relativistic Flying Mirrors — Demonstration of Efficient Reflection of Laser Light from Plasma Waves —

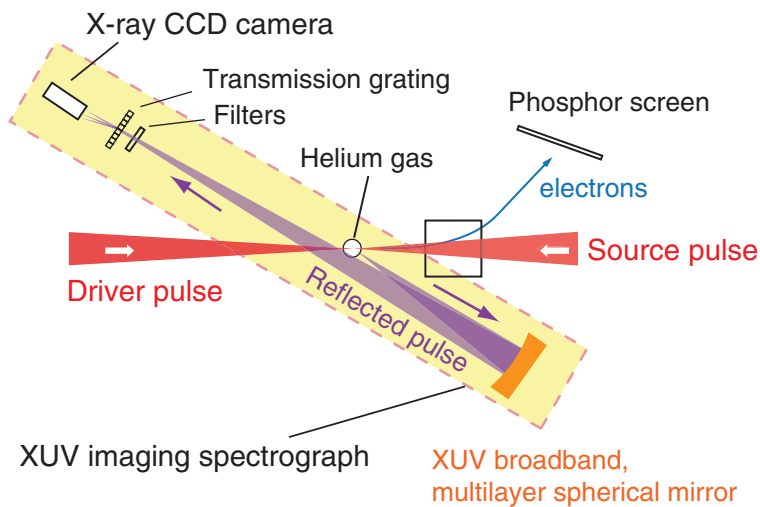


Fig.4-4 Setup of the counter-propagating flying mirror experiment

The driver (source) pulse has an energy of 400 mJ (42 mJ) and a pulse duration of 27 fs (34 fs). They are focused onto He gas with spot diameters of $\sim 30 \mu\text{m}$. An extreme ultraviolet (XUV) imaging spectrograph covering the wavelength range from 12.5 to 22.0 nm is used to measure the reflected light from the flying mirrors. The spectrograph consists of a broadband multilayer spherical mirror, a transmission grating, filters, and an X-ray CCD camera.

We invented flying mirrors that propagate in plasma almost at the speed of light by using intense laser pulses. The flying mirror is a dense plasma electron shell whose velocity is equal to the group velocity of laser pulses propagating in the plasma. Because it can be used as a mirror that reflects light, the flying mirror is expected to be an effective device for increasing the intensity of the laser and converting it to ultrashort, coherent X-rays. In 2007, we demonstrated that such a flying mirror was produced and that it could reflect incoming laser pulses. However, the number of reflected photons was smaller than the theoretical estimate.

To improve reflectivity, we improved two major points in our experiment. In the first experiment, the laser used was relatively weak, just 3 TW. Therefore, we used the 10 TW J-KAREN laser at our institute. In addition, we changed the experimental configuration. In the first experiment, the source pulse (pulse to be reflected) was directed at an angle, but we adopted a counter-propagating setup.

In the counter-propagating setup, a laser pulse that produces flying mirrors (driver pulse) and the source pulse

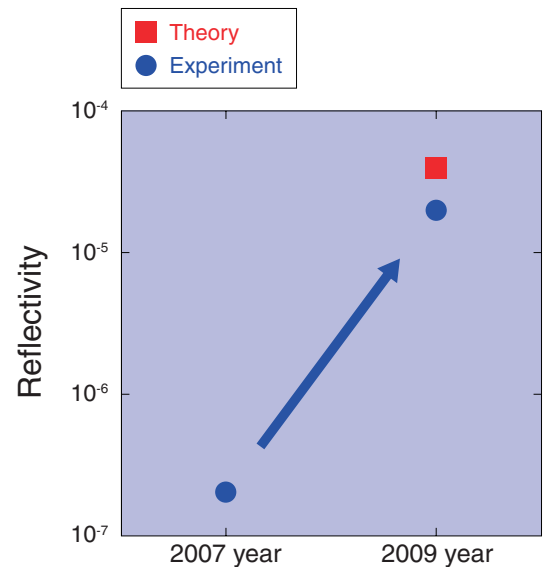


Fig.4-5 Improvement of the reflectivity of the flying mirrors

In the first proof-of-principle experiment (2007), the reflectivity of the flying mirrors was 1000 times smaller than that the theoretical estimate. However, this time (2009), it is close to the theoretical estimate, which indicates high efficiency.

should be overlapped within $30 \mu\text{m}$. For this purpose, we have developed a new monitoring system that samples a part of the returning laser pulses. In addition, we have implemented an extreme ultra-violet (XUV) imaging spectrograph with a wide acceptance angle range to measure the reflected light in the counter-propagating setup as shown in Fig.4-4.

After careful adjustment of the collision of the two laser pulses in plasma, we observe a broad spectrum ranging from 12.5 to 22.0 nm in the XUV spectrograph. This corresponds to the flying mirror velocity that is 98%~99% of the light speed. This value is consistent with the one calculated from the plasma density. The obtained photon number is 7.9×10^9 , and the reflectivity is 2×10^{-5} . The reflectivity, as shown in Fig.4-5, is half of the theoretical estimate. Thus, we have proved that the flying mirror has a high reflectivity as predicted theoretically. The photon number is higher than that in 2007 by 10^6 . This result verifies the realization of high-brightness X-ray sources based on flying mirrors.

Reference

Kando, M. et al., Enhancement of Photon Number Reflected by the Relativistic Flying Mirror, Physical Review Letters, vol.103, issue 23, 2009, p.235003-1-235003-4.

4-3 Evaluation of Polarization of Soft X-rays — Soft X-ray Optics and Polarization Analysis —

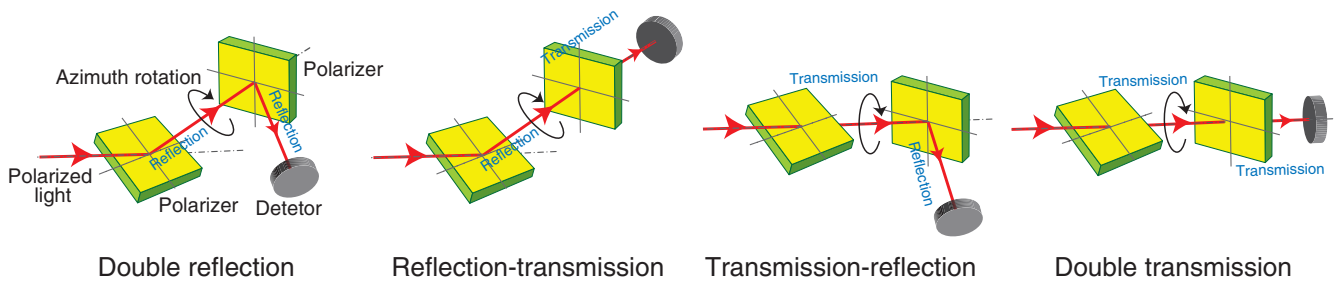


Fig.4-6 Schematic of four optical configurations for polarization analysis

The polarization abilities of the polarizers and the polarization state of the light, which is typically synchrotron radiation (SR) light, can be quantitatively evaluated simultaneously from the reflection (or transmission) intensity depending on the azimuthal angle of the polarizer in just front of the detector.

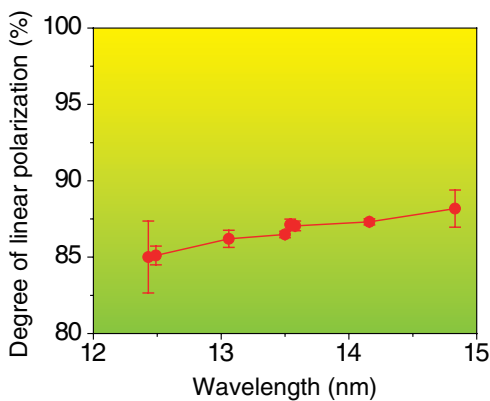


Fig.4-7 Linear polarization degree of soft X-rays in the vicinity of 13 nm

Two multilayers were used as the polarizers in double-reflection geometry in the linear polarization measurement. The degree of linear polarization is constant at 85%~87%, and it is in good agreement with the simulation result.

Polarized light in the soft X-ray region is used for studying materials such as magnetic materials. In an experiment using polarized light, it is important to evaluate the polarization state parameters, e.g., the degrees of linear and circular polarization, because these affect the experimental results. The polarization state can be quantitatively evaluated by polarization optical components such as polarizers. It has been difficult to determine the polarization state in the soft X-ray region because the developments related to polarizers and instruments for evaluating the polarization properties have so far been insufficient in the case of the soft X-ray range, unlike in the case of visible light. Our purpose is to develop soft X-ray polarizers and to evaluate experimentally the polarization state of sources of soft X-ray synchrotron radiation (SR) light by using a newly developed polarization analysis instrument.

Fig.4-6 shows the optical configurations of two polarizers for polarization analysis. From the azimuthal rotation of the polarizer, both the polarizers and the polarized light can be quantitatively characterized. It is unique that four

configurations can be realized by remote control and the polarizers have position- and angle-adjustment functions in a vacuum environment.

It is well known that multilayers which compose of Mo and Si act as soft X-ray polarizers such as a reflection polarizer for around 13 nm wavelength. The multilayer polarizers were fabricated and the linear polarization measurement of a SR light source was performed with the polarizers in double reflection geometry. The results revealed that regardless of the wavelength, the degree of linear polarization in the vicinity of 13 nm is 85%~87%, as shown in Fig.4-7, and the fabricated multilayer polarizers have high polarizing abilities. Soft X-ray polarization analysis has been established successfully by using the new instrument developed in this study.

Our next task is to investigate the polarization state of circular polarized light in the soft X-ray range, and this investigation is expected to contribute to research on magnetic materials and quantum beams.

Reference

Imazono, T. et al., Development and Performance Test of a Soft X-ray Polarimeter and Ellipsometer for Complete Polarization Analysis, Review of Scientific Instruments, vol.80, issue 8, 2009, p.085109-1-085109-8.

4-4 Development of Spin Contrast Variation Technique — Verification Study with a Simplified Model System —

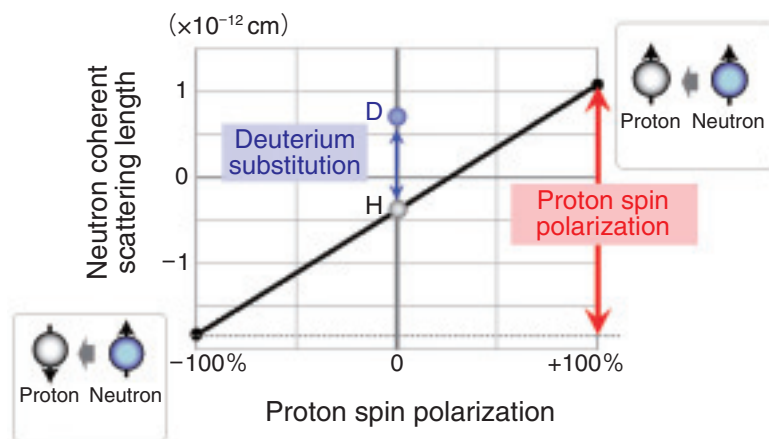


Fig.4-8 Control of neutron coherent scattering length

Neutron coherent scattering length can be significantly modified by aligning the spins of the neutron beam and of the protons in the sample.

Hybrid polymer materials in which fillers (reinforcing particles) are dispersed in the polymer matrix are known to show excellent mechanical properties, and they are widely used for manufacturing automobile parts and daily commodities. Recently, for better performance, several types of fillers are added to materials. However, searching for the best mixing ratio among several additives requires considerable effort. An investigation of the interactions between fillers can help in framing guidelines for blending.

Small-angle neutron scattering (SANS) can help in identifying the best mixing ratio. Structural information on each component in a multicomponent system can be abstracted by using the “contrast variation technique,” which modifies only the neutron scattering contrast of a sample while retaining its structure. For this purpose, a deuterium substitution technique (Fig.4-8, blue arrow) has been used conventionally. However, preparing deuterated plastic or rubber materials is costly. Therefore, there has been a need for another technique.

Both a neutron beam and a proton in a sample have spin. By passing a neutron beam through a magnetic multilayer mirror, a neutron beam with a single spin direction can be obtained. On the other hand, by using “dynamic nuclear polarization,” in which microwaves are radiated on a sample in a strong magnetic field and at a very low temperature, the spins of the protons in the sample can be aligned in one direction. By combining the two above-mentioned

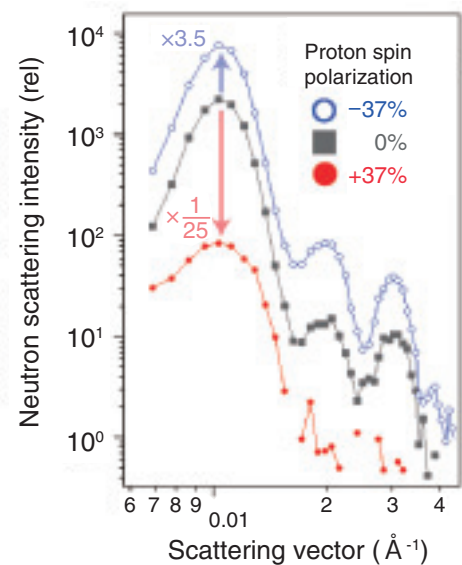


Fig.4-9 Small-angle neutron scattering (SANS) profiles for proton spin polarized states

Neutron scattering intensity decreased for positive spin polarization and increased for negative spin polarization.

techniques, we can vary the neutron coherent scattering length considerably (Fig.4-9, red arrow).

We tried to verify the effectiveness of the combined use of both techniques by considering a simple block copolymer sample. In this sample, glassy polystyrene domain and rubbery polyisoprene domain are alternately stacked. Thus, the sample is a simplified model system for a tire-rubber material, which is discussed later.

We obtained SANS profiles of the sample with its proton spins being polarized (Fig.4-9). The scattering intensity decreased to 1/25 at a proton spin polarization of +37% and increased by 3.5 times at a proton spin polarization of -37%. This can be explained by the modification of the neutron scattering contrast resulting from the proton density difference between the two domains. The experimental results were reproduced by a theoretical calculation. We thus successfully verified that the technique works appropriately.

Now, we are applying this technique to a silica-filled styrene-butadiene random copolymer (SBR) rubber, which is widely used for manufacturing fuel-efficient tires. It is known that the fuel efficiency of the tires strongly depends on the dispersion of silica reinforcing particles in the rubber material. Therefore, it is important to evaluate the dispersion of silica quantitatively for developing tires with greater fuel efficiency. By using this technique, structural information pertaining to only silica can be abstracted. Rubber companies are now paying considerable attention to this technique.

Reference

Noda, Y. et al., Inhomogeneous Dynamic Nuclear Polarization of Protons in a Lamella-Forming Diblock Copolymer Investigated by a Small-Angle Neutron Scattering Method, *Journal of Applied Crystallography*, vol.44, issue 3, 2011, p.503-513.

4-5 Clarification of Hidden Electronic Character Using Synchrotron Radiation X-ray

— Orbital State of Excited Electron Identified by Polarization-Analyzed Resonant Inelastic X-ray Scattering —

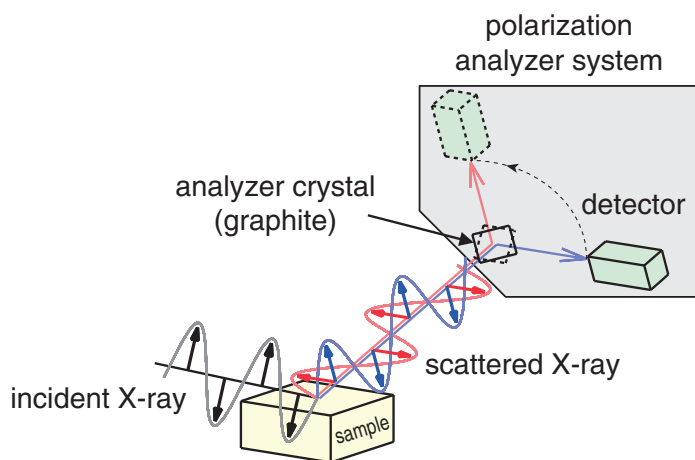


Fig.4-10 Schematic view of polarization analyzer installed at BL11XU at SPring-8

Incident X-ray emitted from the storage ring is polarized within the scattering plane (black arrows) and irradiated on the sample. On the other hand, the scattered X-ray is a mixture of two polarization components (blue and red arrows) which are separated by the analyzer.

Strongly correlated transition metal compounds attract great interest because they exhibit a variety of interesting phenomena such as high-temperature superconductivity in cuprates and colossal magnetoresistance in manganites. It is widely recognized that the orbital degree of freedom of the d electrons often plays a crucial role in the occurrence of these phenomena. For example, it controls the anisotropy of the electron mobility and propagation of interactions. Generally, orbital excitations, where the orbital state changes by gaining energy, are difficult to observe by conventional optical spectroscopy techniques because they are dipole-forbidden. Resonant inelastic X-ray scattering (RIXS) using brilliant synchrotron radiation X-rays is a potent method to measure orbital excitations. However, various excitations are often entangled in the spectrum of RIXS, and it has been difficult to distinguish between them experimentally so far.

In order to identify the orbital excitations, we utilize the polarization, which is an inherent and important characteristic of the photon, by developing a polarization analyzer for the scattered X-rays in RIXS. The analyzer is schematically shown in Fig.4-10. So far, most RIXS studies have focused on energy and momentum dependencies, while polarization has been overlooked. Incident X-rays emitted from SPring-8 are horizontally polarized, and the polarization

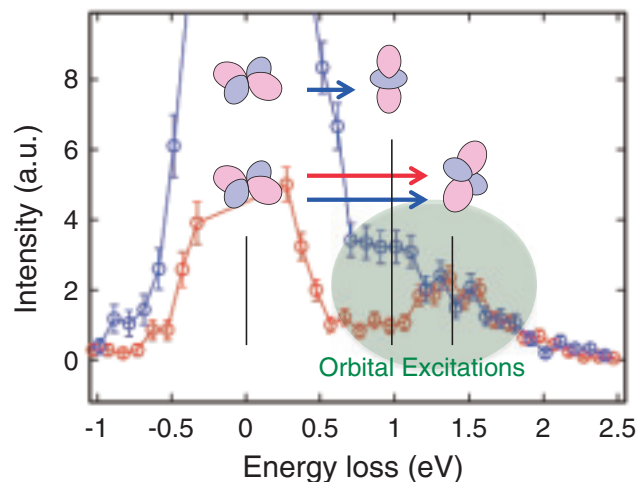


Fig.4-11 Polarization-analyzed resonant inelastic X-ray scattering spectra of KCuF_3

Orbital excitations are observed at 1.0~1.5 eV. The polarization of the scattered X-rays is perpendicular (red arrows in Fig.4-10) and parallel (blue arrows in Fig.4-10) to the scattering plane in the red and blue spectra, respectively.

of the scattered X-rays is analyzed by rotating the analyzer crystal and the detector about the axis of the beam.

Fig.4-11 shows polarization-analyzed RIXS spectra of KCuF_3 , which is an archetypal material with orbital order. Orbital excitations are observed at 1.0~1.5 eV. The 1.4 eV peak of the red curve corresponds to the excitation indicated by the thick red arrow. On the other hand, in addition to the peak at 1.4 eV, a spectral weight exists around 1.0 eV for the blue curve, and it comes from the orbital excitation indicated by the short blue arrow in Fig.4-11. This implies that the two orbital excitations show clear dependence on the scattered photon polarization. The dependence can be interpreted on the basis of a phenomenological consideration of the symmetry of the RIXS process that yields a necessary condition for observing the excitations.

The proposed technique enables us to identify electronic excitations that are closely related to the physical properties in transition metal compounds independently of the parameters of theoretical models, since the symmetry of the orbital states is rigorously connected to the polarization of the photon. The technique is expected to facilitate the understanding of attractive physical properties and functions of transition metal compounds.

Reference

Ishii, K. et al., Polarization-Analyzed Resonant Inelastic X-ray Scattering of the Orbital Excitations in KCuF_3 , *Physical Review B*, vol.83, no.24, 2011, p.241101-1-241101-4.

4-6 Toward Domain Observation Using Coherent X-rays

— Multiple-Length-Scale Approach Revealing the Nature of High-Functional Solids —

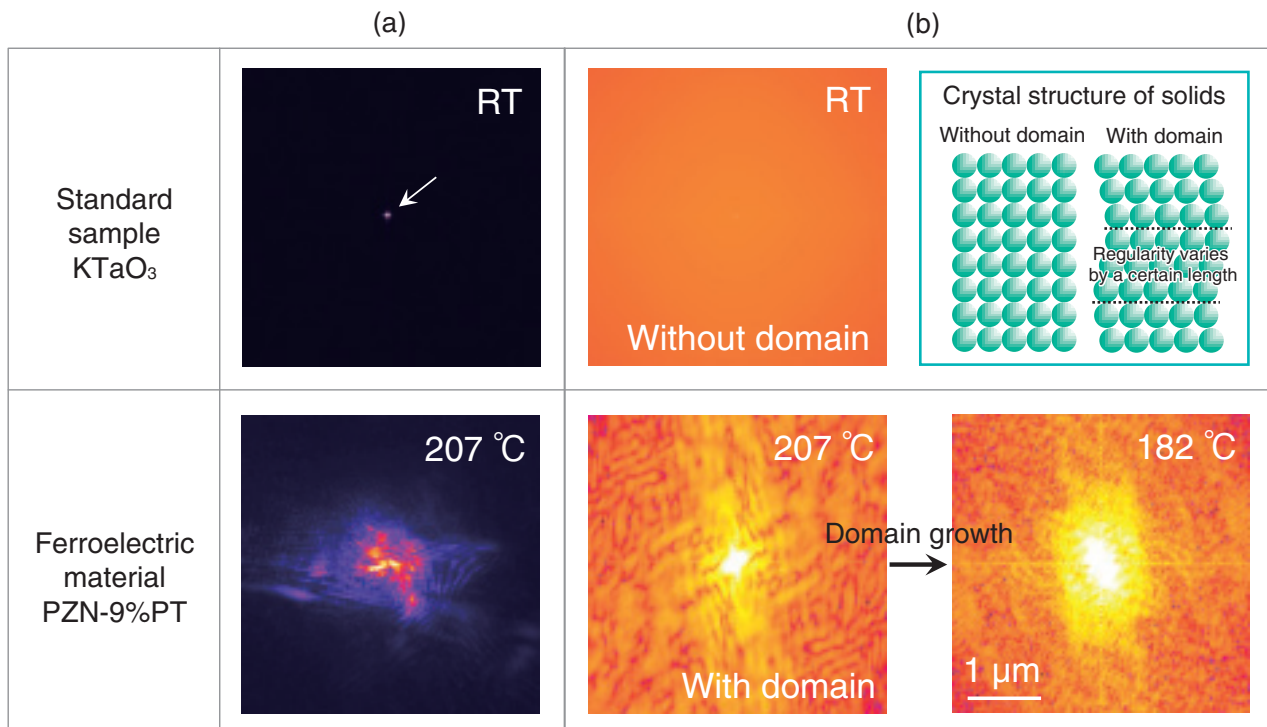


Fig.4-12 Domain configurations observed by using coherent X-rays

(a) Coherent X-ray diffraction patterns of solids without (standard sample: KTaO₃) and with (ferroelectric material: PZN-9%PT) domains. A clear difference can be observed. (b) Domain configurations reconstructed from (a) and their temperature evolution. (Inset) Schematic of the crystal structure of solids without and with domains.

A crystal is a solid material whose 10^{23} constituent atoms are arranged in an orderly repetitive pattern extending in all three spatial dimensions. In some cases, the arrangement rules change with a certain length, which leads to the spontaneous formation of domains (Fig.4-12 inset). Domains are well known to enhance the physical properties of solids. Therefore, the investigation of the precise nature of these domains is crucial for application in industry and fundamental physics.

High functionality is generally seen in relaxors, giant magnetoresistive effects, shape memory effect, etc. We believe that these effects should be based on a common rule. Thus, the domain formation process and the relationship between the domains and the high functionality should be clarified for industrial application and fundamental physics.

A new X-ray diffraction method based on the use of coherent X-rays can be employed to promote the research trend. Such coherency is suitable for observing the incoherency in the crystals, i.e., domains.

We developed a new coherent X-ray diffraction (CXD) apparatus at BL22XU of SPring-8 for observing nanometer-

to-micrometer-scale domains. We achieved a multiple-length-scale approach from macroscale (10 μm) to nanoscale (0.4 nm), which cannot be observed by a conventional X-ray diffraction method. Thus, the relationship between the physical properties and the multiple-length-scales in solids can be investigated.

Fig.4-12(a) shows the CXD patterns of the standard sample KTaO₃ (upper panel) and the ferroelectric material 91% Pb(Zn_{1/3}Nb_{2/3})O₃-9% PbTiO₃ (PZN-9%PT: lower panel). The CXD pattern of PZN-9%PT is much more complex than that of KTaO₃ because of the domain structure in the former. The Fourier transformation in Fig.4-12 (a) shows a homogeneous image for KTaO₃ and an inhomogeneous image for PZN-9%PT, reflecting a domain with a size of hundreds of nanometers. The domain structure evolves to about 1 μm as the temperature decreases. The existence of the 1 μm domain is revealed to enhance the dielectric permittivity in Hz-kHz alternating electric field by a factor of 2.

This research was supported by a Japan Science and Technology Agency grant (CREST: Core Research for Evolutional Science and Technology).

Reference

Ohwada, K. et al., Contribution of Intermediate Submicrometer Structures to Physical Properties Near T_c in Pb(Zn_{1/3}Nb_{2/3})O₃-9%PbTiO₃, Physical Review B, vol.83, issue 22, 2011, p.224115-1-224115-7.

4-7 Mechanism of Performance Improvement of Hydrogen Storage Materials — Structural Determination of Additives by X-ray Absorption Spectroscopy —

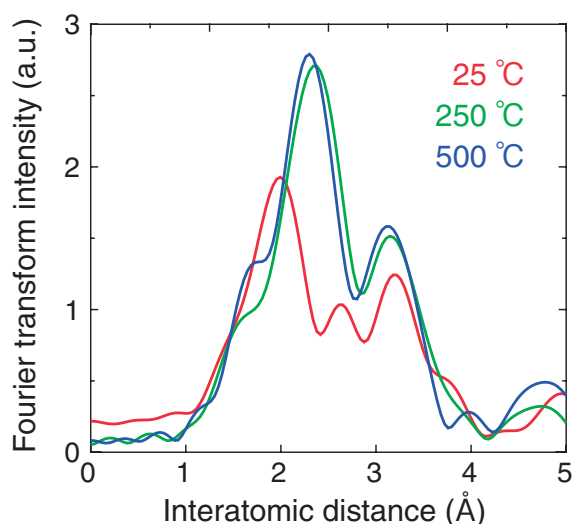


Fig.4-13 Local structure around Ti

The X-ray absorption fine structure (XAFS) technique is a powerful tool for the element-selective determination of the local structure. This figure shows the local structure of the Ti additive in $\text{Mg}(\text{BH}_4)_2$. The Fourier transform spectrum shows a large peak corresponding to the location of the coordination atoms. This provided element-selective information about the local structure.

Development of advanced onboard hydrogen storage materials with high hydrogen gravimetric density is urgently required. Magnesium borohydride ($\text{Mg}(\text{BH}_4)_2$), which has a hydrogen density of 14.9 wt%, has been regarded as one of the potential hydrogen storage materials. Its potential applications are, however, restricted by its high dehydrogenation temperature ($>300\text{ }^\circ\text{C}$). In a recent study, it has been observed that Ti additives lower the initial dehydrogenation temperature of $\text{Mg}(\text{BH}_4)_2$. This result motivated us to clarify the effect of the addition of Ti on the dehydrogenation reaction of $\text{Mg}(\text{BH}_4)_2$.

In this study, we observed the local atomic structure around Ti compounds by the X-ray absorption fine structure (XAFS) technique. Local structural analysis of Ti additives in $\text{Mg}(\text{BH}_4)_2$ indicated that structural transformation occurs between 25 and 250 $^\circ\text{C}$ (Fig.4-13). It was important to confirm whether this structural transformation was related to the dehydrogenation reaction.

In order to study the correlation between the structure and the dehydrogenation properties, the XAFS and the dehydrogenation intensity were simultaneously observed (Fig.4-14). The Ti *K*-edge energy shift showed an abrupt change in the range 100~150 $^\circ\text{C}$, indicating a structural

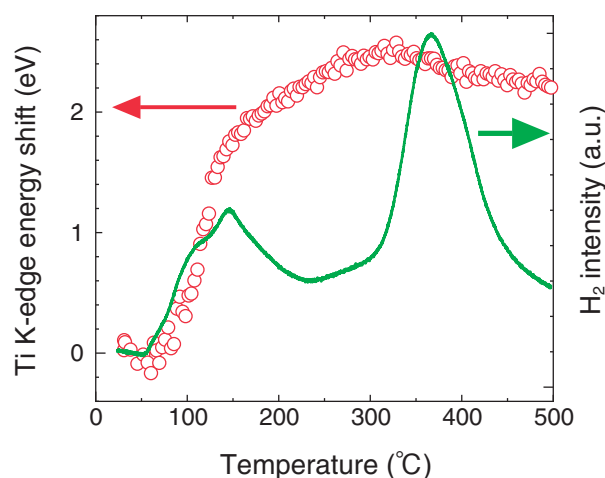


Fig.4-14 Ti *K*-edge energy shift and dehydrogenation curve

Continuous XAFS measurement enables us to simultaneously observe the local structural change in Ti additives and the dehydrogenation curve. This figure shows that the structural change in Ti additives is directly related to the first dehydrogenation peak.

change in the Ti compound. This temperature range was almost the same as the width of the first peak in the dehydrogenation curve. On the other hand, the *K*-edge energy shift did not show any change at around 360 $^\circ\text{C}$, where the main peak in the dehydrogenation curve was observed. As a result, we wholly concluded that the local structural change in the Ti compound was directly related to the first dehydrogenation peak, which appeared in the range 100~150 $^\circ\text{C}$ and was not strongly influenced by the main dehydrogenation peak at 360 $^\circ\text{C}$. The dehydrogenation peak in the range 100~150 $^\circ\text{C}$ was revealed to be due to the dehydrogenation reaction of $\text{Ti}(\text{BH}_4)_3$. For this reason, addition of the Ti compound brought about a decrease in the dehydrogenation temperature. $\text{Ti}(\text{BH}_4)_3$ was converted to TiB_2 , which is more stable.

Simultaneous measurement of the local structure of the Ti compound and the dehydrogenation curve for the hydrogen storage material clearly demonstrates the correlation between the structural change in the additive and the chemical reaction. We believe that such simultaneous measurements would reveal the key component for the development of more efficient hydrogen storage materials.

Reference

Matsumura, D. et al., Correlation between Structure of Titanium Additives and Dehydrogenation Reaction of Magnesium Borohydride Studied by Continuous Observation of X-ray Absorption Spectroscopy, *Materials Transactions*, vol.52, no.4, 2011, p.635-640.

4-8 Development of Novel Rare-Earth-Recognition Compound – For Efficient Separation and Purification of Rare-Earth Elements –

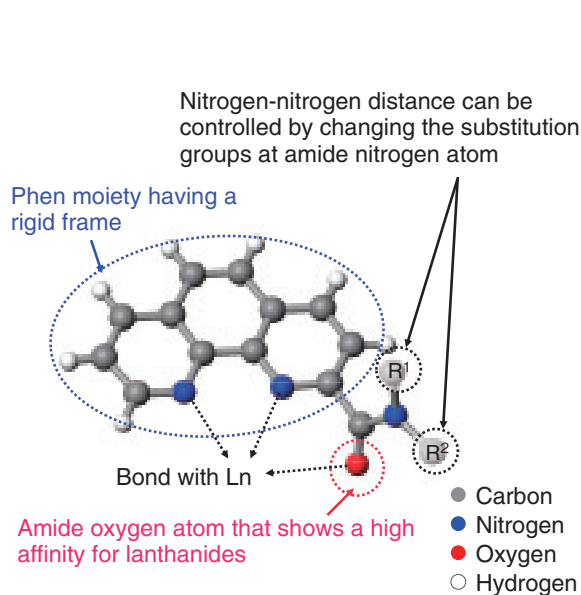


Fig.4-15 New lanthanide-recognition compound PTA

Amide oxygen forms a strong bond with lanthanides, and phenanthroline moiety which has a rigid frame recognizes slightly differences in the ion size of lanthanides.

Lanthanides (Ln) are essential for high-technology industries, because they contribute to the performance improvement and/or size and weight reduction of high-technology products. This is possible because of the unique chemical properties of Ln. To further improve the performance and/or save energy of such products, it is important to improve the purification technique for Ln materials. However, all Ln elements have same stable valence states and similar ionic radii: therefore, the intra-series separation of Ln is extremely difficult. In this study, we synthesized a novel organic ligand PTA (= *N*-alkyl-*N*-phenyl-1,10-phenanthroline-2-carboxamide, Fig.4-15) which exhibits strong bonding with Ln, and by utilizing PTA, we succeeded in recognizing a slight difference in the ion size of Ln.

PTA is mainly composed of an amide group and a phenanthroline (Phen) moiety. An amide oxygen atom shows a high affinity for Ln, and an amide nitrogen can be substituted by various substitution groups. The Phen moiety has a rigid frame that is not easily expanded, contracted, or twisted, and can bond with Ln through two nitrogen atoms. Generally, the affinity of Phen for metal ions decreases significantly in acidic conditions because of the protonation of nitrogen atoms. However, in the case of PTA, the nitrogen atoms in the Phen moiety show a high affinity for Ln even in highly acidic conditions because of the effect of the amide

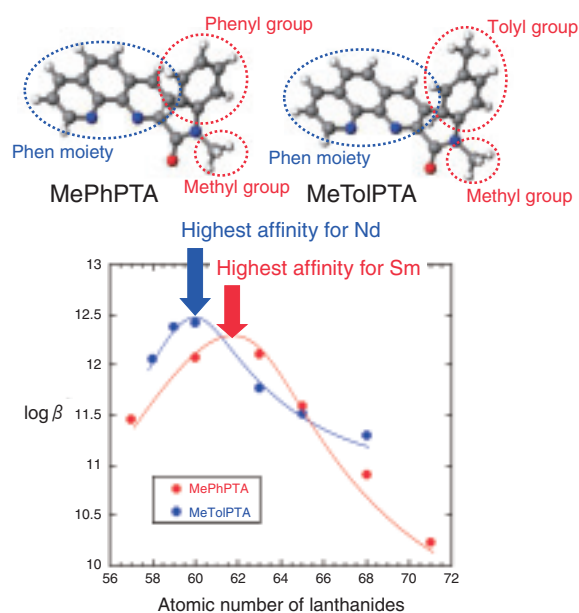


Fig.4-16 PTA consisting of different substitution groups and its affinity for lanthanides

This is a graphic chart in which the horizontal axis shows the atomic number of lanthanides and the vertical axis shows the affinity of PTA for lanthanides. The size recognition property can be controlled by modifying the substitution groups.

oxygen atom that is not easily protonated and strongly attracts Ln even in acidic condition^[1]. Furthermore, it has been revealed that the selectivity tendency of PTA for Ln changes upon modifying the substitution groups at the amide nitrogen. For example, PTA consisting of methyl and phenyl groups as substitution groups at the amide nitrogen shows the highest affinity for Sm: in contrast, a PTA in which the phenyl group is replaced by a tolyl group shows the highest affinity for Nd (Fig.4-16)^[2]. In other words, the suitable ion size for complexation changes upon changing the substitution groups. In PTA, the change in substitution groups causes a slight change in the nitrogen-nitrogen distance in the Phen moiety. Thus, we synthesized some PTA derivatives having different substitution groups and investigated the chemical structures of these Ln complexes by using X-ray crystallography and other methods. The results revealed that a correspondence between the ion size of Ln and the form of the rigid Phen moiety is required for strong bonding between them. Moreover, the suitable ion size can be controlled by the modulation of the form of the Phen moiety (nitrogen-nitrogen distance), followed by the modification of substitution groups.

The separation of Ln on the basis of the ion-size recognition property of PTA will facilitate the establishment of an innovative single-element separation technique for Ln.

References

- [1] Kobayashi, T. et al., Effect of the Introduction of Amide Oxygen into 1,10-Phenanthroline on the Extraction and Complexation of Trivalent Lanthanide in Acidic Condition, *Separation Science and Technology*, vol.45, issue 16, 2010, p.2431-2436.
- [2] Hasegawa, Y., Yaita, T. et al., Selective Separation of Samarium (III) by Synergistic Extraction with β -Diketone and Methylphenylphenanthroline Carboxamide, *Talanta*, vol.85, issue 3, 2011, p.1543-1548.

4-9 How to Produce Rare-Earth Metals by Ourselves? — Recovery of Rare-Earth Metals from Hot Springs —

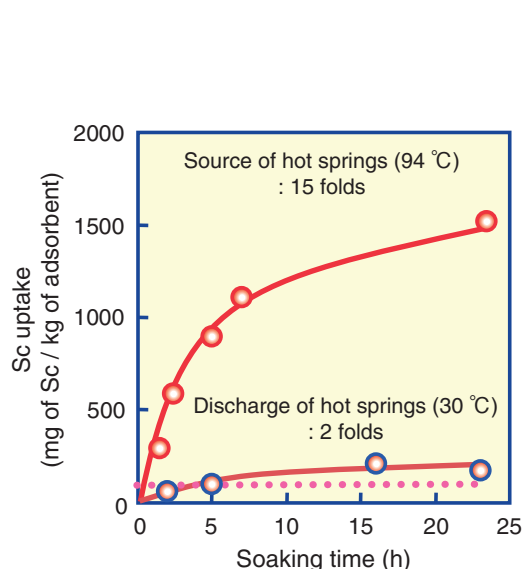


Fig.4-17 Amount of scandium (Sc) uptake as function of contact time in hot springs

Grafted adsorbent for Sc was soaked into hot springs (94 °C and 30 °C) for 23 hours. A wavy line shows the ore concentration of Sc.

Rare-earth elements are defined as the 17 elements comprising scandium (Sc), yttrium, and 15 lanthanides. In the earth's crust, Sc is the 30th most abundant element. Sc is called a rare-earth metal not because it is particularly scarce but rather because it is difficult to obtain. Ores containing Sc as the main component are extremely rare, and Sc is primarily obtained as a by-product of uranium extraction from uranium ores. The conventional processes for recovering useful rare-earth metals have the disadvantages of not only environmental pollution but also poor recovery efficiency; therefore, finding adsorbents that can efficiently recover these metals, particularly Sc, by adsorption is necessary. This is so because during the recovery of a substantial amount of metal ions, no slag is produced during the collection process because the adsorbent collects the metal directly from solution.

Hot springs are an integral part of Japanese culture. Approximately 3000 hot springs are located in Japan, which have long been appreciated and enjoyed by the people of Japan. In addition, hot springs contain many dissolved metals such as vanadium and Sc. If these metals could be collected from hot springs, the industrial demand for these metals would be covered. A suitable metal adsorbent can be synthesized by a radiation-induced graft polymerization

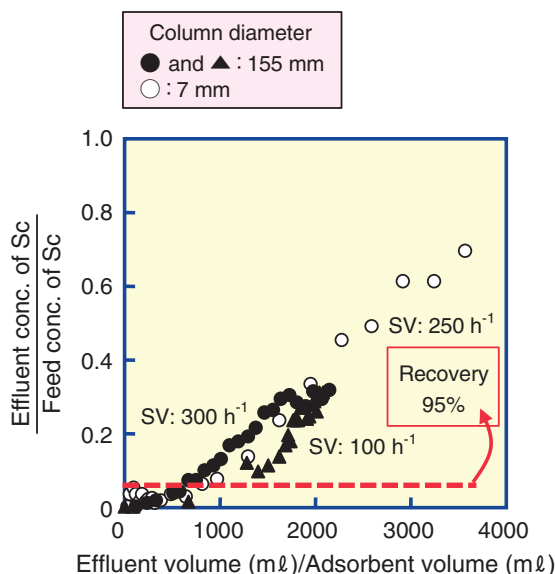


Fig.4-18 Breakthrough curves showing effects of flow rate on lab scale (7 mm ϕ) and on pilot scale (155 mm ϕ)

In the column mode test, the hot springs was passed through the column with flow rates of 100 and 300 h⁻¹ SV (space velocity). The breakthrough curves are essentially independent of flow rate.

technique on a fibrous trunk. Fig.4-17 shows Sc uptake as a function of contact time. After contacting in a hot springs for 23 h, the Sc uptake reached 220 mg of Sc/kg of adsorbent from the hot spring discharge, and 1500 mg of Sc/kg of adsorbent from the hot spring source. These values correspond to 2 times and 15 times the Sc content of 100 mg/L in an ore, respectively. On the basis of the data obtained from batch adsorption, we set up pilot-scale (115 mm ϕ) adsorption equipment at a hot spring site in Kusatsu Town (Gunma Prefecture, Japan). In the column mode test, the column was placed such that the hot spring water passed through the column with flow rates of 100 and 300 h⁻¹ SV (space velocity). The breakthrough curves are essentially independent of the flow rate, as shown in Fig.4-18. The breakthrough point and capacity were almost same as those on a lab scale (115 mm ϕ).

When we selected a fibrous material as a trunk polymer, the adsorption rate was extremely higher than that for a commercial resin. This implied that the space required for water treatment equipment could be reduced. The advantage of a minimized space is that it makes it possible to install such equipment into a narrow space such as that in a hot springs resort.

Reference

Seko, N., et al., Novel System for Recovering Scandium from Hot Spring Water with Fibrous Graft Adsorbent, Nippon Ion Kokan Gakkai-shi (Journal of Ion Exchange), vol.21, no.3, 2010, p.117-122.

4-10 Purification of Factory Waste Gases Using By-Product Ozone — Electron Beam/Catalyst System for Purification of Waste Gases under Practical Gas-Flow Conditions —

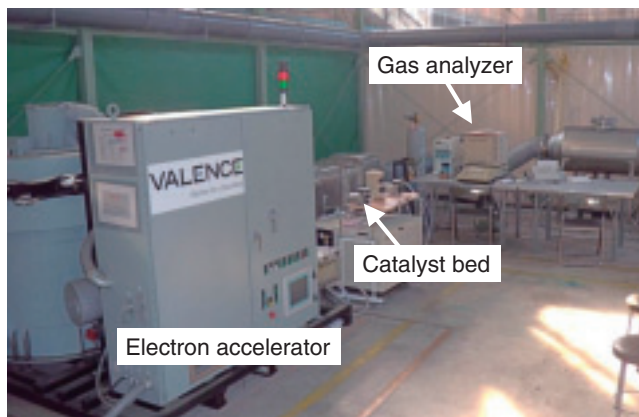


Fig.4-19 Electron beam/ozonolysis catalyst (MnO₂) system

Toxic organics in an airstream (gas flow rate: 500 m³/h; gas velocity: 5 m/s) are oxidized into adhesive products under electron beam irradiation. The products are mineralized into CO₂ using active oxygen species produced from by-product ozone over an ozonolysis catalyst.

The presence of paint-solvent organics in waste gases emitted from painting factories has led to the production of photochemical oxidants in the atmosphere. We have developed a waste-gas purification system that can oxidize such organics into CO₂ by electron beam (EB) irradiation combined with catalytic oxidation. In previous studies, we found that an ozonolysis catalyst was the best matching catalyst since active oxygen species produced from the decomposition of by-product ozone over the catalyst under EB irradiation are effective in oxidizing organics. For the practical use of the purification system in factories emitting waste gases (flow rate: 1×10^4 to 2×10^4 m³/h; gas velocity: ~5 m/s), the effectiveness of the purification system should be evaluated under pilot-scale conditions (flow rate: 500~1000 m³/h; gas velocity: ~5 m/s).

In the present study, an EB/ozonolysis catalyst system was constructed for conducting a pilot-scale test for the mineralization of organics in an airstream (Fig.4-19). This system consists of a compact electron accelerator and a

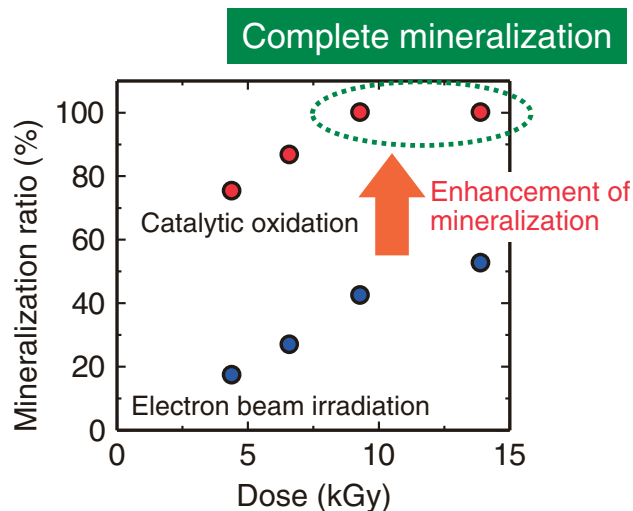


Fig.4-20 Enhancement of mineralization of toxic organics using electron beam/catalyst system

A mixture of xylene and toluene (each with a concentration of 5 ppmv) in an airstream was mineralized into CO_x (CO₂ and CO) under electron beam irradiation with and without catalytic oxidation. The mineralization ratio was obtained from the ratio of the carbon concentration of CO_x to that of the input organics.

honeycomb-type manganese dioxide (MnO₂) bed to efficiently decompose ozone in a turbulent airstream. The catalyst was heated to 100 °C for the desorption of the EB-generated nitric acid to deactivate the catalyst.

An airstream containing a mixture of xylene and toluene (concentration of each compound: 5 ppmv; flow rate: 500 m³/h; gas velocity: ~5 m/s) was introduced in the EB/MnO₂ system. The mineralization of these organics into CO₂ and CO was examined in the presence and absence of the catalyst. The presence of the catalyst enhanced the mineralization of unreacted xylene/toluene and their irradiation products: the mineralization ratio increased from 42% to 100% when the catalyst was used with an irradiation dose of 9.3 kGy (Fig.4-20).

In view of the present results, we intend applying this purification system to actual waste gases in cooperation with chemical engineering companies for protecting the earth's environment.

Reference

Hakoda, T. et al., An Electron-Beam Irradiation/Catalytic Oxidation System for Purification of Aromatic Hydrocarbons/Air Mixture under Practical Gas-Flow Condition, *Industrial & Engineering Chemistry Research*, vol.49, no.12, 2010, p.5517-5522.

4-11 Low-Barrier Hydrogen Bond in Protein

– Neutron Protein Crystallography Casts Light on a New Factor Important of Drug Design –

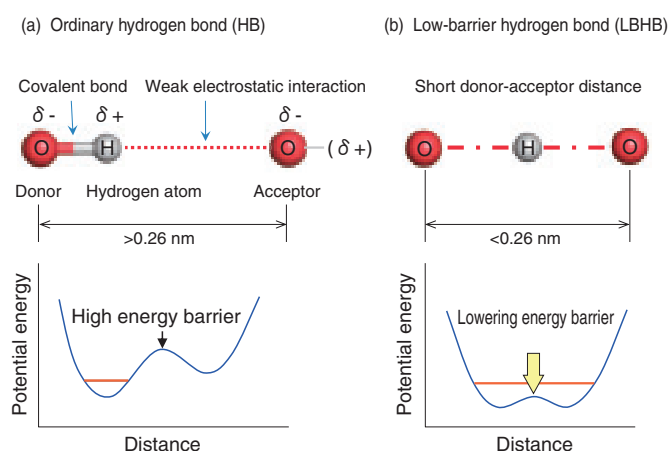


Fig.4-21 General aspects of an ordinary hydrogen bond (HB) and a low-barrier hydrogen bond (LBHB)

(a) Ordinary HB. (b) LBHB. As a donor and an acceptor approach each other, the energy barrier decreases. Subsequently, both atoms share an H atom and form an LBHB.

Hydrogen bonds (HBs) play an important role in the stabilization of protein structures and in enzymatic catalysis. We first demonstrate that a particular kind of HB, low-barrier hydrogen bond (LBHB) (Fig.4-21), exists in a protein and regulates protein function.

The LBHB has been reported to be formed in organic molecules in several specific conditions, e.g., under high pressure or in crystalline state. The formation of LBHBs in proteins was proposed in the early 1990s. However, since there have been no direct observations of LBHBs in proteins, it has been a matter of debate. To identify an LBHB directly, it is essential to observe the position of the hydrogen (H) atom. We succeeded in demonstrating the existence of an LBHB in a photoreceptor protein, photoactive yellow protein (PYP), by using high-resolution neutron crystallography. This analysis identified 819 H positions and showed the existence of an LBHB (Fig.4-22). Since crystallization buffers were prepared with heavy water, H atoms involved in HBs were replaced by deuterium (D) atoms. A D atom is located near the point midway between the phenolic oxygen (O) atom of the photon-absorbing chromophore *p*-coumaric acid (pCA)

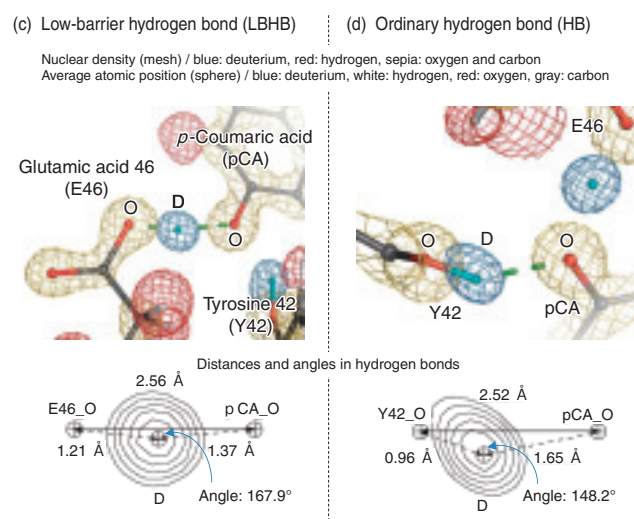


Fig.4-22 LBHB and ordinary HB in photoactive yellow protein (PYP)

(c) LBHB. The H atom is located near the point midway between two donor atoms (the carboxylic O atom of glutamic acid 46 and the phenolic O atom of the chromophore *p*-coumaric acid). (d) Ordinary HB. The H atom is covalently bound to the phenolic O atom of tyrosine 42.

and the carboxylic O atom of glutamic acid 46 (E46) of PYP. This deuterium atom is not covalently bound to either of the two O atoms. This experimental result provides direct evidence of the HB being an LBHB. It is known that the interatomic distance between the two O atoms increases after photon absorption by pCA. In such a situation, the LBHB cannot be formed. In this study, we propose a novel mechanism for photon signal transduction: upon the conversion of the LBHB into an ordinary HB, a light signal is transmitted from the chromophore to the protein. In addition, the present neutron crystallographic analysis indicates that the prerequisites for LBHB formation are that the donor-acceptor distance should be small and the donor and acceptor should have similar pKa values.

The present results show that neutron crystallography, which can directly identify H positions, is an important technique that can help improve our understanding of the molecular mechanism of protein function. The conversion between the LBHB and the ordinary HB has the potential to regulate protein function. The creative use of these HBs is expected to be a new guideline of drug design.

Reference

Yamaguchi, S., Kurihara, K., Kataoka, M. et al., Low-Barrier Hydrogen Bond in Photoactive Yellow Protein, Proceedings of the National Academy of Sciences of the United States of America, vol.106, no.2, 2009, p.440-444.

4-12 Role of Electric Fields Produced by Heavy-Ion Irradiation in DNA Damage

— Is Occurrence of Clustered DNA Damage Promoted by the Electric Fields? —

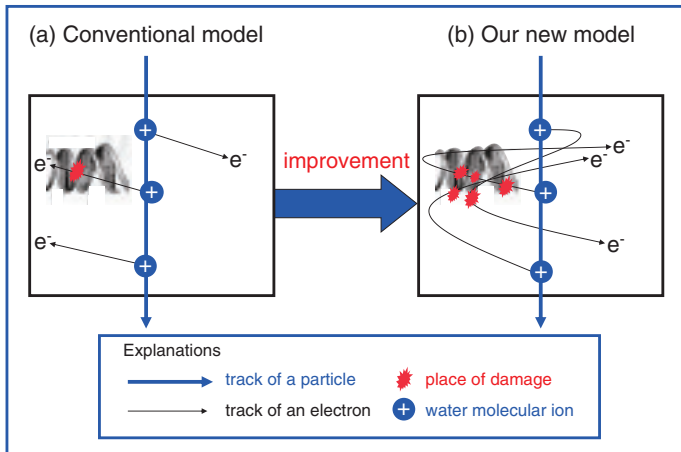


Fig.4-23 Images of DNA damage in the case of (a) conventional model and (b) our new model

Movement of electrons is in straight and zigzag paths in (a) the conventional model and (b) our model, respectively, and the yield of DNA damage resulting from electron impact in our model is much larger than that in the conventional model.

Cancer therapy with carbon ions has a powerful therapeutic effect. This may result from the fact that carbon ions cause clustered DNA damage, which is defined as multiply damaged sites, within a region corresponding to a DNA length of several nanometers. Clustered DNA damage is thought to be produced by electron impact. Although evidence on the biological significance of clustered DNA damage has been accumulated, it remains largely unknown how clustered DNA damage results after irradiation. We proposed a mechanism and quantitatively showed its feasibility. The mechanism is as follows: the electric field traps the emitted electrons near a radiation track, and these electrons cause a cluster of DNA lesions.

Fig.4-23 shows images of the movement of electrons produced by irradiation of a particle in the case of the conventional model and our new model. A comparison of Fig.4-23 (a) with Fig.4-23 (b) led us to propose that our model may show a high probability of the production of clustered DNA damage.

Fig.4-24 shows some positions where H_2O^+ ions are produced upon irradiation of water with a 36 MeV carbon ion

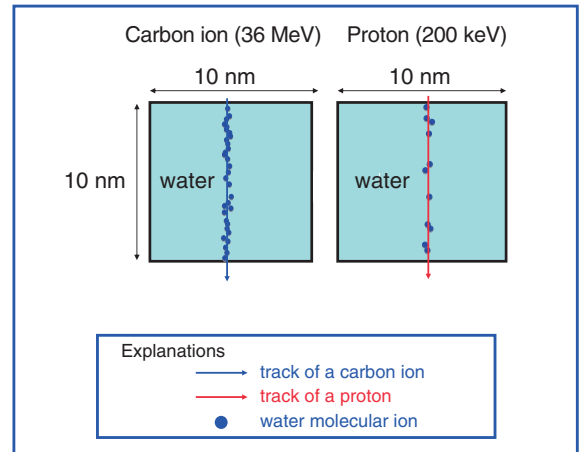


Fig.4-24 Positions where the water ions are produced
Positions of water ions produced by a carbon ion with an energy of 36 MeV and a proton with an energy of 200 keV upon moving through a distance of 10 nm in water.

and a 200 keV proton. The water molecules are ionized approximately every 0.3 nm and 0.8 nm along the tracks of the carbon ion and proton, respectively. We also calculate the number of electrons trapped by the electric fields of H_2O^+ ions within a diameter of 2 nm from the track. These numbers are 15 and 3 for the carbon ion and proton irradiation, respectively. Since the ionization event often takes place at an energy near 200 keV in the case of proton impact, the number of electrons trapped near the track after the carbon ion irradiation is much larger than that after the proton irradiation. Furthermore, for a carbon ion, the number of H_2O^+ ions produced by electron impact as calculated by using our model is four times as large as that calculated by using the conventional models. This is because of the fact that the chances of collision of electrons with a H_2O molecule increase for the situation shown in Fig.4-23 (b) in the case where a DNA is located near the track. That is, the electrons trapped near the track may cause clustered DNA damage. In future, we intend carrying out simulations involving DNA in a cell and studying the role of the electric fields in the occurrence of clustered DNA damage in greater detail.

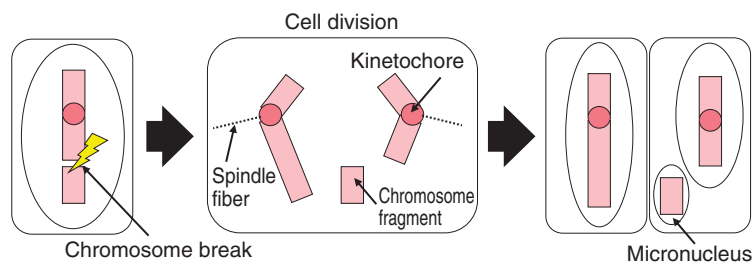
Reference

Moribayashi, K., Incorporation of the Effect of the Composite Electric Fields of Molecular Ions as a Simulation Tool for Biological Damage due to Heavy-Ion Irradiation, Physical Review A, vol.84, issue 1, 2011, p.012702-1-012702-7.

4-13 Persistent Chromosomal Aberration Caused by Ionizing Radiation

— Appearance of Micronuclei in Descendants of γ -ray-Irradiated Plant Cells —

Before appearance of micronuclei



After appearance of micronuclei

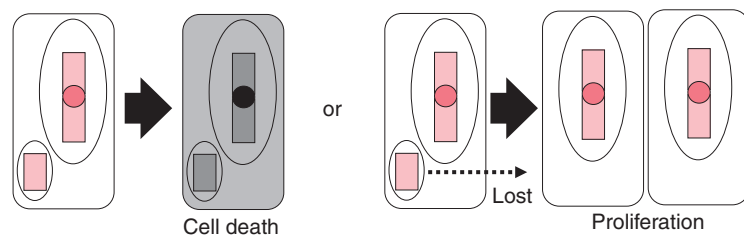


Fig.4-25 Appearance of micronuclei and their fate

During cell division, chromosomes are drawn by a spindle fiber attached to their kinetochore and brought to the opposite sides of the cell. Chromosome fragments without any kinetochore get left behind, forming micronuclei after cell division. While most of the cells with micronuclei can proliferate, they lose a part of the genetic information since micronuclei are not inheritable and disappear soon.

Plants have chromosomes consisting of DNA and protein in their cell nuclei. When ionizing radiation (IR) and oxidative stress induce chromosomal aberration such as micronuclei (MN) (Fig.4-25), the genes corresponding to the chromosomes with aberrations undergo mutation. Recent studies have found evidence for the persistent occurrence of chromosomal aberrations in the descendants of irradiated mammalian cells. We thus cultured irradiated plant cells and measured the frequency of micronucleus induction in order to examine chromosomal aberrations in the descendants of irradiated plant cells.

In our experiments, tobacco cultured cells were irradiated with 40 Gy of ^{60}Co γ -rays. Irradiated and non-irradiated cells were cultured in discrete vessels and aliquots of proliferated cells were transferred into new vessels every 7 days. Furthermore, a fraction of the cultured cells was collected to determine the number of cells and MN.

Irradiated cells as well as non-irradiated cells actively proliferated and the number of irradiated cells increased 2²³-fold in the investigation period. In irradiated cells, the

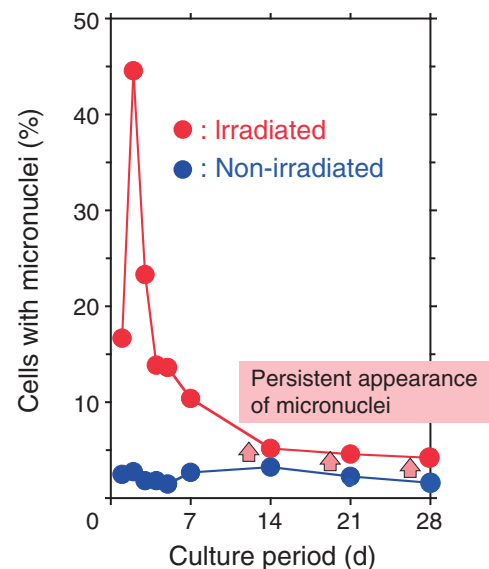


Fig.4-26 Persistent appearance of micronuclei after irradiation

In irradiated cells, the fraction of cells with micronuclei decreased from the day 3 and reached the minimum, their number being greater than non-irradiated cells by almost twofold. Hence, it was concluded that micronuclei persistently appeared in the descendants of irradiated cells.

fraction of cells with MN reached the maximum on day 2 and decreased with cell proliferation from day 3. It reached a minimum on day 14 and later, being greater than non-irradiated cells by almost twofold (Fig.4-26). From the fact that MN disappear soon, it is certain that MN persistently appeared after 20 or more cycles of cell division in the irradiated tobacco cells. It is supposed that oxidative stress is induced in the descendants of irradiated cells via an unknown mechanism and that MN appear persistently since IR enhances oxidative stress in the irradiated cells, which in turn induces chromosomal aberration.

In summary, we found that MN persistently appear in the descendants of irradiated plant cells. Cells with MN finally lose their genetic information, partly because MN are not inheritable. We thus point out that genetic information of irradiated plants can be altered later as well as immediately after irradiation. It is necessary to obtain a good understanding of the significance of the persistent appearance of chromosomal aberration for mutation breeding of plants using IR.

Reference

Yokota, Y. et al., Enhanced Micronucleus Formation in the Descendants of γ -ray-Irradiated Tobacco Cells: Evidence for Radiation-Induced Genomic Instability in Plant Cells, *Mutation Research / Fundamental and Molecular Mechanisms of Mutagenesis*, vol.691, issues 1-2, 2010, p.41-46.

To Clarify Phenomena Threatening Nuclear Safety

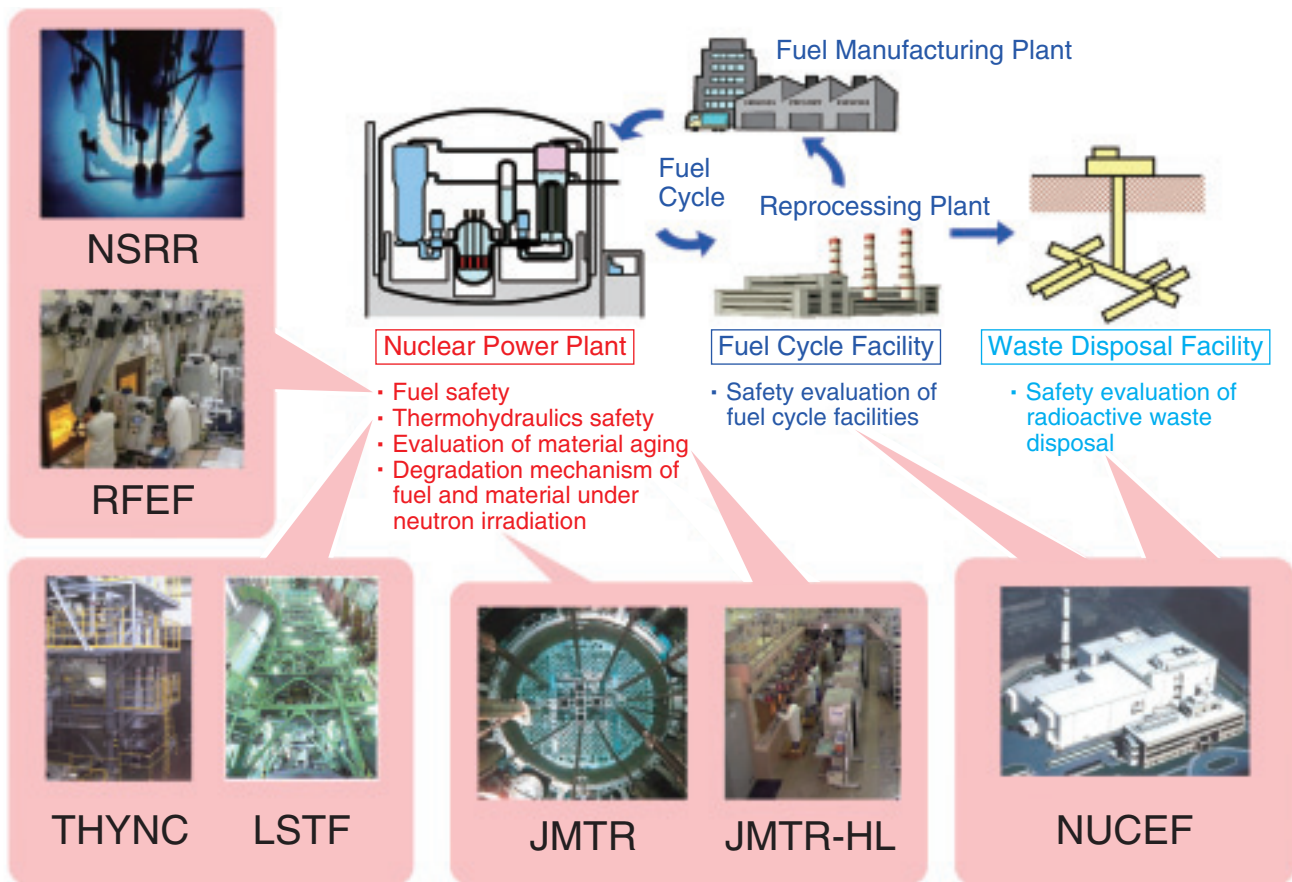


Fig.5-1 Nuclear safety research areas and related facilities in JAEA

The Nuclear Safety Research Center produces experimental data using various facilities in JAEA. These data for risk assessment and safety evaluation of nuclear facilities contribute internationally to develop evaluation methods and criteria.

Possibilities of serious accidents in nuclear installations and their consequences have been studied at the Nuclear Safety Research Center (NSRC) in order to ensure the safe use of current nuclear facilities. A massive and severe accident was caused at the Tokyo Electric Power Company, Incorporated Fukushima Daiichi Nuclear Power Station (NPS), by the Great East Japan earthquake and tsunami. The NSRC has been cooperating with the Japanese government to institute proper emergency responses based on research findings and developments. Nevertheless, most specialists at the NSRC regret that they were unable to prevent the accident. Continuous efforts should be made to avoid serious damages while we utilize nuclear energy. As human technologies are not perfect, proper understanding of a situation and continuous improvement in the developed technologies are important to make best and safe use of the technologies. The International Atomic Energy Agency, which investigated the accident at the Fukushima Daiichi NPS, pointed out the importance of the “continuous improvement.”

The different phenomena that could threaten nuclear safety have been studied at the NSRC by using the various facilities shown in Fig.5-1. These are special facilities where radionuclides are handled and accident conditions are safely simulated.

In this chapter, the results of recent safety research on the following topics are presented: degradation of fuel cladding properties (Topics 5-1, 5-2), degradation of material properties, integrity of reactor structures in the event of earthquakes (Topics 5-3, 5-4, 5-5), possible reactor power fluctuations because of earthquakes (Topic 5-6), radioactivity evaluation in the reactor (Topic 5-7), release of radioactive iodine in severe accidents (Topic 5-8), long-term stability of radioactive waste (Topic 5-9), and decommissioning of nuclear facilities (Topic 5-10). We believe that continuous research on these technical subjects is indispensable for promoting the continuous improvement in nuclear technologies, including those for safety regulation and electric-power generation. In particular, research on severe accidents should be prioritized.

5-1 Origin of Hydrogen Embrittlement of Fuel Claddings — Calculation of Hydrogen Effect on Resistance to Crack Propagation —

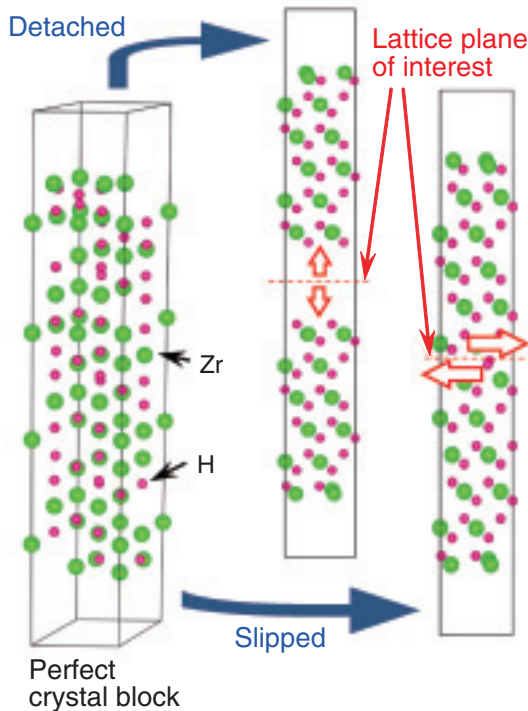


Fig.5-2 Schematic views of first-principles calculations of zirconium hydride

We modeled typical crystal structures consisting of zirconium and hydrogen (hydride is shown here as an example) and evaluated the resistance of lattice planes to detachment and slip.

Hydrogen embrittlement of Zr alloys is an important issue in safety evaluation for nuclear power plants because hydrogen embrittlement results in the mechanical degradation of the fuel cladding. In the reactor operation, the Zr-based cladding is oxidized by waterside corrosion, and it absorbs the generated hydrogen. Only a small part of the absorbed hydrogen is dissolved into the Zr matrix to form a hydrogen solid solution, while the remaining part of the absorbed hydrogen forms zirconium hydride precipitates. Cracks or voids generated inside or around hydride precipitates are known to be the direct cause of observed macroscopic embrittlement. However, it is not microscopically clear how such cracks or voids are generated.

We have performed first-principles calculations to accurately evaluate the microscopic properties of various materials, and thereby to investigate the role of hydrogen in the embrittlement of Zr alloys. The crystal structures of hydride and hydrogen solid solution were modeled (Fig.5-2), and the resistance of their lattice planes to detachment and slip operations were evaluated.

We found that the resistance to detachment in hydride was about 20% lower than that in pure Zr. Further, hydride has a

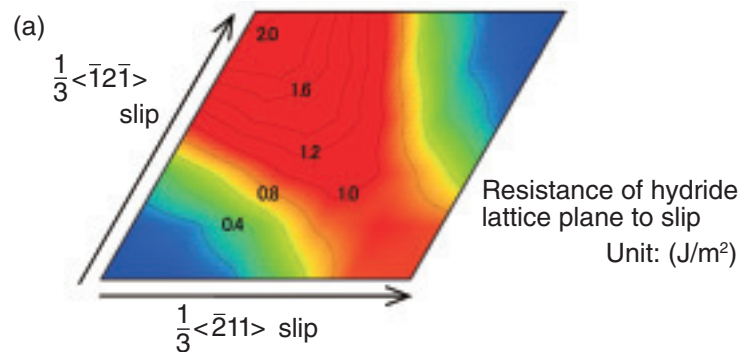
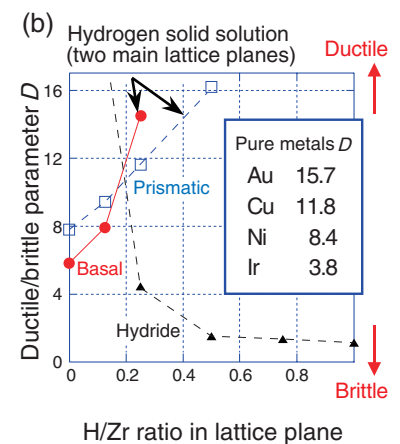


Fig.5-3 Influence of hydrogen concentration on resistance to slip and crack propagation

The contour plot (a) shows that resistance to slip is high in hydride lattice, irrespective of slip direction. The plot (b) shows that resistance to crack propagation decreases and increases with an increase in the hydrogen concentration in hydride and the hydrogen solid solution, respectively.



resistance to slip of at least about 1.0 J/m^2 , irrespective of the slip direction, which is about four-times higher than that of pure Zr and hydrogen solid solution ((Fig.5-3 (a)).

A simple ductile/brittle parameter D considered to be a measure of the resistance to brittle crack propagation was evaluated by using the first-principles calculation results (Fig.5-3 (b)). Generally, D increases with an increase in the resistance to detachment and decreases with an increase in the resistance to slip. The value of D is large for the ductile metal Au and small for brittle metal Ir. The small D value of Zr hydride indicates its crucial brittle nature and implies that crack generation inside hydride precipitates is the origin of the observed macroscopic embrittlement.

Such studies of the elementary processes of hydrogen embrittlement support the ongoing development of safety evaluation methods that can accurately take into account the hydrogen effects. Furthermore, promoting understanding of such influential phenomena on the reactor safety also provides valuable information on how to manage serious situations in nuclear power plants that have not been previously experienced or anticipated.

Reference

Udagawa, Y. et al., Ab Initio Study on Plane Defects in Zirconium-Hydrogen Solid Solution and Zirconium Hydride, Acta Materialia, vol.58, issue 11, 2010, p.3927-3938.

5-2 Evaluating Safety Performance of Oxidized Fuel Cladding

— Investigation of Test Methods for Evaluating Fuel Integrity in Loss-of-Coolant Events —

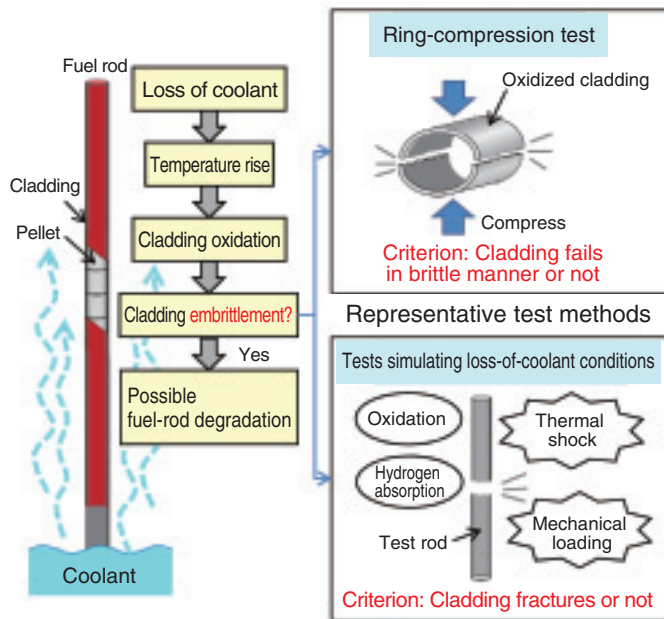


Fig.5-4 Representative test methods for evaluating fuel integrity in loss-of-coolant events

Embrittlement of fuel cladding should be avoided to ensure reactor safety in loss-of-coolant events. In the US, ring-compression tests on oxidized cladding are conducted and in Japan, tests simulating loss-of-coolant conditions are conducted for safety evaluation.

During the operation of a nuclear reactor, the fuel temperature is below 600 K. As observed during the accident at the Fukushima Daiichi NPS, owned by the Tokyo Electric Power Company, Incorporated, the temperature rises drastically because of reduction in the reactor coolability. The fuel cladding reacts with the coolant and is rapidly oxidized above 1200 K. The severely oxidized cladding becomes brittle and may shatter due to thermal shock or mechanical loading.

Ring-compression tests on the oxidized cladding are used in the US and European countries to examine the embrittlement conditions, while tests simulating loss-of-coolant conditions are conducted in Japan to determine the fracture/no-fracture conditions of the fuel rod in relation to the cladding embrittlement (Fig.5-4). The trend toward higher fuel burnup and use of new cladding alloys has increased the need for international discussions on the test methods and safety criteria on the cladding embrittlement.

In the present study, ring-compression tests were conducted on irradiated cladding specimens, which had been tested by simulating loss-of-coolant conditions, in order to

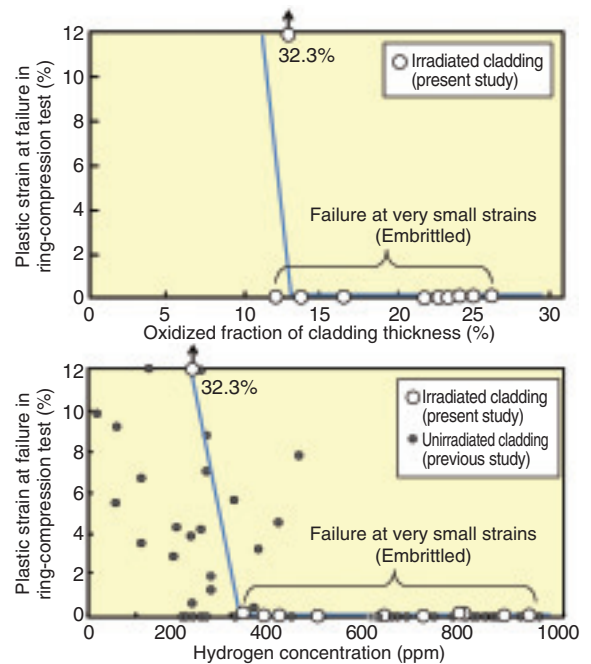


Fig.5-5 Results of ring-compression tests on cladding specimens that experienced loss-of-coolant conditions

Cladding specimens fail at very low plastic strains when oxidation and hydrogen content are high. Most of the specimens are regarded as embrittled in ring-compression tests, though specimens did not fracture in tests simulating loss-of-coolant conditions.

compare the two above-mentioned test methods and to consider the test methods for appropriately evaluating the fuel integrity in loss-of-coolant events.

Fig.5-5 shows that most of the specimens failed at very small plastic strains in the ring-compression tests, though they did not fracture in the tests simulating loss-of-coolant conditions. In other words, there is a discrepancy between the criteria derived from the two tests. Analytical studies showed that this discrepancy is caused by differences in the magnitude and the extent of localization of the stresses generated in the specimens during the tests.

The present results indicate that the conditions where the cladding is exposed should be taken into account to confirm the fuel integrity with scientific rationality. Moreover, considering the accident at the Fukushima Daiichi NPS, safety should be ensured during long-term cooling, including in the case of earthquakes, and handling after loss-of-coolant events. We would make contributions for establishing safety criteria and improving the reactor safety by developing test methods applicable to such post-loss-of-coolant events.

Reference

Nagase, F. et al., Ring Compression Ductility of High-Burnup Fuel Cladding after Exposure to Simulated LOCA Conditions, Journal of Nuclear Science and Technology, vol.48, no.11, 2011, p.1369-1376.

5-3 For Reliable Evaluation of Corrosive Conditions in Reactor Core — Enhancement of Technology for Water-Chemistry Evaluation —

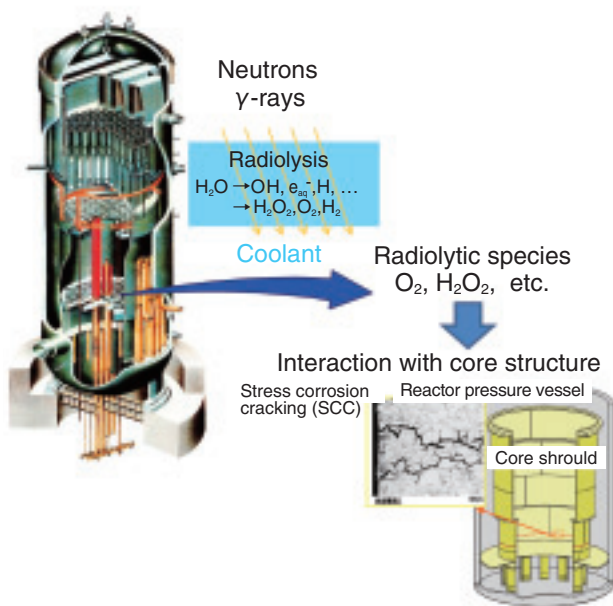


Fig.5-6 Water radiolysis and corrosion in a reactor core
Oxidizing species such as hydrogen peroxide and oxygen are generated in the coolant as a result of water radiolysis. These species cause SCC in the core shroud.

Light-water reactors (LWRs) use high-purity water as the primary coolant and the neutron moderator. As a result of water radiolysis, oxidizing species such as oxygen and hydrogen peroxide are generated in the water. The generated oxidizing species interact with structural materials, causing material degradation such as stress-corrosion cracking (SCC). It is therefore important to accurately evaluate water chemistry in the reactor core for ensuring long-term safe operation of LWRs (Fig.5-6). Water chemistry in the reactor core can be estimated through a combination of theoretical analyses and in-situ electrochemical corrosion potential (ECP) measurement, supporting the validity of the theoretical analyses by ECP measurement. One drawback of this process is that the number of locations for ECP measurement is limited in LWRs. For ensuring the accuracy of the theoretical analyses, theoretical model validation based on in-pile ECP measurement under a wide range of irradiation conditions is required.

In this study, ECP data obtained from an in-pile loop of an experimental reactor under mixed neutron and γ -ray irradiation were evaluated by theoretical analyses. The in-pile

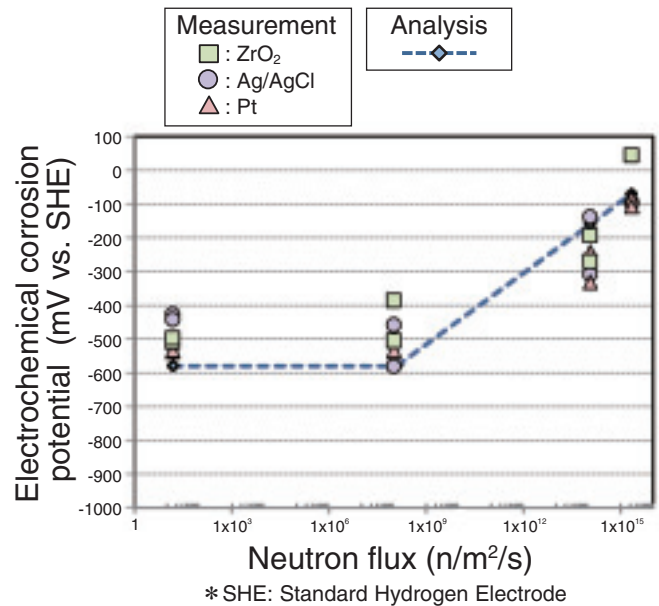


Fig.5-7 Comparison between calculated and measured values of ECP

ECP is an index for expressing the degree of corrosion in an environment. ECP for stainless steel in a reactor core was measured by using three types of ECP sensors, i.e., ZrO_2 , $Ag/AgCl$, and Pt . ECP varies with irradiation conditions (e.g., neutron flux). The measurement data are reproduced in the analysis.

ECP data were obtained under a wide range of neutron flux levels (from quite low to high), which is equivalent to the range of neutron flux levels in the core shrouds of LWRs. The ECP measurement data are plotted as a function of neutron flux in Fig.5-7. In this case, hydrogen was injected in the water to reduce the concentration of the oxidizing species that has a strong relation with the ECP, i.e., the ECP decreases with a decrease in the concentration of the oxidizing species. As can be seen in the figure, the ECP for low values of the neutron flux was low because of the effect of hydrogen injection. However, the measured ECP increased with an increase in the neutron flux because the generation of oxidants due to irradiation exceeded the suppression effect due to hydrogen injection. The calculated ECP values agreed well with the measured values, showing that the theoretical model is applicable to a wide range of irradiation conditions with sufficient accuracy.

This theoretical model will be extended to evaluate the corrosion environment under sea water and γ -ray irradiation for developing countermeasures against the corrosion of the containment systems of Fukushima Daiichi NPS.

Reference

Hanawa, S. et al., ECP Measurements under Neutron and Gamma Ray in In-Pile Loop and Their Data Evaluation by Water Radiolysis Calculations, Proceedings of Nuclear Plant Chemistry Conference (NPC2010), Quebec City, Canada, 2010, 10p., in CD-ROM.

5-4 Research on Corrosion Resistance of Reactor Pressure Vessel — Evaluation of Degradation of Thermally Affected Stainless Steels by Microstructural Analysis —

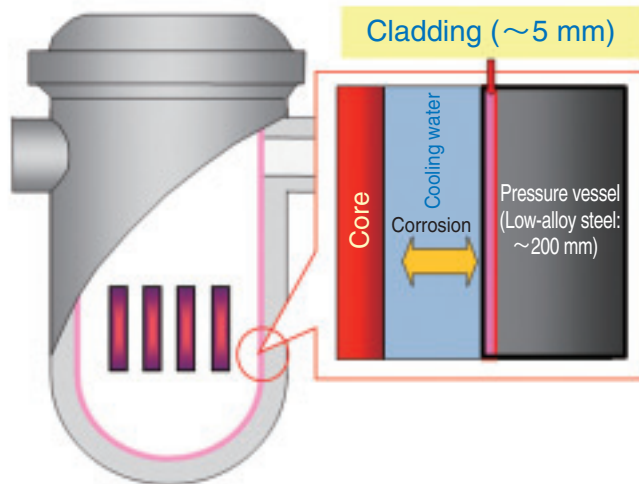


Fig.5-8 Reactor pressure vessel and cladding layer

The inner wall of the reactor pressure vessel is covered by stainless steel weld overlay cladding. The cladding prevents the pressure vessel from being corroded by the cooling water.

The reactor pressure vessel (RPV), which is about 200 mm thick, is a very important structural component that enhances the safety in the vicinity of the core. The RPV is made of high-toughness low-alloy steel, which is susceptible to corrosion. Therefore, the inner wall of the RPV is covered by 5-mm-thick stainless steel weld overlay cladding in order to prevent it from being corroded by the cooling water (Fig.5-8). The cladding, with a Cr content of over 11%, is resistant to corrosion owing to the formation of a passive surface layer.

The cladding consists of two metallic γ and δ phases. It is known that thermal aging causes the hardening and embrittlement of the δ phase upon long-term operation at the operating temperature of the reactors, i.e., ~ 300 °C. If these changes in the δ phase lead to the formation of cracks penetrating the cladding, there might be a threat of the cooling water coming in direct contact with the low-alloy steel and corroding the RPV. For the safe operation of the reactor, it is necessary to examine its integrity. Further, for the examination of the integrity, it is necessary to have a good knowledge of the mechanisms responsible for the degradation of the cladding. We aim to perform an effect assessment of

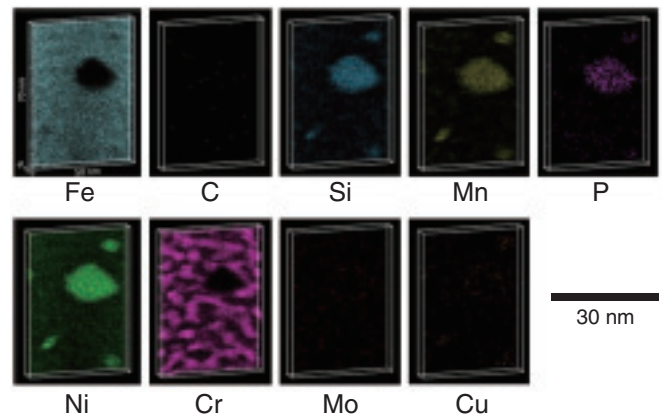


Fig.5-9 Atom maps of the δ phase in the aged cladding

The black areas represent the absence of atoms. The formation of a Si-Mn-P-Ni rich cluster and the undulation of the Cr distribution are shown. These nanostructural changes cause the degradation of the cladding.

the microstructural changes in the cladding on the corrosion resistance of the RPV using the state-of-the-art three-dimensional atom probe (3DAP) technique, which is suitable for nanometer-scale analysis of objects.

The 3DAP technique enables us to observe the distribution of atoms in three-dimensional real space with nearly atomic-scale resolution. The observation of the cladding after heat treatment at 400 °C for about a year, equivalent to the operation of the reactor for a few decades, shows microstructural changes. The Si-Mn-P-Ni rich cluster and the undulation of the Cr distribution are observed (Fig.5-9). Quantitative analysis shows that the undulation has a wavelength of about 10 nm. The undulation appears to retard the formation of the passive layer, resulting in the cladding having lower resistance to corrosion. We are planning to carry out research on the relation between microstructural changes and corrosion resistance in the near future.

The results of this study are expected to be useful for the effective examination of the corrosion resistance of RPVs and for the improvement of the safety of reactors.

Reference

Takeuchi, T. et al., Study on Microstructural Changes in Thermally-Aged Stainless Steel Weld-Overlay Cladding of Nuclear Reactor Pressure Vessels by Atom Probe Tomography, *Journal of Nuclear Materials*, vol.415, issue 2, 2011, p.198-204.

5-5 Development of Evaluation Method for Crack Growth Associated with Large Earthquakes

— Accurate Prediction of the Crack Growth Rate of Piping Materials —

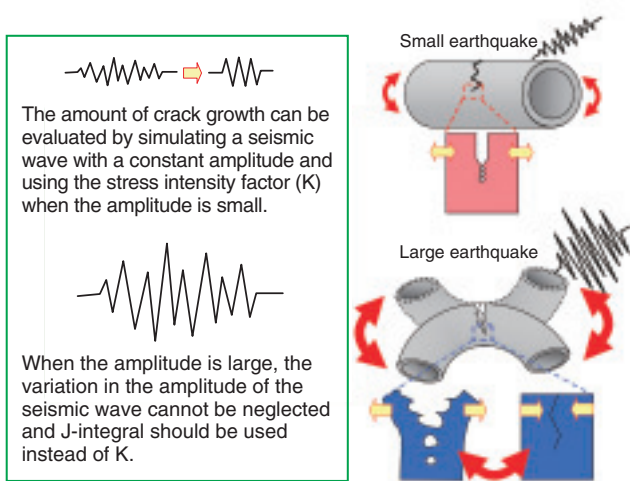


Fig.5-10 Illustrations of earthquake waves (left) and the crack growth behaviors in piping subjected to earthquakes (right)

Fig.5-10 shows earthquake waves and crack growth behaviors in piping subjected to earthquakes. Wide cracks are formed during large earthquakes. The influence of irregular wave amplitudes cannot be neglected in large earthquakes because a large-amplitude wave can affect the subsequent crack growth behavior.

The amount of crack growth must be evaluated when a crack is found in any component important for plant safety. However, an evaluation method for crack growth during seismic loading has not been explicitly stipulated in codes and standards. In recent years, Japanese nuclear power plants have experienced multiple large earthquakes, such as the Niigata-ken Chuetsu-Oki earthquake in 2007 and the Great East Japan Earthquake in 2011. For such large earthquakes that exceed the design basis seismic loading, an appropriate method is required to predict the crack growth behavior. The amount of crack growth can be evaluated using the stress intensity factor range (ΔK). However, ΔK is inappropriate for the high level of loading in the case of large earthquakes. Therefore, we have studied an evaluation method for crack growth during large earthquakes, which is shown in Fig.5-10; the method is based on the J-integral range (ΔJ), which is applicable for a high level of loading.

At first, crack growth rate tests were performed to understand the crack growth behavior under large-amplitude cyclic loading. It was confirmed from the results that ΔJ should be used instead of ΔK to evaluate the crack growth.

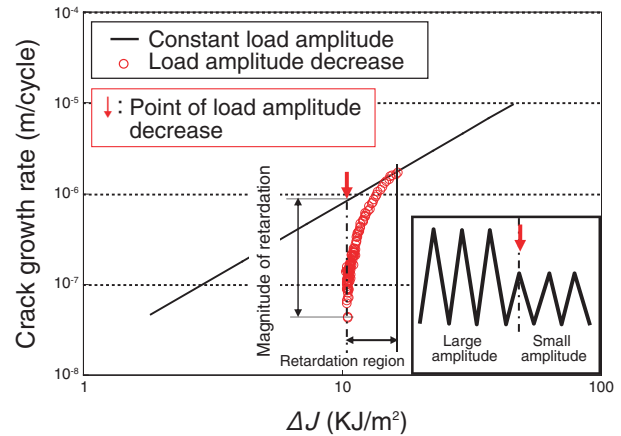


Fig.5-11 Test results for the crack growth rate when the amplitude of the applied wave was decreased (austenitic stainless steel)

Fig.5-11 shows the crack growth rate after the decrease in the load amplitude. The results clearly show that the crack growth rate decreased immediately after the amplitude was decreased, and it recovered when the crack had grown to some extent. The retardation effect was also confirmed for another combination of material and load amplitude.

Next, crack growth tests were performed with cyclic loads. The load amplitude was changed stepwise, as shown in Fig.5-11. When the amplitude was increased, the crack growth rate could be predicted from the results of constant amplitude loading. In contrast, it can be seen from Fig.5-11 that the crack growth rate was retarded when the amplitude was decreased. On the basis of analytical studies, it was shown that the magnitude of the retardation can be estimated from the plastic region size in front of the crack.

Furthermore, a method to calculate ΔJ per cycle has been developed. This method calculates ΔJ for any cyclic wave pattern by considering the irregular loading history such as that in the case of earthquakes.

Considering the above results, we have proposed a crack growth evaluation method for large earthquakes; the method is a combination of methods for the evaluation of the crack growth rate on the basis of ΔJ , the estimation of the retardation effect, and the calculation of ΔJ . The proposed method is expected to be used for the prediction of crack growth during large earthquakes.

Reference

Yamaguchi, Y. et al., A Proposal for Evaluation Method of Crack Growth due to Cyclic Overload for Piping Materials Based on Elastic-Plastic Fracture Mechanics Parameter, Nippon Kikai Gakkai Ronbunshu, A Hen, vol.77, no.777, 2011, p.685-689 (in Japanese).

5-6 Core Power Stability under Strong Earthquake

— Neutron-Coupled Thermal Hydraulic Calculation under Seismic Acceleration —

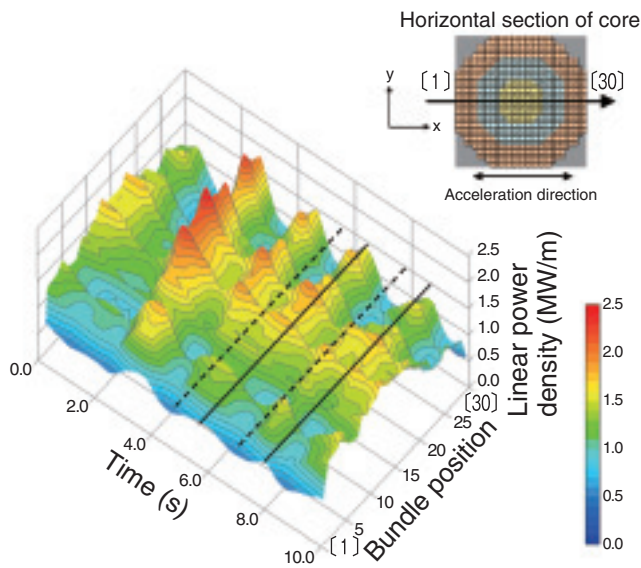


Fig.5-12 Linear power density variation of fuel bundles
The distribution of power per unit length on the center line in the horizontal section at the middle of the core. At both ends of the cross-section, ([1] and [30]), the power oscillated with completely the opposite phase.

When a nuclear reactor is subjected to a huge earthquake, the seismic vibration propagates through the core internals and may shake the coolant. Normally, the reactor is shut down safely by the insertion of control rods into the core (scram) when seismic acceleration over a set point is detected. However, in the case of scram failure, power instability in the core of a boiling water reactor (BWR) may occur because of the seismic vibration. The oscillation of the coolant flow affects the distribution of the volumetric rate of steam (void fraction) in the core. The rate of nuclear reaction then fluctuates because of the variation in the void fraction (void-reactivity feedback).

To evaluate the effect of seismic vibration on core stability, we performed detailed numerical analyses of an actual BWR stability using the TRAC/SKETCH code developed by the JAEA. This code can calculate both the nuclear reaction and boiling coolant flow in the core simultaneously. The code was remodeled to take the effect of seismic acceleration into account. In the previous study, the vertical sinusoidal acceleration was suggested to cause fluctuation in the power throughout the core in the same phase. The present study clarified that the horizontal sinusoidal acceleration occasionally

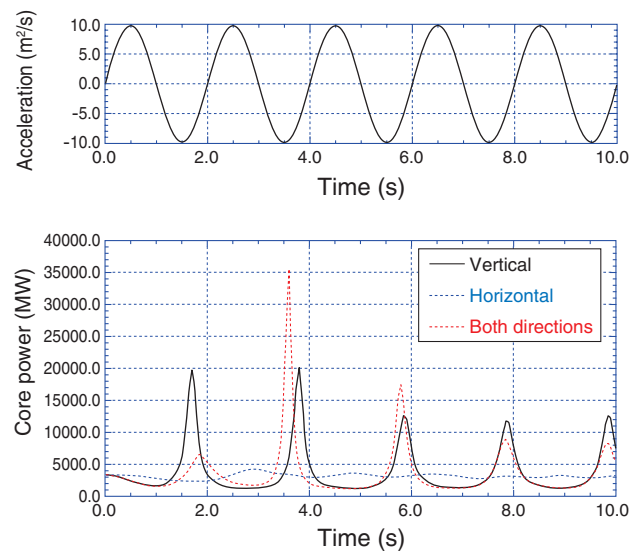


Fig.5-13 Effect of accelerating direction on core power
The upper figure shows the input sinusoidal acceleration with a period of 2 s, and the lower figure shows the core power obtained by numerical analysis. The simultaneous addition of the horizontal and vertical accelerations occasionally caused complicated fluctuations.

causes core power fluctuations with the opposite phase at both ends of the cross-section, as shown in Fig.5-12. Furthermore, Fig.5-13 indicates that the vertical sinusoidal acceleration has a more significant effect on the power fluctuation than the horizontal one. It also shows that the simultaneous addition of the horizontal and vertical accelerations causes complicated fluctuations, such that a depression of the power increase is followed by a remarkably high power increase.

An actual seismic acceleration consists of the superposition of waves with various periods. Investigations of the effect of the period clarified that the core power fluctuates considerably under acceleration with a relatively long period (2~4 s). This indicates that earthquakes occurring even comparatively far away might affect the core stability, because long-period seismic waves do not decay readily.

On the basis of the above knowledge, we are advancing this research to predict the stability of the BWR under various operating conditions.

This research was supported by a Japan Science and Technology Agency grant (CREST: Core Research for Evolutional Science and Technology).

Reference

Satou, A. et al., Neutron-Coupled Thermal Hydraulic Calculation of BWR under Seismic Acceleration, Proceedings of Joint International Conference on Supercomputing in Nuclear Applications and Monte Carlo 2010 (SNA+MC2010), B1, 2010, 10367.pdf, 5p., in USB flash drive.

5-7 How to Evaluate the Radioactivity in a Nuclear Reactor under Operation? — System Development for Evaluating the Radioactivity in the Reactor —

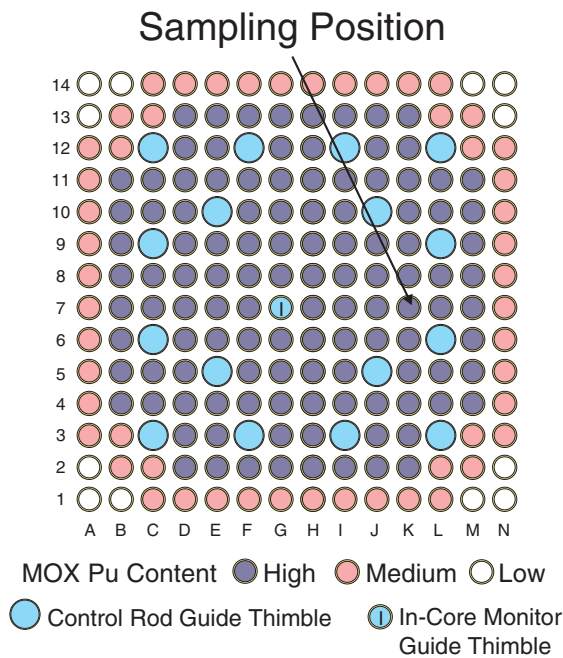


Fig.5-14 Sampling position in MOX fuel assembly for the measurement of nuclide composition

A fuel rod was taken from the sampling position, and the nuclide composition was analyzed after cutting and dissolving the sample.

In nuclear fuels, many nuclides are generated through nuclear reactions such as fission and neutron capture; these nuclides are also converted to other nuclides by nuclear reactions and radioactive decay. Hence, the radioactivity of nuclear fuels changes continuously. It is necessary to estimate the exact number of nuclides in a nuclear fuel in order to evaluate its properties, such as criticality parameters, and to obtain an accurate measure of its radioactivity and heat generation. Hence, we have developed the integrated burnup calculation code system - SWAT.

In this system, the effective neutron reaction cross sections are calculated using SRAC or MVP, which are neutronics calculation code systems developed in the JAEA, and these cross-section data are used by ORIGEN2, which is a widely used burnup calculation code. Furthermore, in order to include the latest available data about the generation ratio of fission products (FP) from neutron fission reactions and the half-lives of the products, the second version of the JNDC FP data library and the JENDL FP decay data library 2000 are also included in the system. Using these libraries, the SWAT system can predict the generation and transmutation of heavy

Table 5-1 Analysis of nuclide composition data by SWAT pertaining to the sample shown in Fig. 5-14

Isotopes	C/E *
^{235}U	1.03
^{238}U	1.00
^{239}Pu	1.05
^{240}Pu	1.00
^{241}Pu	1.03
^{134}Cs	0.96
^{137}Cs	1.03

(* C/E is the ratio of calculation data to experimental data)

nuclides, i.e., actinides such as uranium and plutonium, and their FP on the basis of the latest data. The sampling position of a fuel pin is shown in Fig.5-14. A fuel sample is taken from the spent nuclear fuel and the nuclide composition is measured after cutting and dissolving the sample. Table 5-1 lists the SWAT analysis of the nuclide composition data for the sample shown in Fig.5-14. SWAT can predict the nuclide compositions of major nuclides within a deviation of 5%.

We have also developed the ORIGEN22UPJ system, which can predict the number of nuclides as precisely as SWAT can, by including the effective neutron reaction cross section data libraries prepared by SWAT in ORIGEN2. This system can give results similar to those given by SWAT. Furthermore, because of its high-speed performance resulting from the use of state-of-the-art computer systems, results can be obtained within a few seconds. Because of these advantages, ORIGEN22UPJ was used for evaluating the radioactivity in the reactors at the time of the Fukushima Daiichi NPS accident. We have been contributing to the evaluation of the accident consequences by the Government of Japan.

Reference

Suyama, K. et al., SWAT3.1—The Integrated Burnup Code System Driving Continuous Energy Monte Carlo Coeds MVP and MCNP, JAEA-Data/Code 2009-002, 2009, 124p. (in Japanese).

5-8 Estimation of Gaseous Iodine Revolatilization under Severe Accident Conditions – Application of Iodine Chemistry Reactions to Plant Evaluation –

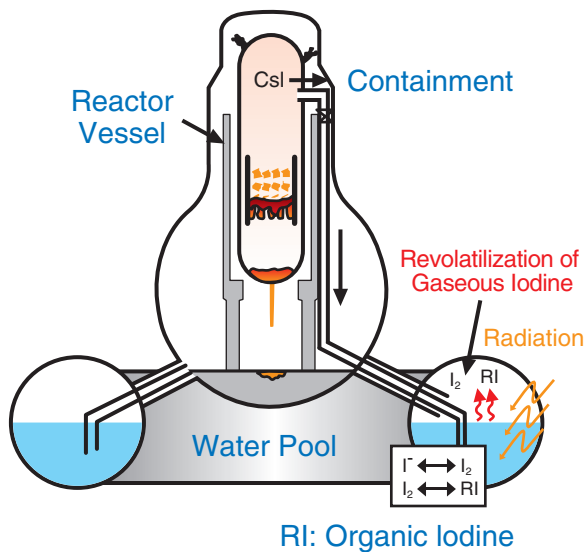


Fig.5-15 Revolatilization of iodine under severe accident conditions

In the early phase of severe accidents, iodine dissolves as I^- in the containment water pool. When nonvolatile I^- is converted into volatile I_2 or organic iodine under the effect of radiation, there is a possibility of an increased source term.

To evaluate the public risk from severe accidents of light-water reactors, the source term, which is defined as the timing and the characteristics of the release of radionuclides into the environment, needs to be evaluated first. Among radioactive nuclides, iodine is the most significant contributor to public health consequences. The iodine behavior in plants is as follows: once a large amount of iodine released from the core dissolves in the containment water pool, it revolatilizes to the gas phase as the highly volatile I_2 and organic iodine through chemical reactions under severe accident conditions (Fig.5-15). Iodine chemistry is a complex phenomenon influenced by a variety of boundary conditions such as temperature, pH of the pool water, radiation dose rate, and impurities. Therefore, reactions in iodine chemistry are some of the uncertain factors in the source term evaluation.

To reduce the uncertainties in the source term evaluation, we performed experiments for improving and expanding the chemical reaction database and mechanistic models for iodine chemistry under severe accident conditions and developed a simulation code for the kinetics of iodine chemistry (Kiche).

We incorporated Kiche in a thermal hydraulics and radionuclide behavior analysis code of light water reactors to

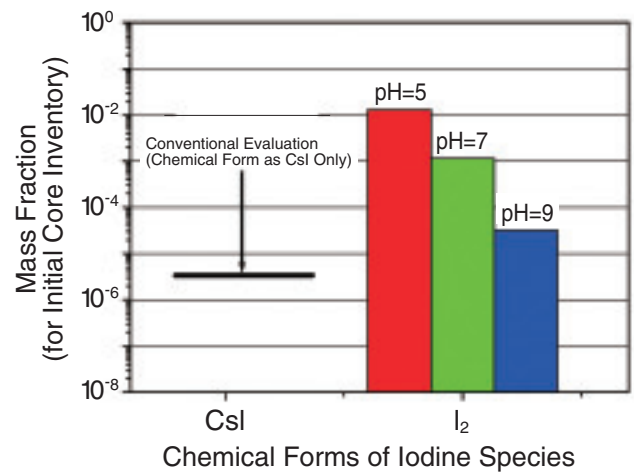


Fig.5-16 Iodine distribution in the containment atmosphere
Mass fraction of iodine in the containment atmosphere at the phase of accident termination tends to increase as a particularly acid condition owing to the effect of the revolatilization of gaseous iodine.

estimate source term (THALES 2) to enhance the efficiency of simulating the iodine behavior using THALES 2.

In addition, we carried out source term assessment for various accident scenarios.

Fig.5-16 shows the results of iodine distribution in the containment atmosphere for an accident termination scenario in which the containment is not damaged by a core damage accident triggered by the loss of core coolant injection for a 1100 MWe BWR.

In conventional evaluations, we considered only the chemical form of CsI. The mass fraction of CsI was finally around 10⁻⁶ when the reduction effect of the gravitational settling and the containment spray was taken into account. When iodine chemistry was considered, it became clear that (1) revolatilization and accumulation occurred intermittently from the liquid phase to the containment atmosphere of I_2 and (2) the accumulation of I_2 increased as the acid condition.

The results show that long-term pH control of liquid phases is important to inhibit the revolatilization of gaseous iodine.

In future studies, we plan to evaluate the effect of organic iodine and the accidents at Fukushima Daiichi NPS.

Reference

Ishikawa, J. et al., Investigation for Evaluation Containment Source Term of BWR4/Mark-I Plant Considering Iodine Chemistry in Suppression Pool, JAEA-Research 2010-051, 2011, 42p. (in Japanese).

5-9 What Accelerates Dissolution of High-Level Waste Glass? — Effects of Magnesium Ions in Solution —

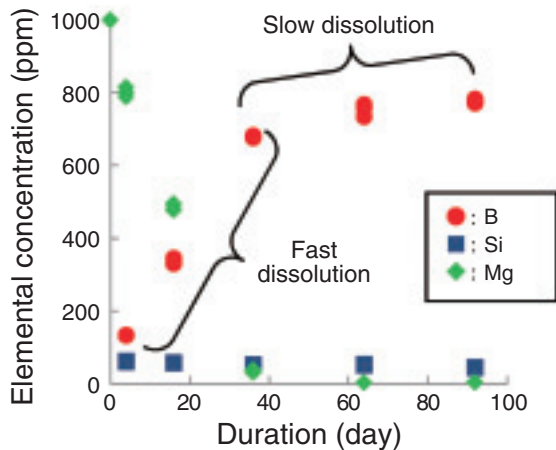


Fig.5-17 Elemental concentrations in the leachate versus time in the leach tests in $MgCl_2$ solution at $90^\circ C$

Boron (B) concentration is a quantitative indicator of glass dissolution. A higher glass dissolution rate is observed under the presence of Mg ions in leachate, while the rate drops after the depletion of Mg ions.

High-level radioactive liquid waste generated during the reprocessing of spent nuclear fuel is vitrified into high-level waste (HLW) glass. It has been planned to dispose of HLW glass in geological repositories at a depth of 300 m or deeper by encapsulating HLW glass in an iron overpack and covering it with bentonite clay buffer. Vitrification is one of the methods for the treatment of highly contaminated radioactive waste generated in the aftermath of the accident in Fukushima Daiichi NPS.

It is assumed that after several hundred or several thousand years, the groundwater would permeate the bentonite buffer and corrode the overpack. This may result in radionuclides leaching from HLW glass into the permeating groundwater. For safety assessment of geological disposal, it is important to fully understand the leaching behavior, namely, dissolution behavior, of HLW glass.

Glass dissolves at a high rate when silicon (Si), a glass-network former, in it dissolves. Under stagnant groundwater likely to be present in a deep geological repository, it is presumed that glass would dissolve at a low rate because the concentration of Si in water around glass would reach near

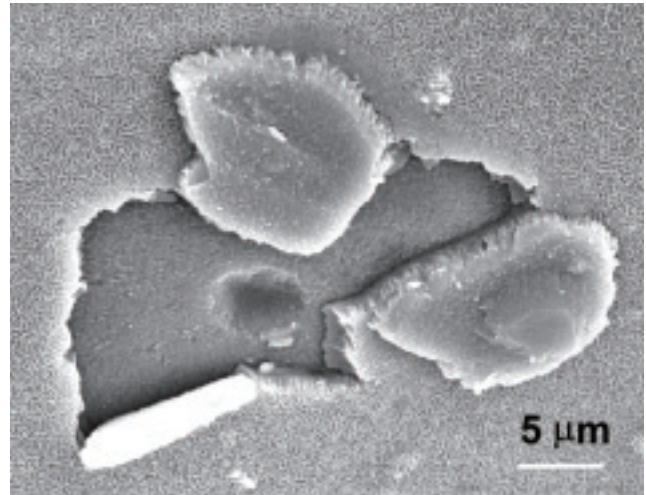


Fig.5-18 A scanning electron microscope image of the surface of glass leached in $MgCl_2$ solution at $90^\circ C$

It is observed that an altered layer is formed on the glass surface and is partially flaked off the surface. This altered layer measures around $1.0 \mu m$ in thickness and mainly consists of Mg and Si.

saturation.

It is also important to investigate the groundwater components that enhance glass dissolution.

In the present study, static leach tests were conducted on simulated HLW glass in a magnesium chloride ($MgCl_2$) solution to investigate the effect of Mg ions on glass dissolution.

When Mg ions existed in the solution, the glass dissolved at a higher rate (Fig.5-17), and an altered layer including Mg and Si was observed on the surface of the leached glass (Fig.5-18).

The obtained results implied that glass dissolution at a higher rate during the first period of around 40 days was accompanied with the formation of magnesium silicates that consumed glass-network-forming Si. However, after this period, the rate decreased as Mg ions depleted in the solution because Si was not consumed to form magnesium silicates.

In order to understand the dissolution of HLW glass, it is essential to know the elements that are likely to consume Si. Radionuclides would be hardly leached from HLW glass in the long term if such elements are scarce in the groundwater.

Reference

Maeda, T. et al., Corrosion Behavior of Simulated HLW Glass in the Presence of Magnesium Ion, International Journal of Corrosion, vol.2011, Article ID 796457, 2011, 6p.

5-10 Toward Safe Decommissioning of Nuclear Facilities — Development of Safety Assessment Code for Decommissioning Activities —

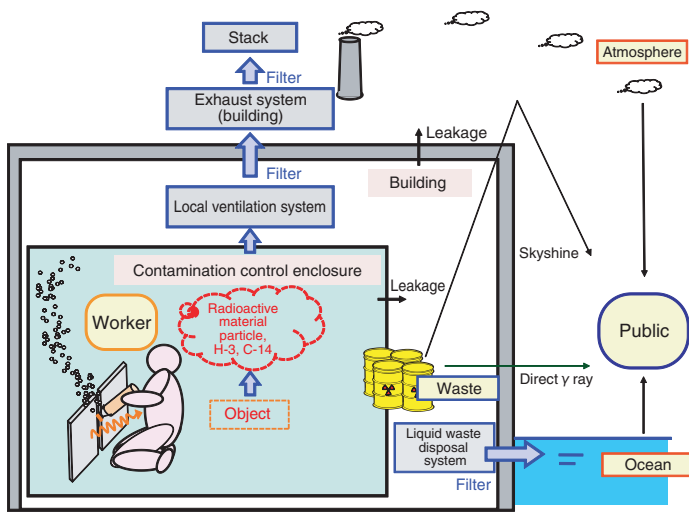


Fig.5-19 Pathways of radioactive materials to the environment for estimation of the public dose

Radioactive aerosols and vapors are dispersed into the work space through dismantling activities, and are then released or leaked to the atmosphere through filters and buildings, or released to the ocean through filters in the disposal system. The public exposure dose is evaluated considering various pathways, for example, the internal dose by inhalation of radionuclides in the air, the external dose from radionuclides on the ground surface, and the internal dose from the ingestion of food.

Aging or damaged nuclear facilities (e.g., Fukushima Daiichi NPS) should be decommissioned so as to ensure both engineering and radiological safety. Prior to the decommissioning process, a decommissioning plan, including a safety assessment for the public and the workers, is sent to the regulatory body for approval. The safety assessment requires the estimation of public and worker doses by considering various exposure pathways in normal and accidental situations during decommissioning, where the amounts of radioactive aerosols and vapors dispersed into the atmosphere and the ocean are calculated on the basis of the radioactive inventory, dismantling procedures, and schedule. A computer code system was developed for this safety assessment. A schematic illustration of the radionuclide pathway model used for normal situations is shown in Fig.5-19.

One of the most important parameters in the model is the radionuclide dispersion ratio to the air during the cutting of radioactive materials such as contaminated pipes. So far, the dispersion ratio has been obtained by experiments using non-radioactive pipes. To assess the existing data, we carried out cutting experiments using contaminated pipes, and confirmed

Table 5-2 Calculated results of collective dose to workers compared with actual dose

The calculated external dose agreed well with the actual dose using the actual working time and dose-rate distribution in the area. The dose from the removal of equipment in the reactor and turbine buildings showed a higher value than the actual one because all the contaminated equipment was assumed to be located near workers, for evaluation of the worst-case scenario.

Object	(in person-mSv)			
	External dose		Internal dose	
	Estimate	Actual	Estimate	Actual
Reactor internals	52.0	73.1	0	0
Reactor pressure vessel	103.9	82.7	0	0
RPV connected piping	95.8	63.2	0	0
Shielding concrete	31.9	27.3	0	0
Equipment (R. B.)	231.8	35.6	15.0	0
Equipment (T. B.)	5.7	0.6	4.3	0

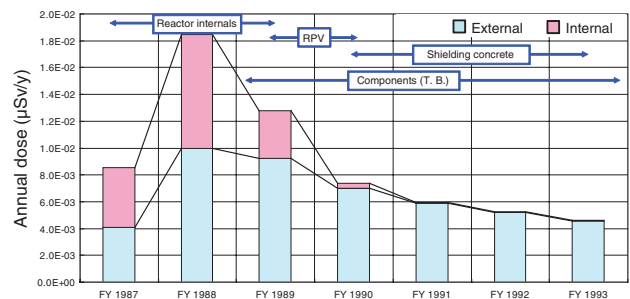


Fig.5-20 Calculation results for annual public dose during JPDR decommissioning project

The annual public dose is found to be negligibly low. After identifying several important pathways, the dose during the period of dismantling of the reactor internals is found to be dominant.

that the existing data gave reliable and conservative estimates.

The dismantling activities of the Japan Power Demonstration Reactor (JPDR) have yielded information available for dose assessment. We applied the safety assessment code to the dismantling of JPDR, and compared the calculated results with the actual data. Table 5-2 shows the external dose to workers. It is found that the calculated results agree well with the actual data. Fig.5-20 shows the calculated results of the annual public dose. The results show that the public dose is negligibly low, that the dose during the period of dismantling of the reactor internals is dominant, and also that most internal and external doses are attributed to the exposure of radionuclides released to the ocean or the ingestion of sea food. The internal dose of carbon-14 is due to the ingestion of agricultural crops.

The code will be continually applied to forthcoming decommissioning activities of nuclear facilities.

This study was funded by the Nuclear and Industrial Safety Agency (NISA) of the Ministry of Economy, Trade and Industry (METI).

Reference

Shimada, T., Sukegawa, T. et al., Development of Safety Assessment Code for Decommissioning of Nuclear Facilities (DecDose), Journal of Power and Energy Systems, vol.4, no.1, 2010, p.40-53.

For Evolution of Nuclear Science

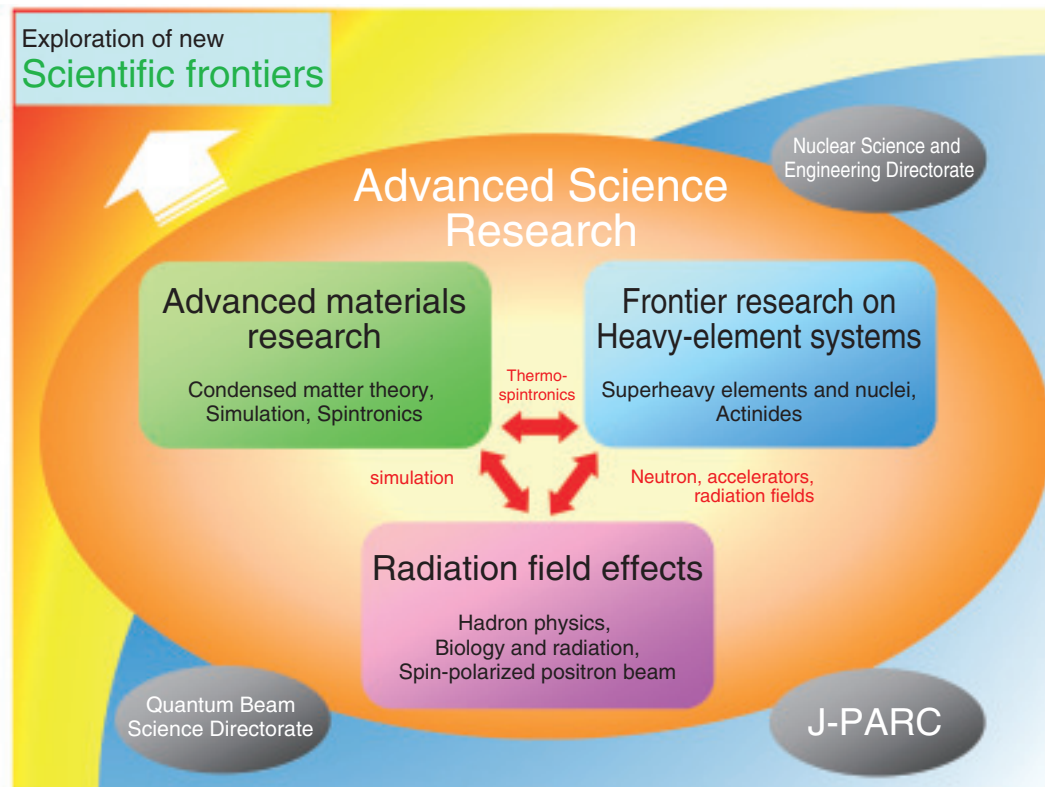


Fig.6-1 Exploration of new scientific frontiers with various collaborations

As the sole institute for atomic energy research in Japan, both basic and goal-oriented researches are within the scope of our mission. Nuclear engineering is supported by many fields of basic science and technology, and innovations in each research field would contribute to the evolution of nuclear engineering.

The purpose of Advanced Science Research Center is to promote cutting-edge researches on selected topics in basic sciences, which would enable the exploration of new frontiers in nuclear science.

“ASRC Visions” for the midterm starting April 2010 are to promote the most advanced basic research, to establish an international center of excellence (COE), and to create new research and technologies. The research projects being pursued can be categorized into three fields, i.e., basic research on advanced materials, frontier research on heavy-element systems, and basic research on radiation fields.

The research topics in the first research field include the development of molecular spin-transport materials and condensed matter theory. Frontier research in nuclear physics and characterization of superheavy elements, and on actinide compounds constitutes the second research field. The third field spans from hadron physics to biology. Collaboration among different research groups in ASRC and with other directorates is essential to explore the frontiers depicted in

Fig.6-1. The research highlights for 2010 are the discovery of an innovative mechanism for spin-flow creation, discovery of an unexpected fission behavior in Hg-180, and identification of anomalous electron scattering relevant to unconventional superconductivity in uranium compounds; these highlights are described in the following pages in detail.

For solving the problems caused by the accident at Fukushima Daiichi NPP, a biological method developed at ASRC has been applied.

For example, we have found the specific function of an organic acid released by microorganisms, which solubilizes the adsorbed metal ions on a mineral. New biotechnology utilizing such specific biological functions would be developed for the remediation of soils and plants contaminated by radionuclides (Fig.6-2).

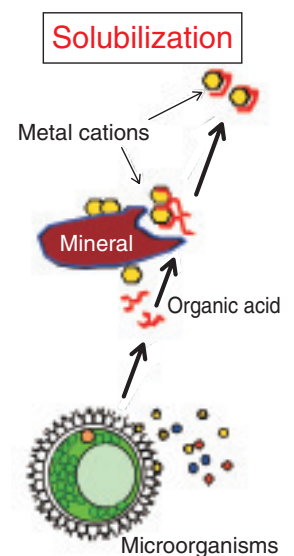


Fig.6-2 Solubilization of absorbed metal ions on minerals by organic acid

6-1 Magnetic Flow Turns Electronics into Spintronics

— Discovery of New Principles for Generating Spin Currents —

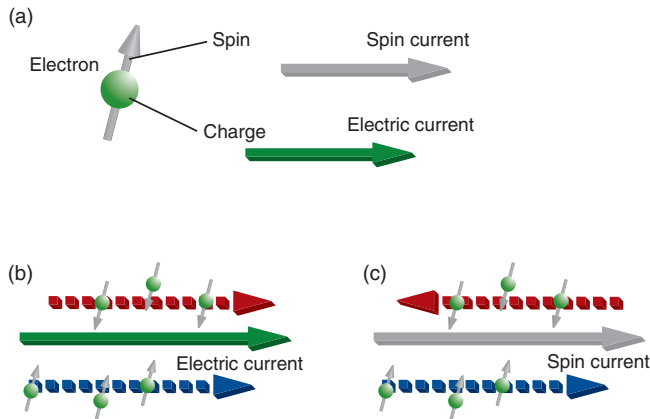


Fig.6-3 Electron's charge and spin

(a) A flow of charge leads to an electric (charge) current, whereas a flow of spin leads to a spin current. (b) An ordinary electric current consists of an equal number of up- and down-spin electrons, leading to zero net spin current. (c) Generation of spin currents requires an ingenious method to create a “counter flow” of the up and down spins.

Electronics is indispensable in our daily life in the information society. As the next-generation technology, “spintronics” has attracted global interest. We have devised new methods for generating “magnetic flow,” which is the main ingredient of spintronics^{[1]-[3]}.

As the name implies, electronics is the art of controlling electrons in solids. The electron has two aspects: “charge” and “spin” (Fig.6-3). The charge is the origin of electricity, and its flow leads to an electric (charge) current. On the other hand, the spin gives rise to magnetism and its flow is called spin current. To date, developments in the field of electronics have been based solely on charge currents. Spintronics aims to improve the current technology by harnessing both the currents equally. It has been recognized, however, that it is quite a hard task to utilize spin currents, unlike the case of charge currents. In this context, we have discovered new principles for generating spin currents.

First, we have found that a spin current can be generated by producing a temperature gradient in a magnetic insulator^[1]. The thermally induced spin current is converted to

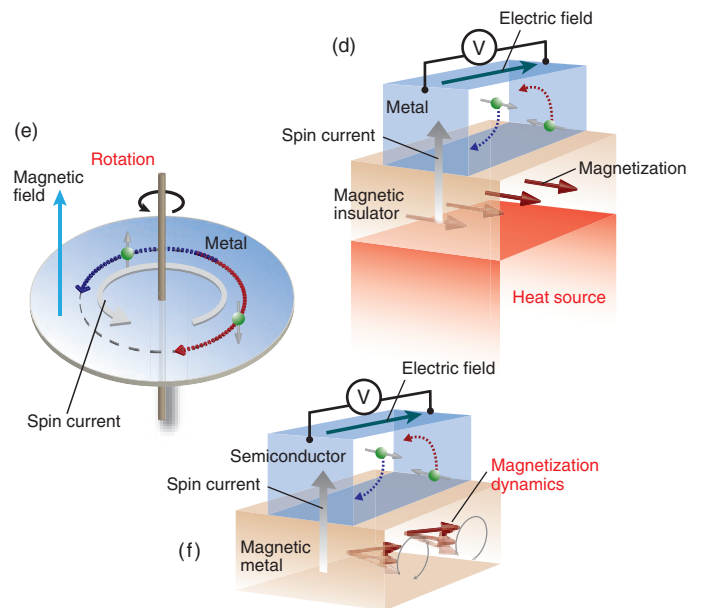


Fig.6-4 New methods for generating spin currents

(d) Heating a magnetic insulator produces a spin current along with heat flow. The spin current is converted to electric power in an attached metal. (e) In a rotating metallic disk in a magnetic field, a spin current is generated around the axis of rotation. (f) Ferromagnetic resonance of a magnet injects a spin current into the adjacent semiconductor with high efficiency.

an electric current via the inverse spin Hall effect in an attached metal (Fig.6-4(d)). This finding can facilitate the development of new architecture for thermoelectric devices.

Second, we theoretically predict that a rotating body (Fig.6-4(e)) can produce a spin current, by combining general relativity and quantum mechanics^[2]. This finding opens up opportunities for the direct conversion of quantum mechanical rotation into its classical counterpart, which can lead to inventions of nanoscale motors.

Third, using magnetization dynamics induced by ferromagnetic resonance (Fig.6-4(f)), we have succeeded in injecting spin currents into semiconductors with a very high efficiency (10^3 times larger than before)^[3]. Since semiconductors are basic materials for conventional electronic devices, the impact of this finding on the spintronics community is astonishingly large.

A variety of such high-efficiency methods of spin current generation can contribute to the advancement of basic science, which is necessary for building an energy-saving society in the near future.

References

- [1] Uchida, K., Ieda, J. et al., Spin Seebeck Insulator, *Nature Materials*, vol.9, no.11, 2010, p.894-897.
- [2] Matsuo, M., Ieda, J. et al., Effects of Mechanical Rotation on Spin Currents, *Physical Review Letters*, vol.106, issue 7, 2011, p.076601-1-076601-4.
- [3] Ando, K., Takahashi, S., Ieda, J. et al., Electrically Tunable Spin Injector Free from the Impedance Mismatch Problem, *Nature Materials*, vol.10, no.9, 2011, p.655-659.

6-2 Detection of Electron Spins in Ferromagnets Using Spin-Polarized Positron – Development of Highly Spin-Polarized Positron Beam –

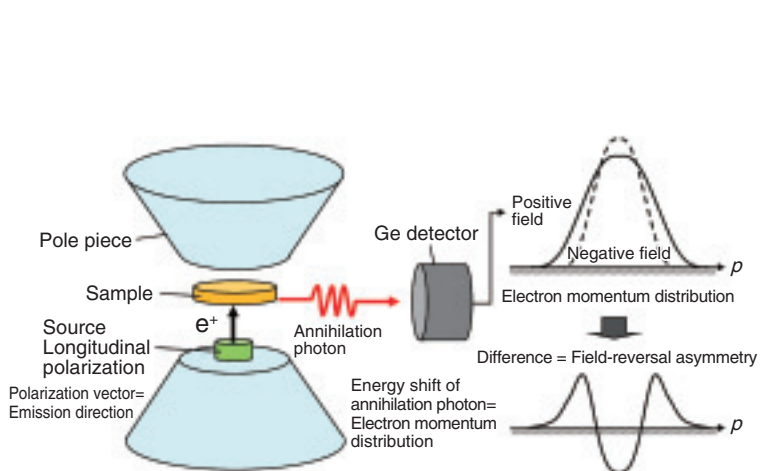


Fig.6-5 Schematic diagram of annihilation radiation spectrum measurements

Longitudinally polarized positrons from the source are implanted into the magnetized sample, and annihilation photons are detected by the Ge detector. The energy shift of the annihilation photon corresponds to the electron momentum distribution in ferromagnets.

Conventional electronic devices are based on electric current flow. Recently, so-called spintronics devices based on electron spins have been extensively studied. It is desirable for the development of new methods for the investigation of electron spins to accompany discoveries of novel spin-related phenomena. We are currently trying to obtain a highly spin-polarized positron beam for use as a probe for studying spin-related phenomena.

Although it was very difficult to polarize positrons, we focused on highly spin-polarized positrons emitted from a ^{68}Ge - ^{68}Ga source. In this study, we produced a ^{68}Ge - ^{68}Ga source through proton bombardment and used it for the investigation of the spin states of ferromagnets. Fig.6-5 shows a schematic diagram of annihilation radiation spectra measurements performed by using the highly spin-polarized positron source developed in this study. The annihilation photon was emitted when the spin-polarized positrons were annihilated with the excess electron spin in the ferromagnets in a magnetic field. The energy of the annihilation photon was Doppler shifted because of electron motion. Spin-up

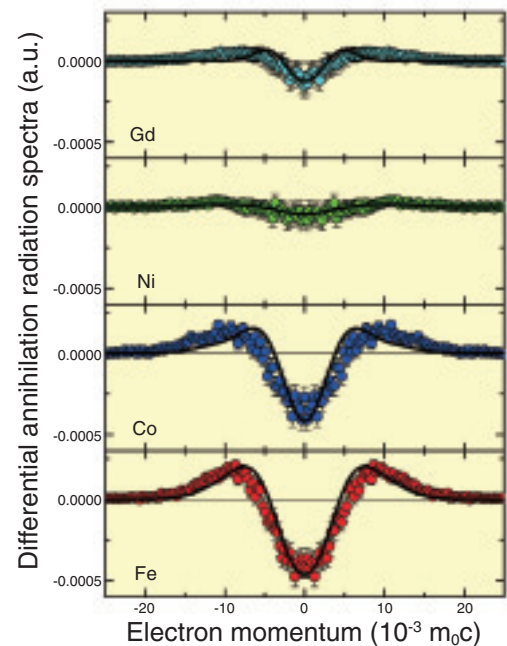


Fig.6-6 Differential annihilation radiation spectra of Fe, Co, Ni, and Gd samples

The measured annihilation radiation spectra (open circles) can be well reproduced through calculations (solid lines).

positrons preferentially annihilate with spin-down electrons. The electron-spin polarization of ferromagnets can be changed by magnetic field reversal. Thus, the annihilation radiation spectra are modulated upon magnetic field reversal. To highlight this change, the differential annihilation radiation spectra under positive and negative magnetic fields are displayed in Fig.6-6. We found a clear magnetic field effect on the annihilation radiation spectra. We also found that the strength of the magnetic field effect on the spectrum is related to the effective magnetization. Thus, spin-polarized positron annihilation will be useful for the study of the electron spin state associated with ferromagnets.

In the near future, we intend to work toward producing an energy-tunable highly spin-polarized positron beam. We intend investigating spin-related phenomena near surfaces, such as the spin-Hall effect. Positron annihilation spectroscopy is a powerful technique for detecting vacancy defects. Further, spin-polarized positron annihilation spectroscopy can also be used for the study of vacancy-induced magnetism.

Reference

Kawasuso, A., Fukaya, Y. et al., Spin-Polarized Positron Annihilation Measurements of Polycrystalline Fe, Co, Ni, and Gd Based on Doppler Broadening of Annihilation Radiation, *Physical Review B*, vol.83, issue 10, 2011, p.100406-1-100406-4.

6-3 Discovery of a New Type of Fission

– The Fission of ^{180}Hg is not Influenced by Shells of Fragments –

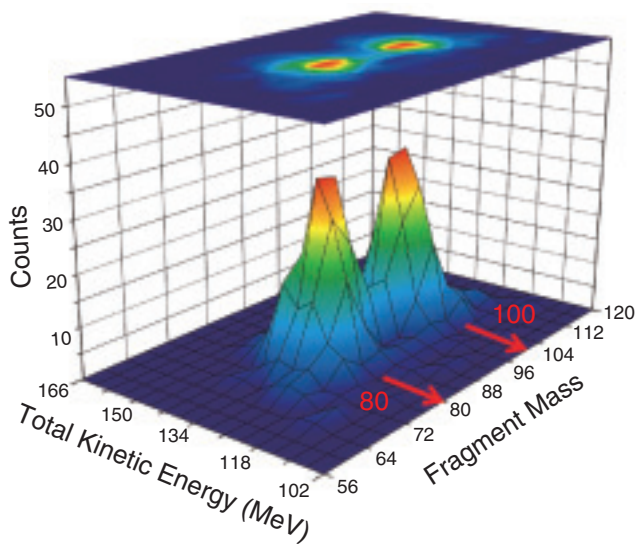


Fig.6-7 Fission properties of ^{180}Hg

The number of registered fission fragments as functions of the mass and total kinetic energy (sum of the kinetic energies of both fragments). Fission fragments with mass numbers of 80 and 100, corresponding to ^{80}Kr and ^{100}Ru , respectively, have the most abundant yield.

When the phenomenon of nuclear fission was discovered, a nucleus was modeled to be a liquid drop with a charge and fission was considered to occur when a nucleus overcomes the fission barrier (saddle point). This classical model, however, cannot explain some features such as mass asymmetry in the neutron-induced fission of ^{235}U . Therefore, the effects of the energy levels of the protons and neutrons in a nucleus were taken into account. A nucleus with a closed-shell structure has high binding energy and thus a low mass (energy). The fission proceeds in such a manner that nuclei with closed-shell structures are preferentially formed to have the smallest energy at the end of nuclear rupture. In the neutron-induced fission of ^{235}U , one fragment is preferentially formed in the vicinity of ^{132}Sn , which has the closed proton and neutron shells. The other is the complementary fragment. The effects of the ^{132}Sn nucleus on fission have been observed in the fissions of the actinide nuclei.

In this study, our aim was to see if the present fission model can explain the fission of nuclei that are more unstable than ^{235}U . We chose ^{180}Hg as the proton-rich nucleus and for the first time, conducted an experiment to study the fission properties in such a light-nucleus region. According to the

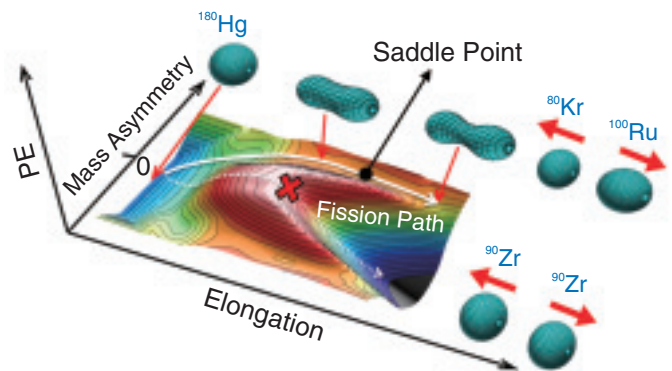


Fig.6-8 Fission path of ^{180}Hg

Potential energy (PE) of ^{180}Hg is calculated as a function of the elongation and mass asymmetry. Mass asymmetry is observed at the saddle point. The calculation for such a light-element system was carried out for the first time.

present knowledge, two ^{90}Zr isotopes should be produced because ^{90}Zr has a closed neutron shell. The experimental result, however, revealed that the most dominant masses were 80 and 100, as shown in Fig.6-7, which suggested the production of ^{80}Kr and ^{100}Ru . The yield of ^{90}Zr was significantly small. ^{180}Hg underwent the new type of fission, and it was not regulated by shells of the fragments.

Fig.6-8 shows the potential energy of ^{180}Hg , calculated for the first time as a light element to understand how the fission proceeds on the nuclear-shape. Because of the high fission barrier at the mass-symmetry, the symmetric fission fragments ^{90}Zr are not produced (dotted curve in Fig.6-8). On the other hand, in the case of mass asymmetry, the saddle point appears at a low barrier height, which can be easily overcome to yield mass-asymmetric fission fragments (solid curve in Fig.6-8).

Fission of unstable nuclei provides information about the level structures of the protons and neutrons for the extremely elongated nuclear shape. Understanding the structure will help improve the fission model for evaluating nuclear data and studying the reaction between heavy ions.

Reference

Andreyev, A.N., Nishio, K. et al., New Type of Asymmetric Fission in Proton-Rich Nuclei, Physical Review Letters, vol.105, issue 25, 2010, p.252502-1-252502-5.

6-4 Unconventional Superconductivity in Uranium Compounds

— Correlation between the Anomalous Electron Scattering and Superconductivity in URu₂Si₂ —

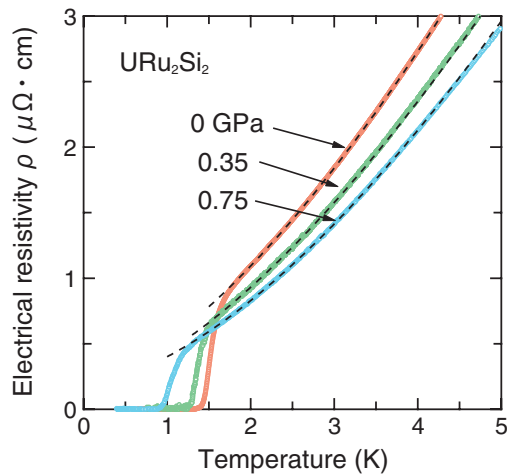


Fig.6-9 Temperature dependence of the electrical resistivity ρ in URu₂Si₂ at 0, 0.35, and 0.75 GPa

1 GPa corresponds approximately to 10000 atm. The steep decrease in ρ below 1.5 K is due to the superconducting transition in URu₂Si₂. The dotted lines show the results of fitting the data with the theoretical equation.

Superconductivity (SC) is a macroscopic quantum mechanical phenomenon. In conventional metals such as lead, two electrons are bound together by lattice vibrations in the superconducting state; however, lattice vibrations may not play an important role in the formation of superconducting pairs of electrons in strongly correlated electron systems such as copper oxides or heavy fermion compounds. The physical properties of SC in these systems differ from those in conventional superconductors.

SC of the uranium compound URu₂Si₂ has attracted much attention because of the novel superconducting properties of URu₂Si₂. SC is strongly related to the electronic state of an unknown ordered phase. The nature of this ordered phase has not been determined for more than 25 years. The only information available is that symmetry breaking of the electronic state occurs in the ordered phase. This phase is known as “hidden order.”

We measured the electrical resistivity ρ in URu₂Si₂ at high pressures, since the electronic property of the ordered state is reflected through the scattering of electrons. For example, the usual electron-electron scattering gives the T^2 term in the

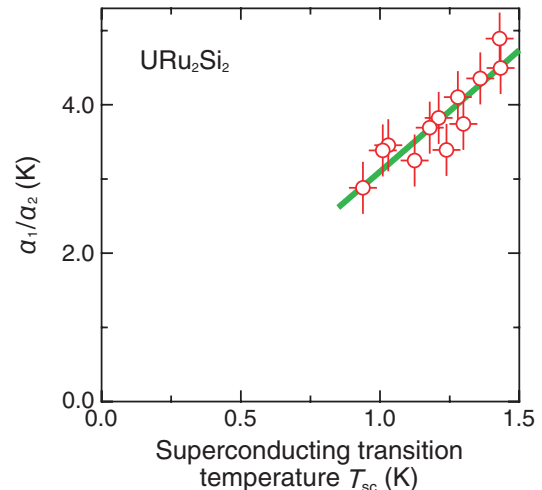


Fig.6-10 Analysis of the resistivity in URu₂Si₂ at high pressures

Relation between the superconducting transition temperature T_{sc} and α_1/α_2 . The red line at each data point denotes the error bar.

resistivity. We focus on the effects of pressure on the superconducting transition temperature T_{sc} and the electrical transport. As shown in Fig.6-9, the value of T_{sc} decreases with increasing pressure. We analyze the temperature dependence of ρ using the expression $\rho = \rho_0 + \alpha_1 T + \alpha_2 T^2$. We assume that ρ is the sum of the T -linear resistivity related to the unusual scattering of electrons and the usual T^2 -term. We determine the pressure dependencies of α_1 and α_2 from the fit of the data with the expression, shown by the dotted lines in Fig.6-9.

α_1/α_2 and T_{sc} are suggested to have a linear relation, as shown in Fig.6-10. The pressure dependence of α_2 is very weak; hence, the value of T_{sc} depends primarily on the coefficient α_1 . This suggests a strong correlation between and a common origin for anomalous electron scattering and SC. This finding is the basis for further studies on the hidden and SC states in URu₂Si₂.

Electrons in actinide compounds also exhibit many interesting physical phenomena. We will continue to search a new concept to understand these phenomena.

Reference

Tateiwa, N. et al., High-Pressure Electrical Resistivity Measurement on Heavy Fermion Superconductor URu₂Si₂ Using Super Clean Crystal, Journal of Physics: Conference Series, vol.273, no.1, 2011, p.012087-1-012087-4.

6-5 Biological Nanoparticle Production Factory — Recovery of Heavy Elements by Using Microorganisms —

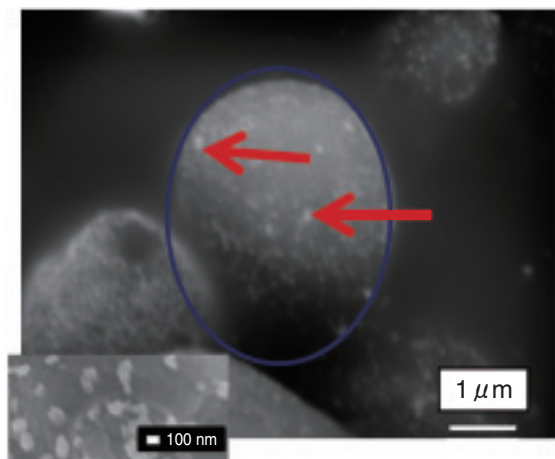


Fig.6-11 SEM photograph of yeast after exposure to cerium ions in aqueous solution for four days

Blue ellipse shows a yeast cell. Nanoparticles that contain cerium and phosphorous and that are formed on the cell surface are shown by red arrows. The lower left figure shows a magnified image of the nanoparticles.

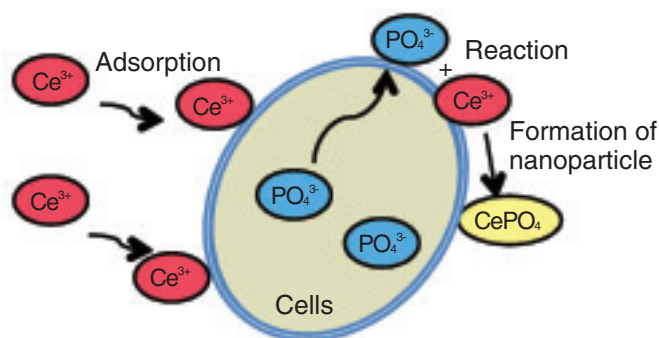


Fig.6-12 Nanoparticle formation mechanism on cell surface of microorganism

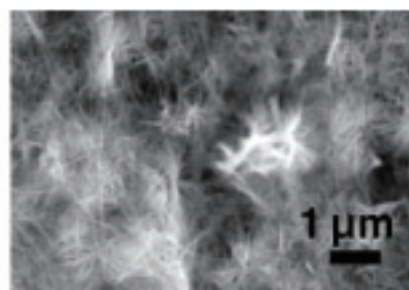


Fig.6-13 Cerium phosphate precipitates formed abiotically in aqueous solution

For the metabolism, microorganisms possess various functions. Unfortunately, only a limited number of biological functions have been elucidated so far. A new biological function of a microorganism may be found by using heavy elements that are not essential elements.

We tested yeast *Saccharomyces cerevisiae* after exposing it to cerium ions in an aqueous solution. The concentration of cerium ions decreased with increasing exposure time, while the concentration of phosphorous increased. Electron microscopy analysis showed that many nanoscale particulates, including cerium and phosphorous, were produced on the cell surface (Fig.6-11). Since phosphorous ions were not added to the solution, the cerium ions adsorbed on the cell surface reacted with the phosphorous ions discharged from the yeast cell, and nanoparticles (Fig.6-12) were formed. Electron diffraction analysis showed that the nanoparticles formed were of monazite (CePO_4), which is a rare-earth-element phosphate mineral. Although cerium phosphate was precipitated in a solution containing cerium ions and phosphoric acids in

an abiotic system, the size and shape of the precipitates differed from those of the precipitates formed on the yeast cell surface (Fig.6-13). Therefore, it can be said that the yeast cell functioned like a factory that produces nanoparticles of cerium phosphate. The production of nanoparticles on the cell surface of a microorganism is a new development in biotechnology, and it differs drastically from conventional engineering techniques.

We consider the microbial cell surface to be a reaction field where the heavy metal ions outside the cell react with the essential elements released from the interior of the cell. It is thought that a microorganism will be capable of not only collecting heavy elements but also isolating a specific element from others. The biological techniques for the accumulation and selection of metal ions will be applied to the recovery and separation of actinides in the nuclear fuel reprocessing process and to the development of a mathematical model for estimating the migration of actinides in groundwater.

Reference

Jiang, M., Ohnuki, T. et al., Biological Nano-Mineralization of Ce Phosphate by *Saccharomyces Cerevisiae*, Chemical Geology, vol.277, issues 1-2, 2010, p.61-69.

Establishment of Basis for Nuclear Energy R&D, and Development of Innovative Technology

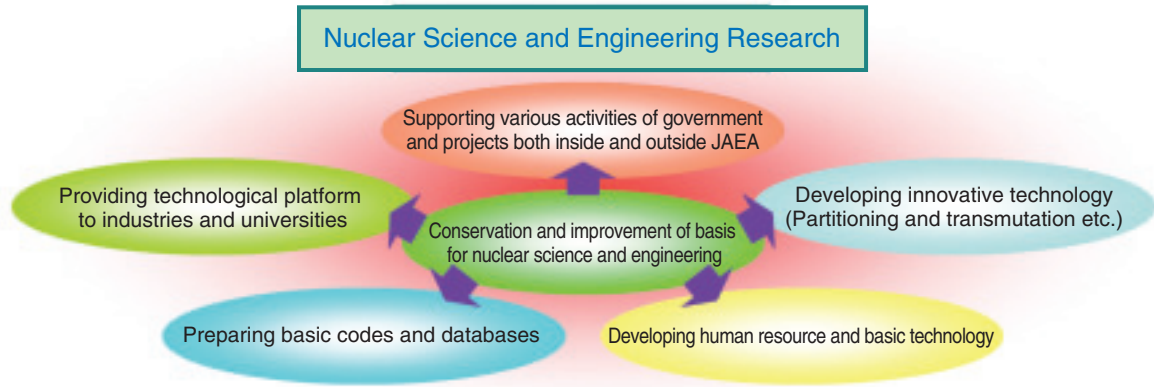


Fig.7-1 Roles of nuclear science and engineering research

Nuclear science and engineering research is aimed at the promotion of research, development, and utilization of nuclear power through the various activities shown in Fig.7-1. To this end, research is being conducted in the areas of nuclear data and reactor engineering, fuel and material engineering, and environment and radiation science. Joint research with industry and academia is also being promoted via the Nuclear Engineering Research Collaboration Center (NERCC).

In the area of nuclear data and reactor engineering, cutting-edge theories are being developed and experiments and computational simulations are being performed to contribute to the design and development of nuclear systems. R&D on partitioning and transmutation technology is also being conducted to mitigate difficulties in the management of long-lived nuclear wastes.

In the area of fuel and material engineering, basic research on innovative nuclear fuel cycles and materials is being promoted. In particular, emphases are put on research on the fuel behavior in nuclear reactors, separation processes for high-level waste, and mechanisms of material damage in nuclear reactors and reprocessing plants.

In the area of environment and radiation science, research on environmental behavior of radionuclides and dose assessment is being conducted. Moreover, R&D of microanalytical techniques for the nonproliferation of nuclear materials and removal techniques for environmentally harmful materials is also being carried out.

Collaborative activities with the industry include the development of a production technique for medical radioisotopes using an accelerator-driven neutron source; this collaboration is currently under way. Basic data for waste vitrification are also being collected to contribute to the successful operation of a reprocessing plant.

On the basis of the scientific and engineering basis consolidated so far, we are contributing to the recovery of the Fukushima Daiichi Nuclear Power Station run by the Tokyo Electric Power Company, Incorporated, and to the environmental restoration of contaminated land. We have estimated the radioactivity released from the plant on the basis of analyses using Worldwide Version of System for Prediction of Environmental Emergency Dose Information (WSPEEDI) (Fig.7-2). Radiological analysis of contaminated water and

soil is also being carried out. Moreover, a decontamination technique is being developed to reduce the dose rate of the contaminated land (Fig.7-3).

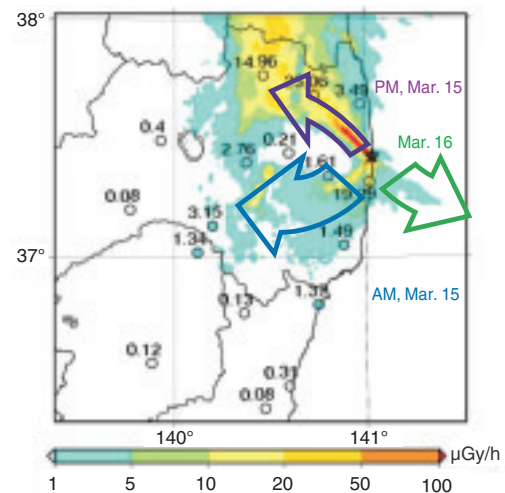


Fig.7-2 Analytical result obtained by using WSPEEDI

This is an estimated result for the behavior of radioactive nuclides from March 15 to 16, 2011. The high dose rate in the northwest direction from the plant (☆) can be explained by this analysis.



Fig.7-3 Soil solidification technique using polyions

The spraying of a resinous polyion complex on contaminated land and its removal after solidification along with the surface soil (since cesium is concentrated on the surface of the land) can be expected to facilitate effective decontamination.

7-1 Nuclear Polarization Controlled by a Laser Beam

— Dynamic Nuclear Self-Polarization Induced by Circularly Polarized Light —

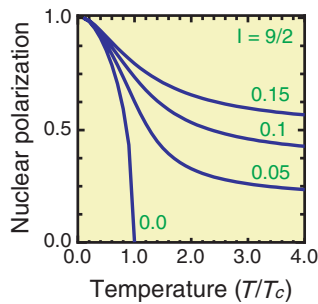


Fig.7-4 Temperature dependence of nuclear polarization
The spin of the lattice nuclei is assumed to be $I = 9/2$. The numbers beside the curves are the values of the parameters (α) relevant to conduction-electron polarization. When $|\alpha| > 0$, the lattice nuclei are polarized even at temperatures above the critical temperature ($T/T_c > 1$).

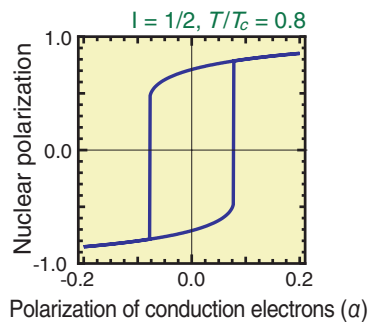


Fig.7-5 Hysteresis loop of nuclear polarization
The abscissa is the parameter α relevant to conduction-electron polarization. The spin of the lattice nuclei is assumed to be $I = 1/2$.

Nuclear magnetic moment, one of the important parameters that help in understanding the structure of nuclei, is often measured using NMR techniques. However, in this case, the nuclei under study require to be polarized. While various methods of nuclear polarization have been developed, there is no versatile method available. In order to carry out systematic studies on the nuclear structures of short-lived neutron-rich isotopes such as In, we are developing a method for nuclear polarization by applying a technique called dynamic nuclear self-polarization (DYNASP).

DYNASP was theoretically predicted by Dyakonov et al. This phenomenon is observed in type III-V semiconductors when electrons are excited to the conduction band by linearly polarized light. The lattice nuclei are self-polarized through the contact hyperfine interaction between the electrons and the lattice nuclei. A large nuclear polarization suddenly occurs below the critical temperature (T_c). We have generalized the DYNASP theory by taking into account the conduction electrons polarized by circularly polarized light. We have found that circularly polarized light enhances

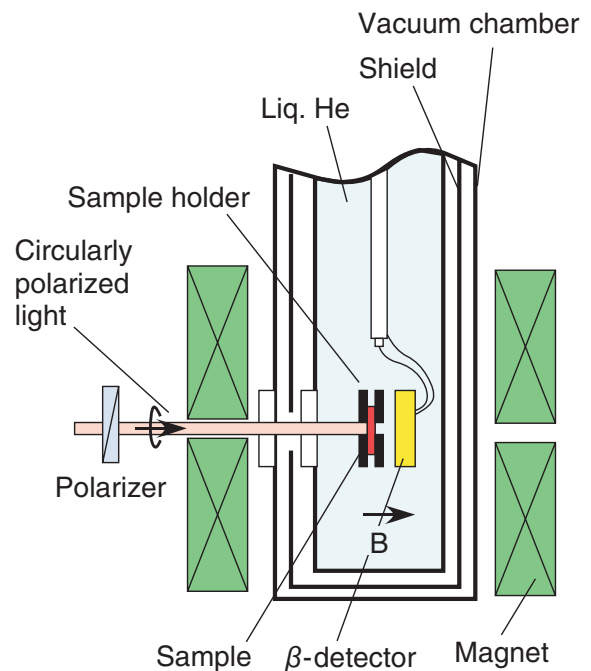


Fig.7-6 Schematic experimental setup for studying DYNASP
A laser beam is injected from the left hand windows. β -rays emitted from a neutron-activated sample are measured. When the lattice nuclei of the sample are polarized, anisotropy of the β -ray emission can be seen.

nuclear polarization, thus increasing the sensitivity of the NMR measurements. Fig.7-4 shows the temperature dependence of the nuclear polarization. When the conduction electrons are not polarized ($\alpha=0$), a large nuclear polarization is observed only at temperatures below T_c , and the polarization vanishes above T_c . When the conduction electrons are polarized ($|\alpha|>0$), nuclear polarization occurs even above T_c . Another interesting feature of DYNASP has been revealed by using circularly polarized light; nuclear polarization shows a hysteresis, illustrated in Fig.7-5. The hysteresis enables easy control of the direction of the nuclear polarization by adopting an optical method.

To examine the DYNASP phenomenon, we are preparing an apparatus, which is shown in Fig.7-6. Once the generalized DYNASP is confirmed, we will apply the technique to magnetic moment measurements. A combination of the DYNASP technique with NMR techniques is expected to be useful in semiconductor studies and in applications such as quantum computing.

Reference

Koizumi, M. et al., Dynamic Nuclear Self-Polarization with Circularly Polarized Light, Journal of Applied Physics, vol.110, issue 1, 2011, p.013911-1-013911-8.

7-2 Simulated Melting and Solidification of Metal

— Extension of Mechanistic Liquid-Gas Two-Phase Flow Analysis Method —

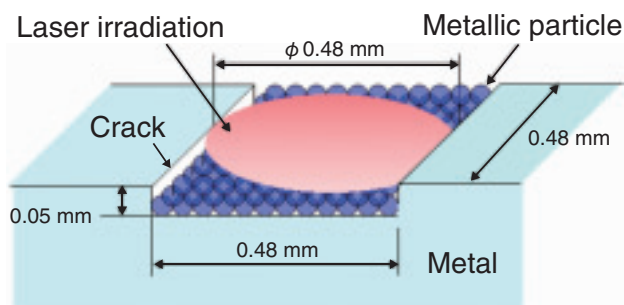
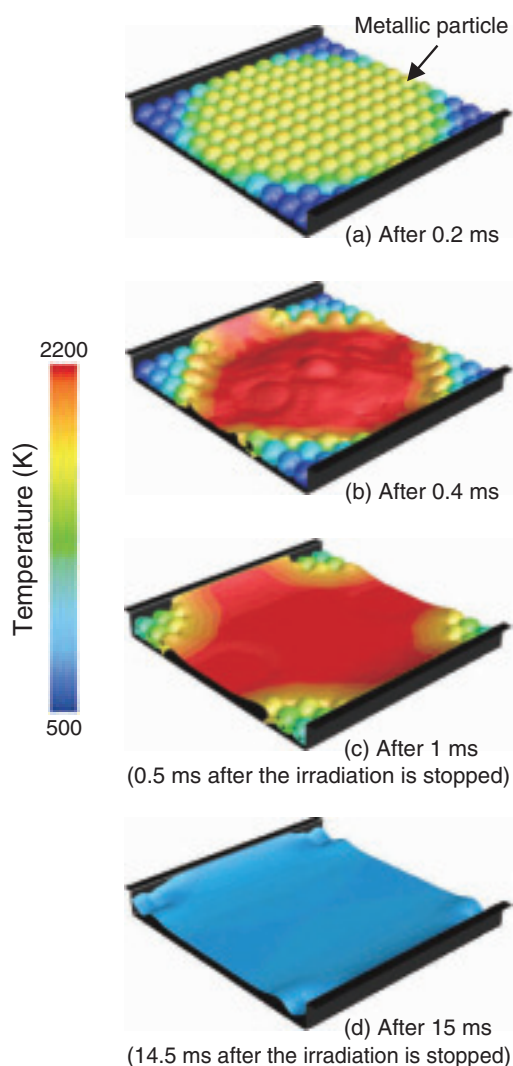


Fig.7-7 An example of crack repair using laser welding
Laser is irradiated roundly toward metallic particles from the upper part of the crack ($0.48 \times 0.48 \times 0.05$ mm), as can be seen in red. A diameter of one metallic particle is 0.04 mm. Irradiation causes the metallic particles to melt. After the laser irradiation is stopped, the temperature of the liquid metal decreases gradually. The crack is sealed when the liquid metal completely becomes hard.

Fig.7-8 Time variations of the predicted temperature distribution in the crack

Upon laser irradiation, (a) the temperature of the metallic particles rises in the circular domain in which the laser is irradiated; (b) the metallic particles melt after the temperature reaches their melting temperature, and the laser irradiation is stopped 0.5 ms after the irradiation started; (c) the metallic particles outside the circular domain melt from the residual heat and become liquid, and the temperature falls gradually; finally, (d) solidification of the liquid metal takes place.



As a part of the development of a repair technique based on laser welding for nuclear power plants, we are developing a three-dimensional numerical analysis method to simulate the melting and solidification of metals by fiber-laser irradiation.

The outline of the laser welding process is shown in Fig.7-7. As an example, when a crack is detected on the outer surface of a pressure vessel in a nuclear power plant, minute metallic particles are first sprayed on it, and then the particles are melted by using a laser so that they seal the crack. Finally, the outer surface of that can be repaired.

In order to enable the laser welding simulation, a mechanistic liquid-gas two-phase flow analysis method which has already developed is extended for simulating the phase change between the liquid and solid phases, on the basis of the melting and solidification temperatures of the metal. In the present analysis, the laser output 160 W is

irradiated roundly up to 0.5 ms to the minute metallic particles as shown in Fig.7-7.

Fig.7-8 shows the predicted temperature distributions in a crack. (a) The temperature of the metallic particles increases in the circular domain irradiated by the laser; (b) the metallic particles melt when the temperature reaches their melting temperature, and the irradiation is stopped 0.5 ms from the start; (c) the metallic particles outside the circular domain melt because of the residual heat, and the temperature decreases gradually with time; finally, (d) solidification of the melted metallic particles occurs.

The present numerical analysis is indispensable and can be used as a substitute for similar experiments. This research has received high evaluation from the related societies, such as winning a best paper award at the International Symposium on Visualization in Joining & Welding Science through Advanced Measurements and Simulation (Osaka, 2010).

Reference

Takase, K. et al., Numerical Visualization on Melting and Solidification of Micron-Sized Metallic Particles by Laser Irradiation, *Yosetsu Gakkai Ronbunshu* (Quarterly Journal of the Japan Welding Society), vol.29, no.3, 2011, p.43s-47s.

7-3 Approach for Realization of Transmutation Technology — Issues Pertaining to Reactor Design for Accelerator-Driven System —

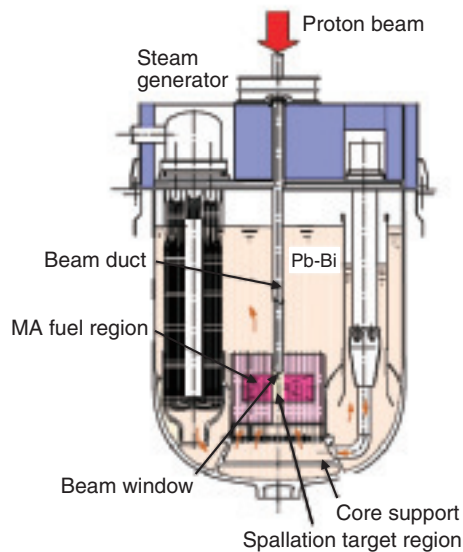


Fig.7-9 Conceptual diagram of ADS
Spallation neutrons generated by protons in the spallation target region are used to transmute MAs.

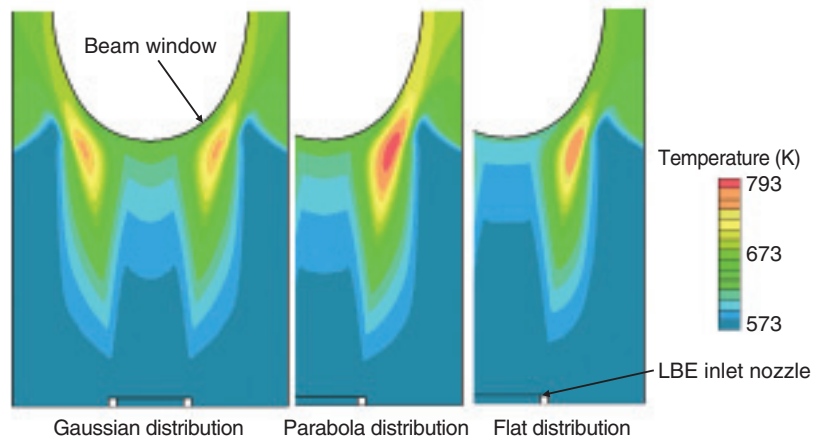


Fig.7-10 Temperature distribution in LBE spallation target region
Heat generation in the spallation reaction is one of the key factors to be considered for the beam window design. In this study, we changed the distribution of the incident proton current density to reduce the thermal stress and aimed to create a feasible design.

To reduce the burden of high-level waste (HLW) disposal, the transmutation technology has been investigated. This technology would reduce the decay time of the potential toxicity of the HLW from several tens of thousands of years to several hundred years and reduce the area required for a geological repository. An Accelerator-Driven System (ADS), which is a combination of an accelerator and a sub-critical core (Fig.7-9), has been studied for the purpose of transmuting minor actinides (MAs) in the HLW.

Since the ADS is a hybrid system of an accelerator and a sub-critical core, there are many inherent issues. In particular, the following issues relating to the reactor design are important from the viewpoint of the feasibility of the ADS: (1) nuclear design accuracy and (2) design of a beam window, which is the boundary between the accelerator and the sub-critical core.

For nuclear design accuracy, it is expected that calculation results for MA transmutation systems include a large uncertainty because MA nuclear data have large errors owing to the lack of experimental data. We estimated the uncertainty in the ADS calculation result by using the covariance data prepared in the nuclear data^[1]. We confirmed that the uncertainty in the ADS nuclear design was larger than that in

the existing fast reactor nuclear design. We also found that the uncertainty could be reduced by up to 40% by performing integral experiments with MAs with a mass on the order of kilograms.

The feasibility of the beam window is one of the critical issues because the beam window would be used under the following severe conditions: heat generation by protons, corrosion of the lead-bismuth eutectic (LBE), and irradiation damage caused by neutrons and protons. We aimed to create a feasible concept for the beam window by performing calculations pertaining to proton and neutron transport, and thermal-hydraulic and structural analyses. The calculation results showed that the following conditions would be the most feasible under the current design conditions: an elliptical beam window made of T91 steel and a parabolic distribution for the incident proton beam current density (Fig.7-10)^[2].

Research and development of the ADS is in the basic research stage. We are investigating not only the reactor design but also the material, accelerator, and thermal-hydraulic system by collaborating with other foreign laboratories.

References

- [1] Sugawara, T. et al., Analytical Validation of Uncertainty in Reactor Physics Parameters for Nuclear Transmutation Systems, *Journal of Nuclear Science and Technology*, vol.47, no.6, 2010, p.521-530.
- [2] Sugawara, T. et al., Conceptual Design Study of Beam Window for Accelerator-Driven System, *Journal of Nuclear Science and Technology*, vol.47, no.10, 2010, p.953-962.

7-4 Change in Fuel Microstructure Induced by Helium Accumulation and Release

— Expansion and Annealing Correlation for Lattice and Bulk —

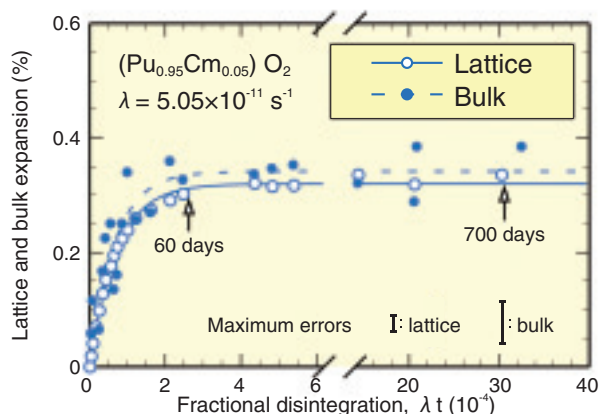


Fig.7-11 Lattice and bulk expansion at room temperature as a function of fractional disintegration

After the saturation at $\approx 0.03\%$ disintegration, no more expansion was observed with increasing He accumulation.

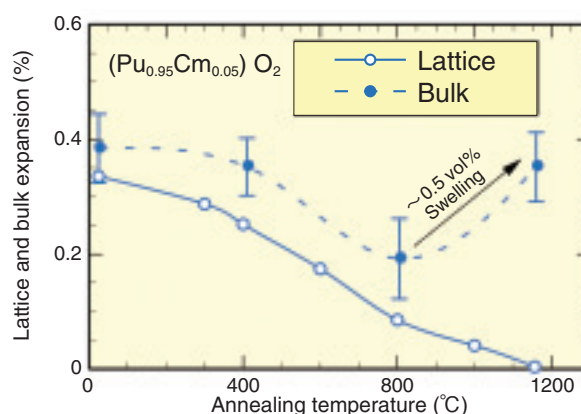


Fig.7-12 Thermal recovery of lattice and bulk as a function of annealing temperature

The diffusion of accumulated He to grain boundaries proceeded above $800\text{ }^{\circ}\text{C}$, and a swelling of $0.5\text{ vol}\%$ was observed in the pellet specimen upon annealing at $1160\text{ }^{\circ}\text{C}$.

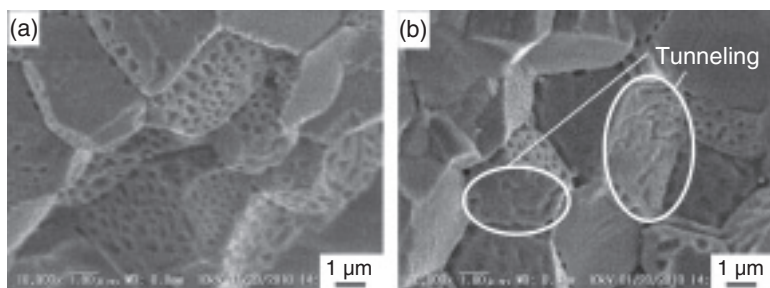


Fig.7-13 SEM images of the fracture surface of a (Pu, Cm) O_2 pellet annealed at $1160\text{ }^{\circ}\text{C}$

(a) Traces of He gas bubbles ($100\sim 200\text{ nm}$) are distributed along the grain boundaries.

(b) Some of these are connected to form tunnels as a gas-release path. No bubbles are observed on the intragranular surfaces.

We have been studying fundamental technologies for minor actinides (MAs) recycling based on the fast breeder reactor (FBR) and U-Pu mixed oxide fuel containing MAs (MA-MOX). In such fuel pellets, the accumulation of point defects and helium (He) induced by α -decay proceeds rapidly during fuel storage after fabrication, since the relatively short-lived nuclides represented by ^{238}Pu , ^{241}Am , and ^{244}Cm are included. Lattice expansion due to self-irradiation damage is a well-known phenomenon. However, the bulk expansion of sintered pellets is not well understood. In addition, the accumulated He may be released as gas at high temperatures when the fuel is loaded into the reactor. Possible changes in the fuel-pellet microstructure should also be investigated.

In this work, a sintered specimen of (Pu, Cm) O_2 containing 5 mol% Cm as the main helium source was prepared as a simplified form of MA-MOX pellet. The following experiments were performed to obtain the fundamental data concerning self-irradiation damage and He accumulation/release. Fig.7-11 shows the lattice and bulk expansion induced by the self-irradiation damage as a function of fractional disintegration (defined by the product of the decay constant and storage time). From the similar expansion curves, it is found that the main factor in bulk expansion is the lattice expansion due to

point-defect accumulation.

After He accumulation corresponding to 0.3% disintegration (≈ 700 days), the thermal recovery of the lattice and bulk was compared in the temperature range up to $1160\text{ }^{\circ}\text{C}$; the results are shown in Fig.7-12. While the lattice parameter recovers to the value for the undamaged sample, the pellet exhibits swelling during annealing at $1160\text{ }^{\circ}\text{C}$. The fracture surface of the annealed pellet was observed by scanning electron microscopy (SEM) to confirm any change in the microstructure. The SEM images are shown in Fig.7-13. The traces of gas bubbles are closely distributed along the grain boundaries; these are very similar to the typical fission gas bubbles observed in high-burnup oxide fuel pellets. According to these experimental results, it is found that the helium gas swelling of an MA-MOX fuel pellet could occur at a very early stage of the burning. We will obtain quantitative data concerning the He behavior, e.g., the diffusion coefficient and the influence of He release on the pellet sintering process.

The present study was from the project "Development of common and fundamental technologies on the evaluation of nuclear fuel behavior for realizing MA recycling" entrusted by the Ministry of Education, Culture, Sports, Science and Technology of Japan (MEXT).

Reference

Takano, M. et al., Annealing Behavior of (Pu,Cm) O_2 : Lattice and Bulk Expansion from Self-Irradiation Damage, Journal of Nuclear Materials, vol.414, issue 2, 2011, p.174-178.

7-5 Great Challenge of Separation of Minor Actinides by Solvent Extraction — Trial Use of Hydrophilic and Lipophilic Diamides —

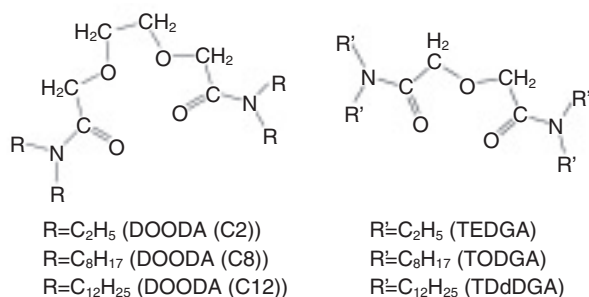


Fig.7-14 Structures of dioxaoctanediamide (DOODA) and diglycolamide (DGA) compounds

It is possible to synthesize DOODA and DGA compounds with different R and R' (general term of alkyl group, like C_2H_5 and C_8H_{17}). DOODA (C2) and *N,N,N',N'*-tetraethyl-3-diglycolamide (TEDGA) are hydrophilic compounds, while tetraoctyl-dioxaoctanediamide (DOODA (C8)), tetradodecyl-doxaoctanediamide (C12), tetraoctyldiglycolamide (TODGA), and *N,N,N',N'*-tetradodecyl-diglycolamide (TDdDGA) are lipophilic compounds.

Table 7-1 Separation factor (SF) of Am/Cm

Higher SF values can be seen for the extraction system with hydrophilic and lipophilic diamides compared to that with only lipophilic diamide.

Extractant	HNO ₃	hydrolytic diamide	SF for Am/Cm
0.3 M DOODA (C12)	5 M	—	1.42
0.3 M DOODA (C12)	5 M	0.01 M TEDGA	3.79
0.08 M TDdDGA	1 M	—	(1.91) *
0.1 M TDdDGA	3 M	0.4 M DOODA (C2)	(3.58) *

* Reciprocal values (Cm/Am) are shown in parentheses.

Am and Cm in highly radioactive liquid waste have a long half-life and cause high heat generation. There is a concept to separate and dispose of these elements by a suitable technique (e.g., transmutation and geological disposal) in order to reduce radioactive waste. Therefore, the mutual separation of Am and Cm is an important research subject. However, the chemical properties of Am are very similar to those of Cm, and the separation methods reported so far have not shown fully the useful results for the practical application.

We have developed novel and promising extractants, like diglycolamide (DGA) and dioxaoctanediamide (DOODA); these diamides can be converted to water-soluble compounds (Fig.7-14). Noting that a solvent extraction system is composed of aqueous and organic phases, we have considered that the separation factor (SF) between Am and Cm may be increased by the synergistic effect when hydrophilic or lipophilic diamide is dissolved in each phase. Fourteen lanthanide (Ln) ions are examined in place of Am and Cm in this work.

From the solvent extraction study involving the use of tetraoctyldiglycolamide (TODGA) and tetraoctyl-dioxaoctanediamide (DOODA (C8)), it has been found that the distribution ratio (*D*) increases or decreases with the atomic number of

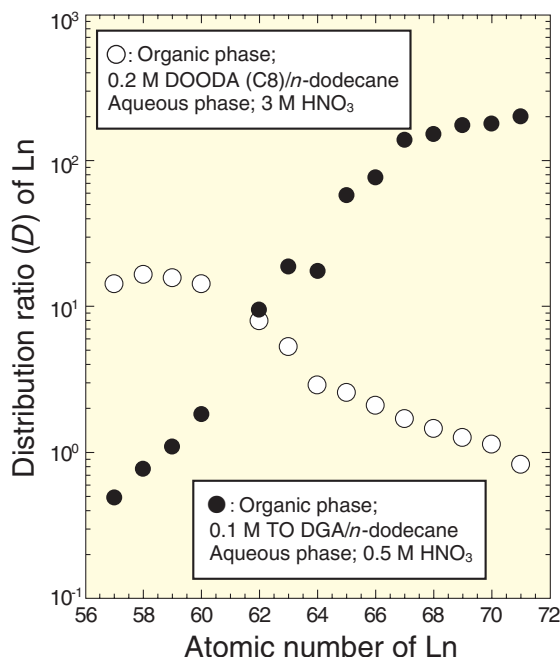


Fig.7-15 Relationship between distribution ratio (*D*) for tetraoctyldiglycolamide (TODGA) and tetraoctyl-dioxaoctanediamide (DOODA (C8)) and atomic number of lanthanides (Ln's)

DOODA (C8) and TODGA have different extraction property of Ln; namely DOODA (C8) has high *D* for light Ln's, and TODGA has high *D* for heavy Ln's.

Ln's (Fig.7-15). This result indicates that lighter and heavier Ln's are more extractable by DOODA (C8) and TODGA, respectively. In the Ln element series, the chemical behavior of Nd(III) and Sm(III) is close to that of Am(III) and Cm(III). In order to examine the synergistic effect on mutual separation, two diamide compounds are used simultaneously in the aqueous and organic phases. Here, the two available diamides may show the opposite trends when used for Ln extraction, as shown in Fig.7-15.

Higher SFs between Am and Cm have been obtained by using two diamides compared to the SF when only one extractant is used, as seen in Table 7-1. Here, the SFs are obtained from the ratio $D(M)/D(M')$, and a high SF implies high separation performance. As shown in Table 7-1, the synergistic effect on the mutual separation between Am and Cm can be seen in this extraction system. If we have a higher SF, a better extraction process can be used. From the results of a simple calculation for multistep extraction, it has been confirmed that an SF value of 3.6 for Am/Cm gives sufficient separation performance. Our efforts toward the development of new extractants and masking agents has been continuing. In the future, we intend working toward achieving high SF values by using effective combinations of diamides, and designing a simple and practical partitioning process.

Reference

Sasaki, Y. et al., Mutual Separation of Actinides from Middle Lanthanides by the Combination of Two Neutral Donors, *N,N,N',N'*-Tetraoctyl-3,6-dioxaoctanediamide and *N,N,N',N'*-Tetraethyl-diglycolamide, *Chemistry Letters*, vol.39, no.8, 2010, p.898-899.

7-6 How Hydrophilic are Actinide Ions?

— Determination of Standard Gibbs Energy of Transfer at Aqueous/Organic Interface —

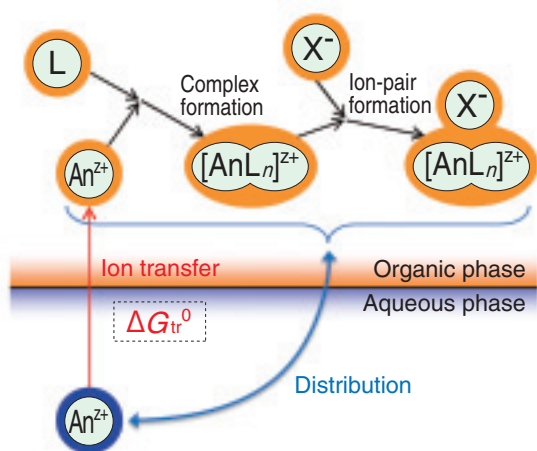


Fig.7-16 Ion transfer at aqueous/organic interface

In a solvent extraction system, the actinide ions transferred from an aqueous phase to an organic phase form complexes with ligands (L) and ion pairs with counter ions (X^-) in the organic phase, and they are then stabilized. The distribution of the ions is determined by the Gibbs energy of transfer (ΔG_{tr}^0), complex formation, and ion-pair formation.

The transferability of an ion at the interface between aqueous and organic phases depends on the chemical potentials of the ion in both phases. Separation of ions by solvent extraction and analysis by using an ion-selective electrode are conducted by utilizing the difference in the ion transferability. Many metal ions require a large energy for their transfer from an aqueous phase to an organic phase (the standard Gibbs energy of transfer at the interface, ΔG_{tr}^0) because they are highly hydrophilic and hardly dissolve in an organic solvent. In solvent extraction, ions are extracted into the organic phase by stabilizing them through complex formation and ion-pair formation in the organic phase (Fig.7-16). Accordingly, the distribution of the ions is determined by ΔG_{tr}^0 of the ions and counter ions, as well as complex formation and ion-pair formation.

First, we determined ΔG_{tr}^0 of the hydrogen ion (H^+) by the electrochemical method for use as a reference, in order to estimate ΔG_{tr}^0 of actinide ions at the interface precisely. Then, we estimated ΔG_{tr}^0 of trivalent- to hexavalent-actinide ions such as uranium, neptunium, and plutonium from the ratio between the concentrations of actinide ion and H^+ in both phases for an equilibrium ion distribution.

ΔG_{tr}^0 values of actinide ions for five types of organic solvents are plotted against those of H^+ in Fig.7-17. It can be

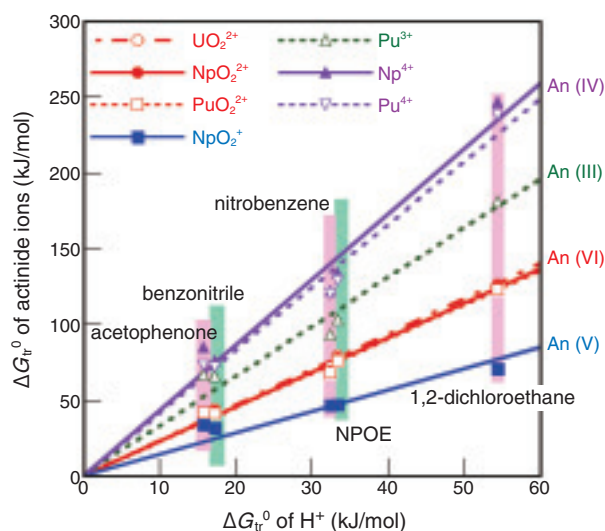


Fig.7-17 Relation between standard Gibbs energies of transfer (ΔG_{tr}^0 s) of actinide ions and those of H^+

ΔG_{tr}^0 values of actinide ions in each oxidation state are almost proportional to those of H^+ regardless of the type of solvent, suggesting that solvation of actinide ions is not special, but similar to that of H^+ .

observed that the ΔG_{tr}^0 values of actinide ions in the same oxidation state are similar to each other irrespective of the type of organic solvent. The ΔG_{tr}^0 values of hexavalent actinide ions (AnO_2^{2+}) are larger than that of the magnesium ion (Mg^{2+}), which is the most hydrophilic among divalent ions whose ΔG_{tr}^0 values are known. ΔG_{tr}^0 values of actinide ions having a lower charge number are smaller. A comparison of the ratios of ΔG_{tr}^0 to the charge number for actinide ions shows that the values of pentavalent neptunium ions (NpO_2^+) are much larger than those of other actinide ions. Thus, NpO_2^+ is particularly hydrophilic among actinide ions. It is considered that this high hydrophilicity is one of the reasons why a large distribution ratio of NpO_2^+ is hardly obtained in any solvent extraction system.

The ΔG_{tr}^0 values of actinide ions determined in this study were for organic solvents with relatively large dielectric constants. If more sensitive methods are applied to determine the concentration of actinide ions, the procedure can be extended to organic solvents having low dielectric constants. Accumulated data on ΔG_{tr}^0 might be useful for developing guidelines for the selection of a solvent for the extraction of actinide ions and for designing an extraction reagent selective for actinide ions.

Reference

Kitatsuji, Y. et al., Standard Gibbs Energies for Transfer of Actinyl Ions at the Aqueous/Organic Solution Interface, The Journal of Chemical Thermodynamics, vol.43, issue 6, 2011, p.844-851.

7-7 Prediction of Irradiation-Assisted Stress Corrosion Cracking of Structural Materials in Nuclear Reactors — Study on Material Degradation Diagnosis Method Using Magnetic Sensor —

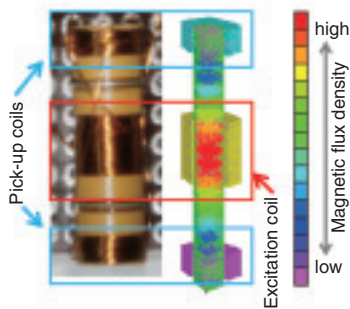


Fig.7-18 “I”-shaped sensor probe and calculation results of its magnetic characteristics

The magnetic flux concentration in the excitation coil is necessary for high-accuracy measurements of magnetic properties.

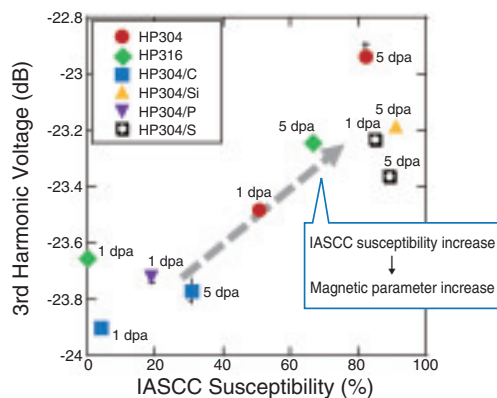


Fig.7-19 Correlation between magnetic data and IASCC susceptibility

These data, showing a positive correlation, were obtained from neutron-irradiated high-purity austenitic stainless alloys with six different chemical compositions.

Many of the problems experienced in light water reactors (LWRs) are caused by damage to structural materials. Stress corrosion cracking (SCC) and irradiation-assisted SCC (IASCC) have been especially serious problems, but their prediction in the design process has not been possible.

Conventional nondestructive evaluation methods for nuclear reactor components are capable of crack detection. In the meantime, if we are able to develop a diagnostic technique that can detect material degradation before crack initiation, it will be useful for reinforcing the safety measures in nuclear reactor systems.

The eddy current method and alternating current (AC) magnetization method were chosen for the development of predictive IASCC diagnosis, because these methods are more suitable for application in actual reactors than any others. In this study, an “I”-shaped sensor probe was developed (Fig.7-18). Calculations and mock-up tests were carried out for optimization of the sensor design to obtain higher measurement accuracy. Moreover, the tolerance to the environmental conditions in the reactor during the maintenance period was confirmed by testing. A remote-control system equipped with the sensor probe was developed, and its performance was evaluated.

The specimens used in the study were as follows: high-purity austenitic stainless alloys with six different chemical compositions, neutron-irradiated up to 1 dpa and 5 dpa; and

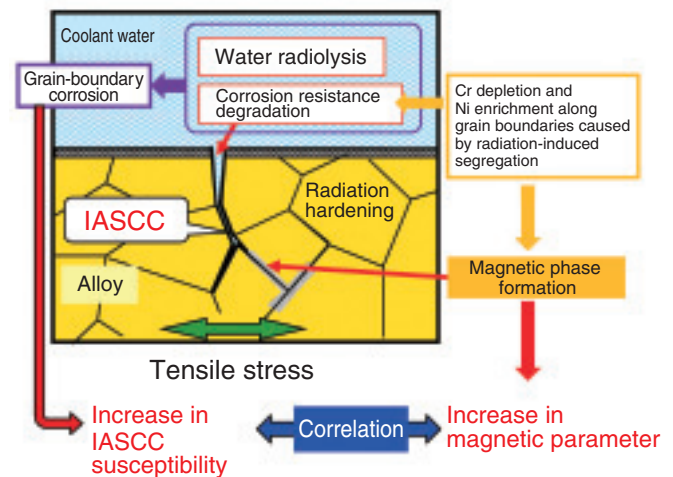


Fig.7-20 Mechanism of correlation between magnetic data and IASCC susceptibility

It was revealed that magnetic-phase formation after Cr depletion and Ni enrichment along grain boundaries, caused by radiation-induced segregation, was the main mechanism of the correlation between the magnetic data and IASCC susceptibility.

type-316L stainless steel, neutron-irradiated with up to three doses around 1 dpa (because 1 dpa is considered as the threshold for IASCC in previous studies). The magnetic data obtained by both the eddy current and AC magnetization methods showed correlations with the IASCC susceptibilities of the specimens (Fig.7-19).

For investigation of the mechanism of this correlation, the relations between the microstructures and magnetic properties of the neutron-irradiated and mock-up specimens were evaluated through experiments and calculations. It was revealed that magnetic-phase formation along the grain boundaries, which came from the change in chemical composition caused by radiation-induced segregation, was the mechanism of the correlation between the IASCC susceptibilities and the magnetic data (Fig.7-20).

The outcome of this research showed the feasibility of predictive diagnosis that can detect material degradation before IASCC initiation. This will contribute to the safety and reliability of nuclear reactors.

The present study includes the results of the project “Development of a diagnostic method of in-core structure material degradation for super-critical water-cooled fast breeder reactors” entrusted by the Ministry of Education, Culture, Sports, Science and Technology of Japan (MEXT). The scientific paper of this study received the first “Best Paper Award” from the Japan Society of Maintenology in 2011.

Reference

Nemoto, Y. et al., A Study of Correlativity between IASCC Susceptibility and Magnetic Property of Stainless Steel, *Hozengaku*, vol.7, no.4, 2009, p.57-68 (in Japanese).

7-8 Analysis of Isotopic Composition without Touching the Sample — Isotope Analysis of Nuclear Fuel Using Resonance Absorption Spectrometry —

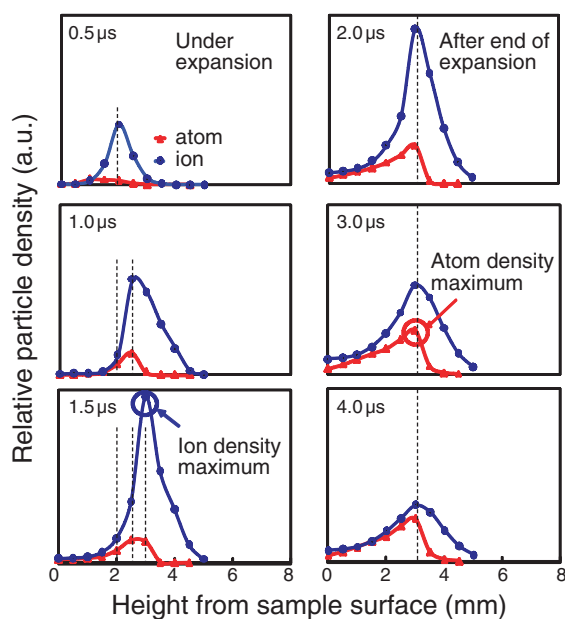


Fig.7-21 Time evolution of plume density distribution

The plume density distribution in 600 Pa helium showed a delay of up to 4 μs after laser irradiation. The red and blue curves depict the densities of neutral and ionized atoms in their ground states, respectively. The delay and height conditions giving maximum densities are indicated with circles.

Low-decontaminated mixed oxide (MOX) fuels containing minor actinides and fission products are attracting much interest as next-generation fuels, especially from the viewpoint of nuclear security. Isotope analysis of the fuel is indispensable for clarifying the amounts of used fissile materials for the purpose of safeguard verification. However, the high radioactivity of the fuel prevents analysts from treating it by hand, and the strong radiation makes radiometric analysis difficult. Hence, we started to develop a laser spectrometry method for fuel analysis, which does not require any direct sample handling or radiometric measurements.

When a solid sample is irradiated with intense laser pulses, a small part of it is released and decomposed into monatomic species, forming an ablation plume. When another laser beam tuned to the resonance frequency of the species is introduced in the plume, only the species of interest absorbs the laser light. Thus, by scanning the laser frequency across each isotopic resonance, we can determine the isotope ratio from the absorbances.

For the realization of highly sensitive and isotope-selective analysis by avoiding Doppler and Stark effects, it is necessary to decelerate the ablation plume expansion. However, the ablated species populate various energy states and the population distribution varies during the expansion. This complexity makes elucidation of the plume dynamics a very

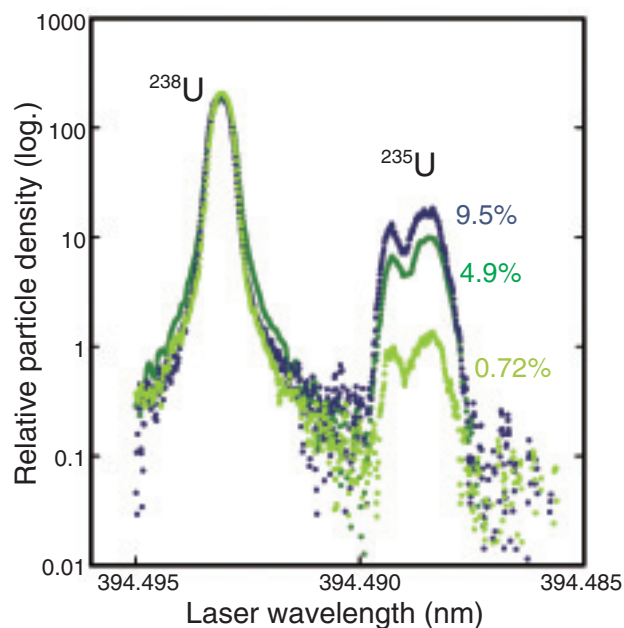


Fig.7-22 Absorption spectra of natural and enriched uranium

The absorption spectra of uranium oxide samples were measured with the conditions indicated by the red circle in Fig.7-21. The peak height of ^{235}U varied in proportion with the isotope ratio of ^{235}U (expressed in % in this figure). The double-peak structure of ^{235}U arises from its nuclear spin.

difficult task. Therefore, we developed a precise laser-frequency control system so that we could measure the temporal and spatial variations in the density distribution, as shown in Fig.7-21. The density peaks stop moving at a delay of about 2 μs and at around this time, the densities are maximized because of relaxation from higher energy states. From this result, we determined the experimental conditions needed to obtain a higher sensitivity, as shown by the circles in this figure. Using the conditions indicated in the red circle, we observed the isotope-selective absorption spectra of atomic uranium, as shown in Fig.7-22. These are the first results demonstrating the possibility of isotope analysis for natural uranium without the need to touch the sample. In addition, we confirmed that the ^{235}U peak height varied in proportion with the isotope ratio of ^{235}U with good linearity.

At present we are applying this method to MOX fuel samples for the realization of the remote isotope analysis of plutonium.

The present study was carried out within the project “Development of laser remote analysis for next generation nuclear fuel and applied study by MOX sample” entrusted to the Japan Atomic Energy Agency by the Ministry of Education, Culture, Sports, Science and Technology of Japan (MEXT).

Reference

Miyabe, M. et al., Spectroscopy of Laser-Produced Cerium Plasma for Remote Isotope Analysis of Nuclear Fuel, Applied Physics A, vol.101, no.1, 2010, p.65-70.

7-9 Towards Prediction of Dispersion of Hazardous Materials in Urban Area — Development of Local-Scale High-Resolution Atmospheric Dispersion Model —

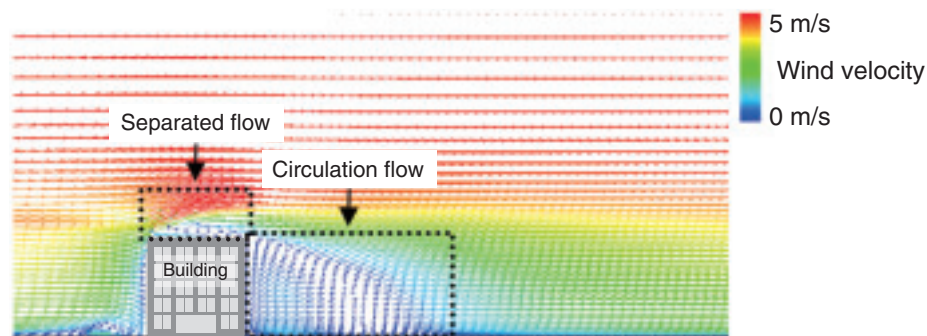


Fig.7-23 Mean wind velocity vectors around a building
Separated and reversed flows are observed at the roof of and behind a building.

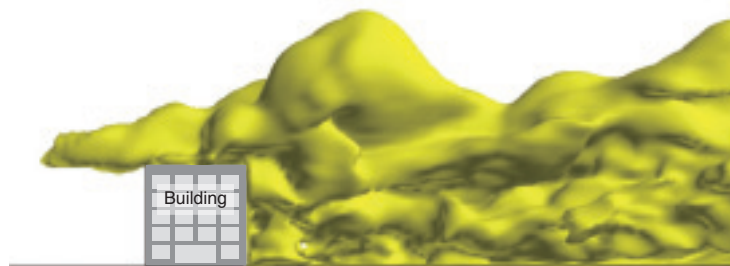


Fig.7-24 Three-dimensional structure of a plume around a building
A plume is found to be entrained into the building wake region owing to reversed flow. The yellow areas on the isosurface indicate 0.05% of the initial concentration.

The subway hazardous gas attack in Tokyo in 1995 and terrorist attacks on major cities in the United States in 2001 have spawned concerns about various possible forms of terrorism, including airborne/aerosolized radioactive and chemical agent attacks. Owing to the increasing threat of various forms of terrorisms, we have the urgent task of planning disaster prevention against accidental and intentional release of radioactive and chemical materials within urban areas. Atmospheric dispersion is influenced by meteorological disturbances and turbulence produced by urban buildings. Therefore, an approach that involves a combination of numerical weather predictions and computational fluid dynamics models would show promise for the prediction of plume dispersion of hazardous materials within urban areas under real meteorological conditions. However, many researchers have adopted time-averaged types of turbulence models. These turbulence models are practical, but cannot accurately simulate complex turbulent flow, such as separated and circulation flows around buildings, or capture peak concentrations. For the assessment of human health hazards from toxic substances, the existence of high concentration peaks in a plume should be considered. In such a situation, unsteady behaviors of a plume cannot be captured by typical

atmospheric dispersion models.

We have developed a Local-scale High-resolution Dispersion Model using Large-Eddy Simulation (LOHDIM-LES) for predicting plume dispersion within urban areas in order to solve the above-mentioned problems. It is well known that an LES model can give detailed information on unsteady behaviors of turbulent flow and plume dispersion. The application of an LES model is expected to facilitate the prediction of not only mean concentrations but also peak concentrations.

As the first step, we attempted to carry out the LES of turbulent dispersion around a building. Figs.7-23 and 7-24 show mean wind vectors and the three-dimensional structure of a plume. Reversed and circulation flows were formed at the roof of and behind the building, respectively. Therefore, first, a plume impinges on the building, and it is then entrained into the wake region owing to the circulation flow. We succeeded in obtaining results comparable to wind tunnel experimental results.

Thus, we have validated the basic performance of the LES atmospheric dispersion model. In a future work, we shall extend the model for the prediction of plume dispersion within actual urban areas.

Reference

Nakayama, H. et al., Development of Local-Scale High-Resolution Atmospheric Dispersion Model Using Large-Eddy Simulation, Part2: Turbulent Flow and Plume Dispersion around a Cubical Building, Journal of Nuclear Science and Technology, vol.48, no.3, 2011, p.374-383.

7-10 Production of Medical RIs Using Accelerator Neutrons — Development of an Innovative RI Production Method —

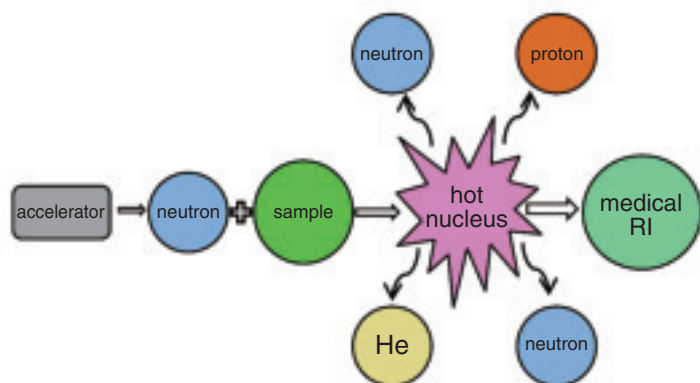


Fig.7-25 Production of medical RIs by using accelerator neutrons
The temperature of sample nuclei irradiated by accelerator neutrons becomes so high that various particles, such as protons, neutrons, and He, are emitted. Consequently, high-quality RIs can be obtained by separating the produced RIs from the sample materials by a chemical or physical process.

A radioisotope (RI) with a half-life ($T_{1/2}$) of less than several days plays an important role in nuclear medicine. The daughter nuclide of ^{99}Mo ($T_{1/2}=66$ h), i.e., $^{99\text{m}}\text{Tc}$ ($T_{1/2}=6$ h), is used for diagnostics, and ^{90}Y ($T_{1/2}=64$ h) is used for cancer therapy. Most medical RIs, including ^{99}Mo and ^{90}Y , are imported in Japan. An unscheduled shutdown of aging research reactors in which most of the ^{99}Mo nuclide was produced has resulted in a critical shortage of ^{99}Mo worldwide. Therefore, the establishment of a reliable production method for ^{99}Mo is very important to ensure the continued medical applications of $^{99\text{m}}\text{Tc}$.

We have proposed a new route for producing medical RIs using accelerator neutrons, as shown in Fig.7-25. In fact, a variety of medical RIs can be produced using accelerator neutrons as the production cross section of a sample nucleus is large at $E_n=10\sim 15$ MeV. For example, the ^{99}Mo production cross section of the $^{100}\text{Mo}(n,2n)^{99}\text{Mo}$ reaction is 1.5 b at $E_n\approx 10\sim 20$ MeV, while the ^{97}Zr production cross section of the $^{100}\text{Mo}(n,\alpha)^{97}\text{Zr}$ reaction is 0.002 b. Note that ^{97}Zr , a radioactive impurity nucleus, is produced in small amounts. The ^{90}Y production cross section of the $^{90}\text{Zr}(n,p)^{90}\text{Y}$ reaction

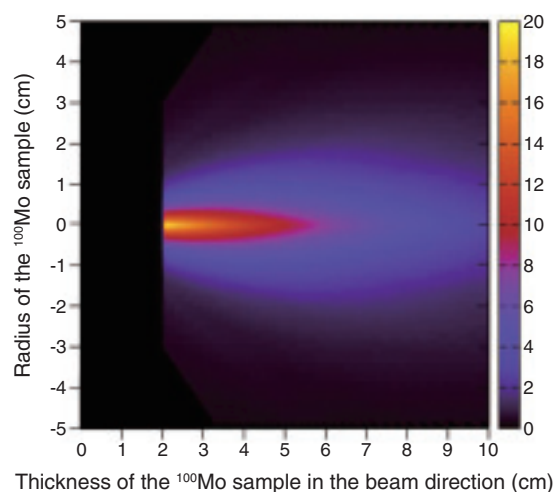


Fig.7-26 Calculated yield distribution of ^{99}Mo
 ^{99}Mo yield distribution in terms of the radius and thickness of the ^{100}Mo sample. ^{99}Mo is produced by the $^{100}\text{Mo}(n,2n)^{99}\text{Mo}$ reaction using accelerator neutrons from the $^{12}\text{C}(d,n)$ reaction. On the ^{99}Mo intensity scale, red indicates a higher intensity than purple does.

is also large. High-quality $^{99\text{m}}\text{Tc}$ and ^{90}Y can be separated from the irradiated Mo and Zr samples by sublimation and ion exchange, respectively. Quasi-mono energetic, high intensity accelerator neutrons ($E_n=10\sim 15$ MeV), therefore, are very useful for the production of medical RIs.

Neutrons (about 10^{15} n/s) with an E_n of about 14 MeV are produced in the $^{12}\text{C}(d,n)$ reaction using 40 MeV 5 mA deuteron beams provided by an accelerator. Such an accelerator is currently under construction in France.

We evaluated the angular and depth distributions of ^{99}Mo that was produced by using the accelerator neutrons to study the effective use of the neutrons, as shown in Fig.7-26. It is shown that the ^{99}Mo yield is restricted to a narrow region at an extremely forward angle with respect to the deuteron beam direction; this observation assisted us in obtaining high-specific-activity ^{99}Mo .

The present results motivated us to employ this new RI production method to ensure constant and assured supply of medical RIs for domestic use and to open a new frontier in medicine and pharmacy.

Reference

Minato, F., Nagai, Y., Estimation of Production Yield of ^{99}Mo for Medical Use Using Neutrons from $^{12}\text{C}(d,n)$ at $E_d=40$ MeV, Journal of the Physical Society of Japan, vol.79, no.9, 2010, p.093201-1-093201-3.

Research on HTGR and Nuclear Heat Applications to Establish a Low-Carbon Society

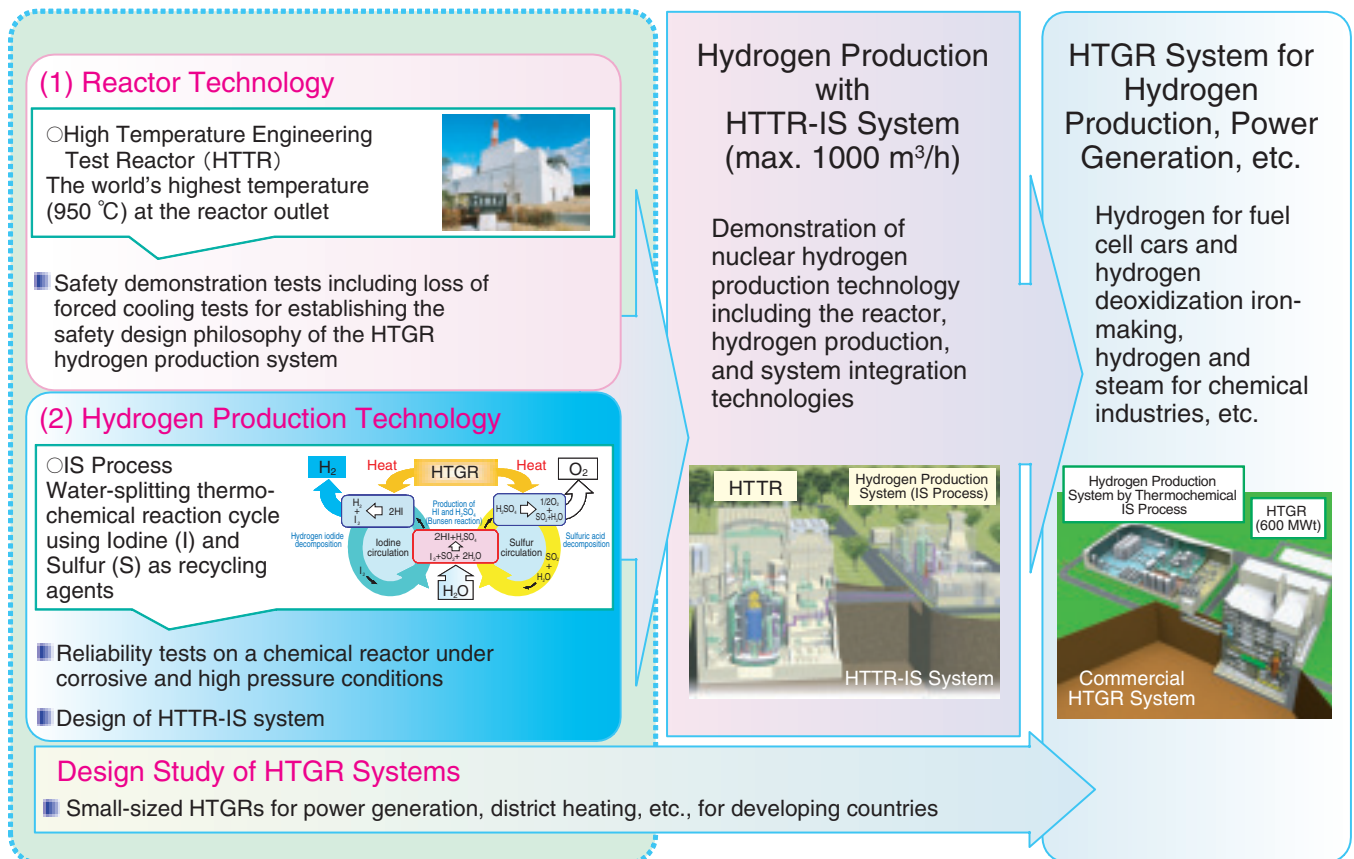


Fig.8-1 Research plan for HTGR and nuclear heat applications

In order to extend nuclear heat applications to non-electric fields such as transportation, iron-making, and chemical industries and establish a low-carbon society, we are carrying out research on HTGR, which can produce heat above 900 °C, and nuclear heat applications.

The breakdown of Japan's energy consumption and CO₂ emission in each field shows that utilization of heat in transportation and industry by combustion of fossil fuels accounts for around 70%. In order to reduce the overall CO₂ emission by more than 50% and thus control global warming and establish a low-carbon society, diversification in the use of nuclear heat is indispensable. In particular, the demand for hydrogen for fuel cell cars, hydrogen deoxidization, and iron making is expected to grow dramatically in the near future. In order to meet the growing demands for energy in developing countries and simultaneously control global warming, deployment of nuclear power plants is necessary. High-temperature gas-cooled reactors (HTGRs), which are inherently safe (Topic 8-1) and economical despite their small size, can supply heat above 900 °C and meet the growing energy demands mentioned above. Thus, HTGRs can meet the energy production requirements for global greenhouse gas reduction. Therefore, we are carrying out research and development of HTGRs particularly with regard to (1) reactor technology and (2) heat utilization technology (Fig.8-1). For developing the reactor technology, we are accumulating important data for commercializing HTGR by using Japan's first high-temperature gas-cooled reactor, named high-temperature engineering test reactor (HTTR); the

output thermal power of the HTTR is 30 MW, and the maximum temperature at the reactor outlet is 950 °C. In January 2011, a test of loss of forced cooling without the vessel cooling system operational (LOCC) in the HTTR was successfully completed under the condition of the reactor power of 9 MW (30% of the rated power). To demonstrate the inherent safety features of HTGR in the case of LOCC, all of the primary gas circulators and one of the two reactor vessel cooling systems for decay heat removal were stopped from the 9 MW steady-state operation. The primary coolant flow rate reduced to zero, and the reactor power decreased rapidly to zero just after the gas circulators stopped working. The increase in the temperature of the vessel and other reactor structures was confirmed within the conservative analytical results obtained prior to the test. For hydrogen production, a thermochemical hydrogen production cycle called the IS (iodine-sulfur) process has been developed step-by-step. Continuous hydrogen production using a bench-scale test apparatus made of glass was successfully achieved, with a hydrogen production rate of about 30 ℓ/h for 1 week. Integrity confirmation tests for a commercially made acid decomposer under corrosive conditions are now being conducted (Topic 8-2).

8-1 Toward a Reactor with Highest Safety Standards

— Development of HTGR Based on Inherent Safety Features —

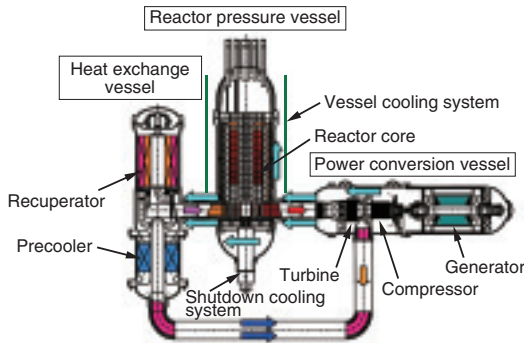


Fig.8-2 Gas-turbine high-temperature reactor

The gas-turbine high-temperature reactor GTHTR300 is designed as a commercial high-temperature gas-cooled reactor (HTGR) plant for electricity generation. High-temperature helium gas heated in the core is used for electricity generation by a helium gas turbine.

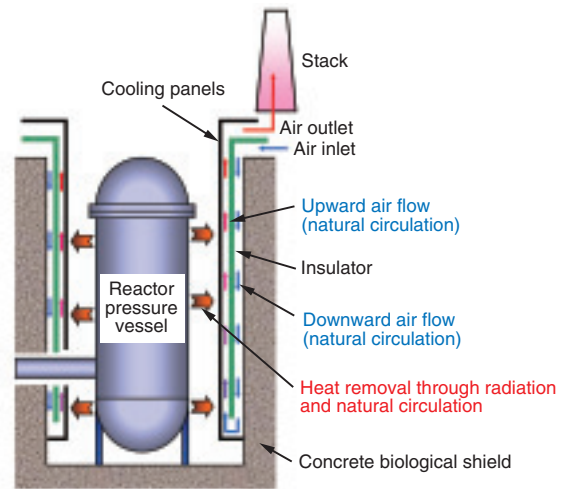


Fig.8-3 Vessel cooling system (VCS)

After an accident, residual heat from the core is transferred from the outside of the reactor pressure vessel to the cooling panels of the VCS through radiation and natural air convection in the reactor cavity; this heat is then dissipated to the environment via the natural circulation of air that flows inside the cooling panels. The VCS is a passive system without active components and does not require electricity.

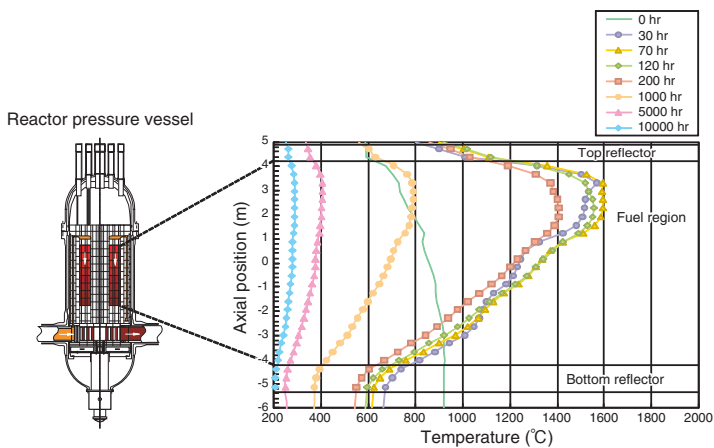


Fig.8-4 Fuel-temperature behavior in the case of loss-of-coolant accidents (analytical results)

Numerical analysis shows that the maximum fuel temperature can be maintained below the temperature limit (1600 °C) by passive cooling with VCS without an active system and actions taken by plant personnel in the case of loss-of-coolant accidents.

The safety of nuclear reactors is a prime concern after the accident at the Tokyo Electric Power Company, Incorporated Fukushima Daiichi Nuclear Power Station. The safety of the high-temperature gas-cooled reactor (HTGR), which is a helium-cooled graphite-moderated reactor, is assured by its inherent safety features, as described below, even in the cases of a station blackout and the loss of forced cooling through the core.

On the basis of the construction and operation of Japan's first HTGR, the High-Temperature Engineering Test Reactor (HTTR), we have performed R&D and created the basic design of a commercial gas-turbine high-temperature reactor, GTHTR300 (Fig.8-2). The fuel for this reactor consists of coated fuel particles. Uranium dioxide is surrounded by four layers of ceramics, whose integrity can be sufficiently maintained below 1600 °C and which act as the primary barrier against the release of radioactive materials. Even if the control rod is withdrawn from the core during any accident, the reactor power decreases naturally to reach a stable condition, i.e., nearly zero power level, because of the large negative reactivity feedback. Fuel integrity can be maintained

because of a large temperature margin with respect to the temperature limit. Analytical results show that in the event of the loss of coolant in the primary pipe due to rupture or the loss of forced cooling through the core due to a station blackout, residual heat can be removed from the outside of the reactor pressure vessel by radiation and natural air convection by using a passive vessel-cooling system (Fig.8-3), and thus, fuel integrity could be maintained (Fig.8-4). This is possible due to the large heat capacity, high thermal conductivity, and low power density of the graphite core. The passive air-cooled dry storage without a storage pool, which ensures heat removal even in the case of a station blackout, can be used for the storage of spent fuel because of its low power density due to decay heat.

In addition to the design of GTHTR300, the inherent safety features of HTGR are demonstrated by tests on HTTR, simulating the anticipated operational occurrences and accidents. The test simulating a station blackout is scheduled.

Through these R&D activities, we are aiming to offer an HTGR with the highest safety standards that is acceptable to the general public in Japan and international society.

Reference

Kunitomi, K., Yan, X., Ohashi, H., Safety Characteristics of GTHTR and Safety Demonstration Test Program Using HTTR, Proceeding of 2011 Small Modular Reactor Symposium, Washington, DC, USA, 2011, paper SMR2011-6611, 6p., in CD-ROM.

8-2 Development of High-Pressure Ceramic Components for Hydrogen Production — Strength Estimation Method for Component Design —

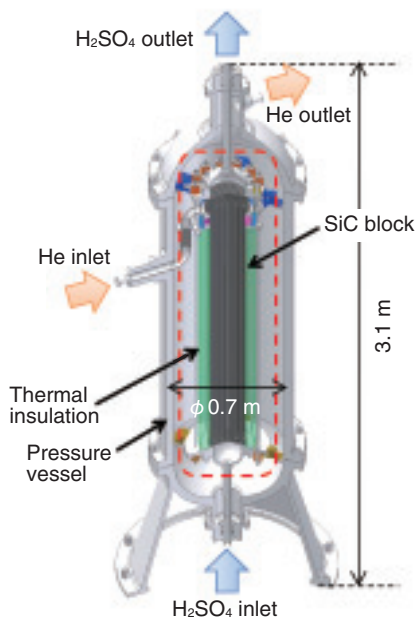


Fig.8-5 Concept of sulfuric acid decomposer for IS process

The concept of a sulfuric acid decomposer was developed. The decomposer consists of a heat exchanger block made of SiC and shows excellent corrosion resistance to sulfuric acid.

We are conducting R&D on nuclear hydrogen production by the Iodine-Sulfur (IS) process that can produce massive amounts of hydrogen from water without CO₂ emission by using the heat supplied by a high temperature gas-cooled reactor.

Since highly corrosive materials such as sulfuric and hydriodic acids are used in the IS process, it is very important to develop components made of corrosion resistant materials. Therefore, we have been developing a sulfuric acid decomposer made of a ceramic material, that is, silicon carbide (SiC), which shows excellent corrosion resistance to sulfuric acid (Fig.8-5).

One of the key technological challenges for the practical use of this ceramic sulfuric acid decomposer is to be licensed in accordance with the High Pressure Gas Safety Act for high-pressure operations of the IS process. Since the strength of a ceramic material depends on its geometric form, etc., the strength evaluation method required for a pressure design is not established. Moreover, if the conventional destructive test is performed for the strength evaluation of a full-size component such as a sulfuric acid decomposer, large cost and time will be necessary. Therefore, a new strength evaluation method is required.

A critical problem in the strength evaluation of a ceramic structure is the large variation in strength. A ceramic material fractures because of the presence of small cracks or crack-like flaws in the material. The scatter of strength is a

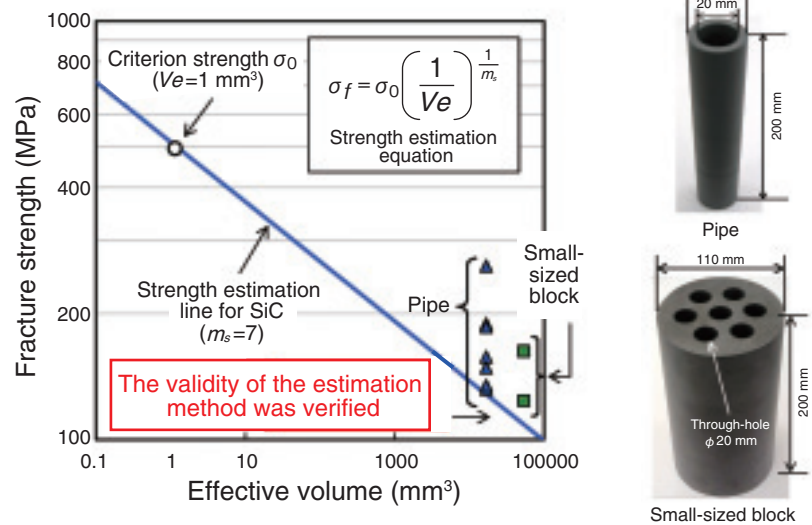


Fig.8-6 Strength estimation method for SiC structure with effective volume and validation test results

We proposed a novel strength estimation method for SiC. The method can be used for designing large-scale structures and its validation was verified by conducting destructive test on SiC models.

consequence of the scatter in the size and distribution of the cracks, which depends on the structure design its shape and size.

In general, the effective volume theory is one of the appropriate theories for estimating the strength of ceramic materials having different sizes by using the effective volume V_e of the materials. The effective volume theory, however, is not applicable to large-scale structures because the shape dependence of crack distribution in ceramic materials is not considered in this theory.

Hence, we propose a novel strength estimation method for SiC structures based on the effective volume theory in order to extend the range of application of the effective volume. The principle logic of the proposed method is that there is a criterion strength σ_0 of a SiC structure without flaws, and an increase in flaws in the structure decreases its strength. The degree of strength decrease is estimated by using the Weibull modulus m_s , which is optimized for SiC (Fig.8-6).

The proposed method was verified by performing a fracture test on small-scale SiC structures: a pipe and a small-sized block. The fracture strength of the models was higher than the value of the estimated strength. It was revealed that the strength of the SiC structures was estimated successfully by using the proposed estimation method.

We will develop a design method for ceramic apparatus with the strength estimation method in order to obtain a license in accordance with the High Pressure Gas Safety Act.

Reference

Takegami, H. et al., Fracture Strength Estimation of SiC Block for IS Process, Nuclear Engineering and Design, vol.241, issue 12, 2011, p.4726-4730.

Executing Decontamination & Dismantling and Radwaste Treatment & Disposal

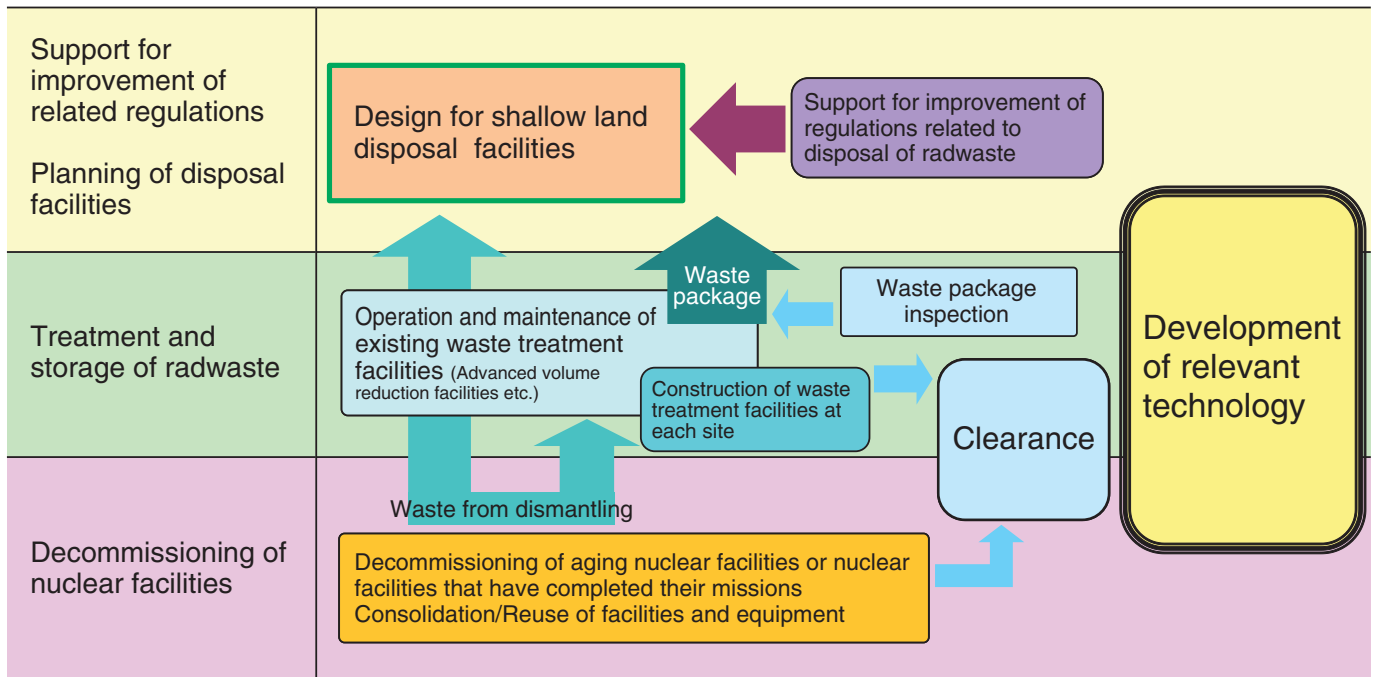


Fig.9-1 Outline of measures for decommissioning and radwaste treatment/disposal

We are setting up systems for the purpose of decommissioning nuclear facilities and for radwaste management. In addition, we are developing related technology, planning and constructing radwaste treatment/disposal facilities, and providing support for the improvement of related regulations.

Decommissioning of nuclear facilities and radwaste treatment/disposal are two of our major missions. In these missions, we will be disposing radwaste generated not only from our research activities but also from universities, institutes, industrial facilities, etc.

We are setting up systems for decommissioning nuclear facilities and for managing radwaste. We are also developing the related technology (Fig.9-1).

R&D for decommissioning

We have been developing a decommissioning engineering system and a waste/scrapped material clearance verification/evaluation system.

As part of development of the decommissioning engineering system, a method used for evaluating the decommissioning cost was assessed by applying it to the actual decommissioning of the Fugen nuclear facility (Topic 9-1).

R&D for waste treatment

For radwaste treatment and disposal, it is important to improve the safety of radwaste disposal and reduce the expense; therefore, technological development is required for

reducing the quantity of radwaste. As part of the technical development, decontamination methods for removing radionuclides from wastes have been developed. Here, we used a decontamination method that involves the use of supercritical carbon dioxide (prepared by pressurizing and heating carbon dioxide) as the separation medium and also as a surfactant. We succeeded in directly dissolving europium oxide, which is used instead of trivalent actinide, in the supercritical carbon dioxide (Topic 9-2).

R&D for waste disposal

For the proper disposal of radwaste packages produced by various research facilities, the evaluation of radioactive content in the waste packages is indispensable. Therefore, we have prepared a basic analytical flow and developed related techniques that allow rapid analysis of the radwaste. In the analysis, reference materials containing known amounts of a radionuclide are needed to ensure that the radioactivity data obtained by the rapid method are reliable. A method for preparing reference material containing a known activity of ^{14}C or ^{36}Cl , which hardly remains at a high temperature in molten radwaste, was developed (Topic 9-3).

9-1 Rational Decommissioning Planning

— Development of Project Management Data Evaluation System —

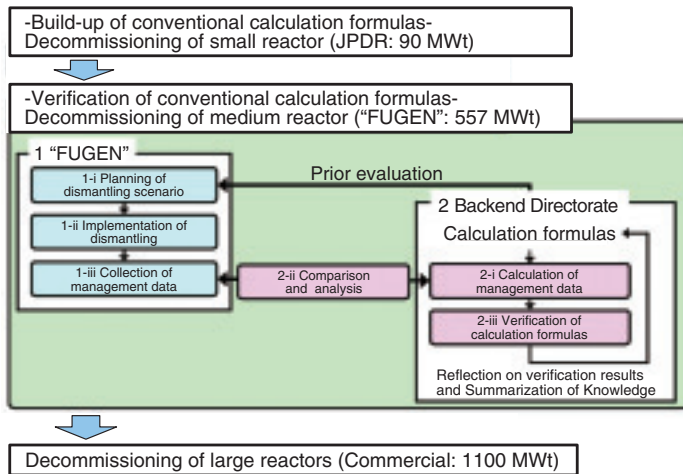


Fig.9-2 Scheme for verification of calculation formulas

The knowledge obtained in this study will be used in the decommissioning of commercial reactors.

We have many nuclear facilities. When these facilities have completed their mission, they will be in the decommissioning stage. For the rational planning of the decommissioning, we are developing a project management data evaluation system (PRODIA).

PRODIA is used to obtain project management data such as manpower needs on the basis of the dismantling scenario and physical data.

The conventional calculation formulas of PRODIA were derived with actual values related to the decommissioning of the JPDR, and therefore, the applicability of the conventional calculation formulas must be verified for decommissioning nuclear facilities of other types and/or with a different scale.

Toward this end, we are studying the applicability of the calculation formulas to the decommissioning of "FUGEN". The plant scale of "FUGEN" is larger than that of the JPDR (as inferred from the thermal outputs of the reactors), as shown in Fig.9-2, whereas the basic structure of the turbine system is almost the same for both plants. Thus, we can study

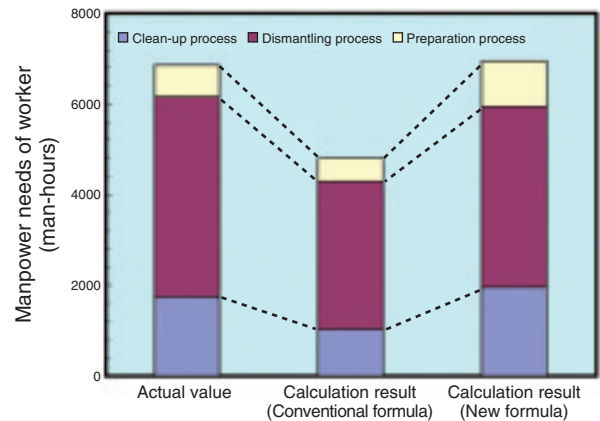


Fig.9-3 Comparison of actual value and calculation results

The conventional formula (preparation/clean-up process: constant expression involving 3 levels of working area; dismantling process: linear expression involving the weight of equipment) gave values smaller than the actual value. The values obtained with the new formula (preparation/clean-up process: linear expression involving the working area; dismantling process: linear expression that includes several work items) showed good agreement with the actual value.

the effect of the plant scale on the project management data.

As the first step in this study, the manpower needs for the dismantling work in 2008 were calculated using the conventional calculation formulas. As shown in Fig.9-3, we found that the value was 73% of the actual value, implying that it will be improper to use the conventional calculation formulas for "FUGEN".

To use PRODIA for further decommissioning planning, we studied the difference between the dismantling of the JPDR and that of "FUGEN" and found that differences in the scale of dismantling operation and the description of work items caused the mismatch between the actual and the calculated values. By reviewing the calculation formulas, as shown in Fig.9-3, we obtained new calculation formulas. The value obtained with the new calculation formulas showed good agreement with the actual value.

For the wide applicability of PRODIA, we will organize the knowledge obtained from the verification of the calculation formulas for the decommissioning of other facilities.

Reference

Shibahara, Y. et al., Study on Evaluation Models of Management Data for Decommissioning of FUGEN, Proceedings of the ASME 13th International Conference on Environmental Remediation and Radioactive Waste Management (ICEM2010), Tsukuba, Japan, 2010, ICEM2010-40102, 7p., in CD-ROM.

9-2 Development of Decontamination Technique for Radioactive Wastes Using Supercritical Fluid

— Reverse Micelle Formation in Supercritical Carbon Dioxide —

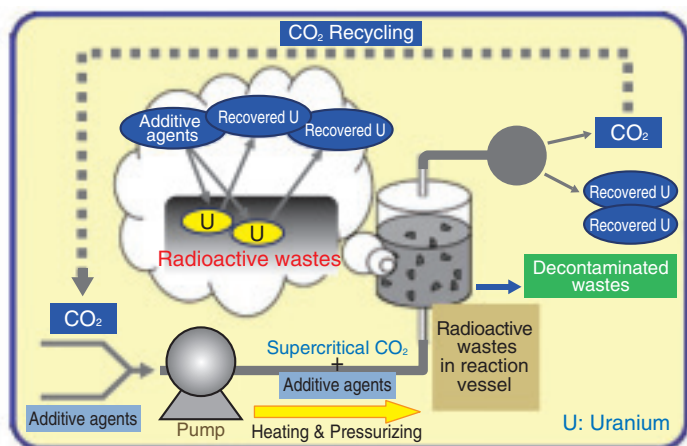


Fig.9-4 Process of decontamination using supercritical fluid Uranium in radioactive wastes is reacted with an additive agent and carried by supercritical CO₂ in a reaction vessel, and the reaction leads to uranium being dissolved in supercritical CO₂. Uranium is collected by extracting and depressurizing the supercritical CO₂.

In order to reduce the cost of radioactive waste management and improve the safety of radioactive waste disposal, it is necessary to reduce the quantity of radioactive waste. Therefore, we develop a technique to remove radioactive nuclides from the waste.

One of the requirements for a decontamination technique is that it should be possible to control the generation of secondary wastes produced during decontamination. We transform carbon dioxide (CO₂) into the supercritical state from the gaseous state by pressurizing and heating it and use the supercritical CO₂ as the separation medium. If supercritical CO₂ is transformed to gaseous CO₂, it almost loses its capability to dissolve a substance, and decontaminated substances are easily separated from the CO₂. In this process, CO₂ does not add to the waste, and the amount of secondary wastes can be greatly reduced. We have already succeeded in decontaminating uranium by using the CO₂ soluble complex of tri-*n*-butyl phosphate and nitric acid as an additive agent (Fig.9-4). However, additive agents, especially those with high reactivity, that can dissolve in supercritical CO₂, are limited, and therefore, it is difficult to apply this technique to the decontamination of plutonium oxide, which is a very stable compound.

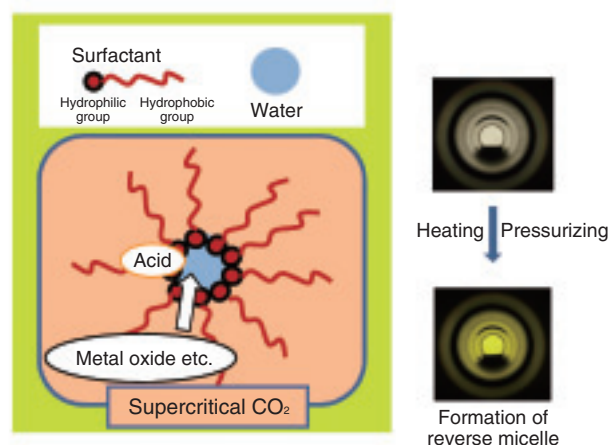


Fig.9-5 Diagram of a reverse micelle in supercritical carbon dioxide

Reverse micelles enclosing water are formed in supercritical CO₂ by using a surfactant. An acid in the water reacts with a metal oxide. The right-hand side photographs show the dissolution of a water soluble indicator (methyl orange) in supercritical CO₂ when reverse micelles are present.

We developed a technique to form reverse micelles in supercritical CO₂. The technique involves the use of a surfactant and increases the reactivity of the supercritical CO₂ by introducing the additive agent. Here, the reverse micelle has a spherical structure containing a small water particle wrapped by the hydrophilic group of the surfactant molecules, and the hydrophobic group is located far from the water particle (Fig.9-5). We examined several surfactants and succeeded in forming reverse micelles containing water, which dissolved nitric acid and metal salts, in supercritical CO₂. Moreover, it was found that the polarity of the hydrophilic group of the surfactant and the size of the hydrophobic group are important factors influencing the formation of stable reverse micelles. We succeeded in dissolving europium oxide in supercritical CO₂.

It was thus observed that the new decontamination technique, in which reverse micelles in supercritical CO₂ were used as a reaction field, showed promise. We shall continue to improve the technique by performing detailed investigations of surfactants and experimental conditions so that it can be used for decontaminating radioactive wastes contaminated with plutonium.

Reference

Kurahashi, K., Tomioka, O. et al., Phase Behavior and Reverse Micelle Formation in Supercritical CO₂ with DTAB and F-Pentanol for Decontamination of Radioactive Wastes, Proceedings of the ASME 13th International Conference on Environmental Remediation and Radioactive Waste Management (ICEM2010), Tsukuba, Japan, 2010, ICEM2010-40257, 4p., in CD-ROM.

9-3 Toward Analysis of Radionuclides in Solidified Products — Preparation of Reference Materials Containing Volatile Nuclides —

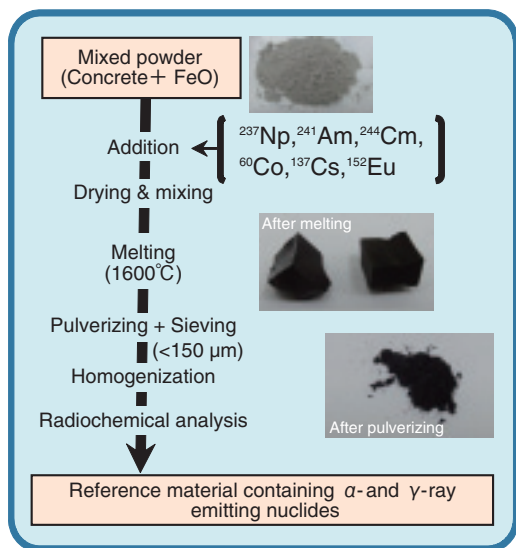


Fig.9-6 Preparation method for reference material of solidified product containing α - and γ -ray emitting nuclides

Reference material of solidified product containing α - and γ -ray emitting nuclides such as ^{241}Am and ^{60}Co was successfully prepared. Additionally, ^{137}Cs was quantitatively retained in the reference material by maintaining low basicity (CaO/SiO_2).

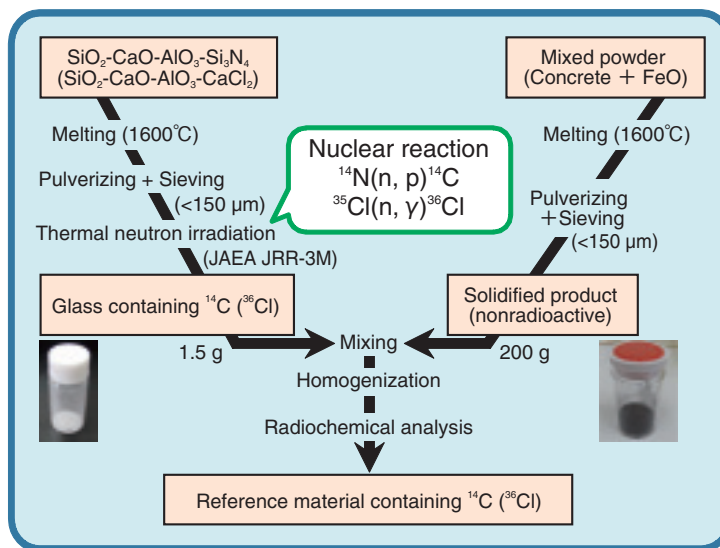


Fig.9-7 Preparation method for reference material of solidified product containing ^{14}C or ^{36}Cl

Reference materials containing volatile nuclides (^{14}C or ^{36}Cl) have been successfully prepared through the nuclear reaction of ^{14}C or ^{36}Cl in a glass.

At the Advanced Volume Reduction Facilities (AVRF) of the JAEA, it has been decided that nonmetallic low-level radioactive solid wastes will be melted in a plasma heating furnace and converted to stable solidified products. For performing disposal of radioactive waste packages containing the solidified products, the evaluation of radioactivity inventories for selected nuclides is necessary. We therefore need to analyze radioactive samples similar to the solidified products to collect radioactivity data.

In order to verify the reliability of the radiochemical analysis, it is necessary to check whether an appropriate procedure has been followed. If we can use a reference material (RM) containing a known amount of the nuclides of interest, the reliability can be evaluated. In this study, preparation methods for simulated solidified products were investigated in order to prepare RMs for the radiochemical analysis of some α -, β - and γ -ray emitting nuclides.

At the AVRF, it has been decided that major non-metallic low-level radioactive solid wastes, namely concrete together with steel drums, will be processed by plasma melting. To simulate a major chemical composition of the solidified

products, non-radioactive concretes and a chemical reagent (FeO) were used. In addition, we employed a laboratory-scale electric furnace to simplify the preparation method.

It is very difficult to ensure that volatile nuclides such as ^{14}C , ^{36}Cl , and ^{137}Cs remain stable at high temperatures in a solidified product. It is well known that volatile metals such as Cs in the solidified products can be stabilized by maintaining low basicity. Under optimized conditions, it was found that solidified products containing ^{137}Cs could be successfully prepared (Fig.9-6). For ^{14}C and ^{36}Cl , which are more easily volatile elements than Cs at a high temperature, it will be difficult to adjust the interest nuclide concentration in the solidified product on the preparation method of Fig.9-6. Therefore, we examined the following preparation method involving a nuclear reaction to produce a known amount of ^{14}C or ^{36}Cl in a glass. A RM containing either ^{14}C or ^{36}Cl was successfully prepared by the glass (1.5 g) and a solidified product (200 g) prepared from a mixture of nonradioactive concretes and FeO (Fig.9-7). We are planning to use the present preparation methods for the collection and evaluation of data on the radioactivity of wastes at the JAEA.

Reference

Ishimori, K. et al., Preparation of Reference Materials on Radiochemical Analysis for Low-Level Radioactive Waste Generated from Japan Atomic Energy Agency, Proceedings of the ASME 13th International Conference on Environmental Remediation and Radioactive Waste Management (ICEM2010), Tsukuba, Japan, 2010, ICEM2010-40111, 7p., in CD-ROM.

Advanced Computing and Simulation Technology to Support Atomic Energy Research and Development

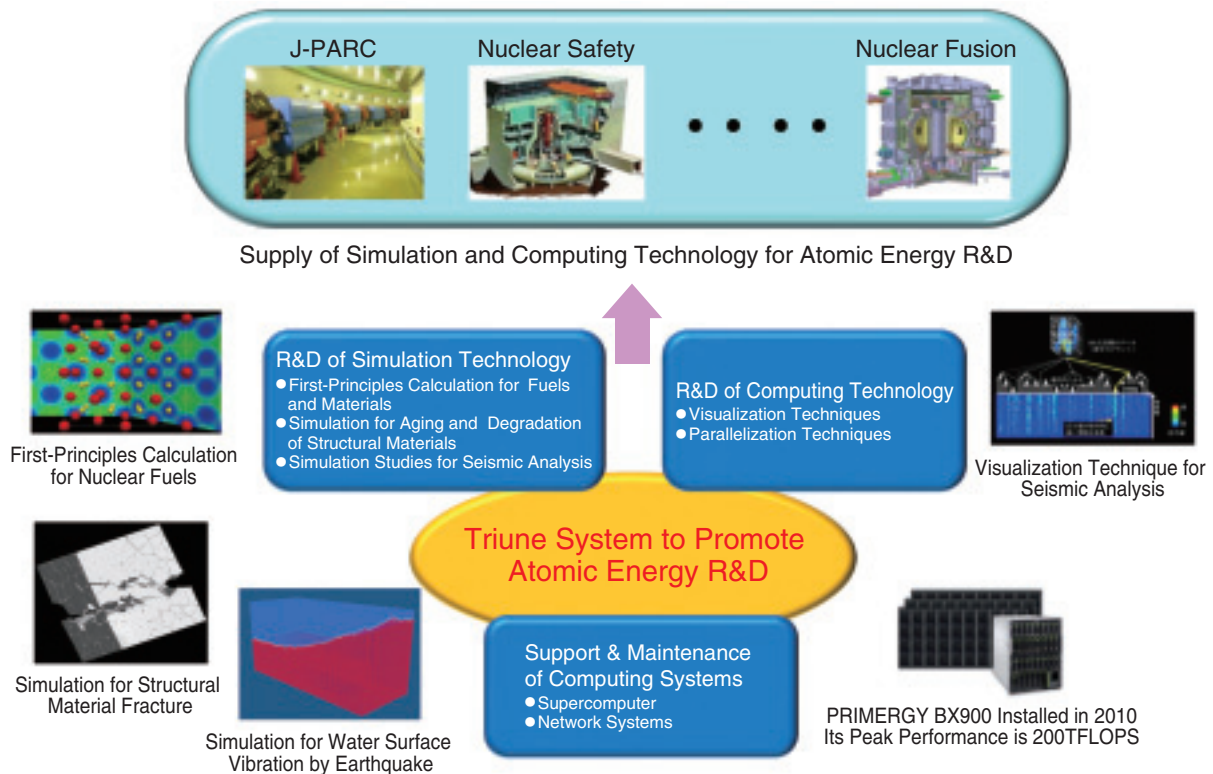


Fig.10-1 Relationship between advanced computing and simulation technology and the present atomic energy research

We play a pioneering role in the research and development of atomic energy technology. Apart from carrying out research on computing and simulation technology, we provide support and maintenance for supercomputers.

Recently, computational science has been recognized as the third methodology, after theoretical and experimental methodologies, and its popularity has increased considerably. For example, the fastest supercomputer in the world, Kei, has been developed. The Center for Computational Science and e-Systems (CCSE) is engaged in the support and maintenance of a supercomputer installed in 2010 and promotes the research and development (R&D) of computing and simulation techniques in the field of atomic energy (Fig.10-1).

Since the main active areas in atomic-energy research are aging management of light-water reactors, establishment of a nuclear fuel cycle, and seismic analysis, we select our R&D areas from these areas and try to resolve various problems via simulations.

In aging management, the R&D objective is to clarify the degradation mechanism and predict the aging process. Toward this end, we utilize first-principles calculations and molecular dynamics for quantum mechanical and atomistic level analyses, respectively, and obtain fundamental data to perform meso- and macroscale fracture simulations. The study is presented in Topic 10-1, and the result of first-principles calculations performed for constructing an atomistic model is shown.

In the area of establishment of a nuclear fuel cycle, a key task is to obtain the material properties of fuel compounds,

including minor actinides. However, experiments for determining such properties are costly and difficult to perform. This area is discussed in Topic 10-2, where a successful R&D result pertaining to the prediction of material properties of plutonium dioxide is presented. This is the first step toward the computational design of fuel materials.

In the area of seismic analysis, since a large earthquake may lead to radioactive water overflow from a spent fuel storage pool and to damage to the pool and structures connected to the pool by increasing the water pressure, a model to precisely analyze turbulence near the water surface and wall is highly desirable. This area is discussed in topic 10-4, a successful R&D result that reproduces experimental results of previous studies has been obtained.

With regard to the R&D of computational techniques, we support the effective use of state-of-the-art techniques for research on various aspects of atomic energy inside and outside the Japan Atomic Energy Agency (JAEA). One example is the improvement of the handling of large-scale data by using the latest visualization technique. Topic 10-3 presents the new technique, which is used to visually detect the part of a structure that is selectively stressed by an earthquake and to easily determine the relationship between the seismic wave amplitude and stress variation.

10-1 Determination of Properties of Nuclear Fuels through Numerical Simulation

— First-Principles Calculations of Electronic States of Plutonium Dioxide —

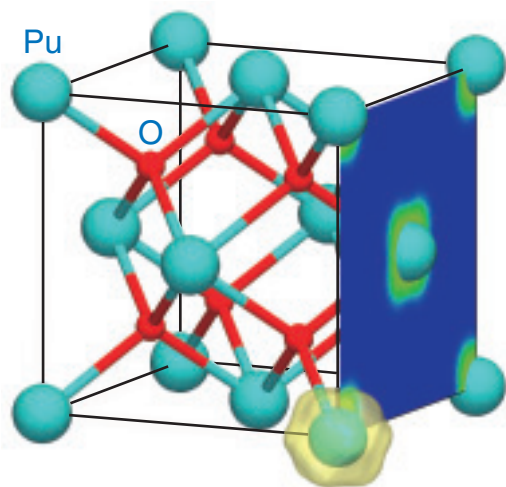


Fig.10-2 Crystal structure of plutonium dioxide and charge density resulting from the presence of f-electrons

The light-blue and red spheres correspond to plutonium and oxygen atoms, respectively. The charge density of f-electrons is depicted in the right-side plane, where the density increases from blue to yellow. The yellow surface around the right lower Pu atom represents the isosurface of the charge density. The charge density is calculated by considering strong correlations and spin-orbit couplings.

In order to develop more secure and more efficient nuclear fuels, we have to have a detailed knowledge of the properties of candidate fuels. However, the determination of the properties through experiments is not easy owing to limitations associated with the handling of nuclear materials and the difficulty in reproducing the high-temperature conditions in nuclear reactors. In such cases, simulations are effective for the evaluation of the properties of nuclear fuels.

Although there are various simulation methods to evaluate material properties, recently, first-principles calculations have come to be very often used. First-principles calculations are considered to be the most reliable method since they use fundamental information only about the interactions of electrons and atoms and need no empirical parameters. However, this method has failed when used for the computation of the electronic states of plutonium dioxide (PuO_2) (Fig.10-2). Specifically, the failure is that the first-principles calculations predict a metallic state of PuO_2 as the ground state, while measurements indicate an insulating state. For a while, the reason for this failure had been believed to be the lack of strong correlations in first-principles calculations;

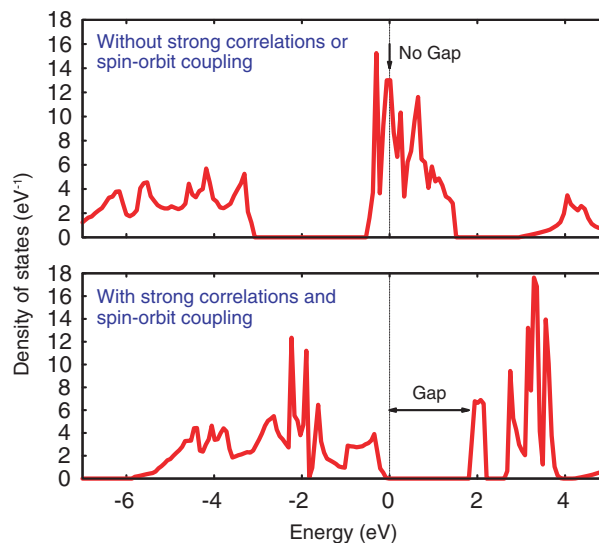


Fig.10-3 Density of states of plutonium dioxide (PuO_2)

The upper panel shows the density of states (DOS) calculated without strong correlations or spin-orbit couplings, and the lower panel shows the DOS obtained by considering strong correlations and spin-orbit couplings. In the upper panel, PuO_2 is considered to be metallic because the DOS with zero energy does not vanish. In the lower panel, the DOS above zero energy has a gap, and therefore, this material is an insulator. Note that the zero energy point corresponds to the Fermi energy.

strong correlations are important in the interactions between so-called “f-electrons” in Pu atoms. However, it was recently reported that first-principles calculations with strong correlations also fail to reproduce the insulating state. We then explored other reasons for the failure. We found that spin-orbit couplings are also necessary to reproduce an insulating state. Although it is known that spin-orbit couplings play a significant role in large atoms such as Pu, they have often been neglected in calculations for PuO_2 so far. We succeeded in reproducing the insulating state by considering both strong correlations and spin-orbit couplings (Fig.10-3).

For the development of new nuclear fuels, information about more complex properties, such as thermal conductivity, and reactions under extreme situations is necessary. In order to obtain the information through simulations, large-scale computing is crucial. In such large-scale computing, reliable results can be achieved by using first-principles calculations. Our success in reproducing the insulating state of PuO_2 by using first-principles calculations is expected to form the basis for the evaluation of more complex properties of nuclear fuels.

Reference

Nakamura, H. et al., Effects of Spin-Orbit Coupling and Strong Correlation on the Paramagnetic Insulating State in Plutonium Dioxides, *Physical Review B*, vol.82, issue 15, 2010, p.155131-1-155131-6.

10-2 Solving the Mystery of Hydrogen-Induced Strength Degradation — Development of Atomic-Scale Model of Hydrogen and Iron Atoms —

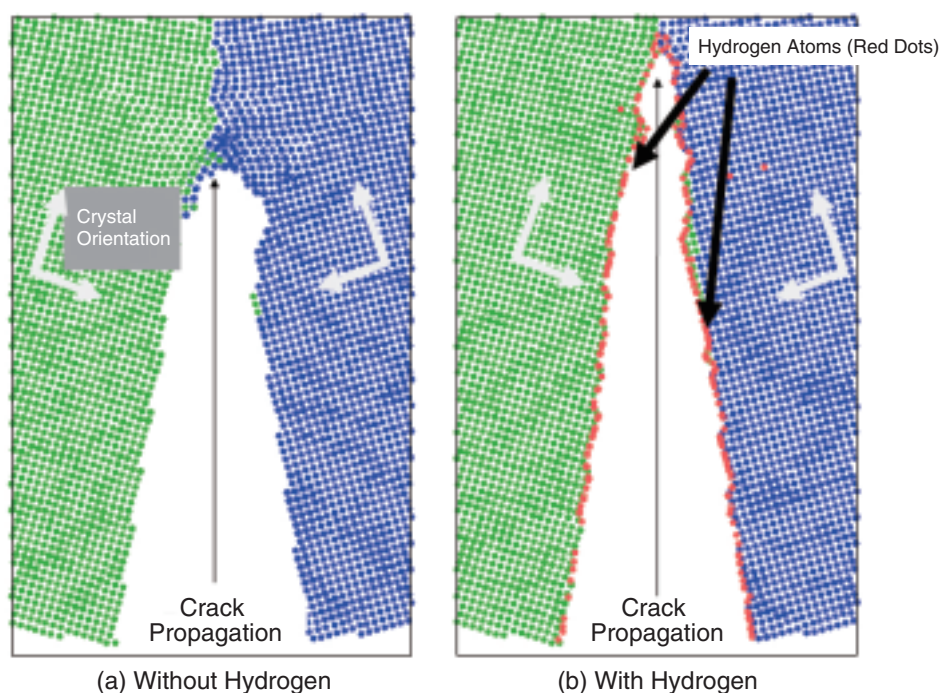


Fig.10-4 Simulation for determining the effect of hydrogen atoms on crack propagation in iron

Using the atomistic model developed in the present work, the crack propagation process has been simulated for two cases: (a) without hydrogen and (b) with hydrogen, which is shown by red dots. A grain boundary is located at the center in each case, and the crystal orientation on the left side of the boundary differs from that on the right side (shown by green and blue dots, respectively). The elapsed time is the same in both cases, and one can see that the crack propagation extends farther in case (b).

In metallic materials such as steel, there exist many local disorders in the atomic configuration; the disorders are referred to as lattice defects, and their number and mobility determine the strength of the material. When hydrogen atoms permeate into the material from the external environment, they interact with the lattice defects and greatly degrade the material strength. Several hypothetical mechanisms, such as weakening of the grain boundaries owing to hydrogen segregation and enhancement of growth of small bubble-like lattice defects (referred to as voids), have been proposed to account for the strength degradation. However, the dominant mechanism remains an open question. To develop reactor materials that are resistant to degradation, it is important to identify the dominant mechanism of degradation and find a way to prevent it.

To solve this problem, we have developed a molecular dynamics model (atomistic model) that is capable of reproducing the atomistic behavior of hydrogen and iron atoms. Several molecular dynamics models for hydrogen and iron have been developed in the past, but they can reproduce only the interactions between hydrogen and some types of lattice defects. On the other hand, we have carried out electronic structure calculations of several dozen cases of lattice defects and hydrogen atom placement to investigate

the interaction between hydrogen and lattice defects in detail. We have developed a model based on the obtained results, which involve a much larger amount of data compared to that in the previous studies. This model facilitates more general calculations of the interaction between hydrogen and lattice defects, and we can now determine which lattice defect plays a more important role in the process of cracking of iron material containing hydrogen atoms.

Fig.10-4 shows simulation results for crack propagation along a grain boundary of iron (a) without hydrogen and (b) with hydrogen atoms segregated on the grain boundary. We have found that compared to the case without hydrogen, hydrogen reduces the strength of the grain boundary by 30% and the crack propagates farther in a given duration when hydrogen atoms are on the grain boundary. It is expected that if we could develop a material in which the accumulation of hydrogen atoms in the lattice defects causing the degradation is prevented, the material strength would increase by a factor of two. We shall continue quantitative investigations into the effect of hydrogen on crack propagation by considering the interaction of hydrogen with other types of lattice defect mechanisms such as void growth to identify the dominant mechanism of hydrogen degradation in steel.

Reference

Ramasubramaniam, A., Itakura, M. et al., Interatomic Potentials for Hydrogen in α -Iron Based on Density Functional Theory, Physical Review B, vol.79, issue 17, 2009, p.174101-1-174101-13.

10-3 Finding Important Information in Experimental or Simulation Results — Proposal of Visualization Technique for Capturing Temporal and Spatial Fluctuations —

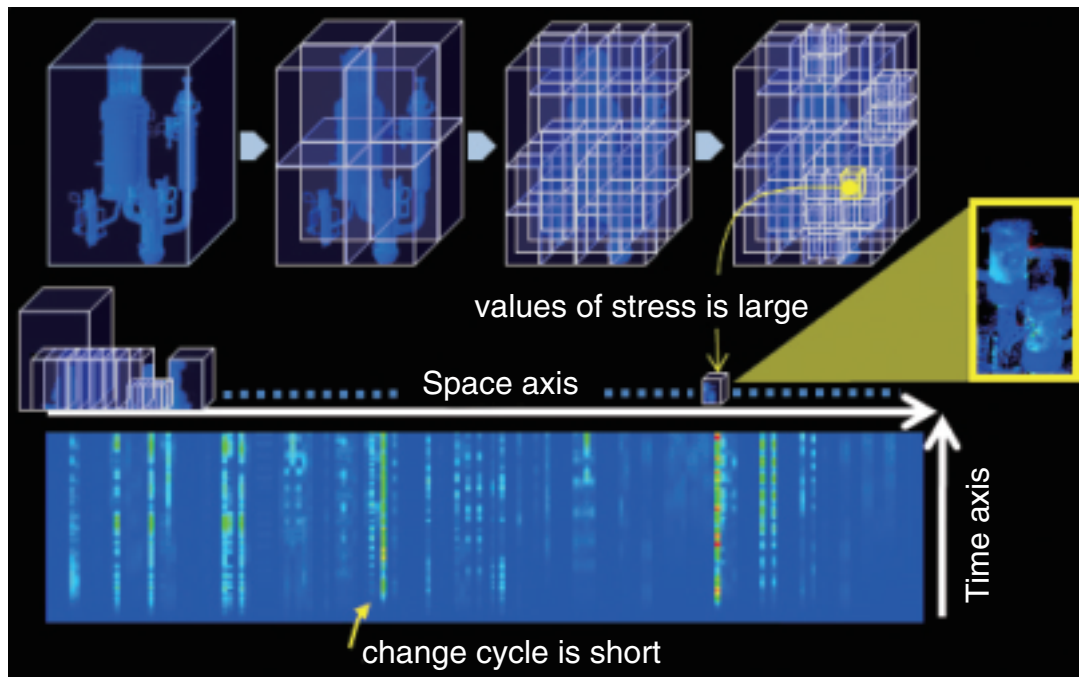


Fig.10-5 Visualization of results obtained from a vibration simulation of a nuclear facility

We show the use of our visualization technique for the analysis of the stress fluctuation in a vibration simulation of a nuclear facility after an earthquake. First, we put a three-dimensional model of the nuclear facility inside a hexahedron and then subdivide the hexahedron into smaller hexahedrons (upper part). Next, we define a space axis by arranging these smaller hexahedrons in one line. Further, we define a time axis perpendicular to the space axis and represent the values of stress by using a color scheme in the plane formed by these two axes (lower part). From this representation, we find time and space with a comparatively large stress (the right image surrounded by yellow lines).

“Homer sometimes nods.” This kind of experience is familiar to everybody. However, in the atomic energy research field, it is important to avoid overlooking valuable information during the design, construction, operation, and inspection of nuclear facilities. We are trying to develop a visualization technique to simultaneously capture temporal and spatial fluctuations in order to prevent important information in experimental and numerical simulation results from being overlooked.

This report describes our visualization technique by considering its application to a vibration simulation of a nuclear facility after an earthquake. The simulation was conducted by the Center for Computational Science & e-Systems (CCSE). It was carried out to detect where in the nuclear facility a comparatively large stress was caused. From the simulation results, it is necessary, but difficult, to find answers to the questions “when,” “where,” and “what” for an event occurring in the nuclear facility. Therefore, we propose a technique in which time and space, corresponding to “when” and “where” respectively, are projected onto the frame of a plane (visualization plane) and each phenomenon corresponding to “what” is graphically represented in the plane.

The projection of time and space onto the frame requires the projection of three-dimensional space onto one axis. We propose a projection method to represent three-dimensional

space as an arrangement of small hexahedrons in one line (space axis); the method involves the use of an octree. Here, the accuracy required for the analysis can be obtained by adjusting the number of subdivisions according to the features of the data (upper part of Fig.10-5). Next, we define a time axis perpendicular to the space axis, and these two axes form a two-dimensional space-time plane (visualization plane). The stress distribution map is generated in terms of space and time by plotting the stress values obtained from the vibration simulation (lower part of Fig.10-5).

In this map, we identified the time and space with a comparatively large stress, and they corresponded to the point of intersection of pipes. Moreover, we understood that the stress is caused at an early stage after the occurrence of the earthquake and that the stress thereafter fluctuates with the passage of time.

By using our technique, we can find parts that are susceptible to an earthquake, without there being a risk of their being overlooked, and suggest improvements for the safety of the nuclear facility, for example, the reinforcement of such parts.

It is expected that our technique will also be applicable to various experiments and simulations that involve parameters with spatiotemporal fluctuations, such as thermal fluctuations and stress fluctuations.

Reference

Miyamura (Nakamura), H. et al., Overview Visualization of Time-Series Dataset, FUJITSU Family Association, 2010, 15p. (in Japanese).

10-4 Understanding Fluid Motion in a Spent Fuel Pool

— Proposal of Fluid Analysis Model including Turbulent Effect near Surfaces and Walls of Pool —

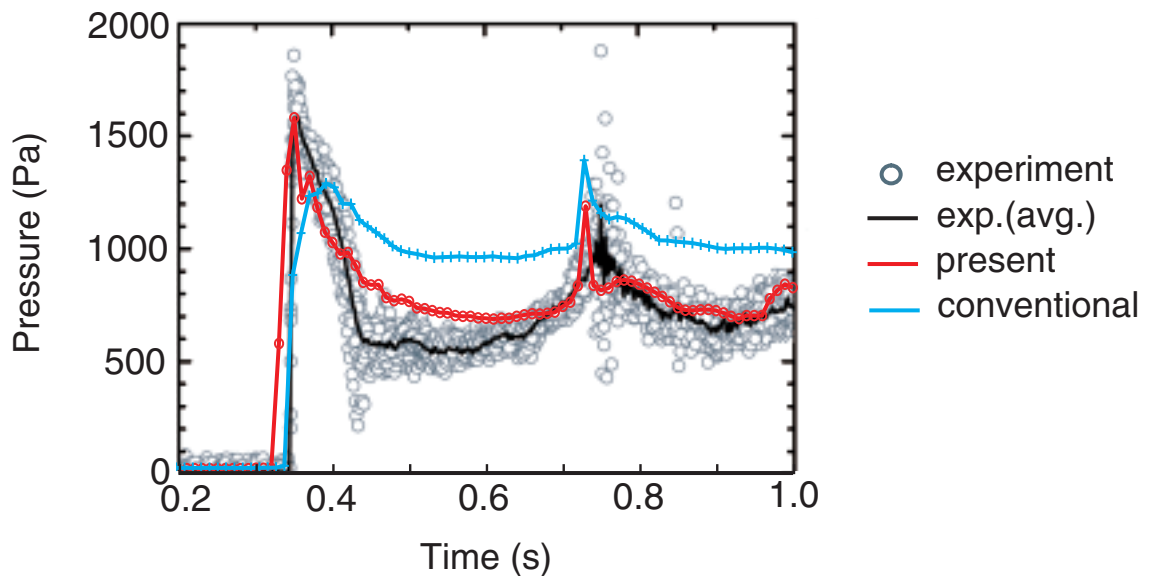


Fig.10-6 Difference in fluid pressure on the wall of a pool between two turbulence models

Fluid pressures on the wall of a pool predicted by our model and a conventional model are compared with that measured in an experiment. The predictions of our model are in good agreement with the experimental results.

At a nuclear power facility, spent fuel from the reactor is temporarily stored in a pool of water called spent fuel pool. During an earthquake, the water surface in the pool will undergo dynamic and complex deformation (i.e., sloshing is induced). This sloshing may lead to the overflow of the radioactive water and damage to the pool and the structure attached to the pool by increasing the fluid pressure. To preclude such an occurrence, it is important to know the wave height and fluid pressure resulting from sloshing.

Experiments and conventional numerical simulation studies on sloshing have shown that the wave height is damped by the drag produced by the structure and that the pressure has its maximum value near the water surface. However, the effects of turbulence on the wave height and pressure are not fully understood when sloshing is sustained for a long time, which leads to a transition from laminar to turbulent flow. Hence, in the presence of sloshing and turbulent flow, only conservative estimates have been possible so far.

We propose a turbulence model that can accurately determine all the six components of Reynolds stress to allow estimation in a more qualitative manner and to elucidate the

physical mechanism of the turbulence effects. In experiments, it is not easy to investigate each component separately, and simulation is more effective for elucidating the mechanism. However, conventional models do not reproduce experimental results. We found that while its accuracy is insufficient when turbulent eddies transform flat near water surfaces and walls, its accuracy is sufficient for isotropic turbulence. We thought that this inaccuracy could be attributed to the fact that the conventional models only determine three components of Reynolds stress.

Numerical simulation results obtained by using the proposed model with all six components are in good agreement with experimental results, as shown in Fig.10-6. Specifically, the calculated pressure values, such as those corresponding to the two pressure peaks and the relaxation process between the peaks, approximate the experimentally determined values well. Furthermore, the predicted wave height also agrees with the experimental value.

In a future work, we intend testing the model by using it for predicting fluid motion during an earthquake; we shall input actual measured seismic waves.

Reference

Uzawa, K. et al., Effects of Turbulence near a Free Surface on the Dynamics of Two-Phase Flow, Proceedings of 19th International Conference on Nuclear Engineering (ICONE 19), Chiba, Japan, 2011, ICONE19-43453, 8p., in CD-ROM.

Development of Nuclear Nonproliferation Technology to Support Peaceful Use of Nuclear Energy

New efforts to develop new nuclear security technologies

At the Nuclear Security Summit in April 2010, the Japanese government announced that Japan would promote research cooperation with the U.S. for the development of technology that would contribute to advances in the measurement and control of nuclear material, as well as the development of technologies related to nuclear material detection and nuclear forensics for the identification of the origin of illicitly trafficked nuclear material. Moreover, the announcement included the establishment of the Integrated Support Center for Nuclear Nonproliferation and Nuclear Security (ISCN) under the Japan Atomic Energy Agency (JAEA) with the aim of improving infrastructure and assisting in the development of human resources and of improving infrastructure. The focus of the ISCN is particularly on Asia in order to strengthen nuclear security. We are working towards the realization of these pronouncements.

Nuclear nonproliferation technology development for Japan and international applications

We have developed technologies for nuclear nonproliferation, including proliferation-resistant technologies, advanced safeguards systems, and nuclear security technologies. In the field of safeguards environmental sample analysis, we have been providing technical support to the International Atomic Energy Agency (IAEA) through the IAEA network Laboratories.

Contributions to the international community based on our technology and experience

We contribute to the establishment of international monitoring systems for nuclear tests. As part of activities

relating to the comprehensive nuclear-test-ban treaty (CTBT), we have operated radio nuclide monitoring stations, transmitted data worldwide, and built a national data center.

Contribution to the development of human resources

The ISCN, established in December 2010, new effort by the government, has conducted training courses and seminars on nuclear security and safeguards for nuclear experts, both in their countries and in Japan, in cooperation with the IAEA and the U.S.

Domestic and international contributions utilizing management and experience of handling nuclear materials

We have had an effective system for the management of our nuclear materials. Moreover, we assist in streamlining inspections, for example, by providing technical support to the Japanese government and IAEA. We also provide support to the IAEA for physical protection, apart from responding appropriately in the case of revisions of Japanese laws.

Role of recognized think tank in Japan as a resource center for Asia

We have researched and analyzed international trends in nonproliferation and nuclear security in order to realize both peaceful use of nuclear energy and nonproliferation. In Asia, Vietnam, for example, we have provided support in nonproliferation infrastructure development through the ISCN by implementing measures that are in accordance with a country's specific circumstances and by sharing our experience.

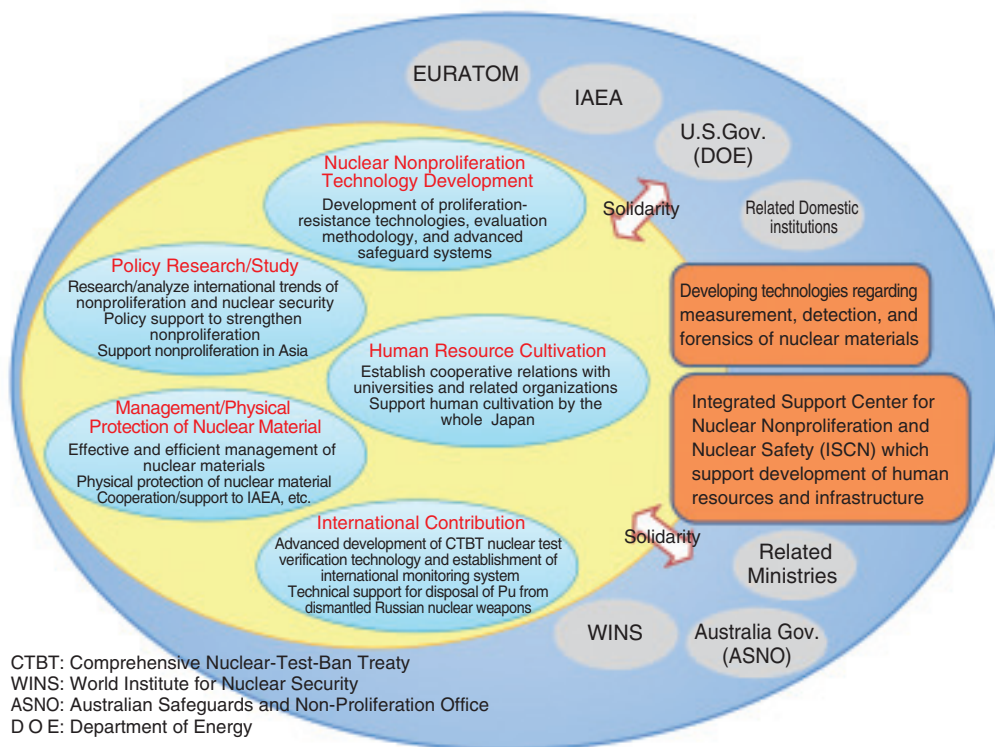


Fig.11-1 JAEA activities pertaining to scientific and technical development for nuclear nonproliferation

We have two primary missions with regard to nuclear nonproliferation: to support the government in developing nonproliferation policies through research and study and to support government and international organizations by developing nuclear nonproliferation technology.

11-1 Evaluation of Japan's Nuclear Non-Proliferation Efforts in Terms of Providing Guidance to Other States

— Key Elements to Win the Confidence in the Peaceful Nature of the Nuclear Energy Use and Recommendations for the Future —

Table 11-1 Key elements for Japan's nuclear non-proliferation efforts and recommendations for the future

We have identified key elements in seven areas and make recommendations for the future.

Areas	Key Elements	Recommendations for the future
Legislative measures	<ul style="list-style-type: none"> ● Pledge to limit nuclear energy use to peaceful purposes ● Legislative measures to ensure this pledge 	<ul style="list-style-type: none"> ● Preparation of guidelines to ensure peaceful use in the licensing process
Commitment and contribution to the international regime	<ul style="list-style-type: none"> ● Commitment not to acquire nuclear explosive devices ● Commitment not to carry out nuclear explosion ● Compliance with bilateral nuclear cooperation agreements ● Commitments and cooperation for other international efforts or to international organizations 	<ul style="list-style-type: none"> ● Proactive contribution to the strengthening nuclear non-proliferation regime ● Consideration of options on the Japan-U.S. Nuclear Cooperation Agreement, which expires in 2018 ● Dispatching more Japanese staff to international organizations
Safeguards	<ul style="list-style-type: none"> ● Ratification of Comprehensive Safeguards Agreement ● Establishment of State System of Accounting for and Control of Nuclear Material ● Ratification of Additional Protocol ● Application of integrated safeguards ● Compliance with safeguards agreement ● Cooperation with IAEA to address challenges for safeguards ● Cooperation for safeguards on institutional and technological aspects 	<ul style="list-style-type: none"> ● Optimization of overall safeguards efforts ● Incorporation of safeguards measures in the design of next-generation fuel cycle facilities ● Proactive contribution to efforts for improving effectiveness and efficiency of IAEA safeguards ● Support for the development of safeguards infrastructure in emerging nuclear states
Measures to ensure transparency	<ul style="list-style-type: none"> ● Adoption of nuclear energy policy and its public disclosure ● Disclosure of the process for the revision of nuclear energy policy and the participation of general public ● Review of the implementation of the nuclear energy policy ● Participation in the discussion for international regime for plutonium use ● Disclosure of information on plutonium utilization 	<ul style="list-style-type: none"> ● Development of rationale to justify the amount of plutonium possessed ● Consideration of the feasibility of multilateral scheme to manage backend of nuclear fuel cycle
Measures at sensitive nuclear facilities	<ul style="list-style-type: none"> ● Deployment of proliferation resistant nuclear technology ● Cooperation on the conversion of research reactors to low enriched uranium use and the return shipment of high enriched uranium 	<ul style="list-style-type: none"> ● Enhancement of proliferation resistance of Fast Breeder Reactor cycle ● Development of international consensus on guidelines to evaluate proliferation resistance
Export control and management of sensitive nuclear technology	<ul style="list-style-type: none"> ● Export control in accordance with Nuclear Suppliers Group Guidelines ● Participation in other international frameworks for export control and counter-proliferation efforts ● Efforts to ensure control of sensitive nuclear technology within the relevant organizations 	<ul style="list-style-type: none"> ● Cultivation of nuclear non-proliferation culture within organizations that handle sensitive nuclear technology ● Consideration of the introduction of domestic law on the management of sensitive nuclear technology
Physical Protection and Nuclear security	<ul style="list-style-type: none"> ● Ratification of the Physical Protection Convention ● Ratification of Nuclear Terrorism Suppression Convention ● Implementation of measures in accordance with the latest version of INFCIRC225 ● Participation in other international efforts for nuclear security 	<ul style="list-style-type: none"> ● Consideration for the early ratification of the Amendment to the Physical Protection Convention ● Consideration of the reliability check system ● Cultivation of nuclear security culture

A. Necessary items regardless of the existence of nuclear activities

B. Items that accompany nuclear activities

C. Items that accompany nuclear fuel cycle activities

Japan has been implementing a nuclear energy program since the 1950s in a transparent manner, explicitly limiting the use of nuclear energy to peaceful purposes, and it has contributed to international efforts to ensure nuclear non-proliferation. This research is aimed at identifying the elements applicable to other states through a review, an analysis, and an evaluation of Japan's past efforts to ensure nuclear non-proliferation.

In this research, we have reviewed, analyzed, and evaluated Japan's nuclear non-proliferation efforts by dividing them into seven areas, and we have identified the key elements and issues for consideration in the future (Table 11-1). The analysis clearly shows that Japan's nuclear non-proliferation efforts have so far satisfied international standards in the respective areas and have even exceeded them in some areas. We have identified issues to be considered in the future. These include proactive contribution to strengthening the nuclear non-proliferation regime and to

relevant international organizations, optimization of overall safeguards efforts under the integrated safeguards, and the ratification of the amendment to the Convention on the Physical Protection of Nuclear Material.

Japan has a unique status as a non-nuclear-weapon state that pursues nuclear fuel cycle activities such as enrichment and reprocessing. Some features of our nuclear non-proliferation efforts may originate from the unique status. Therefore, we have classified our efforts into three categories: A. Necessary items regardless of the existence of nuclear activities, B. items that accompany nuclear activities, and C. items that accompany nuclear fuel cycle activities.

Our experience with regard to categories A. and B. can serve as guidance for states that plan to introduce nuclear power generation; it can clarify what kind of efforts should be made for nuclear non-proliferation. Japan's role is to help such emerging nuclear states in their effort to ensure nuclear non-proliferation, by focusing on these items.

Reference

Yamamura, T. et al., Review and Analysis of Japan's Efforts to Ensure Nuclear Non-Proliferation—Significant Elements in Terms of Winning Trust for the Peaceful Nature of the Nuclear Energy Use and Future Challenges—, JAEA-Review 2010-40, 2010, 180p. (in Japanese).

Tsuruga Head Office

The "MONJU" System Start-up Tests (SST) were restarted in May 2010 and the Core Confirmation Tests (CCT) that constitute the first stage in the third stage of the SST were completed in July 2010. Although the drop of the In-Vessel Transfer Machine (IVTM) occurred after refueling in August 2010, we completed the withdrawal of IVTM on June 24, 2011. We are currently performing the integrity evaluation of the IVTM on the basis of the results of the overhaul inspection. In addition, following the accident at the Tokyo Electric Power Company, Incorporated Fukushima Daiichi Nuclear Power Station, safety measures are being implemented. The "FUGEN" Decommissioning Engineering Center steadily conducts decommissioning. We launched an open-type business in 2010 with the aim to cooperate with local industries in Fukui Prefecture in finding solutions for research challenges facing JAEA in.

Tokai Research and Development Center, Nuclear Science Research Institute (NSRI)

Research reactors (JRR-3, JRR-4, NSRR), accelerators (Tandem etc.), critical assemblies (STACY, FCA, etc.), and hot laboratories (WASTEF, BECKY, etc.) have been operated for R&D activities of the research directorates of JAEA. An innovative technique for the replacement of panels of a large glove box for safely handling radioactive materials was developed in order to reduce the cost and labor for the maintenance of glove boxes (Referred to Topic 12-2). This year the Minister of Education, Culture, Sports, Science and Technology awarded a prize for great originality in science and technology to this technical development. A mirror enabling the supply of high-intensity cold neutron beams was designed at JRR-3. High-quality monoenergetic neutron reference fields were developed so that the technology base for utilizing neutrons can be reinforced. Furthermore, manufactures employed electronics technologies developed at NSRI and X-ray diagnostics to produce a new measuring instrument—a very-high-accuracy X-ray fluorescence analyzer.

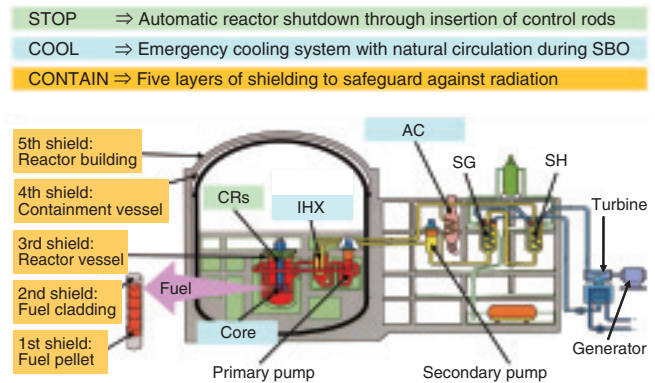
Tokai Research and Development Center, Nuclear Fuel Cycle Engineering Laboratories

At the Plutonium Fuel Development Center, engineering scale tests associated with the fabrication of annular mixed oxide (MOX) pellets and oxygen-to-metal ratio (O/M) adjustment are being carried out to develop the fuel fabrication process named the "Simplified MOX Pellet Fabrication Process" (Topic 12-4). Fifteen fuel assemblies fabricated by the pellets obtained from the test were supplied to "MONJU" for use in its plant performance test.

At the Reprocessing Technology Development Center, seismic reinforcement of Tokai Reprocessing Plant is being carried out. Technical cooperation with the Japan Nuclear Fuel Limited (JNFL), which includes supporting the active test of the Rokkasho Reprocessing Plant (RRP) and training JNFL's engineers, is also carried out.

Various other research and development (R&D) activities, such as advanced reprocessing by using an aqueous method (Topic 12-3) and geological disposal technologies, are being conducted.

Additionally, the safety design of an incineration facility for radioactive waste treatment was discussed.



- The facilities important for safety, including sodium systems, are located 21 m above sea level, and seawater pumps for cooling are surrounded by waterproof walls that offer protection against tsunamis.
- The integrity of reactor cooling systems against earthquakes has been reaffirmed by a seismic safety estimation based on the new guideline.
- Stainless steel is used for the cladding material, and therefore, there is no production or explosion of hydrogen.

Safety design of "MONJU"



Japan Research Reactor-3 (JRR-3)



Nuclear Fuel Cycle Safety Engineering Research Facility (NUCEF)

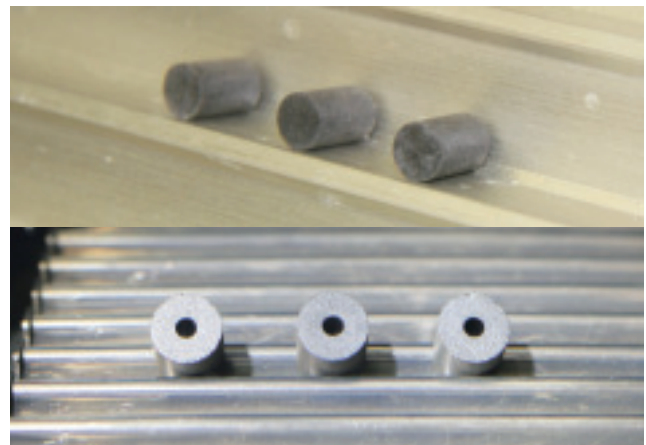


Nuclear Safety Research Reactor (NSRR)



Reactor Fuel Examination Facility

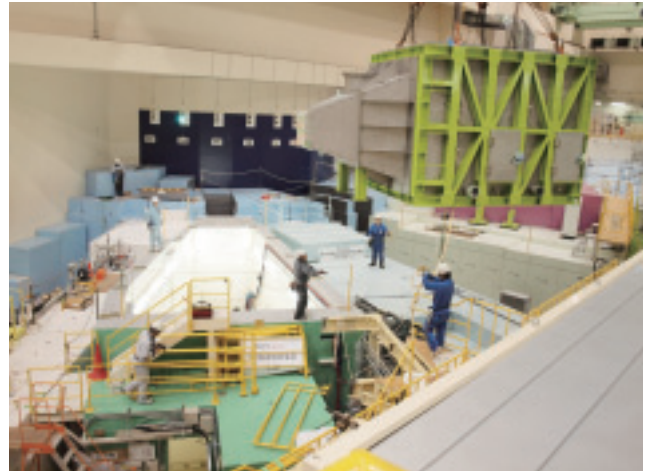
Main research facilities at Nuclear Science Research Institute



Appearances of sintered annular MOX pellets (under development) (Upper: MOX pellets fabricated by conventional method)

J-PARC Center

During the Japanese fiscal year 2010, the intensity of the proton beam delivered to the Materials and Life Science Experimental Facility (MLF) was increased from 120 kW to 200 kW, as planned, and the acceleration test with the 420 kW equivalent beam was also successfully carried out. The intensities of the proton beams to the Nuclear and Particle Experimental Facility and to Neutrino Experimental Facility (NU) were increased up to 3.6 kW and 145 kW, respectively. For the MLF user program, 350 proposals were accepted, which was a 35% increase from the number of proposals accepted in the fiscal year 2009. Moreover, the events indicating the oscillation from muon neutrinos to electron neutrinos were detected for the first time in the world at the Super-Kamiokande detector in Kamioka in Gifu Prefecture situated 295 km away from J-PARC where the muon neutrinos were produced. The annual duration of the operation of J-PARC was about 120 days in which the cumulative neutron-production duration exceeded 2300 h. Users utilized the MLF and NU for 5000 and 16000 person-days, respectively, before the operation was terminated by The Great East Japan Earthquake on March 11, 2011.



Installation of vacuum chamber for neutron instrument BL15 in Materials and Life Science Experimental Facility. BL15 is the first instrument for public utilization in MLF constructed in accordance with the Law for Promotion of Public Utilization of the Specific Advanced Large Research Facilities.

Oarai Research and Development Center

Experiments such as post-irradiation examinations of FBR high burn-up fuels and minor actinide-containing fuels, and sodium tests, were conducted for the Fast Reactor Cycle Technology Development (FaCT) Project. Moreover, construction of the Advanced Technology Experimental Sodium facility (AtheNa) for coolant system equipment as the demonstration plant continued.

In the Japan Materials Testing Reactor (JMTR), refurbishment work on a cooling system and of an instrumentation and control system for JMTR restart has been completed. The International Symposium on Material Testing Reactors was held with the aim to exchange information and hold discussions on topics related to international standard technology.

In the experimental fast reactor Joyo, detailed design of equipment for the recovery of an obstacle on the in-vessel storage rack and of an exchange equipment of upper-core structure were carried out.

In the High Temperature Engineering Test Reactor (HTTR), performance data for basic technology establishment and commercialization of high-temperature equipment were obtained through a loss-of-core-flow test for safety demonstration.



Renewed instrumentation and control system in JMTR control room

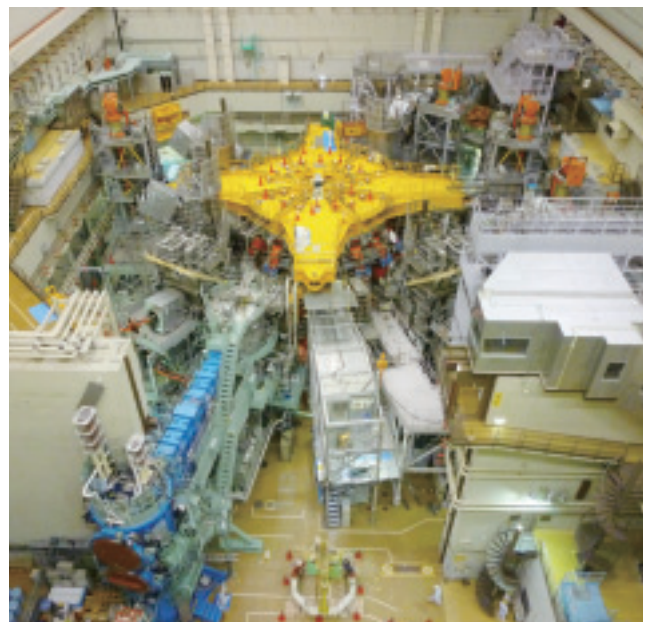
Naka Fusion Institute

Naka Fusion Institute promotes research and development for realizing the practical use of fusion energy.

It is now acting as a domestic agency of the International Thermonuclear Experimental Reactor (ITER) project, and it is mainly involved in the procurement and development of the JA-shared apparatuses. Further, in cooperation with EU, as Broader Approach (BA) activities, the institute is working on the upgrade of the large tokamak device JT-60 to a satellite tokamak device (JT-60SA) that will be used in studies supporting and complementing the ITER project.

In 2010, disassembly of JT-60 was fully started, and it is in progress. Further, the removal of the tokamak auxiliary devices such as the measurement devices, plasma-heating devices, gas-injection device, and platform for measurement devices was carried out. In addition, the removal of approximately 12,000 pieces of the first-wall tiles in the vacuum vessel was completed.

The fabrication for JT-60SA and the procurement of the superconductor to use for the magnetic field coil of real machine in our site have also been continued. On the basis of the experiences in the manufacturing of the prototype, the fabrication of the vacuum vessel was started.



Main part of JT-60 under the disassembly work (March 2011)

Takasaki Advanced Radiation Research Institute

Takasaki Ion Accelerators for Advanced Radiation Application (TIARA), consisting of four ion accelerators, an electron accelerator, and gamma irradiation facilities at the JAEA's Takasaki Advanced Radiation Research Institute, are available to researchers in JAEA and other organizations for performing R&D activities on new functional and environmentally friendly materials, biotechnology, radiation effects of materials, and quantum beam analysis. Practical technology-development activities related to the following are in progress: microbeams, single ion hits, and techniques for uniform wide-area irradiation at a cyclotron, and three-dimensional in-air PIXE analysis and three-dimensional microbeam writing technology with different energy proton beams at the electrostatic accelerators. In 2010, the development of a beam-formation technique was started, which will provide a wide and uniform beam of heavy ions of several hundreds of megaelectronvolt. A chamber was designed and installed in the beam line of the AVF cyclotron for this purpose (Topic 12-10).

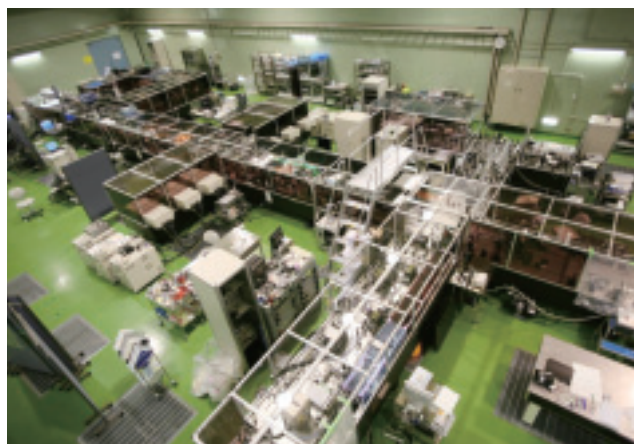


Chamber installed in the LB course of the AVF cyclotron for formation of wide and uniform beam irradiation area

Kansai Photon Science Institute

In the Kizu District, we are improving laser facilities, e.g., the improvement in the quality of a high-intensity laser. In addition, we are developing "High Quality Ultra Advanced Radiation Sources" (QUADRA) in the Consortium for Photon Science and Technology (C-PhoST) as a managing institution. In the Photo-Medical Research Center, we have developed elemental technologies for a laser-driven particle accelerator.

In the Harima District, we have been developing and improving a state-of-the-art measurement technique using intense X-rays at four JAEA beamlines at SPring-8, the world's largest synchrotron radiation facility. In addition, we have also been conducting material science research related to energy and environment, including actinide compounds, which are important in nuclear energy development and all related research, using the JAEA beamlines.



JAEA Kansai Advanced Relativistic Engineering (J-KAREN) laser system

Horonobe Underground Research Center

At the Horonobe Underground Research Center, we are utilizing the underground facilities for promoting an underground research laboratory project for "geoscientific research" and "research and development of a geological disposal technology" suitable for sedimentary rocks.

In fiscal year 2010, the East access shaft was excavated from a depth of 220 m to 250 m. The 250-m-depth drift was connected between the East access shaft and the ventilation shaft in June 2010.

As part of the geoscientific research, we continuously carried out the following: development of techniques for investigating the geological environment, development of techniques for long-term monitoring of the geological environment, development of engineering techniques for use in the deep underground environment, and studies on the long-term stability of the geological environment.

Further, as part of the research and development of a geological disposal technology, we investigated the effect of low-alkaline cement (Highly Fly-ash Contained Silica-fume Cement) on the surrounding groundwater and rock mass in the 140-m-depth gallery.

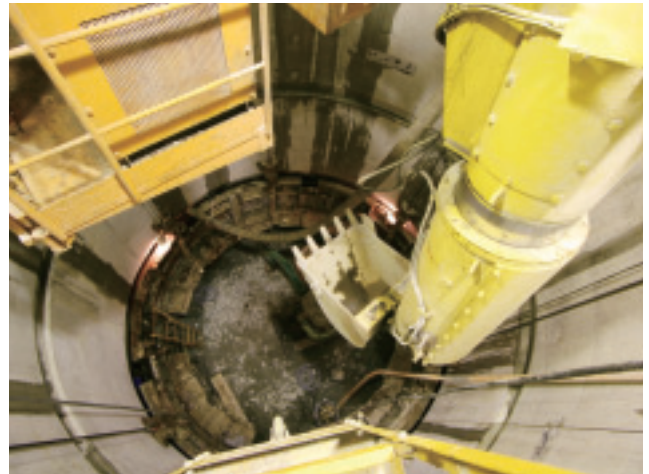
In order to continue the project efficiently, we introduced the Private Finance Initiative (PFI) in January 2011.



West Access Shaft (photo 2011.6.1)

Tono Geoscience Center (TGC)

The TGC's task is to provide the scientific and technical foundations for developing a safe technique for the geological disposal of high-level radioactive waste. This involves research on the long-term stability of the geological environment, and research on the development and improvement of techniques for the characterization of the deep geological environment and a wide range of engineering techniques for deep underground applications at an underground research laboratory in crystalline rock, referred to as Mizunami Underground Research Laboratory (MIU). As of March 2011, the Main and Ventilation Shafts had reached GL -481.3 m and -497.7 m (meters below ground level) (Topic 12-11). Research and development activities, such as geological mapping during excavation and borehole investigations at the stages at GL -300 m and -400 m, were carried out.



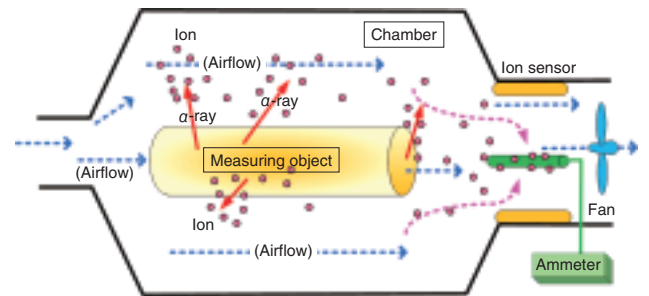
View of the Main Shaft at GL -480 m

Ningyo-toge Environmental Engineering Center

At the Ningyo-toge Environmental Engineering Center, many of the centrifuges that were tested for enrichment are kept in the facility. We are working on the dismantling and decontamination of these centrifuges. It is necessary to dispose them efficiently. Therefore, some tests were conducted in collaboration with the relevant division and company.:

- (1) α radiation measurement technology with ionized-air-type measurement for applicability evaluation of the clearance level. (consignment study: Japan Nuclear Fuel Limited)
- (2) Cross-counter emulsion-flow wastewater treatment system for separating the uranium in wastewater. (coordinated study: Nuclear Science and Engineering Directorate)
- (3) Vaporization rotating-jet incineration system for disposal of organic radioactive liquid waste by analysis. (original study)

The results of these tests are used in developing the centrifuge disposal technology, and the applicability of this technology to the disposal of other equipment and facilities are evaluated.



Measurement principle

The ion ionized by the α -ray is transported by the airflow, and the current measured with the ion sensor is converted into radioactivity

Conceptual diagram of α radiation measurement technology with ionized-air-type measurement

Aomori Research and Development Center

In the Rokkasho district, the use of radioisotopes in the demo R&D building is expected to be allowed by the authorities in FY2011, and now preparation for the full-scale operation of the building as one of three research facilities for the BA activities is now in progress. The computational simulation center (CSC) is also preparing for the installation of the super computer (created by Bull, France) whose operation is slated to start in FY2011.

In the Mutsu district, the following are being simultaneously carried out: (1) A research survey is being conducted to develop a reasonable/economical large-assembly-dismantling methodology for operating a waste disposal plant to be used by research facilities and for decommissioning the nuclear-powered ship Mutsu; this methodology would include the survey of the contaminants. (2) A technology for analyzing ultratrace elements using accelerator mass spectrometry (AMS) is being developed.



The super computer that is advancing installation

12-1 What Was Acquired from Restarted “MONJU” Operation

— Results of the “MONJU” Core Confirmation Test —

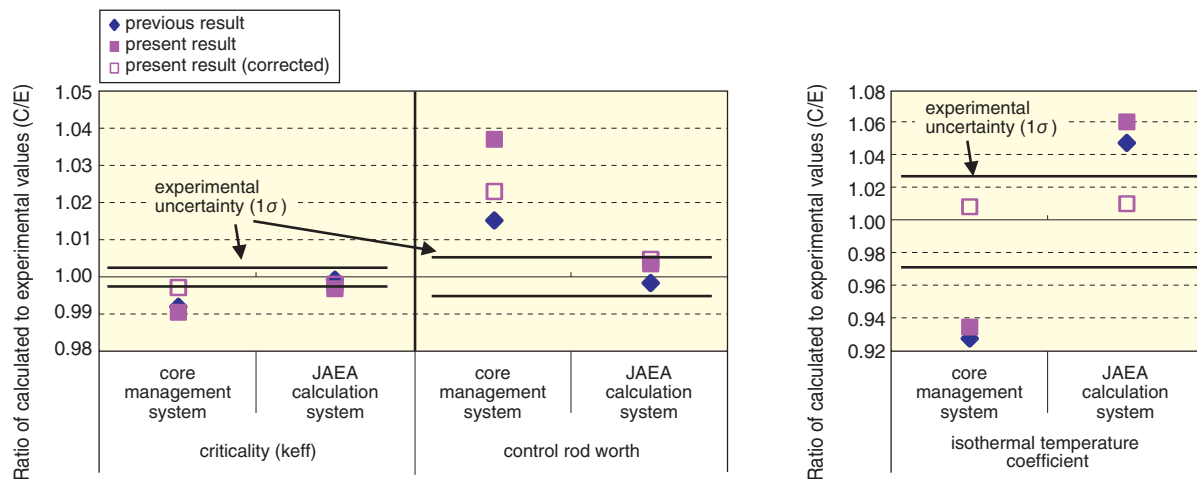


Fig.12-1 Calculated/experimental (C/E) values of neutronics characteristics

Values of criticality, control rod worth, and isothermal temperature coefficient obtained from the JAEA calculation system agree with the measured values within a reasonable uncertainty. The values calculated by the core management system for “MONJU”, corrected based on measured values, are in good agreement with the measured values.

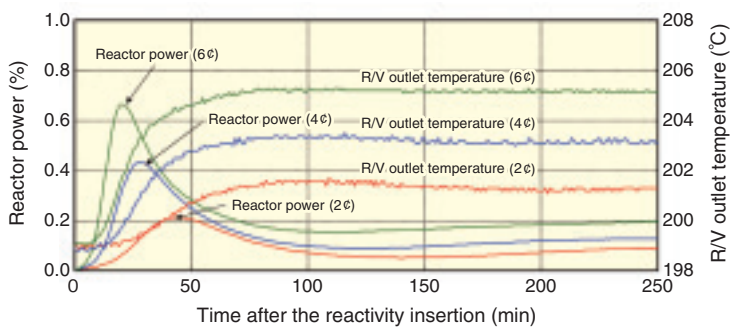


Fig.12-2 Reactor power and coolant temperature transient

The reactor power increased after reactivity insertion owing to control rod withdrawal. Because of the Doppler effect resulting from the increase in the fuel temperature, the reactor power decreased 20~40 min after the reactivity insertion and stabilized.

The prototype fast breeder reactor “MONJU” restarted operation on May 6, 2010, and reached criticality on May 8, 2010. Fourteen years and five months have passed since the sodium leakage on December 8, 1995, from the secondary cooling loop. The system startup test (SST) is planned to be conducted, and it consists of three tests: Core Confirmation Test (CCT), 40%-power Confirmation Test, and Power Rising Test. The 78-day CCT, which involves 20 test items including confirmation of the safety criteria and measurement of several core performance data, ended on July 22, 2010.

In the CCT, basic neutronics characteristics were determined, for example, the criticality and control rod worth. We confirmed that the core characteristics satisfied safety criteria such as those relating to the excess reactivity and reactivity shutdown margin. Furthermore, tests to acquire core characteristics data for R&D were carried out, for example, the flow rate coefficient, isothermal temperature coefficient, feedback reactivity, applicability evaluation of subcriticality measurements, and characterization of the ultrasonic sodium temperature sensors. In addition, dose rate distribution, impurity content of the coolant and cover gas, and flow coastdown rate of the primary pump were measured.

The fuel loaded in the CCT core contained ^{241}Am owing to

the decay of ^{241}Pu as a result of long-term shutdown. The average ^{241}Am content of the core was 1.5 wt%, and therefore, it was expected that the exact calculation of the criticality would be difficult. The calculation accuracy was confirmed by the CCT physics data. Results are shown in Fig.12-1. In the JAEA calculation system that we developed for R&D and for the design of fast breeder reactors (FBRs), etc., the calculated values agreed with the measured values within 1σ . It was confirmed that the values calculated by the core management system for “MONJU”, corrected based on measured values, is in good agreement with the measured values. The feedback reactivity evaluation result is shown in Fig.12-2. The reactor power increased after reactivity insertion owing to control rod withdrawal. Because of the negative feedback reactivity resulting from the Doppler effect etc., the reactor power decreased 20~40 min after reactivity insertion and stabilized.

The SST of “MONJU” was reconducted, and valuable basic data were acquired for FBR development, for example, reactor physics data of the core, which contains a large amount of ^{241}Am .

These data will be used for R&D, such as that discussed in Topic 1-7(p.17).

Reference

Jo, T. et al., Core Confirmation Test in System Startup Test of the Fast Breeder Reactor MONJU, JAEA-Technology 2010-052, 2011, 84p. (in Japanese).

12-2 Low-Cost and Labor-Saving Method for Replacement of Acrylic Panels of a Large Glove Box

— Innovative Panel Replacement Technique Using Bag-In/Bag-Out Method —

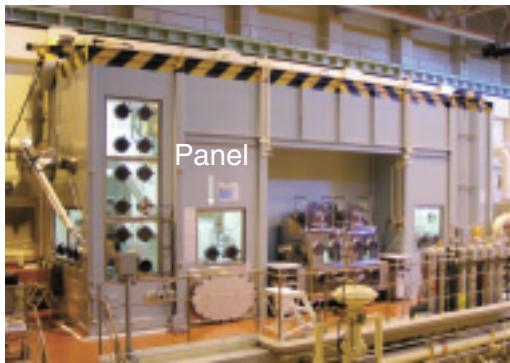


Fig.12-3 Appearance of a large glove box (LGB)

The damaged panel behind the LGB needed replacement at the narrow space.

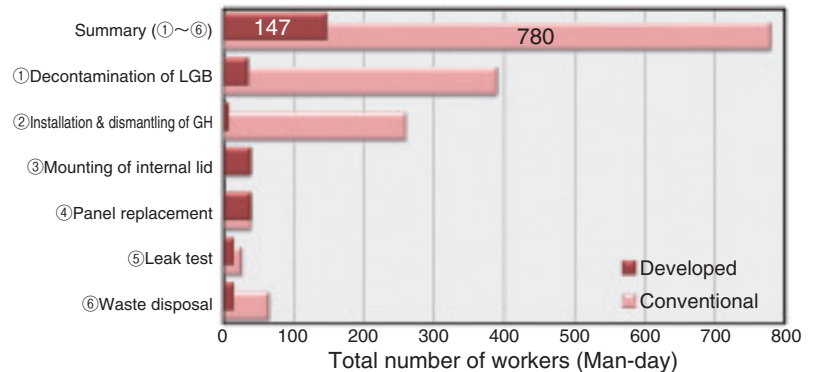


Fig.12-5 Comparison between conventional and developed methods

The total number of workers required for the developed method is approx. one-fifth of that required for the conventional method.

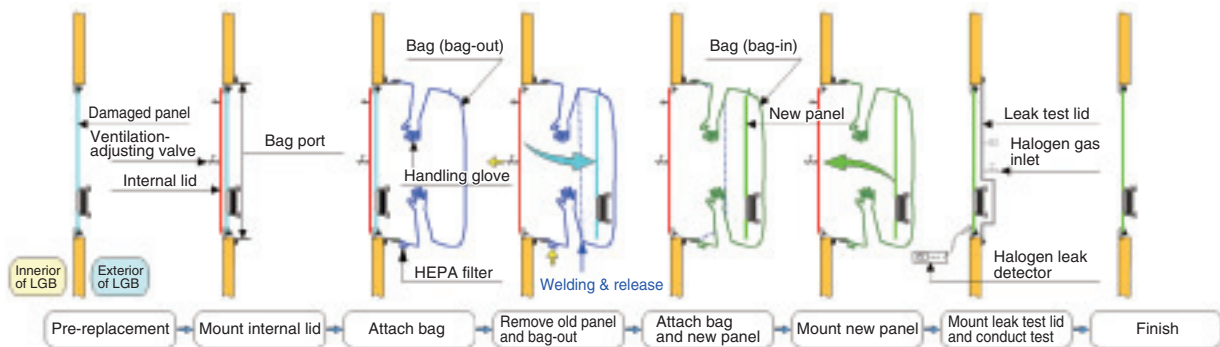


Fig.12-4 Panel replacement procedure with the developed method

An internal lid facilitated the application of the “bag-in/bag-out” method to the panel replacement of the panel of the LGB.

A large glove box (LGB) (Fig.12-3) has been extensively used for the examination of transuranium elements at the Waste Safety Testing Facility (WASTEF). The acrylic panels of this LGB were found to be damaged and were to be replaced.

In the conventional procedure for panel replacement, the panels to be replaced are opened inside a large greenhouse adjoining the LGB to prevent the dispersion of contamination. The operations are performed by workers wearing airline suits. However, this procedure has some drawbacks: the greenhouse should have a large space and the inside of the LGB needs decontamination. To improve the safety and efficiency of the replacement operation, a replacement method based on the bag-in/bag-out method was developed. Normally, the bag-in/bag-out method is not suitable for the handling of large items like LGB panels. The negative inner pressure of the LGB generated a suction force proportionate to the size of the transfer bag. An internal lid was introduced at the opening of the LGB to isolate the area of negative pressure (Fig.12-4). The internal lid prevents the suction of the bag and made it possible to apply the bag-in/bag-out method to replace the LGB’s panel.

The internal lid is equipped with a ventilation-adjusting valve to release and control the air pressure in the bag. The

use of this valve improved the safety and efficiency of the replacement process. The bags are equipped with a high-efficiency particulate air (HEPA) filter to control the air flow from the outside to the inside of the LGB so as to prevent contamination dispersion and reduce the operation time. Another lid, called “leak test lid,” equipped with a halogen gas inlet was developed to easily carry out the leak test (halogen gas leak test method) during/after the replacement.

The results of the performance test for the developed method by using an actual LGB were as follows: (1) Safe and effective replacement of the panel was carried out in the narrow area and (2) the number of days required for the replacement operation was reduced to approximately one-third and the total number of workers required was reduced to approximately one-fifth compared to the requirements of the conventional method (Fig.12-5). In addition, the volume of waste generated in the new method was reduced to approximately one-third of that generated in the conventional method.

The performance test showed that the developed replacement technique was safe, cost-efficient, and labor-saving; therefore, it is expected to be used widely in the field of maintenance of nuclear facilities.

Reference

Sakuraba, N. et al., Replacement Technology for Front Acrylic Panels of a Large-Sized Glove Box Using Bag-in/Bag-out Method, JAEA-Technology 2009-071, 2010, 34p. (in Japanese).

12-3 Removal of Liquid Impurities in Crystal by Sweating

— Purification of Uranyl Nitrate Hexahydrate Crystal by Isothermal Sweating Effect —

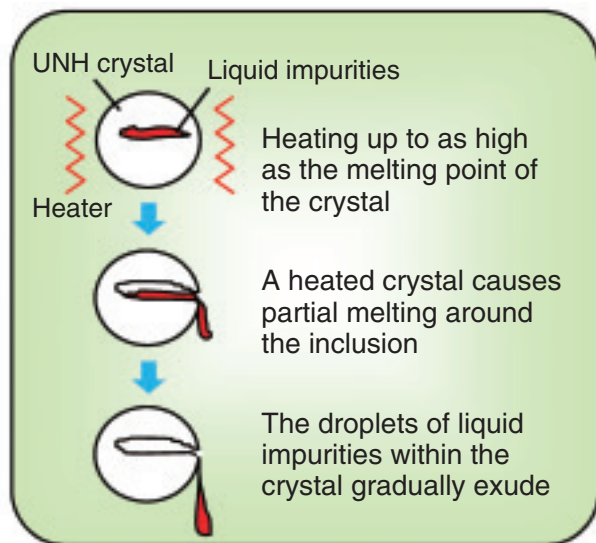


Fig.12-6 Schematic diagram of sweating phenomenon
A UNH crystal containing liquid impurities was heated up to as high as the melting point of the crystal, and the inclusions were drained away from the inside of the crystal along some defects and grain boundaries in the crystalline particle.

The U crystallization process has been studied for the advanced aqueous reprocessing of fast reactor spent fuel. In the crystallization, the U in a dissolver solution of spent fuel is recovered as uranyl nitrate hexahydrate (UNH) crystals. Generally, crystals produced in the crystallizer are often contaminated by the mother liquor, which appears on the surface or inside the bodies of the crystals. Although the liquid impurities on the crystal surfaces are washed off with HNO_3 solution, those included within the crystal are not removed. If the inclusions can be removed, the decontamination factor (DF) will increase. One crystal purification method called “sweating”, which is applied in industry, is proposed for UNH crystal purification. The crystals are purified by heating up to as high as their melting point, and the liquid impurities are removed from the crystal (Fig.12-6). Since the dissolver solution contains more impurities than materials used in industry and the chemical form of UNH is easily changed by heating, the purification effect of UNH by sweating should be evaluated carefully.

Purification experiments were carried out at the Chemical

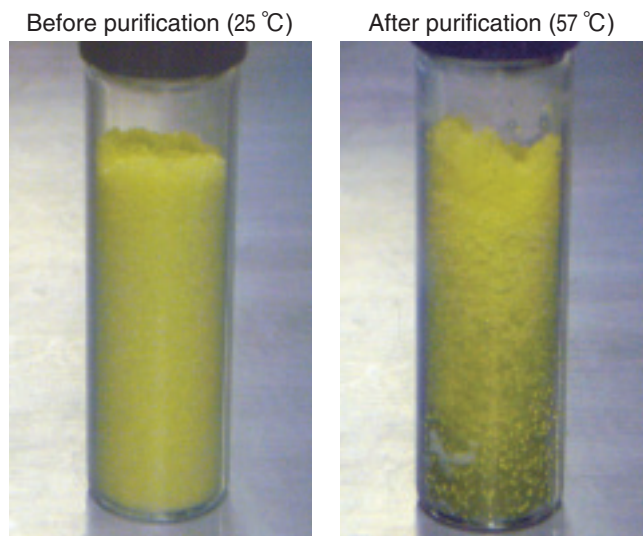


Fig.12-7 UNH crystal before and after purification
The UNH crystals recovered from the dissolver solution of a MOX fuel were placed in a glass vial and immersed in a thermostat bath, which was maintained at 57 °C for 60 min. The incorporated liquid impurities were gathered at the bottom of the glass vial after purification.

Processing Facility (CPF). The dissolver solution of mixed oxide (MOX) fuel containing Eu was cooled, and the UNH crystals were recovered. After washing, the crystals were placed in a glass vial and kept at a constant temperature. The U melt and incorporated mother liquor gathered at the bottom of the glass vial (Fig.12-7), whereas the Eu concentration in the UNH crystal left at the top of glass vial decreased. In this study, the purification of UNH crystals by sweating was confirmed.

Countercurrent equipment, the Kureha Crystal Purifier (KCP), was developed. The crude crystal is fed at the bottom of the column and is carried to the upper side by a conveyor. Part of the crystal is melted by a heating unit, and the crystal is washed with the reflux melts. Higher DFs of liquid impurities can be expected with KCP than in batch-wise purification, because UNH is purified by washing with the molten salt as well as by sweating.

This work was financed by the Ministry of Education, Culture, Sports, Science and Technology of Japan (MEXT).

Reference

Nakahara, M. et al., Removal of Liquid and Solid Impurities from Uranyl Nitrate Hexahydrate Crystalline Particles in Crystal Purification Process, Journal of Nuclear Science and Technology, vol.48, issue 3, 2011, p.322-329.

12-4 Effective Preparation of MOX Pellets

— Development of a New Method for Fabricating MOX Pellets Having Low Oxygen-to-Metal Ratio Using Residual Carbon —

Table 12-1 Testing conditions

Four specimens were separately heated in atmospheres with different P_{H_2}/P_{H_2O} ratios (P_{H_2} : hydrogen partial pressure; P_{H_2O} : moisture partial pressure). Specimen 4 had no carbon, and the influence of carbon on the reduction rate can be understood by comparing specimens 3 and 4.

Specimen	Plutonium content	Carbon content	Heating conditions	P_{H_2}/P_{H_2O} ratio
1	25 wt%	about 3000 ppm	1500 °C×4 h	100(A)* ²
2	25 wt%	about 3000 ppm	1500 °C×4 h	250(B)* ²
3	25 wt%	about 3000 ppm	1500 °C×4 h	833(C)* ²
4	25 wt%	—* ¹	1500 °C×4 h	833(C)* ²

* 1 Prepared without additives
 * 2 Correspond to the atmosphere in Fig.12-10

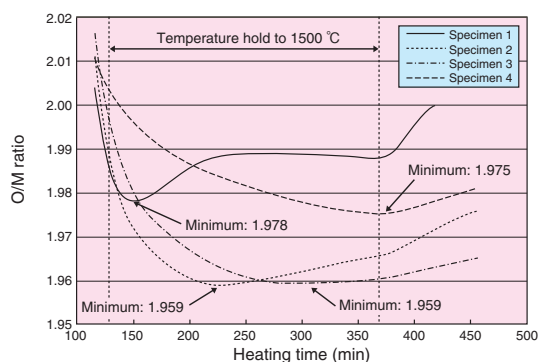


Fig.12-9 Change in O/M ratio during heating

The minimum O/M ratio was observed at the end of the temperature hold for specimen 4 (without carbon) and during the temperature hold for the other specimens (with carbon).

We have developed a method based on the “simplified pellet fabrication process” for the production of Mixed-Oxide (MOX) fuels with low oxygen-to-metal (O/M) ratios to control the chemical interaction between the fuels and cladding for a high burnup of 150 GWd/t. However, a substantial amount of time is required to obtain such MOX pellets by sintering and subsequent annealing. In the current pellet fabrication method, which requires the addition of organic additives to MOX powder, about 3000 ppm of carbon remains in the MOX pellets even after pellets are dewaxed at 800 °C. It is empirically known that the O/M ratio of such MOX pellets can be reduced by using the residual carbon after sintering the pellets at 1700 °C (Fig.12-8). Therefore, a new method for preparing MOX pellets having low O/M ratios was investigated; the method involves the use of residual carbon.

The pellets with carbon (specimens 1~3) and without carbon (specimen 4) were separately heated at 1500 °C in atmospheres having different values of the ratio of the hydrogen partial pressure to the moisture partial pressure (P_{H_2}/P_{H_2O} ratio), as shown in Table 12-1. The O/M ratios of each specimen during the heating were estimated from their weight losses. As shown in Fig.12-9, the O/M ratios of the pellets with residual carbon reached the minimum during the

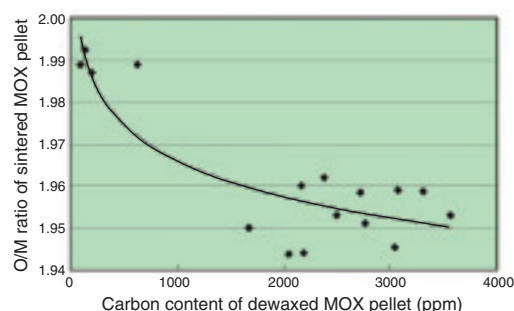


Fig.12-8 Oxygen-to-metal (O/M) ratio vs. carbon content of dewaxed mixed-oxide (MOX) pellets

This figure shows that the O/M ratio decreased upon increasing the carbon content of dewaxed MOX pellets by the current fabrication method.

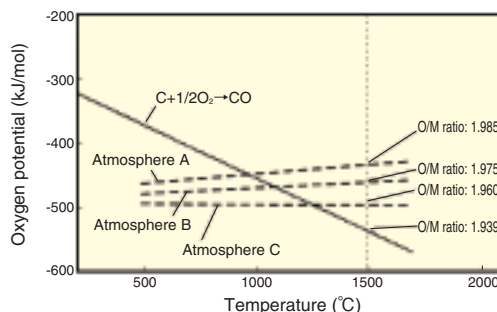


Fig.12-10 Ellingham diagram

The O/M ratio could be effectively reduced by using residual carbon because the oxygen potential equilibrated with the carbon was lower than that equilibrated with each atmosphere at 1500 °C.

temperature hold, whereas the O/M ratios of the pellet without carbon continued to decrease even during the temperature hold. Fig.12-10 shows the oxygen potentials of carbon and the heating atmospheres as a function of temperature. In this figure, the O/M ratios estimated from the oxygen potentials of each atmosphere at 1500 °C are also shown. The oxygen potential of carbon at 1500 °C corresponds to the O/M ratio of 1.939, and is lower than those of the heating atmospheres. Therefore, the O/M ratio of the specimens containing carbon was thought to decrease once toward 1.939 and then increase toward the value corresponding to the oxygen potentials of each heating atmosphere as the residual carbon disappeared in the specimens.

It was found that the influence of the residual carbon was greater than that of the heating atmospheres and that the residual carbon could reduce the O/M ratio in a shorter time. Hence, the addition of carbon to MOX pellets should help in obtaining the desired O/M ratio in large-scale fabrication plants and in overcoming the difficulties associated with the current method such as the inhomogeneous oxygen potentials of sintering atmospheres and the need for a substantial amount of annealing time.

Reference

Murakami, T. et al., Preparation of Low O/M MOX Pellets for Fast Reactors Using Carbothermic Reduction, Proceedings of 2010 International Congress on Advances in Nuclear Power Plants (ICAPP' 10), San Diego, USA, 2010, paper 10015, 7p., in CD-ROM.

12-5 Precise Control of High-Intensity Proton Beams — Beam Handling by the Digital Low-Level RF Control System —

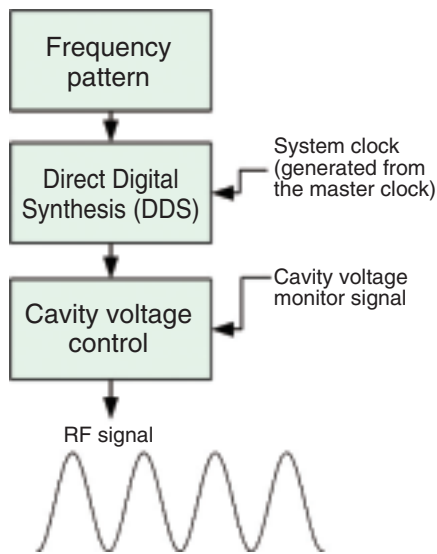


Fig.12-11 Block diagram of the core of the digital LLRF control system

By referring to the master clock, the accuracy of the RF frequency is found to be on the order of 0.1 Hz.

The J-PARC Rapid Cycling Synchrotron (RCS) accelerates proton beams up to an energy of 3 GeV at a repetition rate of 25 Hz and delivers the beams to the Materials and Life Science Experimental Facility (MLF) and the Main Ring (MR). Beam commissioning is in progress with the aim of achieving the design output beam power of 1 MW, while the current beam power is 300 kW. The magnetic alloy (MA) cavity is employed to facilitate stable acceleration of the high-intensity beam. The MA cavity generates a very high accelerating field (20 kV/m), which cannot be generated by traditional ferrite cavities. The RF voltage of the MA cavity is precisely managed by a digital low-level RF (LLRF) control system. The digital LLRF control system (Fig.12-11) generates RF signals using the direct digital synthesis (DDS) technology by referring to the master clock of entire J-PARC facility. The accuracy of the RF signals generated using the DDS technology is over 1000 times higher than that of the signals generated using an analog circuit system, and this considerably improves the reproducibility of beam control. Therefore, beam extraction could be effected at a low-jitter of within 1.7 ns^[1]; thus, the low-jitter performance of this

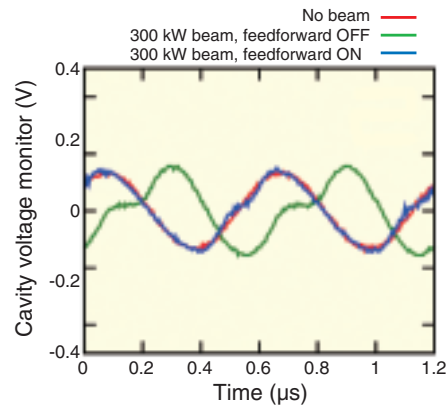


Fig.12-12 Comparison of voltage waveforms without and with feedforward

The voltage distortion and waveform delay observed for the acceleration of a 300 kW beam with feedforward are smaller than those observed for the same beam without feedforward.

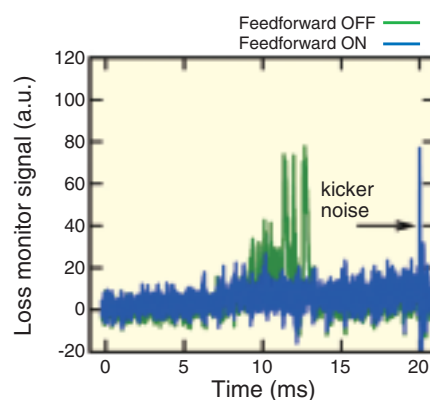


Fig.12-13 Comparison of beam loss in the arc section without and with feedforward

With feedforward (blue) the beam loss is reduced considerably.

synchrotron was the best among that of high-intensity proton synchrotrons around the world. Accurate beam timing helps beam injection to the MR and improves the experimental resolution in the MLF.

The wide-band frequency response of the MA cavity enables efficient beam shape control by RF waveform manipulation, which helps alleviate the space-charge effects of the high-intensity beam. On the other hand, the voltage distortion due to the wideband wake voltage of the high-intensity beam is an issue. We developed a multiharmonic RF feedforward system to solve this issue. The system consists of digital circuits that generate compensation signals from the beam signals collected by a wall current monitor, to cancel the wake voltages. By using the gain and phase patterns, the system responds to changes of the conditions during the acceleration period. We have established a methodology to optimize these patterns^[2]. After optimizing the patterns, the voltage distortion (Fig.12-12) and the beam loss, which was observed during the 300 kW operation, were reduced considerably (Fig.12-13). These results are very promising for achieving the design beam power of 1 MW.

References

- [1] Tamura, F. et al., Achievement of Very Low Jitter Extraction of High Power Proton Beams in the J-PARC RCS, Nuclear Instruments and Methods in Physics Research A, vol.647, issue 1, 2011, p.25-30.
- [2] Tamura, F. et al., Multiharmonic RF Feedforward System for Beam Loading Compensation in Wide-Band Cavities of a Rapid Cycling Synchrotron, Physical Review Special Topics-Accelerators and Beams, vol.14, issue 5, 2011, p.051004-1-051004-15.

12-6 Polarizing the Spins of Pulsed Neutron Beams

— Development of Neutron Polarizing Devices for J-PARC —

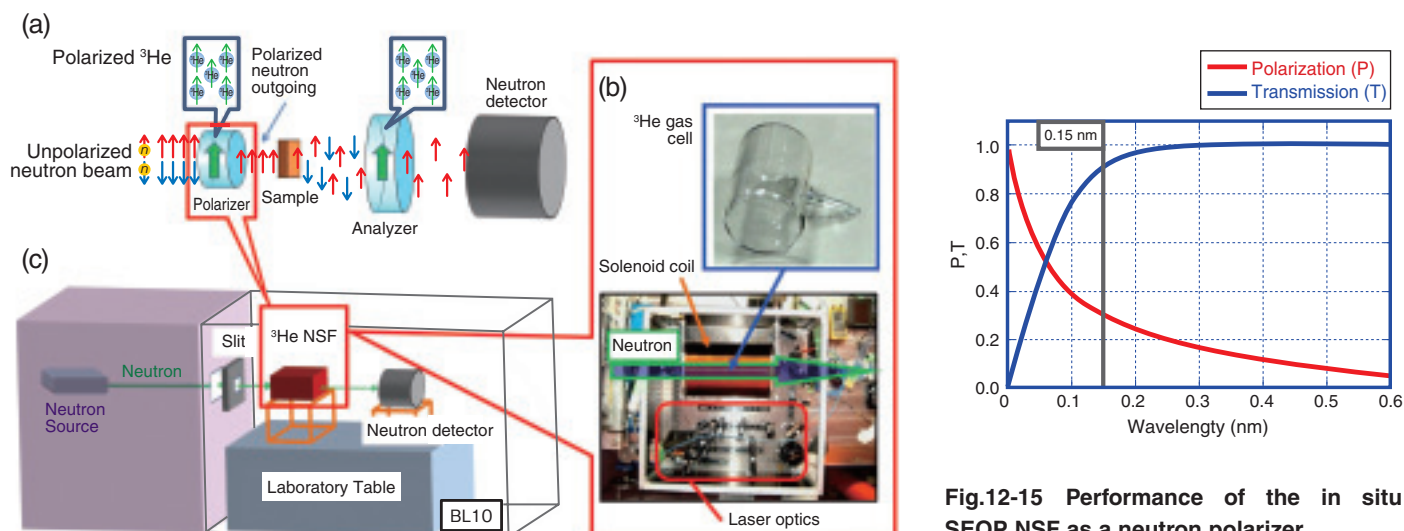


Fig.12-14 Principle of operation of the neutron spin filter and the experimental setup

- (a) Nuclear-spin-polarized ^3He gas selectively removes neutrons with opposite spin states and transmits unaffected neutrons with the same spin.
 (b) Inside the SEOP NSF system: A ^3He gas cell, laser optics, and a solenoid coil are mounted together.
 (c) Experimental setup: ^3He polarization was determined by measuring the neutron transmission at the gas cell.

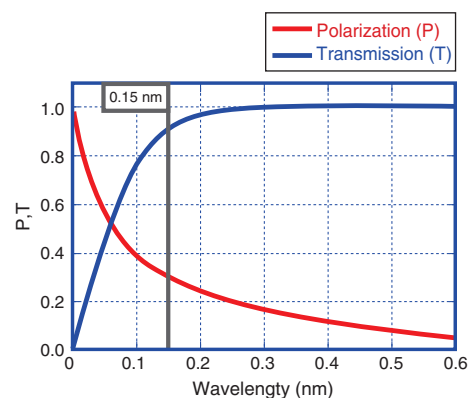


Fig.12-15 Performance of the in situ SEOP NSF as a neutron polarizer

The performance of the NSF depends on the degree of polarization of the ^3He gas, the total amount of ^3He in the cell, and the wavelength of the incident neutrons. The gas cell contained 16.9 atm cm of ^3He , and the ^3He polarization reached 73%. The figure shows the calculated performance of the present NSF system as a neutron polarizer.

Polarized neutron scattering techniques are important and powerful tools in the study of magnetic materials. For several decades, Heusler alloy crystals and magnetic supermirror devices have been widely used to polarize neutron beams. However, such devices cannot effectively manage the pulsed neutron beam of at J-PARC as the beam has a relatively broad energy spectrum.

One of the design requirements for a neutron polarizing device is that the device should be as small as possible so that the contribution to the experimental background, which is derived from shielding, is minimized.

Polarized ^3He gas functions as a neutron spin filter (NSF) (Fig.12-14(a)), and in recent years, ^3He NSFs have been extensively developed around the world. We have designed a compact, in-situ spin-exchange optical pumping (SEOP) polarized ^3He NSF system and employed it as a polarizer for incident beams at the J-PARC (Fig.12-14(b)). In this system, ^3He gas and small Rb droplets are sealed in a glass cell. The cell is heated to 180 °C to vaporize the Rb droplets while applying an external magnetic field. The Rb vapor is optically

pumped using a circularly polarized laser beam, and the electric-spin-polarized Rb in turn polarizes ^3He via hyperfine interaction. The SEOP NSF system was realized through improvements to laser optics in the NSF system.

The performance of the present NSF system was measured at BL10 of the MLF/J-PARC. A schematic of the experimental setup is shown in Fig.12-14(c). Neutron transmission measurements indicated that the ^3He polarization reached as high as 73%. The calculated performance of the NSF as a neutron polarizer is shown in Fig.12-15. The system worked satisfactorily across a wide range of wavelengths with acceptable performance being demonstrated using 0.15 nm neutrons for which, with 30% transmission, 90% polarization was achieved.

Pulsed neutron beams have been successfully polarized at J-PARC using the compact, in-situ SEOP NSF system. The present NSF system may find application in the study of strongly correlated electron systems and the wide variety of physical phenomena in which they are manifested, such as ferromagnetism and superconductivity.

Reference

Kira, H. et al., Development and Test of SEOP Neutron Spin Filter in Japan, *Physica B*, vol.406, issue 12, 2011, p.2433-2435.

12-7 Improving the Safety of Liquid-Metal Facilities

— Countermeasures for Lithium Leak in the IFMIF/EVEDA Lithium Test Loop —



Fig.12-16 The IFMIF/EVEDA lithium test loop (ELTL)

The dimensions of the facility are $15 \times 15 \times 25$ m. 2500 kg of lithium is loaded in the ELTL.

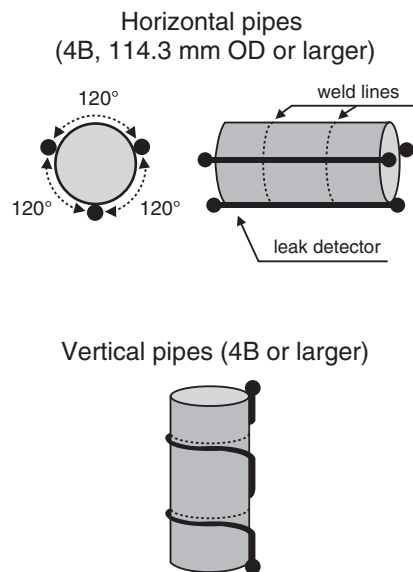


Fig.12-17 Conceptual sketch of the lithium leak detector for pipes

In order to detect any lithium leak, the detectors are arranged near the weld line of the pipes.

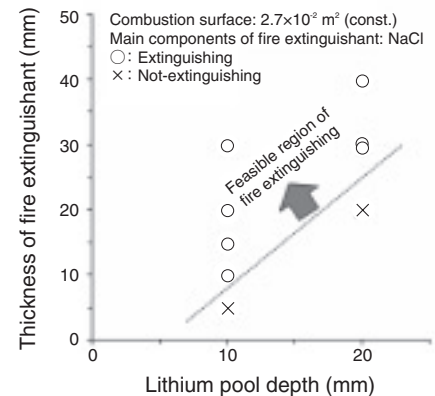


Fig.12-18 Relationship between the lithium pool depth and thickness of the chemical fire extinguishant (Natrex-L) required for fire extinguishing

The volume of fire extinguishant required for the ELTL was estimated from the experimental results.

We are planning a demonstration test of the lithium target system, which is the neutron source for the International Fusion Materials Irradiation Facility (IFMIF). The IFMIF/EVEDA lithium test loop (ELTL)(Fig.12-16) used for the demonstration test is a large-scale equipment, and it consumes a considerable amount of lithium, which has been classified as a flammable element by the fire service law in Japan. Therefore, it is crucial to establish safety measures for the design and construction of the ELTL in case of lithium leakage. The properties of lithium are similar to those of sodium, which is used as a coolant in Japanese fast breeder reactors (FBRs). Hence, observations on the operation of FBRs and the R&D results for the ELTL are useful for establishing safety measures for the ELTL.

Some examples of the safety measures are as follows:

(1) Detection of lithium leaks: The total pipe length of the ELTL is a few hundred meters, and the number of welding points on each pipe is over 500. A contact-type leak detector (CLD) was adopted for detecting lithium leaks in the pipes and main components of the ELTL. The conductivity of a CLD is between the conductivities of lithium and the sensors so that its composition and reliability are stable. The CLDs are arranged at intervals of 120° along the circumference of horizontal pipes and along the welding lines of vertical pipes to facilitate early detection of lithium leaks (Fig.12-17).

(2) Controlling the spreading of the flammable range of lithium: It is known that an intense chemical reaction occurs when lithium comes in contact with concrete, a major component of facilities. Therefore, the concrete floor is covered with a steel liner to prevent lithium from coming into contact with concrete. Moreover, the floor is designed as a reservoir to control the spreading of the lithium leak and the combustion area.

(3) Disposition of the fire extinguishant: It was found that the performance of chemical fire extinguishants composed of sodium chloride was much better than that of fire extinguishants composed of dry sand and pearlite, which were specified in the fire service law by tests. On the other hand, it was found that a portion of the chemical fire extinguishants spread on burning lithium sank into it because of the difference in their specific gravities. Upon investigating the fire extinguishing properties of the chemical fire extinguishants in detail, the relationship between the lithium pool depth and the amount of the chemical fire extinguishant (Natrex-L) required for extinguishing the fire was obtained (Fig.12-18). This knowledge is used to devise the safety measures for the ELTL.

The construction of the ELTL was completed in November 2010. Its basic performance meets the requirements of the demonstration test, which will start in FY 2012.

Reference

Furukawa, T., Hirakawa, Y. et al., Safety Concept of the IFMIF/EVEDA Lithium Test Loop, Fusion Engineering and Design, vol.86, issues 9-11, 2011, p.2433-2436.

12-8 Viewing the Behavior of Fuel Pellets

— Irradiation Behavior Investigation of FBR Fuel by High-Resolution X-ray CT —

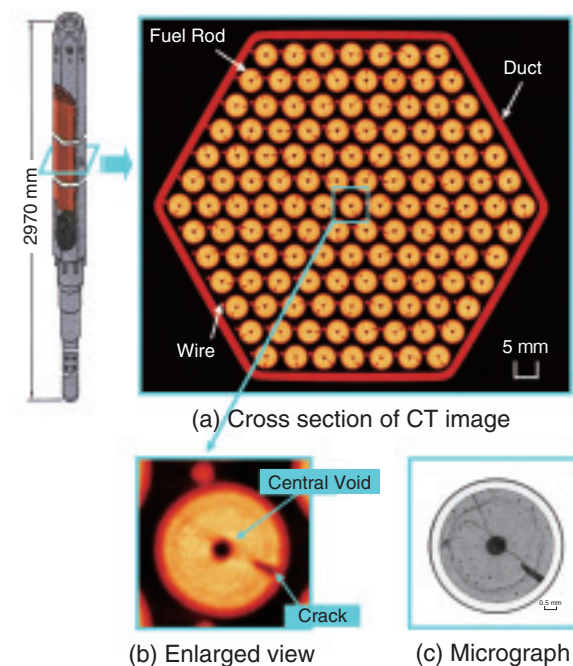


Fig.12-19 High-resolution computed tomography (CT) image of fuel assembly (upper) and enlarged view of fuel pellet (bottom)

(a) A high-resolution CT image of the fuel assembly was obtained successfully.

(b) (c) The central void and crack can be observed clearly like in a micrograph.

In order to develop fast breeder reactor (FBR), it is important to investigate irradiation performance of FBR fuels and materials by Post Irradiation Examination (PIE). In the Fuel Monitoring Facility (FMF), non-destructive examination using the X-ray Computed Tomography (CT) technique was developed to observe irradiation performance of FBR fuel assembly and fuel rod.

In this study, the previous X-ray CT apparatus was upgraded to observe irradiation performance of the FBR fuel in the intact fuel assembly by using high resolution X-ray CT image. In order to obtain high resolution X-ray CT image, highly sensitive silicon semiconductor detectors (number of detector: 30→100) and a tungsten collimator with thin slits (width: 0.3 mm→0.1 mm, number of slits: 30→100) was installed in this X-ray CT apparatus. As a result, the one-pixel size of the CT image was reduced from 0.3 mm to 0.1 mm, and a high resolution X-ray CT image of the irradiated fuel assembly was obtained (Fig.12-19 (a)). The duct tube, fuel rods, wrapping wire, cladding, crack, and central void can

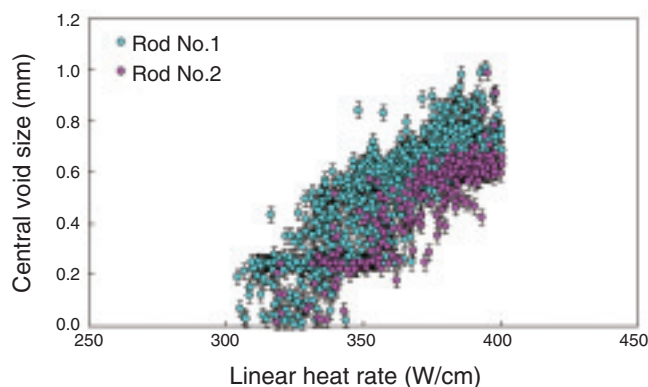


Fig.12-20 Formation of central void

The central voids are formed at more than 300 W/cm, and the effect of fuel pellet specification are checked in Fig.12-20.

be clearly observed in high resolution X-ray CT image (Fig.12-19 (a) (b)). In addition, the X-ray CT image gave almost the same results as those from the destructive examination (Fig.12-19 (c)).

In order to estimate the irradiation behavior of FBR fuel, the central void formed in fuel pellet was analyzed using this technology. Analysis results of central void size in the fuel pellet are shown in Fig.12-20. This figure shows that the central void was formed at more than about 300W/cm, and was dependent on the linear heat rate. Furthermore, this result shows that the central void size was affected by specification of fuel pellet. These results obtained using this technology can be applied to design FBR fuel.

This paper contains some results obtained within the task "Study of the irradiation behavior of the fuel pellets using the high-resolution X-ray CT technique" entrusted from the Ministry of Education, Culture, Sports, Science and Technology of Japan (MEXT).

Reference

Katsuyama, K. et al., Three-Dimensional X-ray CT Image of an Irradiated FBR Fuel Assembly, Nuclear Technology, vol.169, no.1, 2010, p.73-80.

12-9 Challenges to Domestic Production of ^{99}Mo Using JMTR — Development of a New Mo Adsorbent for ^{99}Mo - $^{99\text{m}}\text{Tc}$ Generator —

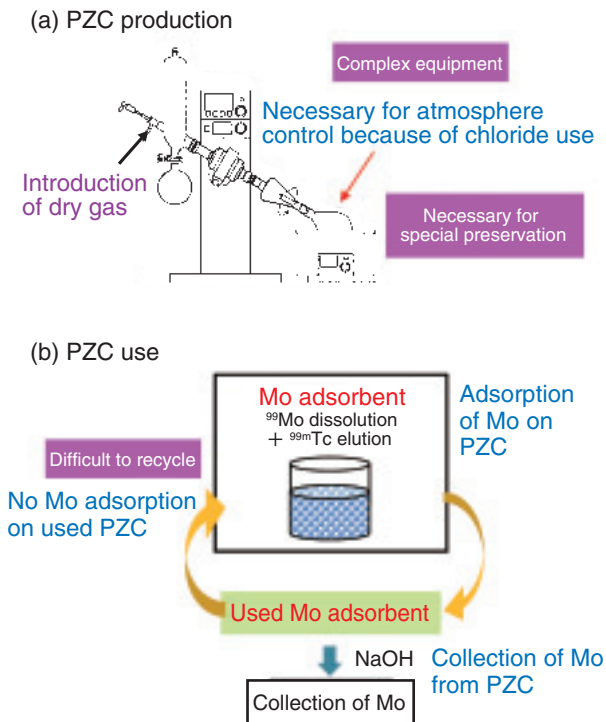


Fig.12-21 Properties of the conventional Mo adsorbent (PZC)

(a) In PZC production, it is necessary to use complex PZC production equipment and preserve PZC using a special method.
(b) Recycling of used PZC is difficult.

$^{99\text{m}}\text{Tc}$ is used as a radiopharmaceutical for diagnosis. $^{99\text{m}}\text{Tc}$ is used in more than 50% of the nuclear medicine diagnosis cases in Japan. $^{99\text{m}}\text{Tc}$ is obtained from the β -decay of ^{99}Mo . The demand for ^{99}Mo in Japan is the second highest in the world; however, the supply of ^{99}Mo depends entirely on the import from foreign countries. A steady supply of ^{99}Mo from domestic production is required because of the unplanned shutdown of aged research reactors that produced ^{99}Mo , in foreign countries, and the difficulty in the airlift to Japan owing to volcanic eruption. ^{99}Mo is obtained by separating the fission products of ^{235}U , from the neutron capture reaction $^{98}\text{Mo}(n, \gamma)^{99}\text{Mo}$, etc. The $^{98}\text{Mo}(n, \gamma)^{99}\text{Mo}$ reaction has been selected for ^{99}Mo production in the Japan Materials Testing Reactor (JMTR). Poly-zirconium compound (PZC) has been studied for use as a Mo adsorbent in a ^{99}Mo - $^{99\text{m}}\text{Tc}$ generator. However, PZC requires complex equipment for synthesis and special preservation methods and is difficult to recycle (Fig.12-21). Hence, the technical development of a new Mo

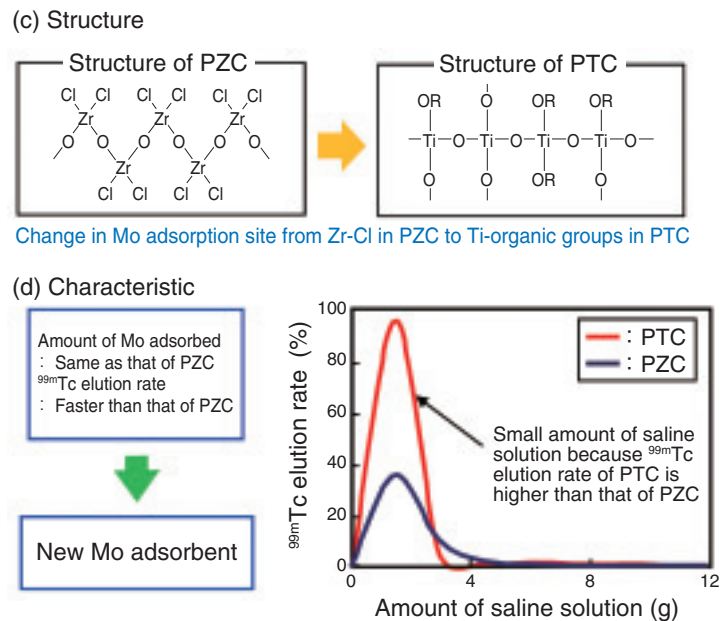


Fig.12-22 The newly developed Mo adsorbent

(c) A new Mo adsorbent with Ti-organic groups as Mo adsorption sites was successfully synthesized without using chloride.

(d) The performance test shows that the new Mo adsorbent adsorbs almost the same amount of Mo as does PZC but has a higher $^{99\text{m}}\text{Tc}$ elution rate.

adsorbent was started to overcome these drawbacks. In this process, first the structure of the Mo adsorbent was analyzed. Next, the Mo adsorption sites were changed from chlorine groups to organic groups (Fig.12-22(c)). Titanium alkoxide was used as the raw material instead of zirconium tetrachloride (ZrCl_4). Consequently, the equipment was simplified because chlorine removal was no longer required. From these studies, a production method for a new Mo adsorbent, polytitanium compound (PTC), was developed.

A performance test was carried out on PTC at Japan Research Reactor No.3 Modified (JRR-3M). It was found that the amount of Mo adsorbed by PTC is the same as that adsorbed by PZC and that the $^{99\text{m}}\text{Tc}$ elution rate of PTC is higher than that of PZC (Fig.12-22(d)). Furthermore, it was found that Mo can be collected from the used PTC and that the Mo-desorbed PTC can be reused. Thus, this development contributes to the reduction of radioactive waste.

Reference

Kimura, A. et al., Development of New Molybdenum Adsorbent, JAEA-Technology 2011-012, 2011, 17p. (in Japanese).

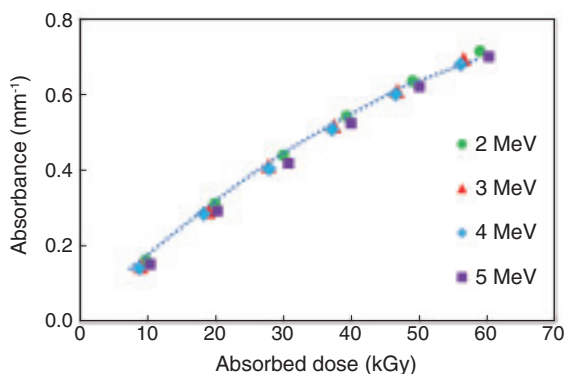
12-10 Expansion of Measurable Dose Range

— Development of Dosimetry for Quality Assurance in Radiation Processing —



Fig.12-23 Clear polymethylmethacrylate (PMMA) dosimeter, Radix W

The components are sealed in an aluminum-laminated pouch to prevent absorption of moisture from the air. The pouch is opened after irradiation. The absorbed dose of the dosimeter is estimated from the optical density measured using a spectrophotometer.



Many medical and healthcare products are sterilized by ionizing radiation. The completion of sterilization is evaluated by measurement of the absorbed dose in products. Insufficient irradiation of the products may have a harmful influence on our health. In the radiosterilization process, the dose value required to complete sterilization is determined using the initial number of bacteria in the products before irradiation. Such dose values range from 1 kGy to several tens of kGy. Reliable dose evaluation over a wide range is therefore important for the quality assurance of irradiated products.

Radix W, a clear polymethylmethacrylate (PMMA) dosimeter based on radiation-induced coloration, is currently used in cobalt 60 γ -ray processing (Fig.12-23). However, its response at a dose range of less than 10 kGy is low and leads to measurement error. Therefore, the dose-response characteristics of Radix W were studied at readout wavelengths of 270~320 nm to improve the measurement accuracy. As shown in Fig.12-24, the dose response for 0.5~10 kGy at 280 nm was higher than that at the conventional wavelength of 320 nm. A wide dose range of 0.5~150 kGy can be measured with high accuracy

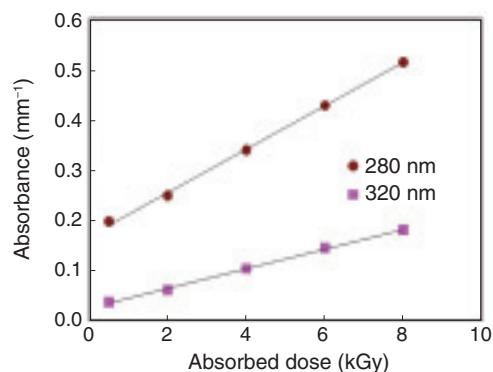


Fig.12-24 Dose-response curves of Radix W for different readout wavelengths

The dose response of Radix W is much higher at 280 nm than at 320 nm. The measurement accuracy for 0.5~10 kGy is improved by changing the readout wavelength from 320 nm to 280 nm. The effect of the irradiation temperature on the dose response is independent of the readout wavelength.

Fig.12-25 Dose-response curves of Radix W for electron beams

The absorbance at the dosimeter surface estimated considering the dose distribution along the depth is independent of the electron energy (the dotted line represents an approximate curve for all the data plotted in the figure).

using only a Radix W dosimeter, employing two readout wavelengths of 280 nm and 320 nm.

However, thin-film dosimeters with thicknesses in the range 10~100 μm have commonly been used in electron-beam (EB) processing with dose rates higher than that used in γ -ray processing. The thin-film dosimeters are not uniform in thickness and are difficult to handle. The characteristics of the Radix W dosimeter, having better uniformity in terms of thickness (diameter), were studied for MeV electron beams. The dose-response curves resulted in one line, independent of the electron energy, in the range 2~5 MeV (Fig.12-25). The Radix W dosimeter can also be applied to electron-dose evaluation.

These results demonstrate that only one kind of dosimeter, Radix W, is useful for routine process control in both γ -ray and EB processing.

The published paper from this study is cited in the international standards on the regulation of dosimetry performance (ISO/ASTM51276), and contributes to quality control in radiation processing with higher reliability.

Reference

Seito, H. et al., Characteristics Study of Clear Polymethylmethacrylate Dosimeter, Radix W, in Several kGy Range, Radiation Physics and Chemistry, vol.78, issue 5, 2009, p.356-359.

12-11 Excavation of Research Tunnels Deep Underground

— Excavation and Construction of Shafts and Tunnels at the Mizunami Underground Research Laboratory —

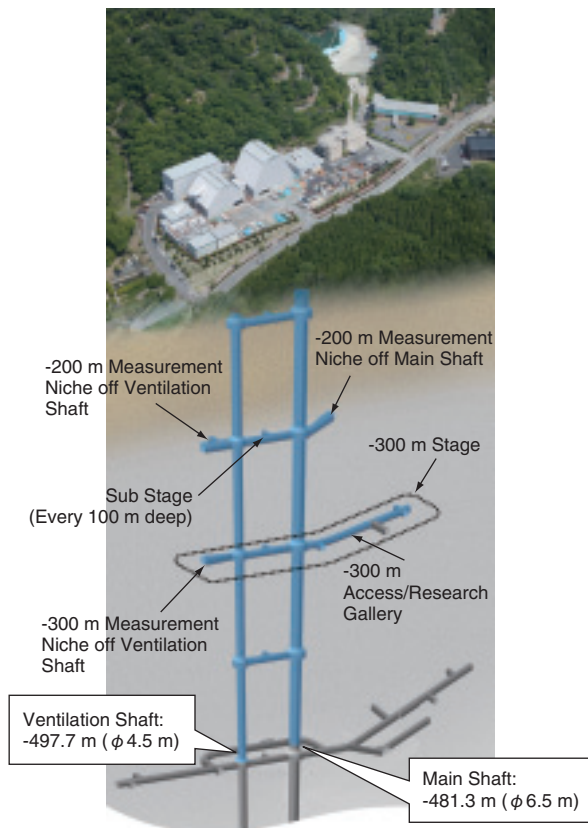


Fig.12-26 Layout of the Mizunami Underground Research Laboratory

Depth of the shafts as of March 31, 2011.

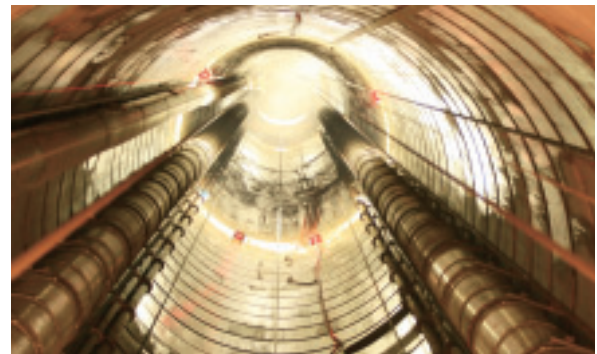


Fig.12-27 View from inside of the Main Shaft: upward perspective
Main Shaft diameter is 6.5 m.



Fig.12-28 Geological mapping underway in the Ventilation Shaft

Ventilation Shaft diameter is 4.5 m.

The Mizunami Underground Research Laboratory, one of the main facilities in Japan for the research and development of technology for high-level radioactive waste disposal, is currently under construction in Mizunami City. As of March 2011, the excavation of the Main and Ventilation Shafts had reached GL -481.3 m and -497.7 m, respectively (meters below ground level, Fig.12-26, Fig.12-27 and Fig.12-28).

- Excavation of Main Shaft (from GL -459.6 m to -481.3 m)
- Excavation of Ventilation Shaft (from GL -459.8 m to -497.7 m)

In order to mitigate potential excess groundwater inflow, pre-excavation grouting was conducted before the excavation of the Ventilation Shaft from GL -421 m to -428 m and from GL -446 m to -453 m. Grouting refers to the injection of material such as cement, into open fractures in a rock mass to stabilize and seal the rock.

While planning the construction, it was necessary to obtain

reliable, preliminary information on the bedrock conditions in terms of the rock mass stability and hydrogeology, and therefore site characterization borehole investigations, including pilot borehole drilling were conducted before the excavations began. The results indicated that large groundwater inflow could be expected during the excavation of the Ventilation Shaft at around GL -200 m and from GL -400 m to GL -460 m and near the -300 m Access/Research Gallery.

While planning the construction, the water-inflow reduction target was established by theoretical analysis of groundwater flow with respect to the bedrock conditions. The subsequent excavations have shown that the pre-excavation grouting was successful, and that the targeted reduction in inflow was achieved. Thus, the results indicate that this methodology is effective in reducing water inflow.

Reference

Mikake, S., Yamamoto, M., Ikeda, K., Applicability of Countermeasures during Excavation and Construction of the Mizunami Underground Research Laboratory, Proceedings of the 40th Symposium on Rock Mechanics, Committee on Rock Mechanics, Japan Society of Civil Engineers, 2011, p.191-196 (in Japanese), in CD-ROM.

12-12 A Trial for Uranium Wastes Assay Used Neutrons!!

— Developments of NDA Tools of Uranium Wastes Drums: NWAS —

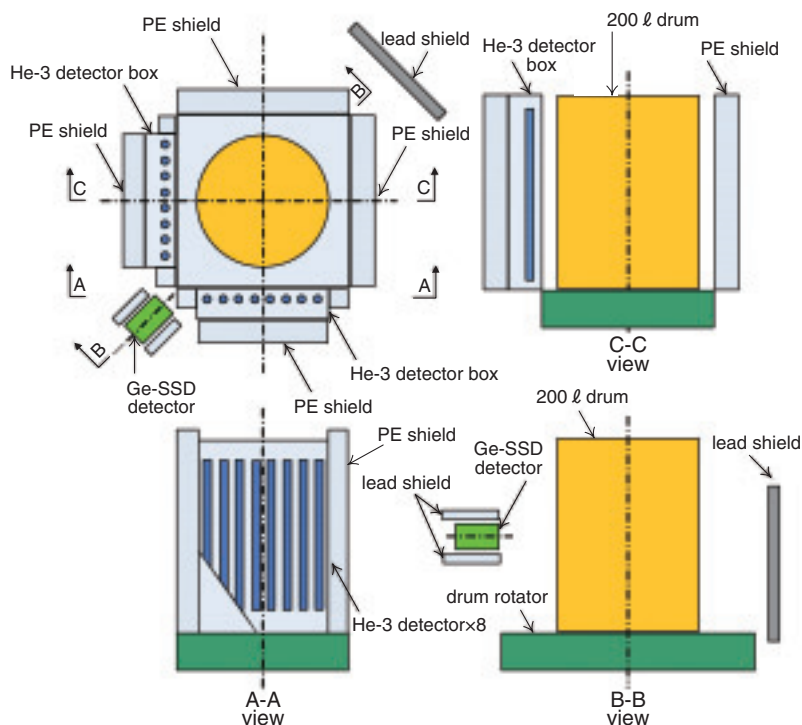


Fig.12-29 The structure of Ningyo Waste Assay System (NWAS)

High density polyethylene blocks are installed in detector boxes, also delivered as shield around wastes drums. The measurements are performed with drum rotation.

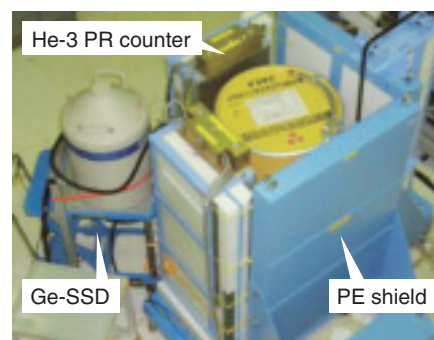


Fig.12-30 The outer and inner views of NWAS

The length of neutron detectors is accorded with drum height. Germanium solid state detector is settled between two neutron detector boxes.

We developed a uranium mass assay systems for 200 ℓ wastes drums generated in Ningyo-toge applied neutron measurements by the nondestructive assay (NDA) method; the system is named Ningyo Waste Assay System (NWAS). The system is composed of 16 helium-3 proportional counters for neutron detection and a high purity Ge solid-state detector for gamma- ray detection (Fig.12-29, Fig.12-30).

The key methodologies of the measurements are the spontaneous fission neutrons derived from U-238 and the (α ,n) reaction generated from α -particles from U-234 captured by low-Z elements, including a particularly large proportion of fluorine atoms. The (α ,n) reaction rate may increase with uranium enrichment, so gamma- ray energy spectrometry is required for each drum. The advantages of neutron measurements are the good penetration of neutrons through high-Z matrices such as steel, and the relatively higher counting efficiency. Both these advantages make this process better than the γ -ray assay for uranium.

The extensive mock-up testing trials were performed using calibrated uranium powder sources of different enrichments and with different kinds of matrices (such as sodium fluoride pellets, alumina pellets, steel bars, and so on) in drums.

Through a series of tests, the calibration factors, i.e., neutron counts versus uranium masses, were obtained.

Through the mock-up testing we were convinced of the relatively low levels of uranium mass (up to 10~20 gU), which varied according to the uranium enrichment or the drum matrix of drums.

Applying the above factors, we have then attempted the measurements of actual wastes drums stored in the Uranium Refining and Conversion Plant at Ningyo-toge. The chemical features of the facility are mainly characterized as uranium fluorides compounds, so the chemical form of the uranium wastes is also characterized as uranium fluorides compounds. NWAS is perfectly suited for the measurements of such wastes.

We have applied NWAS to the following activities: (1) the establishment of material accountancy, and (2) the determination of bulk material from the facility in the wastes drums. Further extensive use is expected if accuracy is improved. Our current work focuses on these challenges.

Our research was accomplished with the support of Los Alamos National Laboratories.

Reference

Zaima, N. et al., On Performance Experience and Measurements with Ningyo Waste Assay System (NWAS), JAEA-Technology 2010-046, 2010, 31p.

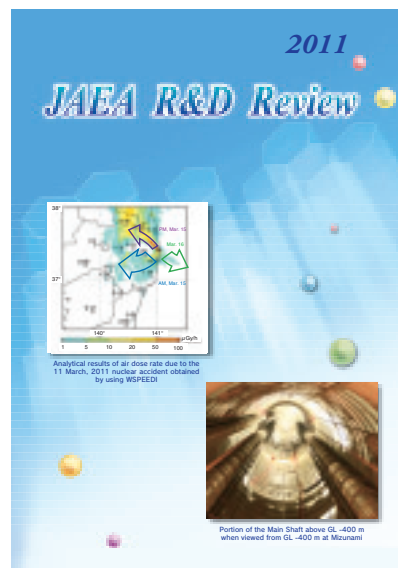
About the Design of the Cover :

The cover is designed to envisage a hopeful future shining in the sky which is a clear blue like the color of the JAEA logo. This is accompanied with white colored hexagons similar to the pattern in a tortoise shell which symbolizes the wish of people for longer lives from ancient times in Japan. Coincidentally, this shape is the same as that of core fuel assemblies for both the prototype fast breeder reactor "MONJU", and the high temperature engineering test reactor "HTTR".

The images on the cover show the analytical results of air dose rate obtained by using WSPEEDI (top left), and view up inside the Main Shaft from GL -400 m (400 m below ground level) at Mizunami (bottom right).

The former shows the estimated results of the behavior of radioactive nuclides discharged from the Fukushima Daiichi NPS during the period from March 15 to 16, 2011. The high air dose rate in the northwest direction from the plant can be explained by this analysis (Topic chapter 7 introduction).

The latter shows the Main Shaft at the Mizunami Underground Research Laboratory. Its diameter is 6.5 m. As of March 2011, the excavation of the Main Shaft had reached GL -481.3 m. The image is view up inside the Main Shaft from GL -400 m (Topic 12-11).



JAEA R&D Review 2011

Editorial Board

Chief editor: Yukio Oyama

Vice editor: Keizo Itabashi

Editors: Shigeru Wada, Yoshio Suzuki, Masaru Watahiki, Tetsukuni Oikawa, Naofumi Kozai, Takamasa Mori, Kazuhiro Sawa, Hiroyuki Yamamoto, Shimpei Matsushashi, Mitsuru Kikuchi, Kazunori Hirao, Masayuki Takeuchi, Fumiaki Yamada, Naotaka Shigeta, Yutaka Kameo, Tetsuro Ishii, Ko Kikuchi, Hiroshi Takada, Makoto Ooka, Masahiro Ishihara, Hiroshi Tanaka, Kazumasa Narumi, Shinichiro Mikake, Hideaki Yoshida

Published by Japan Atomic Energy Agency (JAEA)

Editorial Office: Intellectual Resources Section, Intellectual Resources Department

2-4 Shirakatashirane, Tokai-mura, Naka-gun, Ibaraki-ken 319-1195, Japan

Phone: +81-29-282-6387 Facsimile: +81-29-282-5920

e-mail: ird-seika_shi@jaea.go.jp



Japan Atomic Energy Agency